Boundary Conditions for Granular Flows
at Penetrable Vibrating Surfaces:
Applications to Inclined Flows of Monosized Assemblies
and to Sieving of Binary Mixtures

by

Wael El Khatib

A Dissertation

Submitted to the Faculty

Of

Worcester Polytechnic Institute

In partial fulfillment of the requirements for the

Degree of Doctor of Philosophy

in

Mechanical Engineering

by

_____

April 2013

APPROVED:

_____
Prof. Mark Richman, Advisor

_____
Prof. Nikolaos Gatsonis, Committee Member

_____
Prof. David Olinger, Committee Member

_____
Dr. Jayant Khambekar, Committee Member

_____
Prof. John Blandino, Graduate Committee Representative

Abstract

The purpose of this work is to study the effects of boundaries on granular flows down vibrating inclines, on segregation in granular mixtures induced by boundary vibrations, and on flows of granular mixtures through vibrating sieves. In each case, we employ techniques borrowed from the kinetic theory to derive an appropriate set of boundary conditions, and combine them with existing flow theories to calculate the profiles of solid volume fraction, mean velocity, and granular temperature throughout the flows. The boundaries vibrate with full three-dimensional anisotropy in a manner that can be related to their amplitudes, frequencies, and phase angles in three independent directions. At impenetrable surfaces (such as those on the inclines), the conditions derived ensure that momentum and energy are each balanced at the boundary. At penetrable surfaces (such as sieves), the conditions also ensure that mass is balanced at the boundary. In these cases, the momentum and energy balances also are modified to account for particle transport through the boundary. Particular interest in all the applications considered here is in how the details of the boundary geometry and the nature of its vibratory motion affect the resulting flows.

In one case, we derive conditions that apply to a monosized granular material that interacts with a bumpy, vibrating, impenetrable boundary, and predict how such boundaries affect steady, fully developed unconfined inclined flows. Results indicate that the flows can be significantly enhanced by increasing the total energy of vibration and are more effectively enhanced by normal vibration than by tangential vibration. Regardless of the direction of vibration, the bumpiness of the boundary has a profound effect on the flows.

In a second case, we derive conditions that apply to a binary granular mixture that interacts with a flat, vibrating, penetrable sieve-like boundary, and predict how such boundaries

affect the process in which the particles pass through the sieve. In the special case in which the particles are all the same size, the results make clear that energy is more effectively transmitted to the assemblies when either the total vibrational energy or the normal component of the vibrational energy is increased, but that an increase in the energy transferred to the material can sometimes actually decrease the flow rates through the sieve. Consequently, at any instant of time in the sieving process, there is an optimum level of vibrational energy that will maximize the flow rate.

For the sieving of binary granular assemblies, the physics associated with the effects of energy transfer on the flow rates still applies. However, in these cases, the flows through the sieve are also profoundly affected by segregation that occurs while the particles reside on sieve before the pass through. For this reason, we also isolate the segregation process from the sieving process by considering the special case in which the holes in the vibrating sieve are too small to allow any particles to pass through. In this case, the results show that under most circumstances the region immediately adjacent to the vibrating surface will be populated almost entirely by the smaller particles or by the more dissipative particles if there is no size disparity, and that the reverse is true in a second region above the first.

Acknowledgements

I would like to thank members of my dissertation committee: Prof. Gatsonis: Prof. Blandino: Prof. Olinger; and Dr. Khambekar, for reading my dissertation. Especially, I would like to express my utmost gratitude to my advisor Prof. Richman for his continuous guidance and valuable assistance throughout this research, and in the preparation of this thesis. Without him, this project would not be a success.

I am very thankful for all the help I got from the mechanical engineering department at WPI, especially from Barbara E., Barbara F., Statia C., Randy R., and Larry R.

Special thanks to Dr. Adriana Hera for all her support, and help using MATLAB.

I would like to thank Dr. Najib Khatib for his encouragement to pursue my Ph.D., and for his support and guidance throughout the past decade.

Last, but not least, I would like to thank my friends, especially Anastasios Gavras, and express a special debt of gratitude to my family for their unconditional support and encouragement to pursue my interests.

Table of Contents

Chapter 1

Outline and Literature Review

A granular material is an assembly of discrete solid particles dispersed in a gas. Flow of granular systems is ubiquitous in nature and technology. Handling of these materials is required in such industrial applications as: food processing of products such as rice, beans, grains, and breakfast cereals; mineral processing of such materials as coal; transport of sand and gravel; processing of ceramics such as argil and glaze powder; handling of pharmaceuticals such as triturates and tablets, and chemicals such as plastics. In fact, it is estimated that half of the products and three-quarters of the raw materials in chemical industry are in the form of particulates (Nedderman [1992]). At Dupont, for example, more than sixty percent of their products are found to be powders, crystalline solids, granules, flakes, dispersions, slurries and pastes (Studt [1995]). Estimates are that we waste forty percent (Ennis et. al. [1994]; Knowlton et. al. [1994]) of the capacity of many of our industrial plants because of problems related to the transport of these materials. Also, it is estimated that about ten percent of the world's energy consumption is spent on transporting or processing granular materials. Additional manufacturing processes, for example in the automotive industry, rely on casting large metal parts in carefully packed beds of sand. Even a small improvement in our understanding of granular media behavior could have a profound impact on industry. As a result, these flows have been the subject of many experiment and theoretical investigation. The flow of granular materials are also common in geophysical phenomena such as rock slides, landslide, debris flows, rock falls, underwater sediment slumps, dune formation ,snow avalanches, ice jams.

Depending on circumstances, granular materials generally can exhibit either the properties of a solid or a fluid; they can take the shape of the container in their fluid-like

behavior and they can be stacked in heaps like a solid. The state exhibited by a granular material depends on the local stress conditions. When the granular material exhibits solid behavior, much of the load is supported across frictional bonds between the particles, and the system's strength is limited to the loads those bonds can support. The particles interact through enduring contacts, and when a sufficient fraction of the bonds have been overcome, the system will fail and begin to flow. When the granular materials flows like a fluid, momentum and energy is transported throughout the assemblies by collisions. Many factors influence the motion of granular materials including the size, shape, density, surface roughness and contact stiffness of particles. Also, flow conditions that influence behavior include flow depth, ambient temperature, pressure, humidity, and oftentimes most importantly, the interaction of particles with confining boundaries.

Sieving is probably the oldest and most widely used method for solid-solid separation. It is relatively rapid and simple and, therefore, a popular method, but it has not received the scientific attention it deserves. Because of the many variables involved and the interactions among them, no satisfactory method of predicting the sieving process has yet been developed. In practice, sieving is performed based more on experience and intuition rather than theoretical foundation.

1.1 Outline

To date, much theoretical work has been done in deriving constitutive theories for flowing granular materials. However, much less work has been done in studying the interactions between the flows and the boundaries that contain, excite, and sometimes are even primarily responsible for driving the flows. Our fundamental concern, therefore, is in presenting a general approach to deriving boundary conditions that capture the physics of these interactions. In particular, we are

interested in extending previous work to cases in which the boundaries can vibrate with full three-dimensional anisotropy. Furthermore, in order to properly model the effects of vibrating *sieves*, the boundary conditions should apply at *penetrable* boundaries through which the particles can pass.

In Chapter 2, as background, we introduce the kinetic theory approach to describing flows of granular materials and present an existing kinetic constitutive theory for granular materials consisting of identical particles.

In Chapter 3, we derive a set of boundary conditions that is consistent with the theory presented in Chapter 2. The conditions ensure that momentum and energy are properly balanced at a bumpy *impenetrable* boundary that vibrates with fully three-dimensional anisotropy. The vibrations of the boundary are described in a statistical manner that is related to the amplitudes, frequencies, and phase angles of the vibrations in three independent perpendicular directions.

In Chapter 4, we combine the boundary conditions derived in Chapter 3 with the flow theory presented in Chapter 2 to analyze how gravity-driven inclined granular flows are influenced by boundary vibrations and boundary bumpiness. As a special case, when the angle of inclination is equal to zero, we focus on assemblies of granular materials that are supported from below by horizontal surfaces, and show how the effects of boundary vibrations are coupled to the boundary bumpiness in thermalizing and conveying the assemblies.

In Chapter 5, we shift focus to *penetrable* sieve-like vibrating boundaries, and derive conditions that ensure that mass, momentum, and energy are all balanced at such boundaries when they interact with binary granular mixtures. The sieve geometry of this boundary is very different than the bumpy geometry considered in Chapter 3, but the vibratory motion is characterized in the same manner.

In Chapter 6, we specialize the boundary conditions derived in Chapter 5 to monosized assemblies, and combine them with the flow theory introduced in Chapter 2 to study the sieving of monosized assemblies. The focus of the results is on how the flows through the sieve are affected by the geometry of the boundary (i.e. the spacing between the fibers of the sieve mesh) and the vibrations of the boundary (i.e. both the total energy of vibration and the manner in which it is distributed directionally). The results reveal several important elements of the physics that governs sieving of multi-sized materials.

Finally, in Chapter 7, we combine the boundary conditions derived in Chapter 5 for binary granular mixtures with a constitutive theory for binary granular mixtures that is in many ways the analog of the theory for monosized assemblies introduced in Chapter 2. Using this formulation, results are obtained in two important cases. In the first case, the holes in the vibrating boundary are too small to allow either particle species to pass through, so that vibration-induced segregation can be studied isolated from the sieving process. This is important because the physics governing the manner in which materials are sieved according to size is significantly influenced by the segregation that occurs before the particles ever pass through the sieve. In the second case, the holes in the vibrating sieve are large enough to allow particles to pass through. In this case, we study how the boundary vibrations, boundary geometry, and size disparity between the particles interact to affect the flows through the sieves.

1.2   Review of Previous Work

Over the last three decades there has been a resurgence of interest in the field of granular flows within the engineering and physics communities. (For overviews, see Campbell [1990]; Jaeger and Nagel [1992]; Behringer [1993]; Bideau and Hansen [1993]; Jaeger et. al. [1994];

Mehta [1994]; Jaeger et. al. [1996]; Jean Rajchenbach [2000]; Isaac Goldrisch [2003]; Charle Forterre and Oliver Pouliquen [2008, 2009]).

Much of the theoretical analysis of rapid granular flows exploits the physical similarity between particle interactions in rapid granular flows and molecular interactions in the kinetic-theory view of gases (Ogawa [1978]; Savage and Jeffrey [1981]; Jenkins and Savage [1983]; Jenkins and Richman [1985]; Lun and Savage [1987]; Campbell [1990]; Jaeger and Nagel [1992]; Goldhirsch [1995]; Sela & Goldhirsch [1998]; Poschel and Luding [2001]; Brilliantov and Poschel [2004]). This approach, which involves introducing a statistical description of the particles velocities, provides a formal definition of the mean density, the mean velocity, and the so-called granular temperature, which was first introduced by Ogawa [1978] and represents the kinetic energy associated with the random fluctuations of particles about their mean velocities. The models assume that particles interact by instantaneous binary collisions, and provide a systematic way to derive constitutive relations that relate the stress, the energy flux and the energy dissipation to the mean fields of density, velocity, and granular temperature. The particle properties are typically modeled using a coefficient of restitution, to represent the energy dissipated by the impact. Furthermore, molecular chaos (Boltzmann's stosszahlansatz) is generally assumed, implying that the random motion of even closely neighboring particles is independently distributed. Numerous comparisons (Lun [1991]; Savage [1992]; Lun and Bent [1994]; Lan and Rosato [1995]; Forterre and Pouliquen [2002]; Mitarai and Nakanishi [2004]; Swinney and Rericha [2004]) of the kinetic theory results with experimental measurements and granular dynamics computer simulations (which are free of the assumptions made in the kinetic theories) have shown quite good agreement.

Boundary Effects

To apply the kinetic theory to flows other than homogeneous shear flows with prescribed shear rate required development of consistent boundary condition. Several theoretical studies have incorporated boundary conditions into their problem solution. The first of these (Hui et. al. [1984]) modeled the wall interaction as an equivalent-roughness coefficient but neglected the shear work performed by the boundary due to the velocity slip at the surface. Jenkins and Richman [1986] developed a set of boundary conditions for two-dimensional smooth circular disk flows in the neighborhood of a boundary composed of semicircular hemispheres glued to a flat wall. They assumed that the particle's velocity distribution was Maxwellian, and that the spacing of the glued particles was such that the free particles would always hit a glued particle and could not collide with the flat portion of the boundary. However, a complication became apparent in examining the corresponding solutions to couette-flow problems. The results showed that a steady flow was possible for a given separation distance between the driving surfaces for exactly one average value of the solid fraction. In contradiction, shear-cell experiments and computer simulations of these flows indicate that steady flows are possible for any average concentration.

This work was later extended to non-Maxwellian velocity distributions for disks by Richman and Chou [1988] and to spheres by Richman [1988]. These latter two works suggested a heuristic solution to the uniqueness problem by using the the continuity of normal stress at the boundary to determine the shielding factor that influences the frequency of collisions. Richman & Marciniec [1988] analyzed the flow down an inclined chute with a bumpy wall. Richman [1992] developed boundary conditions that ensured momentum and energy balance at isotropically vibrating bumpy boundaries. A derivation of boundary conditions at a vibrating

plate has been presented in Brey et. al. [2000]. By contrast, Richman and Martin [1992, 1993] had considered boundaries whose fluctuating motion was partially anisotropic, but unrealistically restricted their attention to boundaries that vibrated with the same energies in the two directions tangent to the boundary. Martin [1993] further extended the work to include effects of spatial variation of mean velocity. Richman and Martin [1992] provided a continuum description of a vibro-fluidized system where the constitutive relations were adapted from Jenkins and Richman [1985a]. In a crude attempt to model vibrating sieves, Richman and Wang [1995, 1996] derived boundary conditions for granular flows that passed through the vibrating bumps that were artificially spaced far enough apart to allow particles to pass through.

Jenkins [1992] ignored bumpiness and derived boundary conditions at a flat, frictional wall based on a model of collision that distinguishes between sticking and sliding collisions. By using a simple velocity distribution function to integrate the impulse and change in fluctuation energy over all possible collisions, he calculated the analytical expressions for the collisional exchange of momentum and fluctuation energy between particles and a wall in two asymptotic circumstances; the small-friction/all-sliding limit and the large-friction/no-sliding limit. Jenkins and Louge [1997] improved those boundary conditions by refining the calculation of flux of fluctuation energy at the wall. It was suggested that the appropriate boundary conditions could be found by interpolating between two limits. Jenkins [2001] further outlined the derivation of boundary conditions for granular flows of frictional spheres at a bumpy, frictional wall with either cylindrical or spherical bumps. Xu [2003] then extended the boundary conditions for a frictional, bumpy boundary over a large range of slip velocities and gave the analytical expressions for two dimensional disk flows. In these boundary conditions, material properties,

including the coefficient of friction and the normal and tangential particle-wall restitution coefficients, are needed.

Inclined Flows

Flow on an inclined plane is both one of the most common situations encountered in granular flows, as well as one of the most extensively studied geometries in their theoretical treatment. Inclined planes present a simple geometry for laboratory experiments (Savage [1979]; Drake [1991]; Forterre and Pouliquen [2001]), which have been performed extensively to guide the development of continuum models and to assess the predictions of these models (Johnson et. al. [1990]; Richman and Marciniec [1990]; Ahn et. al. [1992]; Anderson and Jackson [1992]; Forterre and Pouliquen [2002]; Mitarai and Nakanishi [2004]). These studies demonstrate the rich character of solutions corresponding to steady, fully developed flows. It has also been studied using numerical simulations (Baran et. al. [2006]; Silbert et. al. [2001, 2002]; Mitarai and Nakanishi [2005]; Staron [2008]) which incorporate sophisticated particle interactions for relatively large systems with heights of up to hundreds of particles. These provide detailed information about the density, mean velocity and granular temperature profiles. Numerical simulations of Silbert et. al. [2001] on steady, fully developed flows of inelastic spheres down bumpy inclines, indicate a range of flow depths is possible at a fixed angle of inclination, and that the volume fraction decreases as the angle of inclination increases. Similar observations have been made in simulations of flows of inelastic disks (Mitarai [2005]; Lois [2005, 2006]). Also, Pouliquen [1999], when interpreting his experimental results on steady, fully developed inclined flows over a bumpy base, observed that the relationship between the average flow rate, depth of flow, and angle of inclination could be simplified by incorporating the dependence on

the angle of inclination through the relation between it and the depth at which the flow stopped. Numerical simulations of Silbert et. al. (2003) support this observation.

Granular temperature had not been experimentally measured until Ahn et. al. [1988], who used fiber-optic displacement probes to measure one component of velocity fluctuations. Ahn et. al. [1991] used a strain-gauge to measure shear stress, and a set of two fiber-optic probes to measure mean velocity and velocity fluctuation. The mass flow rate was obtained by timed collection of material discharging from a chute. Mean velocities at the chute base and at the free surface obtained by the fiber-optic probes were averaged to give the average mean velocity over the depth of the flow. The mean solid fraction was also obtained along with the shear rate and normal stress. The shear stress was measured directly by the shear gauge.

The simplest kinetic theories have been also applied to steady, fully developed flows down bumpy inclines (Jenkins [1994]; Anderson et. al. [1992]; Richman and Marciniec [1990]). Solutions in the absence of sidewalls that are relatively dense throughout their height are found to exist for bumpy bases that provide fluctuation energy to the flow by virtue of slip. In such solutions, the energy of the velocity fluctuations typically decreases with distance from the base, and the solid volume fraction has a maximum in the interior of the flow. In general, a granular flow will slip relative to a boundary; so, in addition to being dissipated in collisions at the boundaries, fluctuation energy can be generated by slip (Richman [1988]). That is, boundaries can either provide or remove fluctuation energy from the flow. The chute flow study of Richman and Marciniec [1990], in which an approximate analytical solution of a kinetic theory continuum model is developed, demonstrates the existence of two steady flow solutions for a fixed mass flux of material, one a dilute, fast and deep flow and the other dense, slow, and shallow. Multiple

solutions have been observed in the chute flow experiments of Johnson et. al. [1990] and obtained in kinetic continuum models (Anderson and Jackson [1992]; Nott and Jackson [1992]).

Many other kinetic-theory-based models have been applied to examine dense granular flow on a rough inclined plane (Drake [1990]; Azanza [1998]; Pouliquen [1999]; Daerr and Douady [1999]; Hanes and Walton [2000]; Louge and Keast [2001]; Jenkins [2006, 2007]; Ertas and Halsey [2002]; Kumaran [2006, 2007]; Louge [2003]).

Effects of Vibrations:

Due to kinetic-energy dissipation in collisions, energy must be continuously supplied to fluidized granular systems in order to sustain a steady state. This energy can be added by an external force, such as gravity, subjecting the material to vibrations, or shearing the material at a boundary as in a couette flow. In most of the experimental situations, this energy is given through a vibrating plate. Examples include vibrating conveyor belts, hoppers, sorting tables, packing tables, drying plates, and fluidized bed reactors. Vibration of a granular material may also play an important role in natural events such as earthquakes and avalanches. A simple model leading to a relationship between the energy input by a vibrating wall and the energy dissipation in collisions was developed by Warr et. al. [1995], who modeled a vibrated granular medium under gravity as an isotherm atmosphere, with all particles having the mean velocity. They used digital high speed photography and computer image processing to investigate the fluidization behavior of a two-dimensional model granular material undergoing vertical vibration. Profiles of packing fraction, speed, and velocity distribution functions were measured. The unique behavior of dry granular materials becomes manifest when they are energized through external vibrations, revealing a rich variety of phenomena including convection (Faraday [1831]; Savage [1988];

10

Galas and Hernmann [1992]; Taguchi [1992]; Jaeger and Nagel [1996]; Lan and Rosato [1997]; Yang and Hsiau [2000]) fluidization (Brenn and Wassgren [1993]; Clement and Rajchenbach [1991]; Hunt and Hsiau [1994]; Lan and Rosato [1995]; Rihman and Martin [1992]), heaping (Evesque and Rajchenbach [1989]; Douady [1989]), segregation (Dippel and Luding [1995]; Duran et. al. [1993]; Jullien et. al. [1992]; Knight el. al. [1993; Kudrolli [2004]) and the development of surface waves and arching (Clement et. al. [1996]; Melo et. al. [1995]; Wassgren et. al. [1996]; Rericha et. al. [2002]). Clearly, understanding how a granular material responds when subjected to vibration can provide valuable design information.

Thomas et. al. [1989] studied configurations of shallow granular beds that were supported by vibrating horizontal surafces, and found that any of four distinct states could prevail depending on the depth of the bed and the properties of the grains. Jackson [1991] proposed a phenomenological energy flux condition to account for the energy supplied to the flow by the boundary's vibrational motion, and predicted that inclined flows would be strongly influenced by small changes in this motion.

An analytical study of a vibrofluidized granular bed has been performed by Wildman et. al. [2006], by taking the theoretical model of a granular flow developed by Arnarson and Jenkins [2004] implementing the appropriate boundary conditions and solving numerically. Martin et. al. [2012] performed numerical studies of the effect of coherent vertical vibration on the fluidization transition of small systems under shear. More information concerning some of the important issues, questions, and applications of the knowledge of the granular state can be found in a review by Jaeger and Nagel [1992].

Binary Mixtures:

The majority of the rheological studies on granular materials are confined to monodisperse systems, where the particles are of the same density and size. A real granular system is always characterized by some degrees of poly-dispersity at least in size, which often leads to unwanted segregation of the material Apart from size disparity, one should also take into account other important features like Coulomb friction, roughness, and non-sphericity of particles, etc. to truly model a real granular system (Louge [1994]; Lun and Bent [1994]; Luding et. al. [1998]).

Farrell et. al. [1986] followed methods of the dense-gas kinetic theory where the single particle velocity distribution function was represented as a Maxwellian distribution. In this work, only collisional modes of transfer were considered, and thus the resulting constitutive relations are most appropriate for relatively dense flows. The dense-gas kinetic theory approach was also employed by Jenkins and Mancini [1989] for binary mixtures of both circular disks and spheres and by Huilin et. al. [2000] for binary mixtures of spheres. Similar to the work of Farrell et. al. [1986], the single particle velocity distribution was assumed to be Maxwellian in both works. Unlike the previous effort, however, these constitutive theories include both kinetic and collisional contributions to transport, and they are applicable to a general flow field. Furthermore, these theories account for differences in particle size and/or density. A more precise theory for spheres was put forth by Jenkins and Mancini [1989]. In their work, the single particle velocity distribution function was not assumed to be Maxwellian. Instead, it was assumed to take the form of a perturbed Maxwellian, and was determined as an approximate solution to the relevant Boltzmann equations. Furthermore, the equilibrium radial distribution function at contact was treated according to the revised Enskog theory for mixtures (López de

Haro et. al. [1983]), whereas earlier studies used the standard approach of evaluating the radial distribution function at a specific point between the two particles.

With the exception of the theory of Huilin et. al. [2000], a common feature of each of the aforementioned theories for binary mixtures is the assumption of equipartition of granular energy, which refers to the kinetic energy associated with the fluctuating motion of individual particles. Because the equipartition assumption provides an explicit relation between the granular temperature of the large and small particles, the resulting constitutive relations can be expressed as a function of a single temperature. Correspondingly, only one granular energy balance (associated with this temperature) is necessary in order for the system to be fully specified. If the assumption of equipartition of energy is lifted, a granular energy balance for each of the two particle types is required, resulting in a multi-temperature theory. Huilin et. al. [2000] derived balance laws and constitutive relations for a binary granular mixture with unequal granular temperature. The complete pair distribution function for two colliding spheres was assumed as the product of Maxwellian velocity distribution for each species. Numerical simulations on shearing flows of binary mixtures of frictionless, inelastic disks (Alam and Luding [2002, 2003]; Clelland and Hrenya [2002]) indicate the limits beyond which the assumptions of the kinetic theory for inelastic particles are invalid. Alam and Luding [2002] show that for particles of different diameters but the same mass the assumption of equipartition of energy and the predictions of the kinetic theory apply for diameter ratios up to five and coefficients of restitution as low as 0.70. However, Clelland and Hrenya [2002] and Alam and Luding [2003] find that for particles of the same density but different diameters, the difference in mass amplifies the difference in the energies of the species. Consequently, while the predictions for the stress remain valid over the same range diameters and restitution coefficients as for equal masses,

equipartition is satisfied to an error of less than twenty percent only for diameter ratios less than two and coefficients of restitution greater than 0.80. Within such limits, we expect the kinetic theory of Jenkins and Mancini [1989] to provide an acceptable description of transport and segregation.

Particle Segregation:

One of the most important subjects in granular dynamics is to explain the segregation phenomenon (Jaeger et. al. [1996]; Duran [1996]; Khakhar et. al. [1997, 1999]; Campbell [1990]; Thomas [2000]; Hong el. al. [2001]; Felix [2004]; Sarkar [2008]; Chung [2009]). Segregation is known to cause numerous problems during handling, processing, manufacturing, or unit operations of particulate materials. For instance, segregation has been shown to cause large variations in food product packages due to varying bulk density values (Prescott and Carson [2000]). In the pharmaceutical industry, a single batch of powder with the value of hundreds of thousands of dollars could be discarded only because the variation of the amount of active ingredient(s) for five tablets does not meet the U.S. Food and Drug Administration (FDA) standard.

Williams [1963] carried out one of the first qualitative studies on the effect of vibration frequency on the motion of a single large sphere in a bed of sand that was oscillated vertically. He attributes the sphere's observed upward trajectory to the "locking" effect of the overburden pressure that it exerts on the column of materials directly beneath it, thereby preventing it from moving down. If the large particle does experience an upward movement during the vibration, smaller particles could easily move beneath it and become locked. In a subsequent paper (Williams [1976]), he highlights particle properties that can promote segregation (namely

14

particle size, density, shape and elasticity) and he also describes three mechanisms of segregation (trajectory segregation, percolation) of fines and the rise of coarse particles due to vibration.

Depending on segregation mechanisms, thirteen patterns of segregation have been identified: trajectory, rolling, displacement, percolation, sieving, air current, fluidization, agglomeration, concentration-driven displacement, push-away, impact-bouncing, embedding, and angle of repose (de Silva et. al. [2000]). Out of the thirteen segregation mechanism, percolation segregation is the most dominant mechanism during conveying, storage, flow, and mixing. Percolation segregation requires dynamic condition such as those induced by shear and vibration in bulk solids (Vallance and Savage [2000]).

Hsiau and Wang [1999] investigated experimentally the segregation phenomena of a binary mixture in a vertical bed by using image technology, and studied the influence of the vibrational acceleration amplitude was investigated. Ciamarra et. al. [2006] presented extensive molecular dynamics simulations on species segregation in a granular mixture subject to vertical taps. They discuss how grain properties, e.g., size, density, friction, as well as shaking properties, e.g., amplitude and frequency, affect such a phenomenon. Large particles typically rise to the top, as small particles percolate into their voids during shaking (Prescott [1994]; Khakhar et. al. [2001], Rosato [2002]). A numerical study by Rosato et. al. [1987] clarified the geometrical mechanism for size separation described by previous studies. These authors adapted a Monte Carlo (MC) simulation technique used in statistical physics to show that a local geometrical void-filling mechanism can lead to size segregation with larger particles on top, the so-called Brazil nut effect. Anjani and Puri [2009] studied percolation segregation of binary mixtures under periodic movement. One of the efficient approaches to gaining a deeper understanding of percolation segregation mechanism is by studying the cumulative effect of two or more

parameters, i.e., allows one to build a roadmap by understanding the influence of individual parameters and their interactions that contribute toward overall segregation. Based on simulations and statistical physics arguments, Hong and co-workers (2001) proposed that a large particle could sink to the bottom provided it was heavy enough, naming it the reverse Brazil nut effect (Shinbrot and Muzzio [1998]; Hong et. al. [2001]).

Brito et. al. [2008] have investigated the segregation of a dense binary mixture of granular particles that only differ in their restitution coefficient. The main conclusion is that different restitution coefficients alone create segregation in a binary mixture vertically vibrated.

Segregation is mainly affected by physical properties of particulate materials, handling conditions, and environmental parameters. To minimize segregation, various methods have been tried. The common methods include improvement of physical properties (i.e., narrowing size distribution spread, reducing absolute size, and avoiding irregularly shaped particles), proper selection of handling equipment and operational parameters (i.e., lowering free-fall height and employing mass flow bins), and proper control of material handling environmental conditions (i.e., minimizing vibration and maintaining humidity) (Tang and Puri [2004]).

Sieving

Many factors have been identified to affect sieving, including the size and shape of particles relative to the aperture of the sieve, the mesh size of the sieve itself, the amount of material on the sieve surface, the direction of movement of the sieve, the rate of movement of the material relative to the sieve surface, etc. (Apling [1984]; Standish [1985]; Allen [2003]]. Furthermore, the interactions among variables are so complex that no satisfactory method of evaluating and predicting the sieving process has yet been developed (Sultanabawa et. al.

[2001]). This has led to the inefficient operation of industrial sieving equipment as well as misleading and erroneous results of laboratory sieve analysis (Leschonski [1979]). Most studies of the screening process have been concerned with the demonstration of the complicated size distribution and composition of particulate solids, and the comprehensive effect of particulate motion under various operational parameters and screening method that influence screening efficiency (Utsumi et. al. [2001]; Tsai and Chang [2009]; Liu [2009]; Moon et. al. [2008]) or the analysis of screening kinetics (Wodzinski [2003]; Shaviv [2004]).

Chapter 2

General Flow Theory for Monosized Assemblies

The purpose of this chapter is to give a brief outline of a typical kinetic theory for dry granular assemblies of identical, nearly elastic smooth spheres. Such theories consist of balance equations for mass, momentum, and energy, as well as constitutive relations for stress, energy flux, and energy dissipation. While many theories (discussed in Chapter 1) have been proposed, they all have common structures. Because the main contribution of our work (to be described in subsequent chapters) is in deriving boundary conditions that describe the interaction between such flows and the vibrating surfaces with which they interact, we choose a relatively simple constitutive theory to describe here. In deriving the boundary conditions we will make assumptions that are consistent with those made in deriving the constitutive theory described here. Finally, we will employ the boundary conditions, constitutive theory, and balance equations to write down well posed boundary value problems for steady, fully developed flows.

2.1   Balance Equations

We begin by introducing the mean fields of importance for flowing assemblies of identical inelastic spheres, and by writing down the general form of the appropriate balance equations. Following the techniques of kinetic theory of gases, they introduce a probability distribution function f that gives a statistical description of the particles velocities. Thus at time t, the probable number of particles located at position $\boldsymbol{r}$, within volume element $dr_1 dr_2 dr_3 \equiv d\boldsymbol{r}$, with velocities $\boldsymbol{c}$, within the range $dc_1 dc_2 dc_3 \equiv d\boldsymbol{c}$, is given by

$$f(\boldsymbol{c}, \boldsymbol{r}, t) d\boldsymbol{r} d\boldsymbol{c} \quad . \tag{2.1}$$

The number density n of particles within the flow is then

$$n(\boldsymbol{r}, t) = \int f(\boldsymbol{c}, \boldsymbol{r}, t) d\boldsymbol{c} \quad , \tag{2.2}$$

where the integration is carried out over all velocities. If each sphere is of mass m, diameter σ, and mass density is ρ_p, then the solid fraction ν is $n\pi\sigma^3/6$, and the mass density ρ of the flow is either mn or $\rho_p\nu$.

Given any particle property $\phi(\boldsymbol{c})$, such as its velocity $\boldsymbol{c}$ for example, its mean value $\langle\phi\rangle$, is a weighted average based on the distribution of granular velocities:

$$\langle\phi\rangle = \frac{1}{n}\int \phi(\boldsymbol{c})f(\boldsymbol{c}, \boldsymbol{r}, t) d\boldsymbol{c} \quad . \tag{2.3}$$

where the limits of integration are over all velocities. The mean velocity $\boldsymbol{u}(\boldsymbol{r}, t)$ for example, is $\langle\boldsymbol{c}\rangle$.

Because the actual particle velocities deviate about their mean velocity, we also focus on the fluctuation velocity $\boldsymbol{C} = \boldsymbol{c} - \boldsymbol{u}$ (whose mean value $\langle\boldsymbol{C}\rangle$ vanishes), and introduce the full second moment of fluctuation velocity $\boldsymbol{K} \equiv \langle\boldsymbol{C}\otimes\boldsymbol{C}\rangle$. The granular temperature is proportional to the kinetic energy per unit mass associated with these velocity fluctuations, and is the isotropic part of $\boldsymbol{K}$. If $\widehat{\boldsymbol{K}}$ is the deviatoric part of $\boldsymbol{K}$, then $\boldsymbol{K}$ may be decomposed into the sum $T\boldsymbol{\delta} + \widehat{\boldsymbol{K}}$.

The equations that determine the mean fields ν, $\boldsymbol{u}$, and T are the balance of mass

$$\dot{\rho} + \rho\nabla\cdot\boldsymbol{u} = 0 \quad , \tag{2.4}$$

where an overdot denotes the material derivative; the balance of momentum

$$\rho\dot{\boldsymbol{u}} = -\nabla\cdot\boldsymbol{P} + \rho\boldsymbol{g} \quad , \tag{2.5}$$

where $\boldsymbol{P}$ is the pressure tensor, and $\boldsymbol{g}$ is the body force per unit mass; and the balance of energy

$$\frac{3}{2}\rho\dot{T} = -\nabla\cdot\boldsymbol{Q} - tr(\boldsymbol{P}\cdot\boldsymbol{D}) - \gamma \quad , \tag{2.6}$$

where Q is the flux of fluctuation energy, γ is the rate per unit volume of energy lost due to dissipative interactions, and D is the symmetric part of the velocity gradient ∇u.

2.2   Constitutive Relations

For flows of identical, smooth, nearly elastic spheres, we employ the relatively simple theory of Jenkins and Richman [1985] for the dependence of the pressure tensor P, energy flux Q, and the collisional dissipation γ, on the mean fields. Because their theory includes contributions to the transfer of momentum and energy from both particle-particle collisions (which dominate in dense flows) and particle transport (which dominates in dilute flows), it is valid over the full range of solid fraction.

The theory is based on a Maxwellian particle distribution function that is corrected due to the presence of spatial gradients in both the mean velocity $u(r,t)$ and the granular temperature $T(r,t)$. The rate of energy dissipation γ is due entirely to collisions between particles, and is given by,

$$\gamma = \frac{15\mu(1-e)T}{\sigma^2} \quad , \tag{2.7}$$

where e is the coefficient of restitution between flow particles and where

$$\mu = \frac{8\sigma\rho G T^{1/2}}{5\pi^{1/2}} \quad , \tag{2.8}$$

in which the factor $G(\nu)$ is the product of ν and the radial distribution function g_0. In what follows, we modify the choice of g_0 so that $G(\nu)$ becomes:

$$G(\nu) = \frac{\nu}{(1 - \nu/\nu_m)^{5\nu_m/2}} \quad , \tag{2.9}$$

where ν_m is the maximum value (approximately $.65$) of the solid fraction for random packing of identical spheres. This form of G is based on the radial distribution function $g_0(\nu)$ at impact

proposed by Lun and Savage [1986], which has the correct value ($= 1$) and slope ($= 5/2$) in the dilute limit, agrees well with that proposed by Carnahan and Startling $\nu(2 - \nu)/2(1 - \nu)^3$ [1969] for all values of ν up to $.5$, and becomes unbounded as ν approaches ν_m so that collisions between particles may support high pressures at low temperatures.

Both the pressure tensor and the energy flux contain contributions for particle transport and particle collisions. The pressure tensor $\boldsymbol{P}$ is given by

$$\boldsymbol{P} = \left[4\rho G \mathbb{F}T + \frac{\mu}{3}(2E - 5)tr\boldsymbol{D}\right]\boldsymbol{I} - 2\mu E\boldsymbol{D} \quad , \tag{2.10}$$

where the functions $\mathbb{F}(\nu)$ and $E(\nu)$ depend on G according to $\mathbb{F}(\nu) \equiv 1 + 1/(4G)$, and $E(\nu) \equiv 1 + \pi[1 + 5/(8G)]^2/12$. Similarly, the energy flux $\boldsymbol{Q}$ is given by,

$$\boldsymbol{Q} = -\left(\frac{5\mu}{2}\right)\mathcal{M}\nabla T \quad , \tag{2.11}$$

where $\mathcal{M}(\nu) = 1 + 9\pi[1 + 5/(12G)]^2/32$.

Chapter 3

Boundary Conditions for Monosized Assemblies at Impenetrable Bumpy Boundaries that Vibrate with Three-Dimensional Anisotropy

3.1   Balance of Momentum and Energy at the Boundary
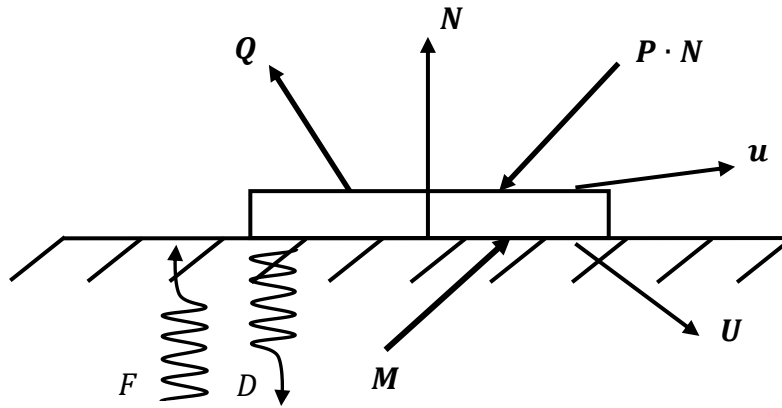
Figure 3.1: A fixed control volume at the boundary

We consider the interactions between a three-dimensional granular flow and an impenetrable boundary that fluctuates about its mean velocity $\boldsymbol{U}$. Appropriate boundary conditions must guarantee that the flow of momentum and energy are balanced at the interface, just as they are balanced everywhere within the flow.

Consequently, we focus attention on a parallelepiped in the flow with two opposite faces of unit area; one face is in the flow and the other is coincident with the boundary (see Figure 3.1). In the limit as the lateral sides shrink to zero, the balance of momentum within the parallelepiped requires that

$$\boldsymbol{M} = \boldsymbol{P} \cdot \boldsymbol{N} \quad , \tag{3.1}$$

where $\boldsymbol{M}$ is the rate per unit area at which momentum is transferred to the flow through wall collisions, $\boldsymbol{N}$ is the unit inward normal, $\boldsymbol{P}$ is the pressure tensor given by equation (2.10), and $\boldsymbol{P} \cdot \boldsymbol{N}$ is the traction vector acting on the flow-side surface of the parallelepiped.

In order to express the balance of energy, we introduce F as the rate per unit area of energy supplied by the boundary to the flow due to its fluctuating motion, and D as the corresponding rate at which energy is dissipated through inelastic collisions at the boundary. Then in the same limit, the balance of energy requires that

$$\boldsymbol{M} \cdot \boldsymbol{U} + F - D = \boldsymbol{Q} \cdot \boldsymbol{N} + (\boldsymbol{P} \cdot \boldsymbol{N}) \cdot \mathbf{u} \quad , \tag{3.2}$$

where the energy flux $\boldsymbol{Q}$ is given by equation (2.11). Rearranging equation (3.2) yields,

$$\boldsymbol{M} \cdot \boldsymbol{v} + F - D = \boldsymbol{Q} \cdot \boldsymbol{N} \quad , \tag{3.3}$$

where $\boldsymbol{v}$ is the slip velocity defined as the difference $\boldsymbol{U} - \boldsymbol{u}$ between the mean velocity of the boundary and the mean velocity of the flow at the boundary. The slip work $\boldsymbol{M} \cdot \boldsymbol{v}$ is the rate at which work is done by equal tractions acting through velocities that differ by $\boldsymbol{v}$. Thus, the boundary can either supply or absorb fluctuation energy depending on the relative sizes of the slip work $\boldsymbol{M} \cdot \boldsymbol{v}$, the supply rate F, and the dissipation rate D. Even when the boundary does not vibrate (i.e $F = 0$) and when all the interactions between the boundary and the flow particles are dissipative (i.e $D > 0$), the boundary may actually supply energy to the flow provided $\boldsymbol{M} \cdot \boldsymbol{v}$, is greater than D.

3.2   Transfer Rates

The transfer rates $\boldsymbol{M}$, F, and D depend on three factors: the boundary geometry; the nature of a typical interaction between a flow particle and a boundary particle; and the boundary motion. In what follows, we address each in succession.

23

The bumpy boundary is a flat surface to which identical, smooth, hemispherical particles of diameter d are randomly fixed at an average spacing s apart. Although individual collisions are frictionless, by virtue of oblique collisions, the boundary can transfer tangential momentum to the flow. For simplicity, the spacing of the particles is never so great as to allow a flow particle to collide with the flat portion of the wall. On average, the nearest neighbors of any hemisphere from a half torus whose inner diameter is $d + 2s$, whose outer radius is $3d + 2s$, and whose height is $d/2$. In Figure 3.2 we show the cross section of a boundary particle and its associated neighboring torus.
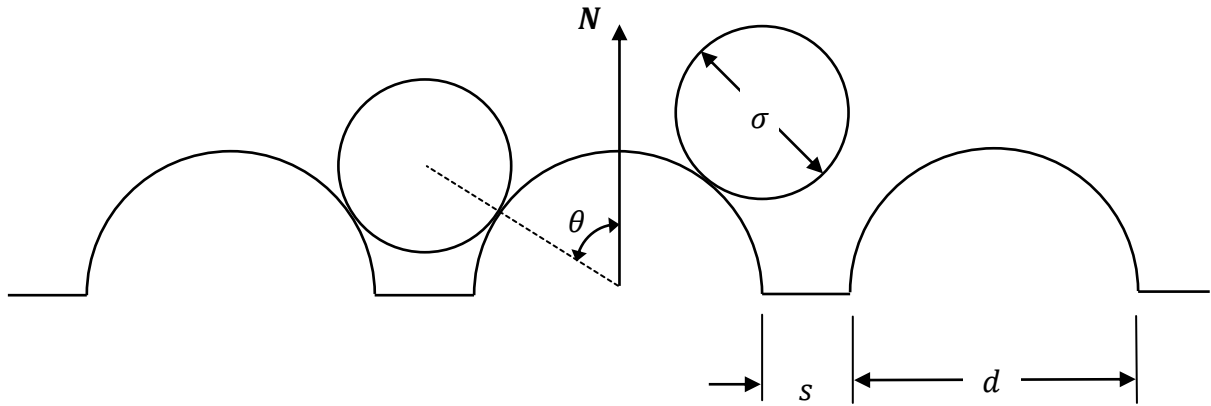
Figure 3.2: The cross section of a boundary particle (Taken from Martin and Richman 1993)

The bumpiness of the boundary is measured by the angle $\theta \equiv \sin^{-1}(1 + s/d)/(1 + \sigma/d)$, which is the maximum possible angle between the unit inward normal and the line directed from the center of a boundary particle to that of a flow particle at impact. As θ increases, the boundary becomes more effective at transferring momentum in directions parallel to its flat surface and, in that sense, becomes "bumpier".

The dynamics of a collision at the boundary are described in terms of the pre-collisional velocities $\boldsymbol{c}$ of the flow particle and $\boldsymbol{\psi}$ of the boundary particle, the unit vector $\boldsymbol{k}$ directed from the center of the wall particle to the center of the flow particle at impact, and the coefficient e_w

of restitution which characterizes the energy dissipated in each collision. If the velocity of the wall particle is unaffected by the collision, then in terms of the relative velocity $\boldsymbol{g} \equiv \boldsymbol{\psi} - \boldsymbol{c}$, the change in linear momentum experienced by the flow particle is

$$m\,(\boldsymbol{c}^* - \boldsymbol{c}) = m\,(1 + e_w)(\boldsymbol{g} \cdot \boldsymbol{k})\boldsymbol{k} \quad , \tag{3.4}$$

where $\boldsymbol{c}^*$ the post-collisional velocity of the flow particle. The corresponding change in energy is

$$\frac{m}{2}(\boldsymbol{c}^* \cdot \boldsymbol{c}^* - \boldsymbol{c} \cdot \boldsymbol{c}) = m(1 + e_w)(\boldsymbol{g} \cdot \boldsymbol{k})\left((\boldsymbol{U} \cdot \boldsymbol{k}) + (\boldsymbol{\Psi} \cdot \boldsymbol{k}) - \frac{1}{2}\,(1 - e_w)(\boldsymbol{g} \cdot \boldsymbol{k})\right) \quad ,$$

$$\tag{3.5}$$

where $\boldsymbol{\Psi} = \boldsymbol{\psi} - \boldsymbol{U}$ is the fluctuation velocity of the boundary particle.
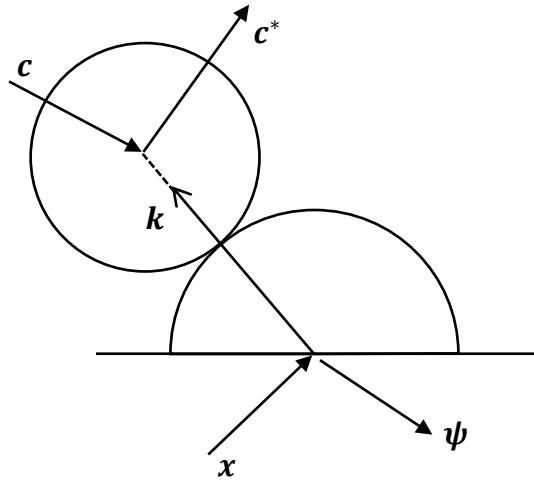
Figure 3.3: A typical boundary collision

In order to treat collisions between a flow particle and a boundary particle in a manner that is analogous to the treatment of a collision between two flow particles, we imagine that the boundary fluctuates randomly about a mean velocity $\boldsymbol{U}$ with a probability distribution function $p(\boldsymbol{\psi})$ that gives the probability per unit volume $d\psi_1 d\psi_2\, d\psi_3 \equiv d\boldsymbol{\psi}$ in velocity space that any boundary particle will have velocity $\boldsymbol{\psi}$ within range $d\boldsymbol{\psi}$.

The motion of the boundary is described by its mean velocity $\boldsymbol{U}$ and its full second moment of fluctuation velocity $\boldsymbol{B}$. These quantities are analogous to $\boldsymbol{u} = \langle \boldsymbol{c} \rangle$ and $\boldsymbol{K} = \langle \boldsymbol{C} \otimes \boldsymbol{C} \rangle$ within the flow and are calculated according to

$$\boldsymbol{U} = \int \boldsymbol{\psi}\, p(\boldsymbol{\psi})\, d\boldsymbol{\psi} \quad , \tag{3.6}$$

and

$$\boldsymbol{B} = \int (\boldsymbol{\Psi} \otimes \boldsymbol{\Psi}) p(\boldsymbol{\psi})\, d\boldsymbol{\psi} \quad , \tag{3.7}$$

in which integrations are over all velocities. The trace $tr\boldsymbol{B}$ is analogous to $3T$ within the flow and is a measure of the total fluctuation energy of the boundary.

At the instant of impact, the center of the boundary particle is located at $\boldsymbol{x}$, and the distance between the centers of the two particles is $\bar{\sigma} \equiv (\sigma + d)/2$. The frequency of collisions per unit area of flat wall that involve flow particles with velocities $\boldsymbol{c}$ in the range $d\boldsymbol{c}$ and wall particles with velocities $\boldsymbol{\psi}$ in the range $d\boldsymbol{\psi}$, and occur within an element of solid angle $d\boldsymbol{k}$ centered about $\boldsymbol{k}$ on the surface of the wall particle is

$$\frac{\lambda}{\pi\, sin^2\theta}\, f(\boldsymbol{c}, \boldsymbol{x} + \bar{\sigma}\, \boldsymbol{k})\, p(\boldsymbol{\psi})\, (\boldsymbol{g} \cdot \boldsymbol{k})\, d\boldsymbol{k} d\boldsymbol{c} d\boldsymbol{\psi} \quad , \tag{3.8}$$

where $f(\boldsymbol{c}, \boldsymbol{r})$ is the velocity distribution function for the flow particles, and where $(\boldsymbol{g} \cdot \boldsymbol{k}) > 0$ for the collision to occur, and the factor λ accounts for the effects of excluded volume and the shielding of the flow particles from the wall particles by other flow particles. Excluded volume effects account for the space occupied by both the flow particles and the boundary particles. Furthermore, the extent of shielding depends on the motion of the flow particles, the motion of the boundary particles, and the arrangement of the boundary particles. Consequently, we anticipate that λ will at least depend on v and T at the boundary, as well as θ and $\boldsymbol{B}$.

The transfer rates M, F, and D are statistical averages of the appropriate change per collision weighted by collision frequency (3.8). According to equation (3.4), M is the weighted average of $m(1 + e_w)(g \cdot k)k$. According to the last two terms on the right-hand-side of equation (3.5), F and D are the corresponding averages of $m(1 + e_w)(g \cdot k)(\Psi \cdot k)$ and $m(1 - e_w^2)(g \cdot k)^2/2$. These may be written compactly in integral form:

$$\begin{Bmatrix} M \\ F \\ D \end{Bmatrix} = \frac{m(1 + e_w)\lambda}{\pi \sin^2 \theta} \int \begin{Bmatrix} (g \cdot k)k \\ (g \cdot k)(\Psi \cdot k) \\ \frac{1}{2}(1 - e_w)(g \cdot k)^2 \end{Bmatrix} (g \cdot k)f(c, x + \bar{\sigma}k)\, p(\psi)\, dk dc d\psi \quad , \quad (3.9)$$

where the velocity integration are carried out over all velocities such that $(g \cdot k) > 0$, and the k- integration is a surface integral over the area of a boundary particle that is accessible to a colliding flow particle.

In order to carry out the averaging procedure, we must first write down the distribution functions $p(\psi)$ and $f(c, r)$. We take $p(\psi)$ as the anisotropic Maxwellian:

$$p(\psi) = \frac{1}{\sqrt{8B\pi^3}}\, exp\left\{-\frac{1}{2}\, \Psi \cdot B^{-1} \cdot \Psi\right\} \quad , \quad (3.10)$$

where $B \equiv det B$. When B is isotropic, $p(\psi)$ reduces to the simple Maxwellian employed by Richman [1992]. This distribution is sensitive to all components of B which are therefore parameters that may be adjusted to reflect the possibility that the boundary vibrates with different fluctuation energies in different directions.

We take $f(c, r)$ to be the corrected Maxwellian that is consistent with the constitutive theory described in Chapter 2:

$$f(c, r) = \frac{n}{(2\pi T)^{3/2}} \left(1 + \frac{1}{2T^2}\, C \cdot \widehat{K} \cdot C\right) exp\left\{\frac{-C \cdot C}{2T}\right\} \quad . \quad (3.11)$$

Here $\widehat{K}$ is the deviatoric part of the second moment of fluctuation velocity, and all mean fields are evaluated at r. For sheared assemblies of nearly elastic spheres, Jenkins and Richman [1985] have shown that $\widehat{K}$ is small compared to T and may be expressed in terms of velocity gradients as

$$\frac{1}{2T}\widehat{K} = -\sqrt{\frac{2}{\pi}}A(\nu)\frac{\sigma}{\sqrt{T}}\,\widehat{D} \quad , \qquad\qquad (3.12)$$

where $\widehat{D} \equiv D - (trD)\delta/3$ is the deviatoric piece of D, and $A(\nu) = \pi[1 + 5/(8G)]/12\sqrt{2}$. Under these circumstances, the largest corrections to the Maxwellian that we have ignored are proportional to gradients of granular temperature and solid fraction. When velocity gradients vanish, $f(c,r)$ reduces to the simple Maxwellian employed by Richman and Martin [1992, 1993].

Because the corrected Maxwellian (3.11) for f is the sum of two terms (i.e. the simple Maxwellian and its correction due to gradients of the mean velocity), each transfer rate M, F and D can be decomposed into two corresponding contributions. The contribution from the simple Maxwellian contains the lowest order approximation to each rate, and the contribution due to velocity gradients is a correction to each. In this manner, we write $M = M^0 + M^c$, $F = F^0 + F^c$, and $D = D^0 + D^c$, where the superscripts *"0"* and *"c"* denote the contributions that arises from the first and second terms in f, respectively. In each case, the integrations over velocities c and ψ in averages (3.9) are carried out by replacing $dcd\psi$ by $|J|dCd\Psi$ where $|J| = 1$, writing velocity vectors C, g, υ and Ψ explicitly in terms of the unit vector k (in the 1-direction) and two additional arbitrary mutually perpendicular unit vectors (in the 2- and 3-directions), and first integrating over Ψ_2, Ψ_3, C_2, and C_3 between $-\infty$ and $+\infty$. Then the fluctuation velocity C_1 is rewritten as $C_1 = \Psi_1 - g_1 + \upsilon_1$, and $dC_1d\Psi_1$ is replaced by by $|J|dg_1d\Psi_1$ where $|J| = 1$.

Finally, integration over Ψ_1 is carried out between $-\infty$ and $+\infty$, and integration over g_1 is carried out between 0 and $+\infty$. The intermediate results can be written compactly in terms of the quantity

$$\Phi = \frac{\boldsymbol{\nu} \cdot \boldsymbol{k}}{\sqrt{2T(\boldsymbol{k} \cdot \boldsymbol{\mathcal{B}} \cdot \boldsymbol{k})}} \quad , \tag{3.13}$$

where $\boldsymbol{\mathcal{B}} \equiv \boldsymbol{\delta} + \boldsymbol{B}/T$ and both T and $\boldsymbol{\nu} = \boldsymbol{U} - \boldsymbol{u}$ are evaluated at $\boldsymbol{x} + \bar{\sigma}\boldsymbol{k}$. The resulting integral expression for the first contribution to the rate at which momentum is supplied to the flow is

$$\boldsymbol{M}^o = \frac{(1 + e_w)\rho\lambda T}{\pi^{3/2}sin^2\theta} \int (\boldsymbol{k} \cdot \boldsymbol{\mathcal{B}} \cdot \boldsymbol{k})\boldsymbol{k}\left[\sqrt{\pi}\left(\frac{1}{2} + \Phi^2\right)erfc(-\Phi) + \Phi exp(-\Phi^2)\right]d\boldsymbol{k} \quad , \tag{3.14}$$

where ρ, λ, and T are evaluated at $\boldsymbol{x} + \bar{\sigma}\boldsymbol{k}$. The corresponding lowest order expressions for F^0 and D^0 are

$$F^0 = \frac{\sqrt{2}(1 + e_w)\rho\lambda T^{3/2}}{\pi^{3/2}sin^2\theta} \int (\boldsymbol{k} \cdot \boldsymbol{\mathcal{B}} \cdot \boldsymbol{k})^{1/2}(\boldsymbol{k} \cdot \boldsymbol{\mathcal{B}} \cdot \boldsymbol{k} - 1)\left[\sqrt{\pi}\,\Phi\,erfc(-\Phi) + exp(-\Phi^2)\right]d\boldsymbol{k} \quad , \tag{3.15}$$

and

$$D^0 = \frac{(1 - e_w^2)\rho\lambda T^{3/2}}{\sqrt{2}\pi^{3/2}sin^2\theta} \int (\boldsymbol{k} \cdot \boldsymbol{\mathcal{B}} \cdot \boldsymbol{k})^{3/2}\left[\sqrt{\pi}\,\Phi\left(\frac{3}{2} + \Phi^2\right)erfc(-\Phi)(1 + \Phi^2)\,exp(-\Phi^2)\right]d\boldsymbol{k} \quad , \tag{3.16}$$

To calculate $\boldsymbol{M}^o$, F^0, and D^0, it remains only to carry out $\boldsymbol{k}$-integrations (3.14), (3.15), and (3.16) over that portion of a wall particles surface that is accessible to flow particles.

In principle, we must also determine the contribution to each transfer rate from the correction term in equation (3.11) for f. However, we are only interested in calculating $\boldsymbol{M}$, F, and D with errors consistent with the assumptions used to derive the constitutive theory given

by equations (2.7), (2.8), (2.10), and (2.11). For example, momentum balance (3.1) demonstrates that the rate of momentum $\boldsymbol{M}$ supplied to the flow must balance the pressure tensor $\boldsymbol{P}$ at the boundary. According to constitutive relation (2.9), the pressure tensor includes both a lowest order contribution (i.e. its isotropic piece) and a first order correction (i.e. its deviatoric piece due to velocity gradients). Consequently, in order to maintain consistency with the constitutive theory, we must include the first order correction $\boldsymbol{M}^c$ to $\boldsymbol{M}$. We carry out the $\boldsymbol{c}$ and $\boldsymbol{\psi}$ velocity integrations by replacing $dc d\psi$ by $|J|dC d\Psi$ where $|J| = 1$, writing velocity vectors in terms of the unit vector $\boldsymbol{k}$ (in the 1-direction) and two additional arbitrary mutually perpendicular unit vectors (in the 2- and 3-directions), and first integrating over Ψ_2, Ψ_3, C_2, and C_3 between $-\infty$ and $+\infty$. Then the fluctuation velocity C_1 is rewritten as $C_1 = \Psi_1 - g_1 + v_1$, and $dC_1 d\Psi_1$ is replaced by $|J| dC_1 d\varphi_1$ where $|J| = 1$ and where $\boldsymbol{\varphi} = \boldsymbol{\Psi} - \boldsymbol{C}$. Integration on C_1 is between $-\infty$ and $+\infty$, and the limits of integration of φ_1 are between $-v_1$ and $+\infty$, or alternatively define $\eta \equiv \varphi_1 + v_1$ (so that $d\varphi_1 = d\eta$) and carry out the integration over η between 0 and $+\infty$ to obtain the following integral expression:

$$\boldsymbol{M}^c = \frac{(1 + e_w)\rho\lambda}{2\pi \sin^2\theta} \int \boldsymbol{k}\left(\boldsymbol{k} \cdot \widehat{\boldsymbol{K}} \cdot \boldsymbol{k}\right) \, erfc(-\Phi) \, d\boldsymbol{k} \quad , \tag{3.17}$$

where all mean fields are evaluated at $\boldsymbol{x} + \bar{\sigma}\boldsymbol{k}$, and the parameter $\widehat{\boldsymbol{K}}$ is given by equation (3.12).

In addition, we must also include the first order correction to $\boldsymbol{M}^0$ due to velocity gradients that are introduced because the mean fields are evaluated at $\boldsymbol{x} + \bar{\sigma}\boldsymbol{k}$ rather than at $\boldsymbol{x}$. On the other hand, energy balance (3.3) demonstrates that the competing effects of $\boldsymbol{M} \cdot \boldsymbol{v} + F - D$ must balance the energy flux $\boldsymbol{Q} \cdot \boldsymbol{N}$ normal to the boundary. However, according to constitutive relation (2.11), the energy flux includes only a lowest order contribution. Consequently, to adequately characterize F and D it is necessary only to calculate the lowest order contributions to F^0, and D^0.

It is only possible to carry out in closed form one of the remaining two-dimensional $\boldsymbol{k}$-integrations over the accessible area of a boundary particle. In order to do so, we introduce an $x_1 - x_2 - x_3$ Cartesian coordinate system in which the x_2- direction is normal and x_1- and x_3-directions are parallel to the flat part of the boundary. We also introduce the right-handed orthonormal triad $\boldsymbol{N} - \boldsymbol{t} - \boldsymbol{\tau}$; the unit vector $\boldsymbol{N}$ points in the x_2- direction, the unit vector $\boldsymbol{\tau}$ points in the x_3- direction, and the unit vector $\boldsymbol{t}$ points in the x_1- direction. In this system, the second moment of boundary fluctuation velocities is

$$\boldsymbol{B} = \begin{pmatrix} V_1^2 & B_{12} & B_{13} \\ B_{12} & V_2^2 & B_{23} \\ B_{13} & B_{23} & V_3^2 \end{pmatrix} \quad . \tag{3.18}$$

In what follows, we consider circumstances under which the off-diagonal components of $\boldsymbol{B}$ are small compared to its diagonal components, the velocity $\boldsymbol{v}$ is small compared to the granular temperature T at the boundary, and the change $\sigma \nabla \boldsymbol{u}$ in velocity is small compared $T^{1/2}$. We then expand the integrands in equations (3.14)-(3.17) in Taylor series about $\boldsymbol{x} + \bar{\sigma} \boldsymbol{N}$ with respect to these small quantities.

To confront the $\boldsymbol{k}$- integrations, we define angles φ and ξ in spherical coordinates with respect to the orthonormal triad $\boldsymbol{N} - \boldsymbol{t} - \boldsymbol{\tau}$, as shown in Figure 3.4.
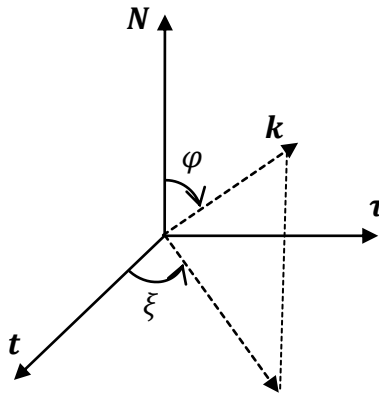
Figure 3.4: Angle-definition for integration over boundary particle surface

The angle φ measures the positive acute angle between vector N and the normal to the surface at any point on the surface of a boundary particle. The angle ξ measures the counter-clockwise angle from vector t, made by the projection on $t - \tau$ plane, of the normal at any point on the surface. Then, φ, ξ and the radius $d/2$ can together describe the position of any point on the surface of boundary particle, with respect to the center of the boundary particle. An elemental unit spherical area dk is given $\sin \varphi \, d\varphi d\xi$, and we carry the integrations on ξ between 0 and 2π, and on φ between 0 and θ where $\theta = \sin^{-1} (1 + s/d)/(1 + \sigma/d)$ is the bumpiness of the boundary discussed earlier. Furthermore, $(k \cdot B \cdot k)k$ can be written in indices form by $(k_i \cdot B_{ij} \cdot k_j)k_k$ where $k_i = \cos \varphi \, N_i + \sin \varphi \cos \xi \, t_i + \sin \varphi \sin \xi \, \tau_i$, and $B_{ij} = \delta_{ij} + B_{ij}/T$.

In this way, we can carry out the φ-integrations in closed form. The resulting integral expressions for M, F, and D may be compactly written in terms of the dimensionless ratio,

$$R \equiv \frac{(V_2^2 - V_1^2 \cos^2\xi - V_3^2 \sin^2\xi)}{(T + V_1^2 \cos^2\xi + V_3^2 \sin^2\xi)} \quad , \tag{3.19}$$

where the 1-, 2-, and 3- directions refer to the t-, N-, and τ- directions, respectively, and the functions $J(R,\theta)$ and $K(R,\theta)$ are defined by

$$K(R,\theta) \equiv (1 + R\cos^2\theta)^{\frac{3}{2}}\cos \theta - (1 + R)^{3/2} \quad , \tag{3.20}$$

and,

$$J(R,\theta) \equiv (1 + R\cos^2\theta)^{\frac{1}{2}}\cos \theta - (1 + R)^{\frac{1}{2}} - I(R,\theta) \quad , \tag{3.21}$$

in which

$$I(R,\theta) \equiv \begin{cases} \dfrac{1}{\sqrt{R}}\left[\sinh^{-1}\sqrt{R} - \sinh^{-1}(\sqrt{R}\cos \theta)\right] & R > 0 \\ \dfrac{1}{\sqrt{-R}}\left[\sin^{-1}\sqrt{-R} - \sin^{-1}(\sqrt{-R}\cos \theta)\right] & R < 0 \end{cases} \quad . \tag{3.22}$$

When the boundary vibrations are isotropic (including when there is no vibration at all), R is equal to zero. When collisions between boundary and the flow particles are nearly elastic, then e_w is close to unity and the integral expression for the components of $\boldsymbol{M}$ is

$$M_i = \rho\lambda \left\{ \left[(V_2^2 + T) + \frac{\sin^2\theta}{2} \left(\frac{(V_1^2 + V_3^2)}{2} - V_2^2 \right) \right] N_i + \frac{\sin^2\theta}{2} [(\boldsymbol{t} \cdot \boldsymbol{B} \cdot \boldsymbol{N})t_i + (\boldsymbol{\tau} \cdot \boldsymbol{B} \cdot \boldsymbol{N})\tau_i] \right\}$$

$$+ \rho\lambda \left\{ \frac{v_j}{\sin^2\theta\sqrt{2}\,\pi^{3/2}} \int_0^{2\pi} \frac{(T+b)^{1/2}}{R} \left[K(R,\theta) - \frac{(1+4R)}{2} J(R,\theta) \right] [t_i\, t_j\, cos^2\xi + \tau_i\tau_j\, sin^2\xi]\, d\xi \right\}$$

$$+ \rho\lambda \left\{ \frac{\sqrt{2}}{\pi^{3/2}} \bar{\sigma} \frac{\partial u_k}{\partial x_j} \int_0^{2\pi} \left[(T+b)^{1/2} \left(\mathfrak{T}_{ijk} + \mathfrak{T}_{ik}N_j \right) + \frac{\sigma A}{\bar{\sigma}} \frac{T^{1/2}}{2} \left(I_{ijk} + \frac{2}{3}N_i\, \delta_{kj} \right) \right] d\xi \right\},$$

$$(3.23)$$

where all mean fields are evaluated at $\boldsymbol{x} + \bar{\sigma}\boldsymbol{N}$, and the quantity b is defined by,

$$b = V_1^2 cos^2\xi + V_3^2 sin^2\xi \quad . \tag{3.24}$$

There are two terms proportional to velocity gradients. The first term is multiplied by $(T+b)^{1/2}$ and is a first order correction to $\boldsymbol{M}^o$ introduced by a Taylor series expansion $f(\boldsymbol{x} + \bar{\sigma}\boldsymbol{k})$ about $\boldsymbol{x} + \bar{\sigma}\boldsymbol{N}$. The second is multiplied by $A(v)$ and is from $\boldsymbol{M}^c$ due to the correction term in equation (3.17). The tensors $\mathfrak{T}_{ijk}$ and $\mathfrak{T}_{ik}$ in (3.23), which arise naturally from the averaging procedure, are given by

$$\mathfrak{T}_{ik} = \frac{1}{sin^2\theta} \left\{ \frac{1}{2R} \left[K(R,\theta) - \frac{(1+4R)}{2} J(R,\theta) \right] [t_i\, t_k\, cos^2\xi + \tau_i\tau_k\, sin^2\xi] \right.$$

$$+ \left. \left[\frac{J(R,\theta) - 2\,K(R,\theta)}{4R} \right] N_i N_k \right\},$$

$$(3.25)$$

and

$$\mathfrak{T}_{ijk} = \frac{1}{sin^2\theta} \left\{ X(R,\theta)N_i N_i N_k - Y(R,\theta) \left[\left(t_j\, t_k\, cos^2\xi + \tau_j\tau_k sin^2\xi \right) N_i \right] \right.$$

$$+(t_i\,t_k\,cos^2\xi\,+\,\tau_i\tau_k\,sin^2\xi)N_j\,+\,\big(t_i\,t_j\,\,cos^2\xi\,+\,\tau_i\tau_j\,sin^2\xi\big)N_k\},$$

$$(3.26)$$

in which

$$X(R,\theta) = \frac{2}{15R^2}\big[(1\,+\,Rcos^2\theta\,)^{3/2}(3Rcos^2\theta\,-\,2)-(1\,+\,R\,)^{3/2}(3R\,-\,2)\big]\quad,\qquad(3.27)$$

and

$$Y(R,\theta)\,=\,X(R,\theta)\,-\frac{2}{3R}\big[(1\,+\,Rcos^2\theta\,)^{3/2}\,-\,(1\,+\,R\,)^{3/2}\,\big]\quad.\qquad(3.28)$$

The tensor I_{ijk} also arises from the averaging and is given by

$$I_{ijk} = (sin^2\theta\,-\,2)N_iN_j\,N_k$$

$$-\frac{sin^2\theta}{2}\big[(t_j\,t_k\,+\,\tau_j\tau_k)N_i\,+\,(t_i\,t_k\,+\,\tau_i\tau_k)N_j\,+\,\big(t_i\,t_j\,+\,\tau_i\tau_j\big)N_k\big]\quad.$$

$$(3.29)$$

Interestingly, as R approaches zero, $\mathfrak{I}_{ijk}$ approaches I_{ijk}. Expression (3.23) for $\boldsymbol{M}$ differs most significantly from that obtained by Richman and Martin [1993] and Martin [1993] because it includes vibrations that can differ in three perpendicular directions.

Equation (3.23) demonstrates that the diagonal components (V_1^2, V_2^2, and V_3^2) of $\boldsymbol{B}$ influence the supply of momentum in the $\boldsymbol{N}$ direction, the off-diagonal $\boldsymbol{t}-\boldsymbol{N}$ and $\boldsymbol{\tau}-\boldsymbol{N}$ components of $\boldsymbol{B}$ are responsible for the supply of momentum in the tangential $\boldsymbol{t}$ and $\boldsymbol{\tau}$ directions, and the off-diagonal $\boldsymbol{t}-\boldsymbol{\tau}$ components of $\boldsymbol{B}$ has no effect on $\boldsymbol{M}$. In addition, equation (3.23) demonstrates that when the flow is uniform (so that the velocity gradients, shear stress and components of the momentum transfer $\boldsymbol{M}$ tangent to the boundary all vanish), the off-diagonal $\boldsymbol{t}-\boldsymbol{N}$ and $\boldsymbol{\tau}-\boldsymbol{N}$ components of $\boldsymbol{B}$ cause the assembly to slip with velocity $\boldsymbol{v}$.

In the same special case to which expression (3.23) applies, the lowest order integral expressions for F and D are

$$F = \frac{\sqrt{2}}{\pi^{3/2}} (1 + e_w) \rho \lambda \, csc^2\theta (T + V_2^2)^{1/2} \int_0^{2\pi} \frac{1}{\sqrt{1+R}} \left[\frac{1}{2} \left(\frac{T+b}{4} - b \right) J(R,\theta) - \frac{T+b}{4} K(R,\theta) \right] d\xi ,$$

(3.30)

and

$$D = \frac{1}{8\pi^{3/2}\sqrt{2}} (1 - e_w^2) \, \rho \lambda \, (T + V_2^2)^{3/2} csc^2\theta \int_0^{2\pi} \frac{1}{(1+R)^{3/2}} [\mathcal{H}(R,\theta) + 3\, I(R,\theta)] d\xi ,$$

(3.31)

where the dependence of b on ξ is given by equation (3.24), the dependence of R on ξ is given by equation (3.19), and where the function $\mathcal{H}(R,\theta)$ is given by

$$\mathcal{H}(R,\theta) = (1 + R)^{1/2} (5 + 2R) - (1 + Rcos^2\theta)^{1/2} (5 - 2Rcos^2\theta) \, cos\,\theta . \quad (3.32)$$

Expression (3.30) and (3.31) for F and D differ most significantly from that obtained by Richman and Martin [1993] and Martin [1993] because it includes vibrations that can differ in three perpendicular directions.

3.3   Deterministic Boundary Motion

The boundary conditions derived in section (3.1) apply to boundaries whose vibrations are random and described by prescribing the second moment $\boldsymbol{B}$ of its fluctuations. Alternatively, we could consider a boundary vibrating harmonically in three perpendicular directions x_1, x_2, and x_3 with corresponding velocities given by

$$\dot{x}_i = A_i n_i \omega \, sin(n_i \omega t + \zeta_i) \qquad (i = 1,2, or\ 3) \quad , \qquad (3.33)$$

where $n_2 = 1$, and n_1 and n_3 are positive integers. The amplitude A_i, phase angles ζ_i, integers n_1 and n_3, and frequency factor ω are all adjustable parameters that influence the rates at which

momentum and energy are transferred to the flows. Calculating similar boundary conditions for these boundaries would require carrying out averages that account for the dependence of the boundaries deterministic velocities on time. Then "steady" flows would occur when the period(s) of the boundary's vibrations were of the same order as the time between collisions between flow particles and the amplitudes of vibration were of the order of the average distance between particles in the flow. Adopting this assumption, we have avoided these complications by assuming that the boundary fluctuates randomly much like the flow particles themselves.

In order to interpret the full second moment $\boldsymbol{B}$ of boundary fluctuations in terms of the more familiar amplitudes, frequencies, and phase angles of a harmonically vibrating boundary, we interpret the components B_{ij} in the rates (3.23), (3.30), and (3.31) for $\boldsymbol{M}$, F, and D as the time averages of the products $\dot{x}_i \dot{x}_j$ over the longest period of oscillation, and find that

$$B_{ij} = \begin{cases} \dfrac{1}{2} A_i A_j n_i n_j \omega^2 \cos(\zeta_i - \zeta_j) & n_i = n_j \\ 0 & n_i \neq n_j \end{cases}. \tag{3.34}$$

According to this correspondence, each diagonal component $B_{ii}(\equiv V_i^2)$ is simply the product $A_i^2 \omega_i^2 / 2$ (where $\omega_i \equiv n_i \omega$).

Interestingly the off-diagonal components of $\boldsymbol{B}$ will vanish when the vibrations in the two corresponding orthogonal directions are either at the same frequency and $\pi/2$ radians out of phase, or at frequencies that are unequal integer multiples of same factor. At the same time, we have already observed that the off-diagonal components of $\boldsymbol{B}$ cause the assembly to slip tangentially relative to the mean motion of the boundary. To understand this, we examine the two-dimensional trajectories of a boundary that vibrates with the same frequency in the x_1- and x_2- directions are given respectively by

$$X_1 \equiv \frac{x_1}{A_1} = cos(\omega t + \zeta_1) \quad , \tag{3.35}$$

and

$$X_2 \equiv \frac{x_2}{A_2} = cos(\omega t + \zeta_2) \quad , \tag{3.36}$$

By eliminating t between equations (3.35) and (3.36), we find that

$$\frac{X_1'}{2sin^2\left(\frac{\zeta_1 - \zeta_2}{2}\right)} + \frac{X_2'}{2cos^2\left(\frac{\zeta_1 - \zeta_2}{2}\right)} = 1 \tag{3.37}$$

where $X_1' \equiv X_1 cos45 - X_2 sin45$ and $X_2' \equiv X_1 sin45 + X_2 cos45$ are coordinates rotated 45^0 from the $X_1 - X_2$ directions.

Equation (3.37) describes an ellipse with a semi major axis $a = 2sin^2((\zeta_1 - \zeta_2)/2)$ and a semi minor axis $b = 2cos^2((\zeta_1 - \zeta_2)/2)$ in the $X_1' - X_2'$ plane. Figure 3.5 shows the boundary trajectory with different phase angles where $\zeta = \zeta_1 - \zeta_2$. When the normal and tangential vibrations are in phase ($\zeta = 0$), the boundary vibrates in a straight line in the X_1'-direction. For fixed values of $A_1, A_2, \omega_1,$ and ω_2, this corresponds to the maximum value of B_{12} and the circumstances under which the boundary would most effectively drive the flow. As the phase angle increases from zero, the trajectory takes the form of an ellipse with semi major axis in the X_1'-direction, until the vibrations are perfectly out-of-phase ($\zeta = 90°$). In this extreme case, the trajectory takes the form of a circle, B_{12} vanishes, and the boundary is incapable of driving the flow. As ζ increases from $90°$ to $180°$, the trajectory evolves from a circle to an ellipse with semi major axis in the X_2'-direction, until it (at $\zeta = 180°$) the boundary moves in a straight line in the X_2' direction. In this extreme case, B_{12} assumes its largest negative value and drives the flow most effectively in the opposite direction.

Figure 3.5: Boundary trajectories

Finally, if we define $3V^2$ as the trace $tr\boldsymbol{B}$, then from the matrix (3.18),

$$3V^2 = V_1^2 + V_2^2 + V_3^2 \quad , \tag{3.38}$$

and, if the dimensionless measure α of total fluctuation velocity of the boundary is $V/\sqrt{\sigma g}$, then in terms of deterministic vibration parameters,

$$\alpha \equiv \frac{V}{\sqrt{\sigma g}} = \frac{\sqrt{A_1^2\omega_1^2 + A_2^2\omega_2^2 + A_3^2\omega_3^2}}{\sqrt{6\sigma g}} \quad . \tag{3.39}$$

In typical applications, operating frequencies are normally on the order of 40 to 150 Hz and amplitudes are on the order of a few particle diameters. So for particles with diameter σ of about $1\ mm$, typical values of α are in the range order of about 1 to 4.

Whereas α is a measure of the total vibrational energy of vibration, the fractions of vibrational energy in the normal **N-**, or tangential **t-** or **τ-**directions are given by the ratios,

$$V_t \equiv \frac{V_1}{V}, \quad V_n \equiv \frac{V_2}{V}, \quad V_\tau \equiv \frac{V_3}{V} \quad , \tag{3.40}$$

respectively. Each ratio can take on values between 0 and 3 in such a way that

$$V_t^2 + V_n^2 + V_\tau^2 = 3 \quad . \tag{3.41}$$

Isotropic vibration corresponds to the case $V_t^2 = V_n^2 = V_\tau^2 = 1$, and vibration in a single direction corresponds to the case when the ratio in that direction is equal to 3 and the remaining two are equal to 0.

Chapter 4

Flows of Unconfined Assemblies Down Vibrating Bumpy Inclines

In this chapter we study the effects of anisotropic boundary vibrations on steady fully developed flows down bumpy inclines. As a special case, we also consider unconfined assemblies on *horizontal* surfaces (i.e. those with no angle of inclination) to study the extent to which vibrations of the surfaces thermalize the assemblies and (possibly) induce mean motion. The assemblies consist of identical inelastic spheres.

In all cases, the anisotropic boundary vibrations are characterized statistically by the anisotropic Maxwellian described in equation (3.10), and the geometry of the bumpy boundaries is described in detail Chapter 3. In general, the second moment of velocity fluctuation B for the boundary is anisotropic, and under certain circumstances the vibratory motion of the surface can induce slip even when it is entirely horizontal as well as up-hill motion when it is inclined.

4.1   Steady, Fully Developed, Parallel Flow Equations

Here we consider steady, fully developed granular flows (that are unconfined from above) in which the mean velocity is parallel to the flat part of the lower bumpy boundary with which they interact, and where the spatial variations of the mean fields occur only in the direction normal to the boundary. In this section we derive the general boundary value problem for these flows.

In Figure 4.1, we employ the same Cartesian coordinate system introduced to write down the boundary conditions; here, x_1- points in the direction of the flow velocity u_1, and x_2- defines the direction normal to the boundary. The mean fields vary in the x_2- direction only, and the

flows are infinite in the x_1- and x_3-directions. The vertical acceleration due to gravity is g, and the angle between the lower boundary and the horizontal is ϕ.
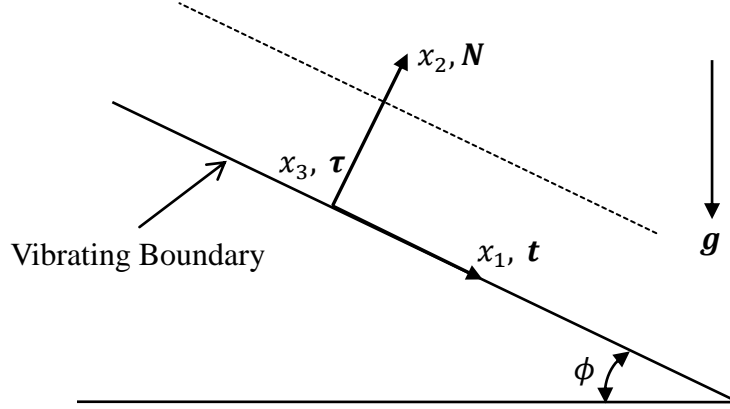
Figure 4.1: The coordinate system

For purposes of nondimensionalization, we introduce the characteristic velocity a. For unconfined flows (which are necessarily compressed by gravity), we take $a = \sqrt{\sigma g}$, where σ is the diameter of the flow particle. The dimensionless fields of solid fraction ν, velocity $u \equiv u_1/a$, and the measure $w^2 \equiv T/a^2$ of granular temperature depend only on the dimensionless coordinate $Y \equiv x_2/\sigma$.

In these flows, the balance of mass (2.4) and the x_3- components of the balance of momentum (2.5) are identically satisfied. If $S \equiv -P_{12}/(\rho_p a^2)$ and $P \equiv P_{22}/(\rho_p a^2)$ are dimensionless shear stress and normal pressure, then x_1-component of the momentum equation is

$$S' = -\frac{\sigma g}{a^2} \nu \sin \phi \quad , \tag{4.1}$$

where a prime denotes differentiation with respect to Y, and the x_2- component of the momentum equation is

$$P' = -\frac{\sigma g}{a^2} v \cos\phi \quad . \tag{4.2}$$

In terms of the dimensionless energy flux $q \equiv -Q_2/(\rho_p\, a^3)$ and dimensionless energy dissipation $\Gamma \equiv \sigma\gamma/(\rho_p\, a^3)$ the balance of energy (2.6) reduces to

$$q' + Su' - \Gamma = 0 \quad . \tag{4.3}$$

The isotropic and deviatoric parts of the constitutive equation (2.10) for the pressure tensor give, respectively, the normal pressure P as

$$P = 4vGF\, w^2 \quad , \tag{4.4}$$

and the shear stress S as

$$S = \frac{2EPu'}{5Fw\sqrt{\pi}} \quad , \tag{4.5}$$

where we have written viscosity μ given by (2.8) in terms of P.

The constitutive equations (2.11) for the energy flux and (2.7) for the energy dissipation give their dimensionless counterparts,

$$q = \frac{2\mathcal{M}Pw'}{F\sqrt{\pi}} \quad , \tag{4.6}$$

and

$$\Gamma = \frac{6(1-e)Pw}{F\sqrt{\pi}} \quad , \tag{4.7}$$

where in both cases we again we have written viscosity μ given by (2.8) in terms of P.

In principle, the fully coupled fifth order system that governs determines v, u, w, P, S, q, and Γ consists of five equations (4.1), (4.2), (4.3), (4.5) and (4.6) involving first derivatives, as well as two equations (4.4) and (4.7) that are purely algebraic. However, for later convenience, we uncouple u from the system and write the system in terms of the stress ratio S/P rather than in terms S or P separately.

From the energy equation (4.3), we employ equation (4.6), (4.5), and (4.7), to eliminate q, u', and Γ. We then differentiate equation (4.4) with respect to Y to write v' in terms of P' and w' wherever it appears in the intermediate result. Finally, we use (4.2) to eliminate P' and (4.4) to eliminate P wherever it does not appear as a ratio S/P. If we define the quantity H as the simple ratio w'/w, so that

$$w' = wH \quad , \tag{4.8}$$

then the energy equation (4.3) can finally be written as

$$H' = (1 - 2h)\frac{H\cos\phi}{(4G + 1)w^2} - [4h + 1]H^2 - \chi^2 \quad , \tag{4.9}$$

where χ^2 is defined by

$$\chi^2 \equiv \frac{1}{2\mathcal{M}}\left[6(1 - e) - \frac{5\pi\mathbb{F}^2 S^2}{2EP^2}\right] \tag{4.10}$$

and h is the function of solid fraction defined by

$$h(v) \equiv \frac{-\frac{d}{dv}\left[ln\left(\frac{\mathcal{M}}{\mathbb{F}}\right)\right]}{2\frac{d}{dv}[ln(vG\mathbb{F})]} \quad . \tag{4.11}$$

The quantity χ^2 is a local measure of the difference between the rate at which energy is dissipated by inelastic collisions and the rate at which energy is supplied to the flow by gravity.

Eliminating P between equations (4.2) and (4.4) yields v' as a function of v, w, and H:

$$v' = \frac{-v\cos\phi - 8G\mathbb{F}Hvw^2}{w^2(1 + 4G + 4v\,dG/dv)} \quad . \tag{4.12}$$

Equation (4.5) can be arranged to express the velocity gradient u' in terms of the ratio S/P according to

$$u' = \frac{5\mathbb{F}wS\sqrt{\pi}}{2EP} \quad . \tag{4.13}$$

4.2   Boundary Conditions

The boundary conditions at the free "surface" require that normal stress and shear stress, vanish there,

$$P = 0 \text{ and } S = 0 \quad . \tag{4.14}$$

Because both the normal pressure P and the shear stress S vanish at the free surface, equations (4.1) and (4.2) yield,

$$\frac{S}{P} = tan\phi \quad , \tag{4.15}$$

so that the stress ratio S/P can be replaced by $tan\,\phi$ wherever it appears, as it does in equation (4.10). The conditions at the free surface also require that energy flux (and therefore w') vanishes there, so that

$$H = 0 \quad \text{or} \quad q = 0 \quad . \tag{4.16}$$

In order to write the boundary conditions that express the balance of momentum and energy at the vibrating bumpy boundary in nondimensional form, we introduce a scaled measure of the dimensionless temperature w, defined by $\Omega \equiv w/\alpha$. The ratio R and the dimensionless counterpart b^* to the quantity b given by equation (3.19) and (3.24) respectively can be written as

$$R = \frac{(V_n^2 - V_t^2 cos^2\xi - V_\tau^2 sin^2\xi)}{(\Omega^2 + V_t^2 cos^2\xi + V_\tau^2 sin^2\xi)} \quad , \tag{4.17}$$

and

$$b^* = V_t^2 cos^2\xi + V_\tau^2 sin^2\xi \quad , \tag{4.18}$$

where $V_t \equiv V_1/V$, $V_n \equiv V_2/V$, and $V_\tau \equiv V_3/V$ have been introduced in equation (3.40) in such a way that $V_n^2 + V_t^2 + V_\tau^2 = 3$. In addition, we have already introduce the parameter $\alpha = V/a$ in equation (3.39) as a measure of the total vibrational energy.

The normal x_2- component of the momentum balance (3.1) requires that $M_2 = P_{22}$. The corresponding component of (3.22) then takes the simple dimensionless form

$$\alpha^2 \lambda v \frac{(1 + e_w)}{2} (\Omega^2 + V_n^2) = P \left[1 - \frac{sin^2\theta R^*}{2(1 + R^*)} \right]^{-1} \; , \tag{4.19}$$

where we have used the facts that ϑ_2, t_2, τ_2, $\mathfrak{T}_{221}$, $\mathfrak{T}_{21}$, and I_{221} are all zero. This equation allows us to eliminate the factor λ wherever it occurs.

The tangential x_1- component of condition (3.1) requires that $M_1 = P_{12}$. If, in the corresponding component of (3.22) we employ equations (3.24), (3.27), (3.38), and (3.51) to respectively eliminate λ, u', $\mathfrak{T}_{121}$, I_{121}, then the dimensionless slip velocity $\vartheta = \vartheta_1/a$ is related to Ω, v and boundary motion and geometry through

$$-\frac{\sqrt{2}v}{\pi^{3/2}\alpha} \int_0^{2\pi} (\Omega^2 + b^*)^{1/2} \mathfrak{T}_{11} d\xi = \frac{sin^2\theta}{2} b_{12}$$

$$+ \frac{5\mathbb{F}S\Omega}{\pi E P \sigma \sqrt{2}} \bar{\sigma} \int_0^{2\pi} \left\{ (\Omega^2 + b^*)^{1/2} \left[\mathfrak{T}_{11} - \frac{Y cos^2\xi}{sin^2\theta} \right] - \frac{\sigma A}{4\bar{\sigma}} \Omega sin^2\theta \right\} d\xi$$

$$+ \frac{S}{P} (\Omega^2 + V_n^2) \left[1 - \frac{R^* sin^2\theta}{2(1 + R^*)} \right] \frac{2}{(1 + e_w)} , \tag{4.20}$$

with $b_{12} \equiv B_{12}/V^2 = V_t V_n cos\zeta$ (in which $\zeta \equiv \zeta_1 - \zeta_2$ is the phase difference), b^* given by equation (4.18), the ratio R^* is given by

$$R^* = \frac{(2V_n^2 - V_t^2 - V_\tau^2)}{(2\Omega^2 + V_t^2 + V_\tau^2)} \; , \tag{4.21}$$

and $\mathfrak{T}_{11}(R,\theta) = cos^2\xi[K - (1 + 4R)/2J]/2R sin^2\theta$ from equation (3.25), and $Y(R,\theta)$ is given by equation (3.28).

The tangential x_3- component of the momentum balance (3.1) at the boundary dictates that because both v_3 and P_{23} vanish, then so too must M_3. When combined with equation (3.23) this, in turn requires that $B_{23} = 0$. That is, if no motion is to occur in the x_3- direction, then the boundary cannot supply momentum in that direction.

The energy flux boundary condition (3.3) requires a balance between the slip work, the energy supplied by boundary fluctuations, the energy dissipated by boundary collisions, and the energy flux. If it is manipulated in a manner similar to the x_1- component of the momentum balance, then the equation that determines w' at the boundary is

$$-\sqrt{\frac{\pi}{2}} \frac{(1 + e_w)(\Omega^2 + V_n^2)^{1/2}}{2csc^2\theta} \left(1 - \frac{R^* sin^2\theta}{2(1 + R^*)}\right) \left\{\frac{Sv}{P\alpha} - \frac{2\mathcal{M}w'}{\alpha\mathbb{F}\sqrt{\pi}}\right\} =$$

$$-\frac{(1 - e_w^2)}{2\pi} \frac{(\Omega^2 + V_n^2)}{8} \int_0^{2\pi} \frac{(\mathcal{H} + 3I)}{(1 + R)^{3/2}} d\xi$$

$$+ \frac{(1 + e_w)}{\pi} \int_0^{2\pi} \frac{1}{(1 + R)^{1/2}} \left[\frac{1}{2}\left(\frac{(\Omega^2 + b^*)}{4} - b^*\right)J - \frac{(\Omega^2 + b^*)}{4}K\right] d\xi,$$

(4.22)

where the left-hand-side contains the slip work and energy flux terms, and the right-hand-side is the difference between the energy dissipated and the energy supplied by boundary collisions. Here v/α is given by (4.22), b given by equation (4.18), and $\mathcal{H}(R, \theta)$, $J(R, \theta)$, $I(R, \theta)$ and $K(R, \theta)$ are given by equations (3.32), (3.21), (3.22), and (3.20), respectively.

4.3   Solution Procedure

Equations (4.8), (4.9), and (4.12) (with the stress ratio $S/P = tan\,\phi$ wherever it appears) determine $w(Y)$, $H(Y)$, and $v(Y)$ to within three constants of integration. In each case, we solve these equations for a prescribed value of mass hold-up m_t, defined by the integral,

$$m_t \equiv \int_0^\beta v dY \quad , \tag{4.23}$$

where $\beta \equiv \sigma/L$ is the dimensionless depth of the thermalized assembly. We employ a fourth order Runge-Kutta technique to integrate these equations from the free surface, where both the normal stress (and therefore v) and the energy flux (and therefore H) are equal to zero. In order to initiate the integrations, we guess at the value of the granular temperature w at the free surface, and then integrate to the depth at which the mass hold-up m_t assumes its prescribed value. At that location, equation (4.20) determines the slip velocity, which in turn is used in equation (4.22) to determine if the energy flux boundary condition is properly satisfied for the chosen values of V_n, V_t, V_τ, θ, α, and e_w. If it is not, we use Newton-Raphson to iterate on the guess for w at the free surface until it is satisfied, and the distance from the free surface at which it is satisfied determines the depth β. Equation (4.13) then may be integrated from the base (where the slip velocity is known) to the free surface (at which $Y = \beta$ is known) to determine the velocity profile $u(Y)$ and the corresponding mass flow rate,

$$\dot{m} \equiv \int_0^\beta v u dY \quad . \tag{4.24}$$

There is a subtle complication in carrying out this procedure. According to constitutive relation (4.4), v must be equal to zero if P vanishes where w does not. In particular, v must equal to zero at the free surface. Because w' is also equal to zero there, equations (4.2), (4.12), and (4.9) demonstrate that P', v', and w'' each vanish at the free surface. Integrations initiated from the top of the flow therefore yield no spatial variations in P, w, and v. This indicates that the theory predicts flows that are actually infinitely deep and that P, w, and v approach their free surface values asymptotically from the base. To overcome this difficulty, we set v at the free surface equal to 10^{-6}, which is equivalent to relaxing very slightly the normal stress condition

there, and allows the integrations to proceed away from zero. The depth β is then taken to be the depth below which 99% of the mass hold-up is contained.

4.4   Horizontal Granular Assemblies

First, we consider granular assemblies that are thermalized and driven by horizontal vibrating boundaries. In these simple flows where $\phi = 0$, according to equation (4.1), the shear stress is constant throughout the assemblies. Because, according to the second stress condition (4.14), the shear stress vanishes at the free surface, it vanishes everywhere. According to equation (4.13), the velocity gradient is proportional to the shear stress, so the velocity gradient also vanishes, and the assemblies move uniformly. The uniform velocity is equal to the slip velocity, which is determined by the tangential momentum boundary condition (4.20) in which $S = 0$. Equation (4.20) clearly demonstrates that in this case the slip velocity is due entirely to the off-diagonal component $b_{12}(\equiv B_{12}/V^2)$ of the second moment $\boldsymbol{B}$. This is consistent with the insight gained from the boundary trajectories shown in Figure 3.5, in which $b_{12} = V_t V_n \cos\zeta$ and where $\zeta \equiv \zeta_1 - \zeta_2$ is the phase difference between the vibrations in the normal and tangential directions.

In Figure 4.2 we show the steady variations of granular temperature w and solid fraction ν with vertical location Y for mass hold-ups $m_t = 2.5, 5, 10, 20$ (when $\alpha = 2$, $V_n^2 = 3$, $\theta = \pi/6$, and $e = e_w = .9$). Although the effect of increasing the mass of the assembly from $m_t = 2.5$ to 20 is to decrease the granular temperature everywhere, the decrease is far more pronounced near the top of the assembly than at the base. At the lower values ($m_t = 2.5$ and 5) of mass hold-up, the boundary vibrations are sufficient to fully thermalized the assemblies and to disperse them at solid fractions that are everywhere significantly less than the random close packed value.
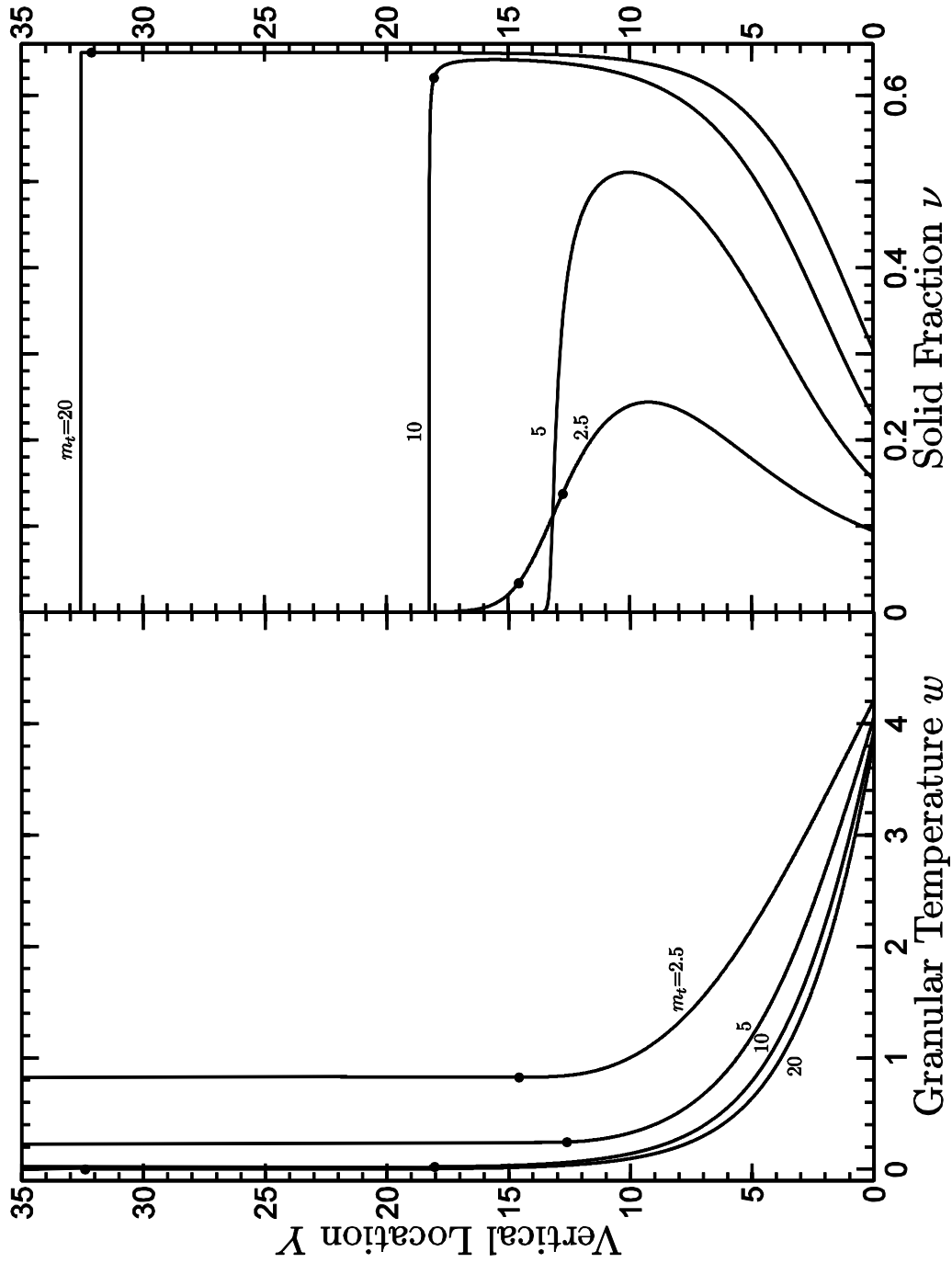
Figure 4.2: The profiles of granular temperature w and solid fraction ν for mass hold-up $m_t = 2.5, 5, 10, 20$ when $\alpha = 2$, $V_n^2 = 3$, $\theta = \pi/6$, $e = e_w = .9$, and $\phi = 0$.

However, at the two higher values ($m_t = 10$ and 20), the assemblies are in effect, only partially thermalized. These more massive assemblies consist of an upper passive region, in which the solid fraction is essentially constant and nearly equal to its maximum value, supported by a relatively thin thermalized region immediately above the base. The solid dots shown on these profiles and all others that follow indicate the location below which 99% of the mass m_t is contained.

We are concerned with the effects of the direction of vibration on the prevailing thermalized states. In Figure 4.3 we examine cases of two-dimensional vibrations and show the variations of granular temperature w and solid fraction ν with vertical location Y for varying degrees of vertical vibrations $V_n^2 = 0, 1, 2, 3$ (when $\alpha = 2$, $m_t = 5$, $\theta = \pi/6$, $V_\tau^2 = 0$, and $e = e_w = .9$). As V_n^2 increases (so that the degree of tangential vibration is converted to normal vibration while the total energy of vibration remains fixed), the boundary becomes more effective at thermalizing the assembly and the flow becomes deeper, more thermalized, and more dilute. In all cases shown here $b_{12} = 0$, so the vibrations in the normal and tangential directions are perfectly out-of-phase and therefore no slip velocity and no mean velocity throughout the assembly are induced.

In Figure 4.4 we show the variations of granular temperature at the top w with boundary bumpiness θ for degree of vertical vibrations $V_n^2 = 0, 1, 3/2, 2, 3$ (when $m_t = 5$, $\alpha = 2$, $V_\tau^2 = 0$, and $e = e_w = .9$). When the vibrations are due entirely to tangential motion ($V_n^2 = 0$), the temperatures increase dramatically as the boundaries evolve from perfectly flat ($\theta = 0$) to extremely bumpy ($\theta = \pi/2$). However, when the vibrations are due entirely to normal motion ($V_n^2 = 3$), the temperature actually decrease as the boundaries become bumpier and experience fewer normal and more oblique impacts. The increase in temperature when $V_n^2 = 0$ is far more
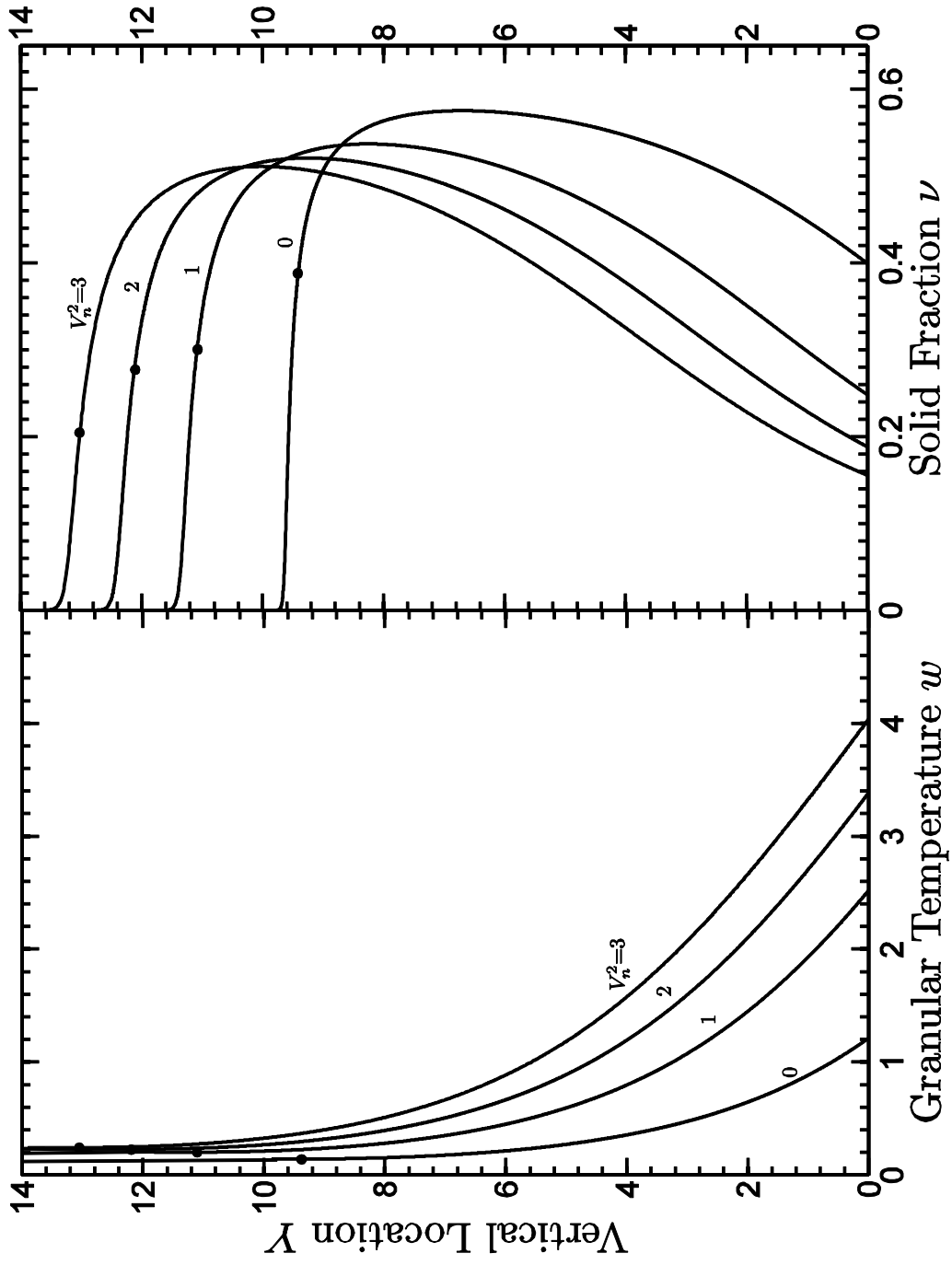
Figure 4.3: The profiles of granular temperature w and solid fraction v for degree of vertical vibration $V_n^2 = 0, 1, 2, 3$ when $\alpha = 2$, $V_\tau^2 = 0$, $m_t = 5$, $\theta = \pi/6$, $e = e_w = .9$, and $\phi = 0$.
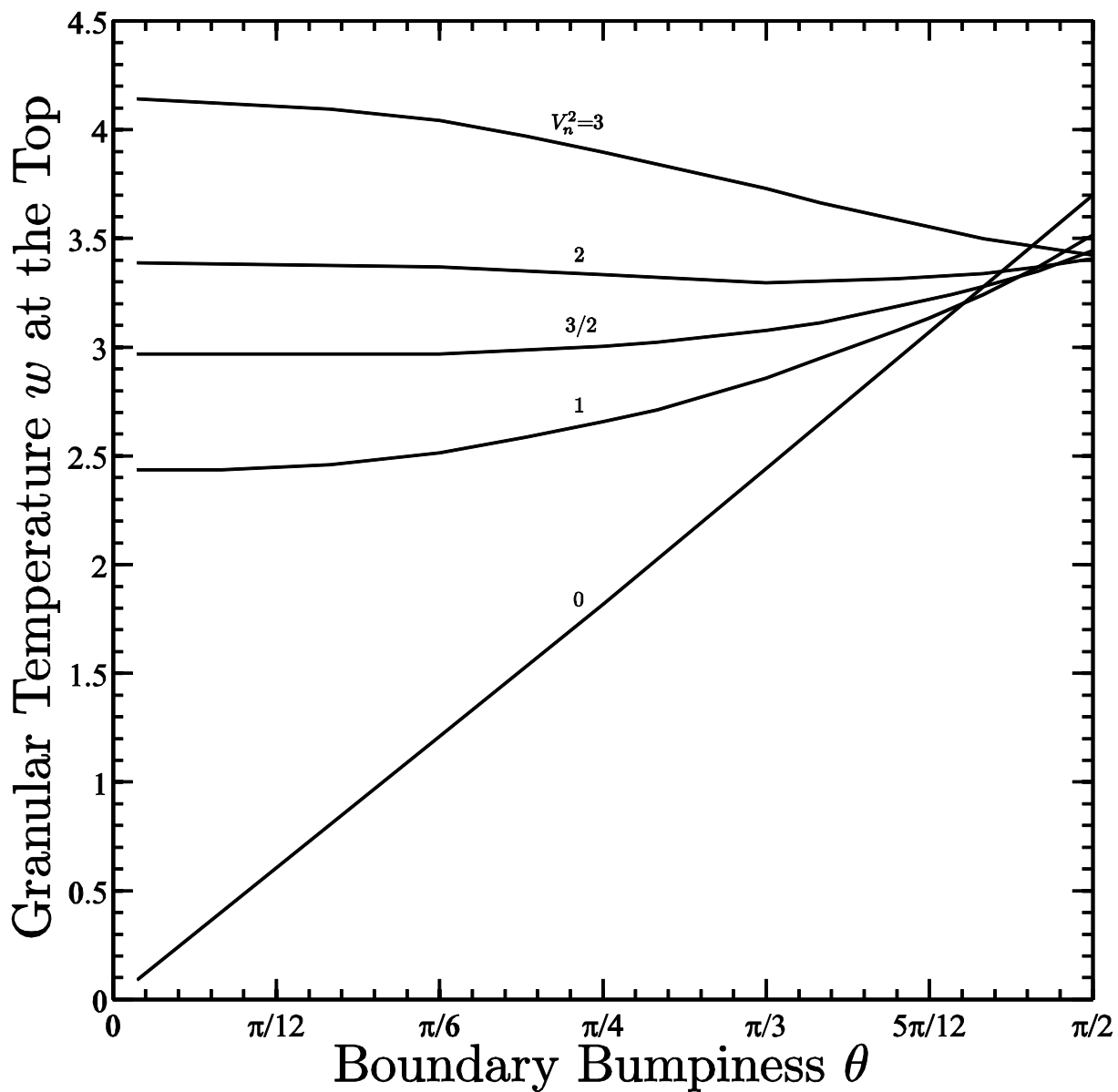
Figure 4.4: The variation of granular temperature w at the top with bumpiness θ for degree of vertical vibration $V_n^2 = 0, 1, 3/2, 2, 3$ when $\alpha = 2$, $V_\tau^2 = 0$, $m_t = 5$, $e = e_w = .9$, and $\phi = 0$.

pronounced than the decrease in temperature when $V_n^2 = 3$, and the differences between the temperatures induced by pure tangential motion and those induced by pure normal motion diminish as increases θ in the range until eventually the boundary becomes so bumpy that the tangential vibrations are *more* effective at thermalizing the assembly than the normal vibrations. Beyond this value of bumpiness θ, the granular temperatures actually *decrease* as the energy of tangential vibrations is converted to energy of normal vibrations.

Of concern also are the velocities (and flow rates) induced by the vibrating surface. In Figure 4.5 we show the variations of the mean velocity u (scaled by the phase difference $cos\zeta$) with degree of vertical vibration V_n^2 (when $\theta = \pi/6$, $m_t = 5, V_\tau^2 = 0$, and $e = e_w = .9$). Equation (4.20) demonstrates that the mean velocity scales with $cos\zeta$. The extreme cases where the vibrations are due entirely to tangential motion or entirely to normal motion, the boundary does not induce any mean motion. As the tangential energy in the first extreme is continuously converted to normal energy in the second while the total energy is fixed, the induced mean velocity increases from zero to its maximum value, and then decrease back to zero. This shows that there is actually an optimum distribution of tangential and normal energy that maximizes the flow rates.

4.5   Inclined Granular Assemblies

Here we are concerned with steady fully developed flows of granular assemblies of identical inelastic particles down vibrating bumpy boundaries.

In these flows, unlike the horizontal case, the angle of inclination ϕ is not equal to zero, the stress ratio $S/P = tan\,\phi$, the shear stress is not equal to zero, and the mean velocity is not uniform. Equation (4.20) demonstrates that in this case the slip velocity is due to two effects: the
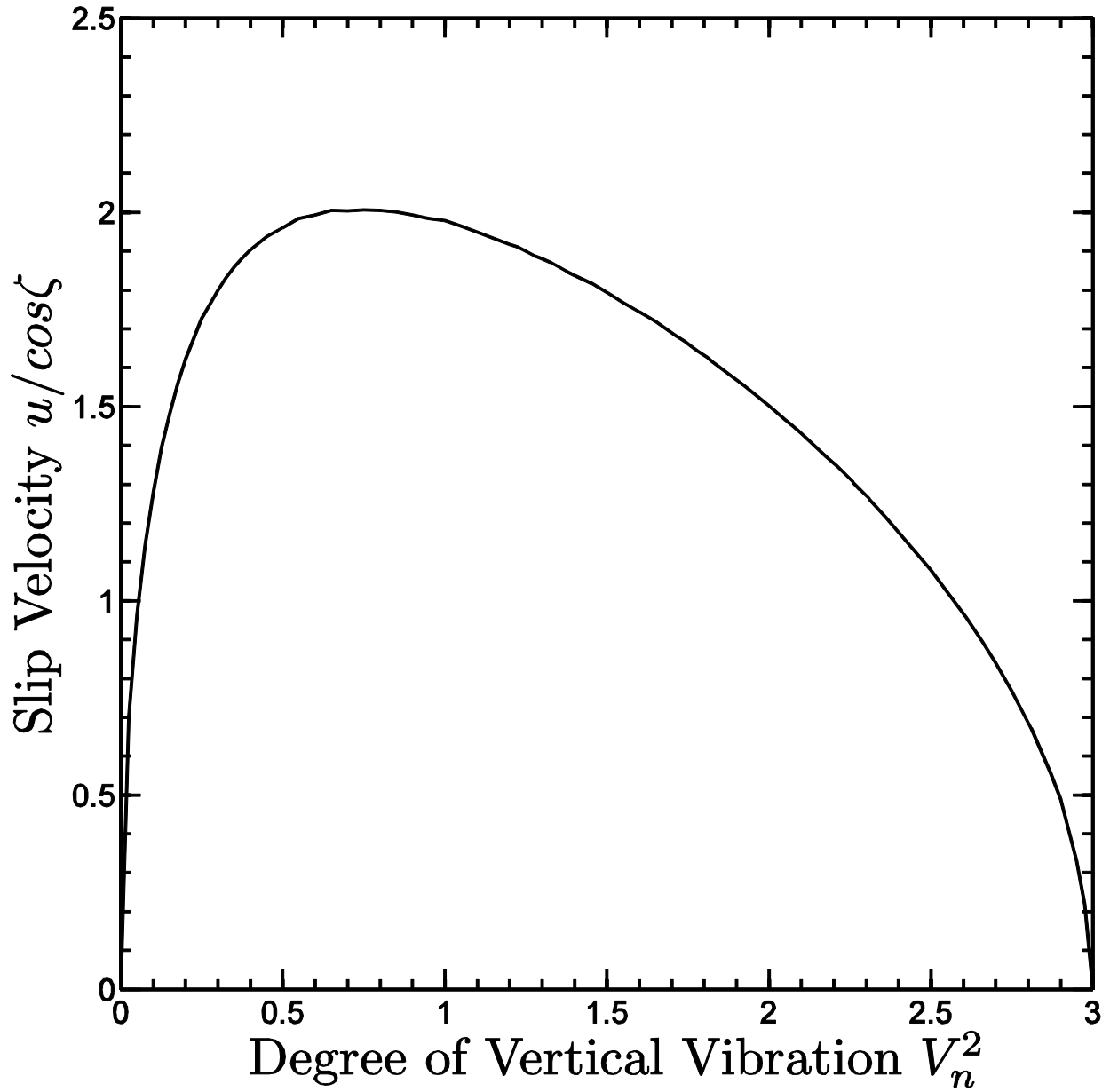
Figure 4.5: The variation of the slip velocity $u/\cos\zeta$ with the degree of vertical vibration V_n^2 when $= \pi/6$, $m_t = 5$, $V_\tau^2 = 0$, $e = e_w = .9$, and $\phi = 0$.

off-diagonal component $b_{12}(\equiv B_{12}/V^2)$ of the second moment $\boldsymbol{B}$; and the stress ratio due to the angle of inclination of the flow.

Although the full solution procedure is outline in Section 4.3, it is complicated in this case by the fact that steady fully developed flows can be maintained on only a limited range of inclination angles. This range depends on the bumpiness of the boundary, the coefficients of restitution between the any two particles and between the any flow particle and the boundary, and the components of $\boldsymbol{B}$ that characterize the detailed manner in which the boundary vibrates.

In Figure 4.6, for example, we focus on the case of a non-vibrating incline (i.e. $\alpha = 0$) and show how that range of inclination angles ϕ (between which steady fully developed flows are possible) varies with boundary bumpiness θ (when $e = e_w = .9$). The area between the curves in the $\phi - \theta$ plane corresponds to the values of ϕ and θ for which steady, fully developed flows are possible. The upper curve shown corresponds to the maximum value of ϕ for which the solution procedure yielded a solution. Above these values, the flows will accelerate down the incline. For a fixed bumpiness θ, as the angle of inclination decreases from it maximum value, the flows generally become shallower. The lower curve in Figure 4.6 corresponds to flows of dimensionless depth $\beta = 2$, below which we interpret to results to mean that gravity is not great enough to overcome the resistance from the bumpiness of the incline. As θ increases, the boundary becomes bumpier, the slip velocity decreases, and the energy supplied to the flow decreases. In order to balance the energy dissipated due to inelastic collisions in the flow and at the boundary, both the work done by gravity and the slip work must increase. Therefore the angle of inclination ϕ must increase.

Even when the incline is not vibrating, the range of ϕ between which steady flows can be maintained is influenced by the dissipative nature of the collisions between any two flow
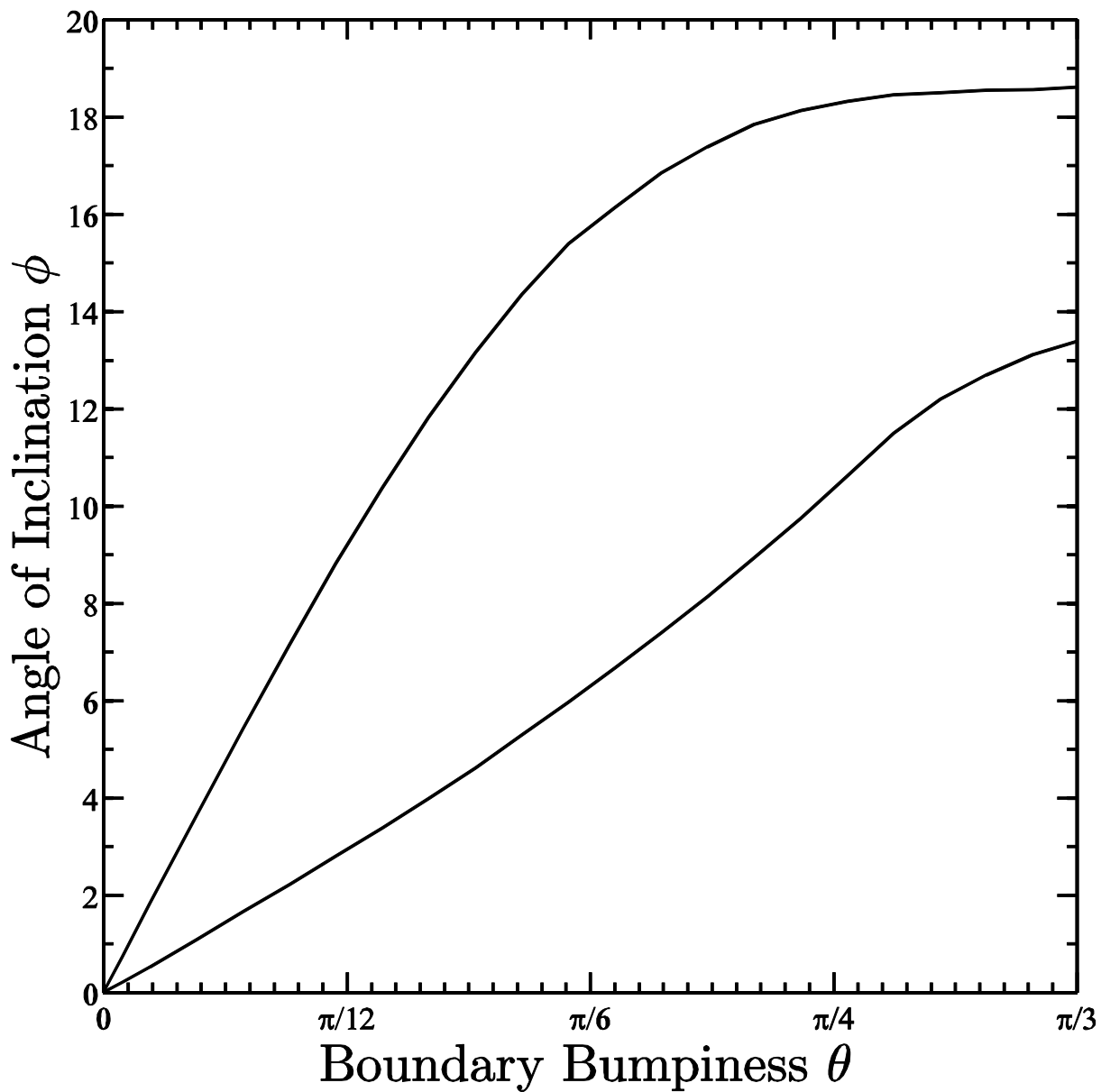
Figure 4.6: The variation with bumpiness θ of the minimum and maximum angles ϕ for steady flows when $\alpha = 0$ and $e = e_w = .9$.

particles (as measured by e) and between any flow particle and the boundary (as measured by e_w). Figure 4.7 shows how the steady range of angle ϕ varies with with coefficients of restitution $e = e_w$ when $\theta = \pi/6$. The area in the $\phi - e$ plane corresponds to the values of ϕ and e for which steady, fully developed flows are possible. The upper and lower curves have the same significance here as in Figure 4.6. When $e = e_w = 1$, no energy is dissipated within the flow or at the boundary. In this case, there is no mechanism to dissipate the energy supplied by gravity, slip work, and the boundary fluctuations. Consequently, in this limit, the theory predicts that there are no angles of inclination at which steady, fully developed flows can be maintained. As the flow becomes more dissipative (i.e. as $e = e_w$ decreases), the range of inclinations at which steady fully developed flows are possible generally increases. In these flows, the rate at which energy is dissipated must balance the rate at which it is supplied by gravity, slip work, and boundary fluctuations. So, as $e = e_w$ decreases, the energy supplied by both gravity and slip work must increase. Consequently range of angles at which steady flows can be maintained must also increase. When $\theta = \pi/6$, for example, the range of angles for steady fully developed flows is from $\phi = 6.36°$ to $\phi = 15.87°$.

Interestingly, at any point ϕ, θ in the steady range shown in Figure 4.6, a variety of flows are possible with different mass hold-ups m_t and different mass flow rates $\dot{m}$. Employing a slightly modified version of the solution procedure described in section 4.3, when the mass hold-up is not prescribed, we can instead prescribe the value of granular temperature at the free surface, integrate downward until the boundary conditions at the base are satisfied, and then calculate the corresponding mass hold-up.

We carried this procedure out for $\phi = 13.5^0$ and $\theta = \pi/6$ (when the average spacing s between the boundary particles is zero and the flow particles are the same size as the bumps).
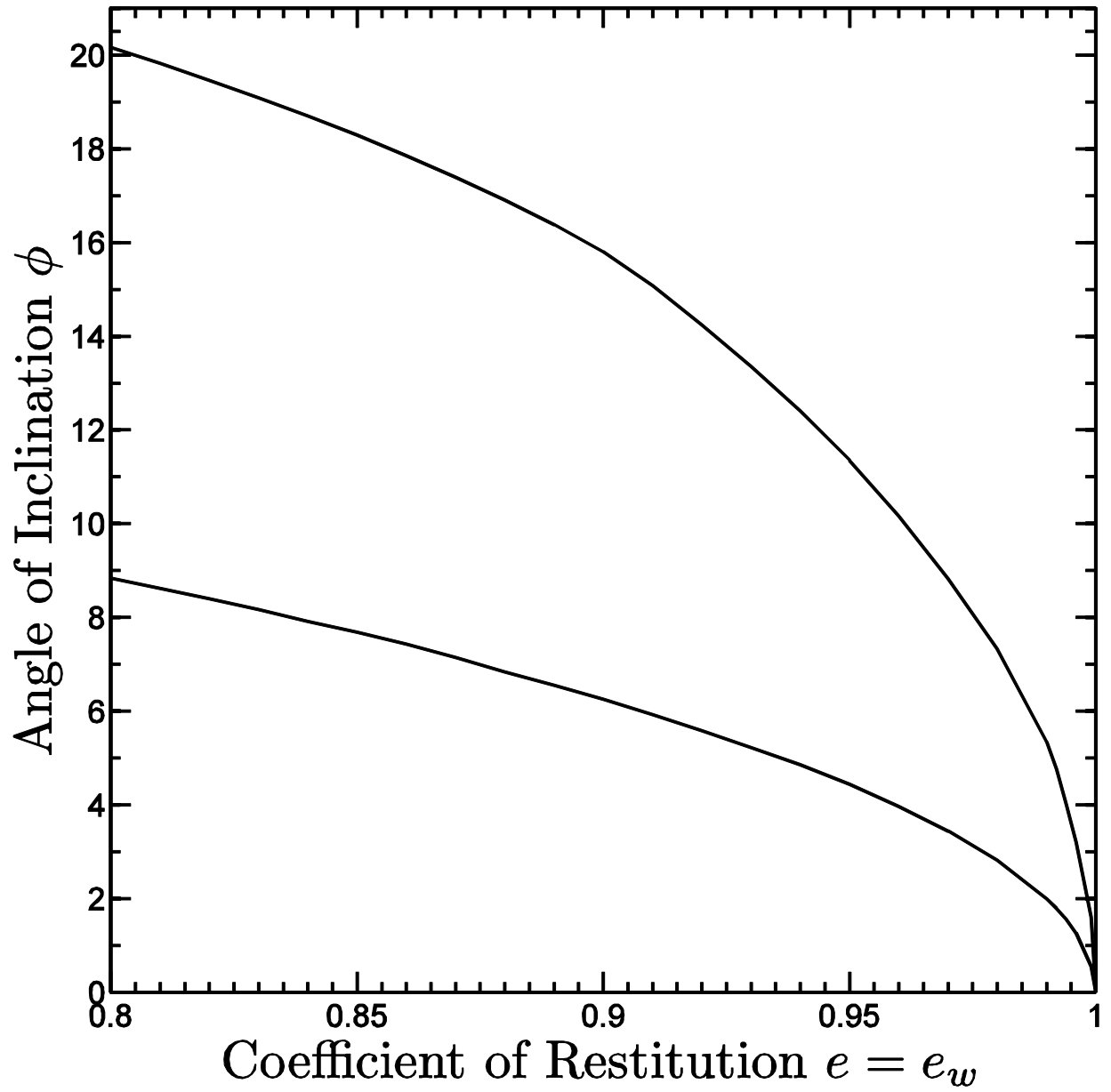
Figure 4.7: The variation with coefficient of restitution $e = e_w$ of the minimum and maximum angles ϕ for steady flows when $\theta = \pi/6$ and $\sigma/d = 1$.

In Figure 4.8 we show the variations of mass hold-up m_t, mass flow rate $\dot{m}$, depth of the flow β, depth-average mean velocity $\bar{u}$, and depth average solid fraction $\bar{v}$ with the free surface value of granular temperature w (for $\phi = 13.5^0$ and $\theta = \pi/6$, when $\alpha = 0$, and $e = e_w = .9$). As w increases, the flows become deeper, faster, and more dilute. The mass hold-up varies in a more complicated way. Interestingly, none, one, two or three steady flows are possible at the same mass-hold-up depending on its value. Each corresponds to a different value of w at the free surface.

In Figure 4.9, for example, we show the profiles of mean velocity u, granular temperature w, and solid fraction v corresponding to the three steady flows that are possible at a mass hold-up of $m_t = 6.6$ (when, $\alpha = 0$, $\phi = 13.5^0$, $\theta = \pi/6$ and $e = e_w = .9$). These correspond to the points labeled #1, #2, and #3 in Figure 4.7. The flow (#3) with a highest granular temperature at the top is significantly faster, more thermalized, and more dilute than the other two (#1 and #2).

In Figure 4.10 we show the variations of the depth of the flow β, mass flow rate $\dot{m}$, depth-average mean velocity $\bar{u}$, depth-average solid fraction $\bar{v}$, and depth-average granular temperature $\bar{w}$ with total vibrational energy α for boundary bumpiness $\theta = \pi/6, \pi/4, \pi/3$ when $V_n^2 = 3$, $\phi = 13.5^0$, $m_t = 6.6$, $\theta = \pi/6$, and $e = e_w = .9$. The results demonstrate how the third flow (#3) in Figures 4.8 and 4.9 evolve as the total energy of vibration increases from zero. For any fixed value of θ, as the total vibrational energy α increases, the flow becomes deeper, faster, more dilute, and more thermalized. For a fixed value of α, as the bumpiness θ of the boundary increases, the flows become less deep, slower, more dense, and less thermalized. The character of the changes that occur within the flow are shown in Figure 4.11, in which we plot the profiles of mean velocity u, granular temperature w, and solid fraction v for vibrational
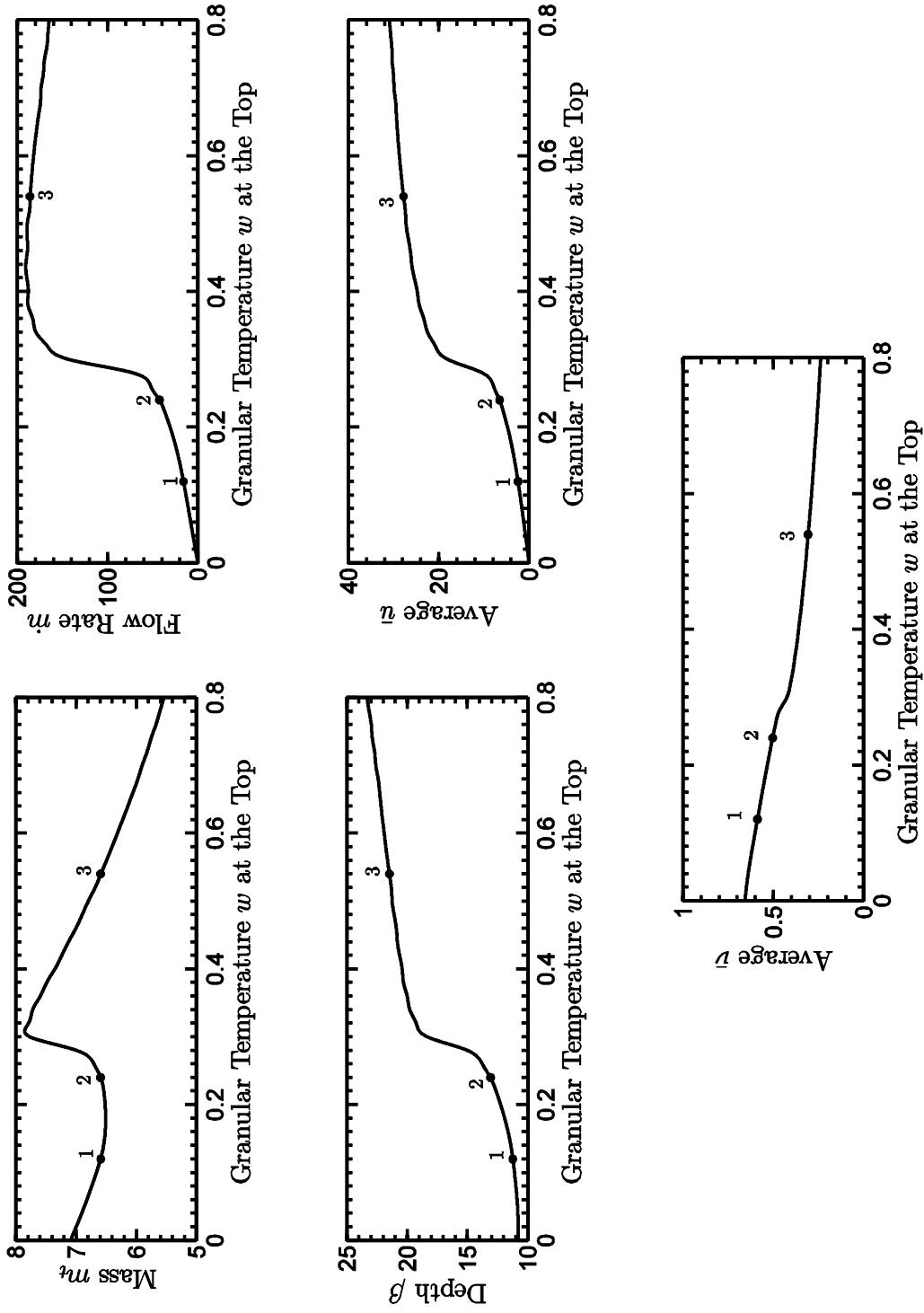
Figure 4.8: The variation of mass hold-up m_t, mass flow rate $\dot{m}$, depth β, average mean velocity $\overline{u}$, and average solid fraction $\overline{v}$ as functions of the granular temperature w at the top when $\phi = 13.5^0$, $\alpha = 0$, $\theta = \pi/6$, $\sigma/d = 1$, and $e = e_w = .9$.
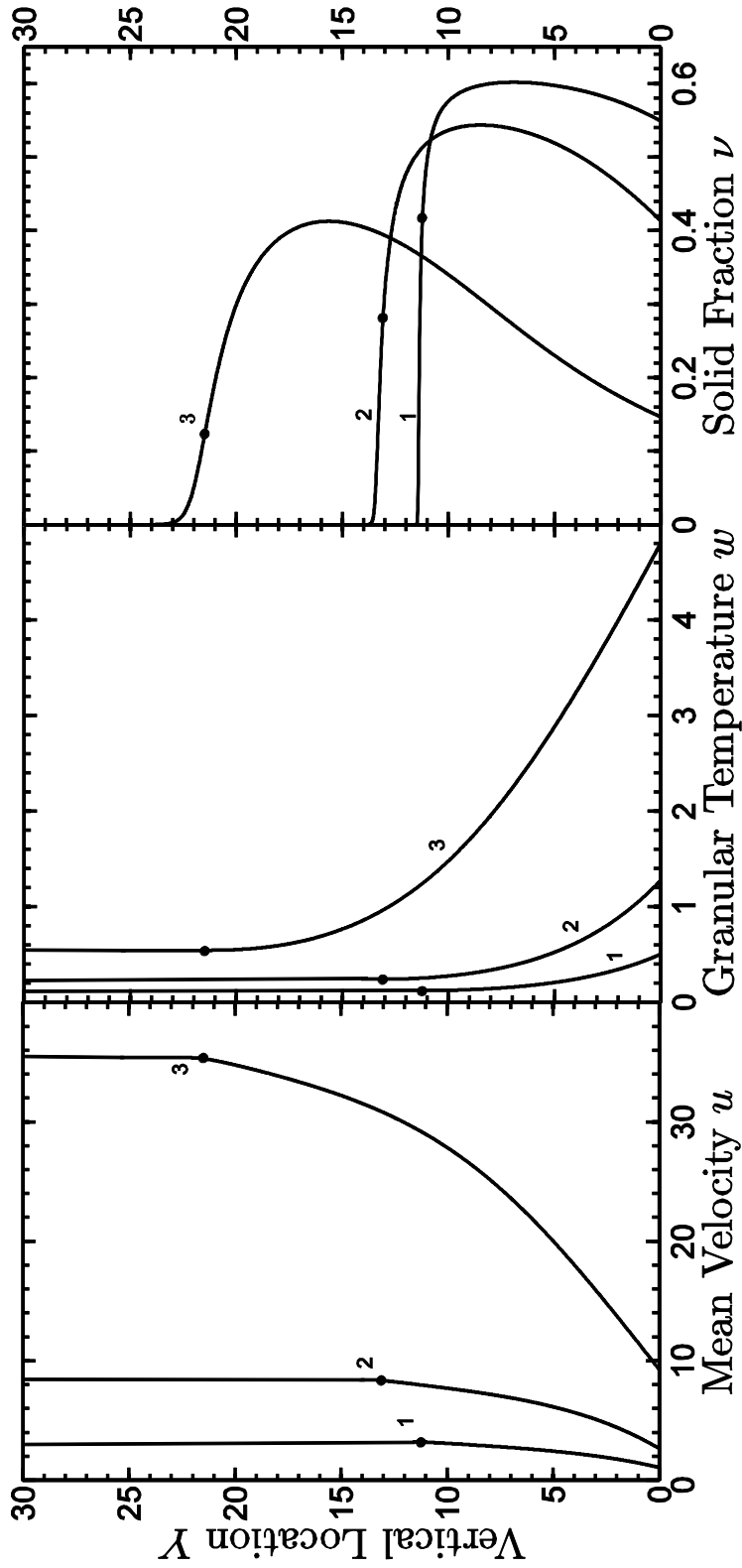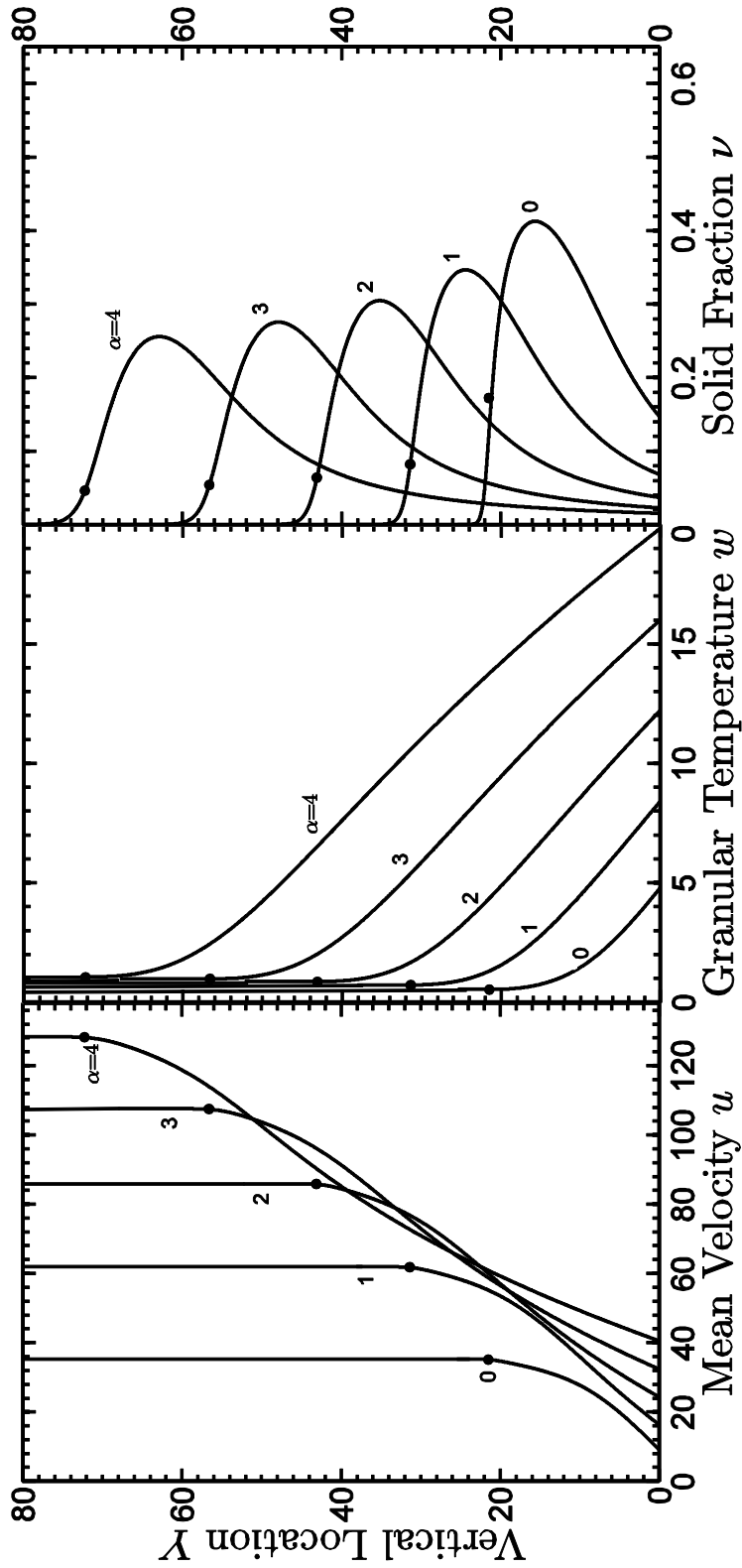
Figure 4.9: The profiles of mean velocity u, granular temperature w, and solid fraction v for mass hold-up $m_t = 6.6$, when $\alpha = 0$, $\phi = 13.5^0$, $\theta = \pi/6$, $\sigma/d = 1$, and $e = e_w = .9$.
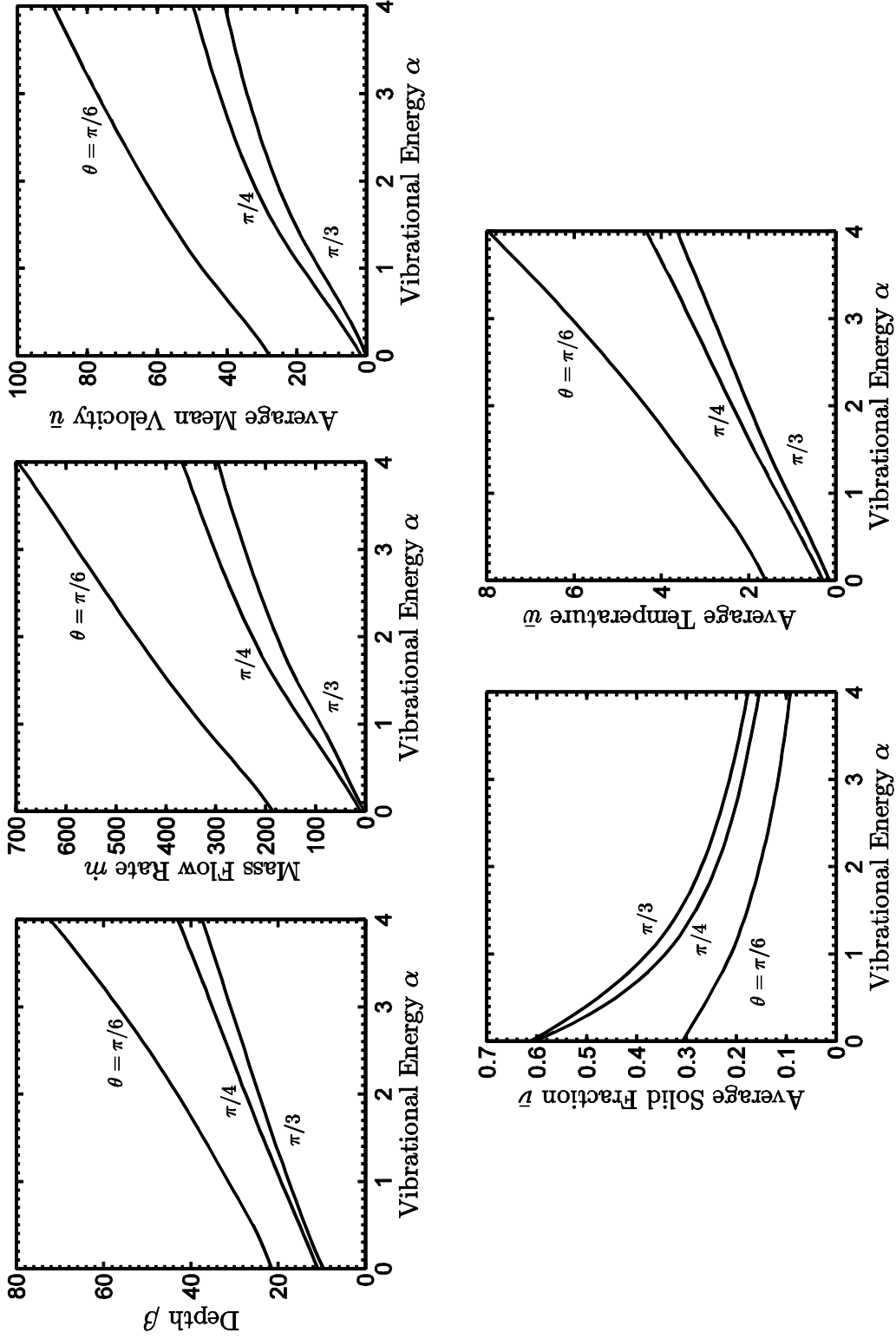
Figure 4.10: The variation of depth β, mass flow rate $\dot{m}$, average mean velocity $\bar{u}$, average solid fraction $\bar{\nu}$, and average granular temperature $\bar{w}$ with vibrational energy α for bumpiness $\theta = \pi/6, \pi/4, \pi/3$ when $V_n^2 = 3$, $\phi = 13.5^0$, $m_t = 6.6$, $\sigma/d = 1$, and $e = e_w = .9$ (For flow #3 in Figure 4.8)

energies $\alpha = 0, 1, 2, 3, 4$ (when $\phi = 13.5^0$, $m_t = 6.6$, $V_n^2 = 3$, $\theta = \pi/6$, and $e = e_w = .9$). Not surprisingly, as the total vibrational energy α increases while the mass hold-up remains unchanged, the assemblies become deeper, faster, more thermalized and more dilute. The mass flow rates increase dramatically because as the vibrational energy increases, the relatively dense region of the flow gets only slightly more dilute but moves at significantly higher speeds down the incline.

A more interesting question is how, for a fixed total vibrational energy, the flows are affected as the boundary vibrations are redistributed in different directions. Figure 4.12 shows the variations of the depth of the flow β, mass flow rate $\dot{m}$, depth-average mean velocity $\bar{u}$, depth-average solid fraction $\bar{v}$, and depth-average granular temperature $\bar{w}$ with degree of vertical vibration V_n^2 for $\alpha = 1$ and $V_\tau^2 = 0$ (when $\theta = \pi/6, \pi/4, \pi/3$, $\phi = 13.5^0$, $m_t = 6.6$, and $e = e_w = .9$). For a fixed value of θ, as the vibrational energy is converted from tangential motion ($V_n^2 = 0$) to normal motion ($V_n^2 = 3$), the flows becomes deeper, faster, more dilute, and more thermalized. This indicates clearly that normal vibrations more effectively transfer energy to the flow than do tangential vibrations. However, the extent to which this is true depends on the bumpiness. Because at relatively flat boundaries the tangential vibrations are not very effective at transferring energy to the flows, the changes observed as the vibrations are converted from tangential to normal are more dramatic as the bumpiness decreases. The character of the changes that occur within the flow are shown in Figure 4.13, in which we plot the profiles of mean velocity u, granular temperature w, and solid fraction v for degree of vertical vibration $V_n^2 = 0, 1, 2, 3$ for $\alpha = 1$ and $V_\tau^2 = 0$ (when $\theta = \pi/6$, $\phi = 13.5^0$, $m_t = 6.6$, and $e = e_w = .9$). As V_n^2 increases from 0 to 3, the flows becomes faster, more thermalized, and more dilute. This is another clear indication that the flows are more effectively enhanced by normal vibrations than

Figure 4.11: The profiles of mean velocity u, granular temperature w, and solid fraction ν for vibrational energy $\alpha = 0, 1, 2, 3, 4$ when $V_n^2 = 3$, $\phi = 13.5^0$, $m_t = 6.6$, $\theta = \pi/6$, $\sigma/d = 1$, and $e = e_w = .9$.
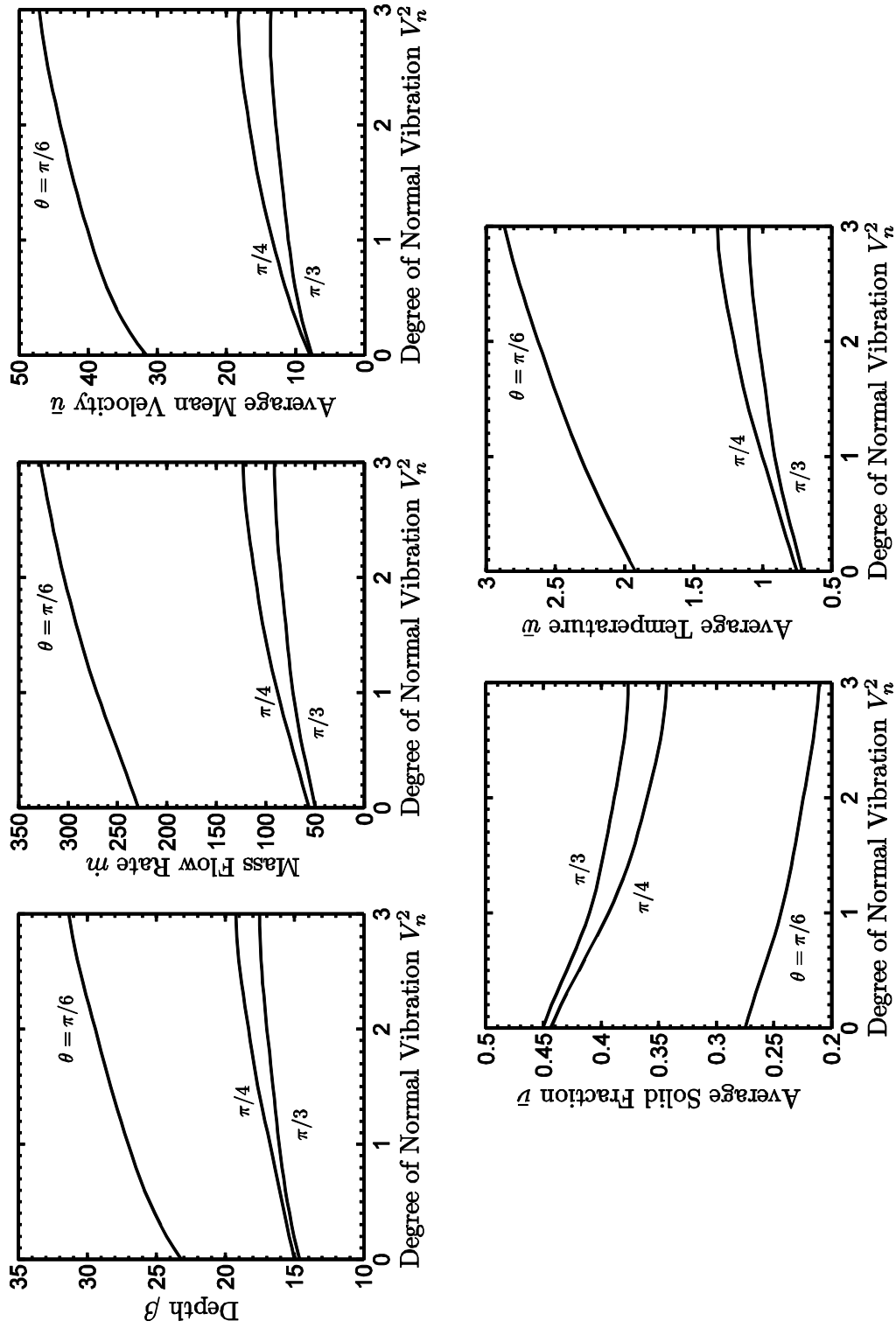
Figure 4.12: The variation of depth β, mass flow rate $\dot{m}$, average mean velocity $\bar{u}$, average solid fraction $\bar{\nu}$, and average granular temperature $\bar{w}$ with degree of normal vibration V_n^2 for bumpiness $\theta = \pi/6, \pi/4, \pi/3$ when $\alpha = 1$, $\phi = 13.5^0$, $m_t = 6.6$, $\sigma/d = 1$ and $e = e_w = .9$.
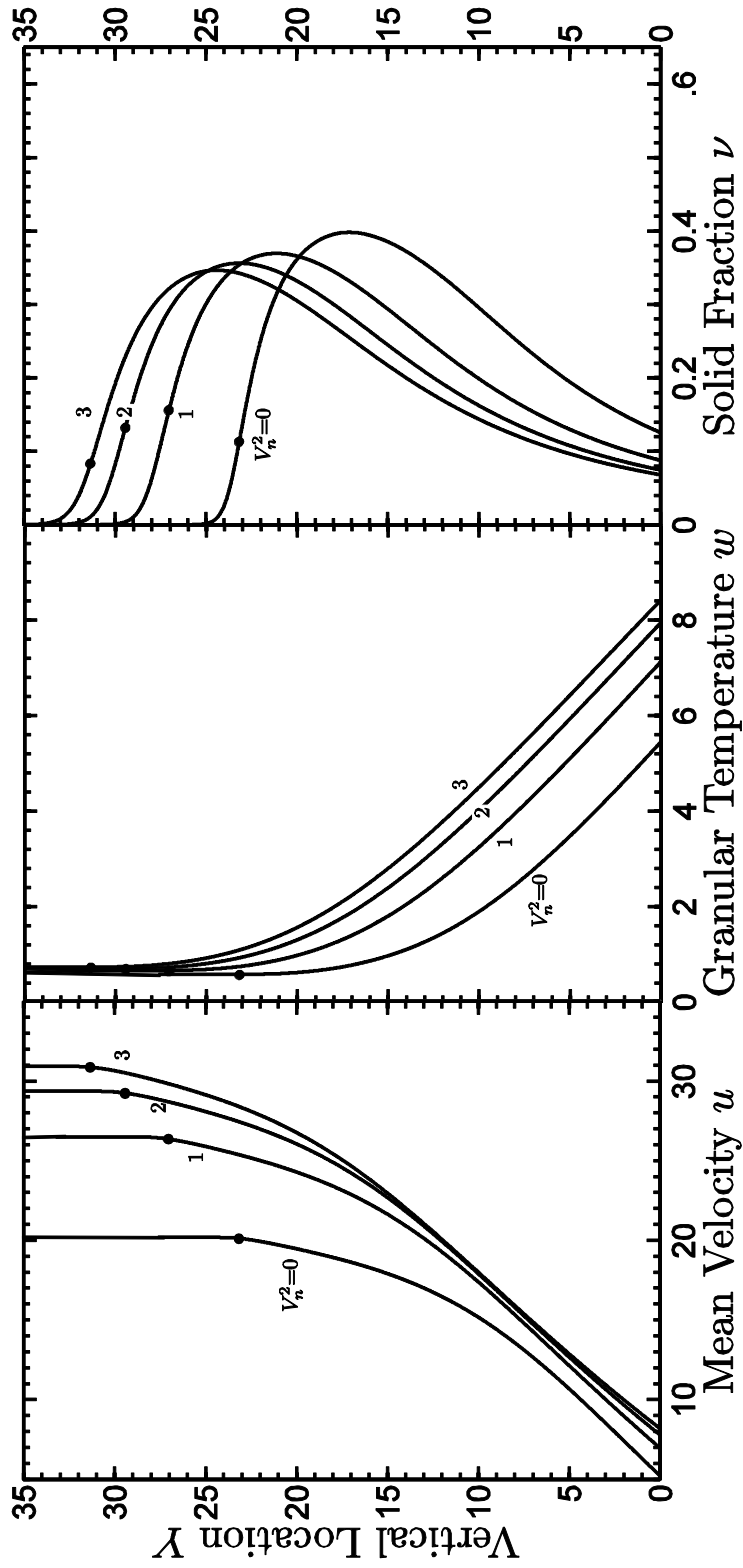
Figure 4.13: The profiles of mean velocity u, granular temperature w, and solid fraction ν for degree of normal vibrations $V_n^2 = 0, 1, 2, 3$ when $\alpha = 1$, $\phi = 13.5^0$, $m_t = 6.6$, $\theta = \pi/6$, $\sigma/d = 1$, and $e = e_w = .9$.

by tangential.

Figures 4.14 and 4.15 are counterparts to Figures 4.10 and 4.12, in which again the depth of the flow β, mass flow rate $\dot{m}$, depth-average mean velocity $\bar{u}$, depth-average solid fraction $\bar{\nu}$, and depth-average granular temperature $\bar{w}$ are shown as functions of vibrational energy α (in Figure 4.14) and normal vibrations V_n^2 (in Figure 4.15). In these figures, however, the bumpiness is fixed ($\theta = \pi/6$) and instead the inclinations ($\phi = 13.6^0, 14^0, 14.4^0$) vary (when $V_n^2 = 3$, $m_t = 6.6$, and $e = e_w = .9$). Again, as either the total vibrational energy or the degree of normal vibrations increases, flows becomes deeper, faster, more dilute, and more thermalized. However, these figures indicate that for a fixed α or V_n^2, the flows become *significantly* deeper, and faster, more dilute, and more thermalized even as the angle of inclination increases only modestly. This sensitivity must be interpreted with care because it is based on the constraint that the mass hold-up remains fixed as the angle of inclination changes.

The same mechanism by which vibrating surfaces can drive horizontal flows with uniform mean velocities may be used to either enhance or impede inclined flows with non-uniform mean velocities. Here we consider a case of a two-dimensional boundary vibration with energy distributed equally ($V_t^2 = V_n^2 = 1.5$) in the tangential and normal directions, in which the phase angle between the two directions of vibration is $\zeta = 180^0$. (This corresponds to $b_{12} = V_t V_n cos\zeta = -1.5$.) For this case, the left panel of Figure 4.16 shows the variation of mass flow rate $\dot{m}$ with angle of inclination ϕ for $\alpha = 2$ (when $m_t = 6.77$, $\theta = \pi/3$ and $e = e_w = .9$). The right panel shows the corresponding mean velocities u_{top} and u_{bottom} at the top and bottom of the assemblies. When $\phi = 0$ the surface is horizontal, the flow rate and mean velocities are uniform to the left (i.e. negative), and as a result $u_{top} = u_{bottom}$. As the angle of inclination ϕ
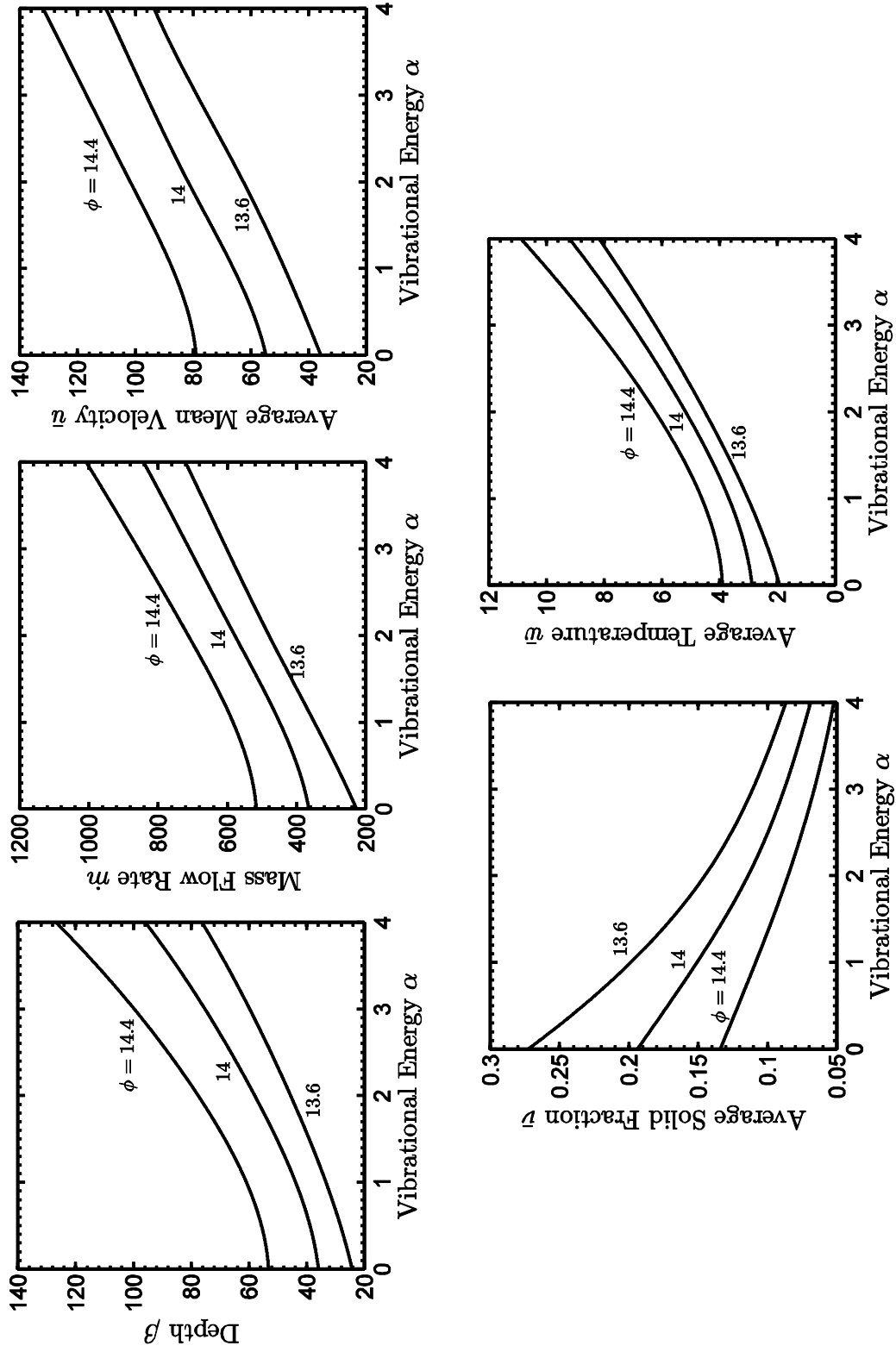
Figure 4.14: The variation of depth β, mass flow rate $\dot{m}$, average mean velocity $\bar{u}$, average solid fraction $\bar{\nu}$, and average granular temperature $\bar{w}$ with vibrational energy α for angle of inclination $\phi = 13.6^0$, 14^0, 14.4^0 when $V_n^2 = 3$, $\dot{m}_t = 6.6$, $\theta = \pi/6$, $\sigma/d = 1$, and $e = e_w = .9$.

68
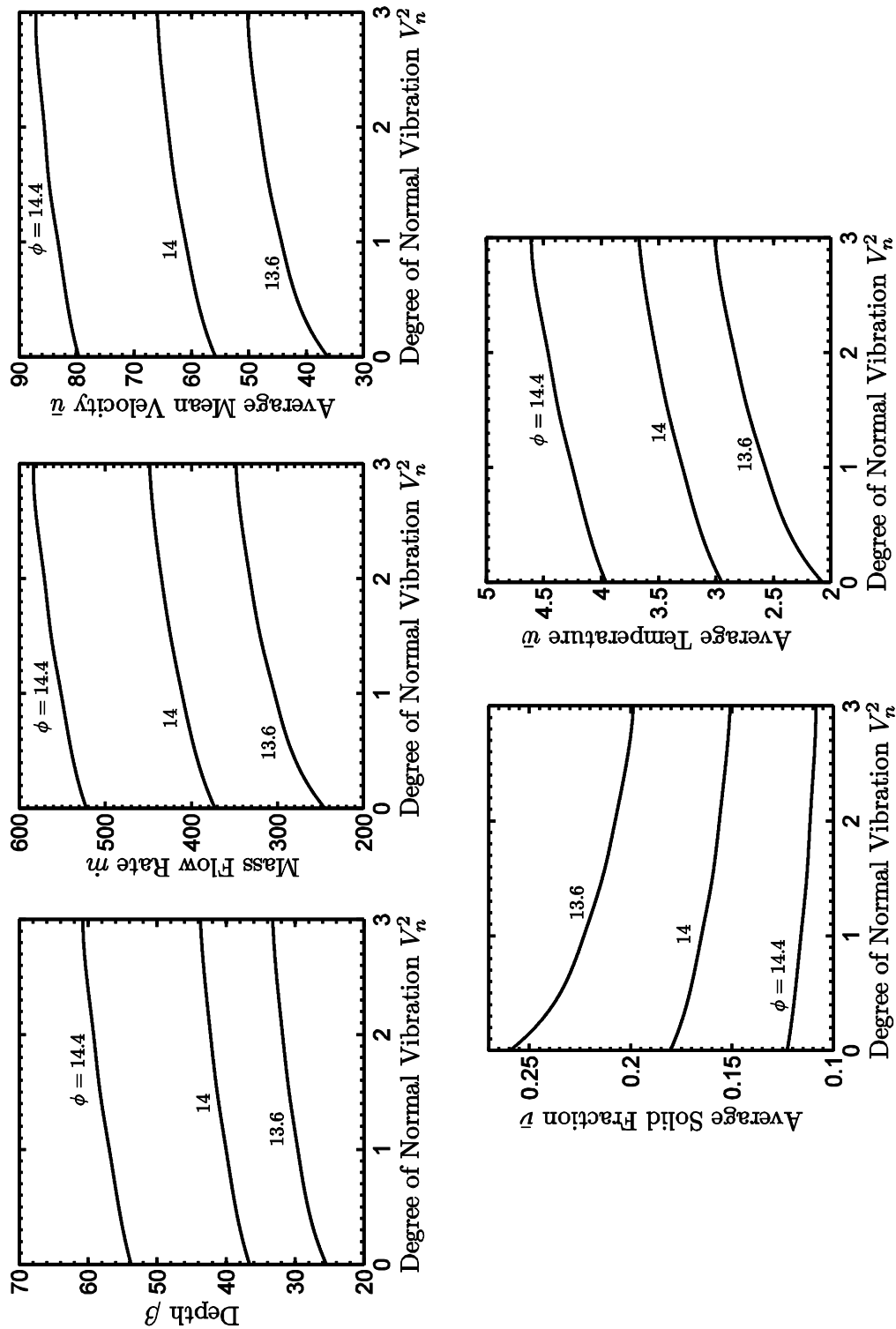
Figure 4.15: The variation of depth β, mass flow rate $\dot{m}$, average mean velocity $\bar{u}$, average solid fraction $\bar{\nu}$, and average granular temperature $\bar{w}$ with degree of normal vibration V_n^2 for angle of inclination $\phi = 13.6^0, 14^0, 14.4^0$ when $\alpha = 1, V_\tau^2 = 0, m_t = 6.6, \theta = \pi/6, \sigma/d = 1$, and $e = e_w = .9$.
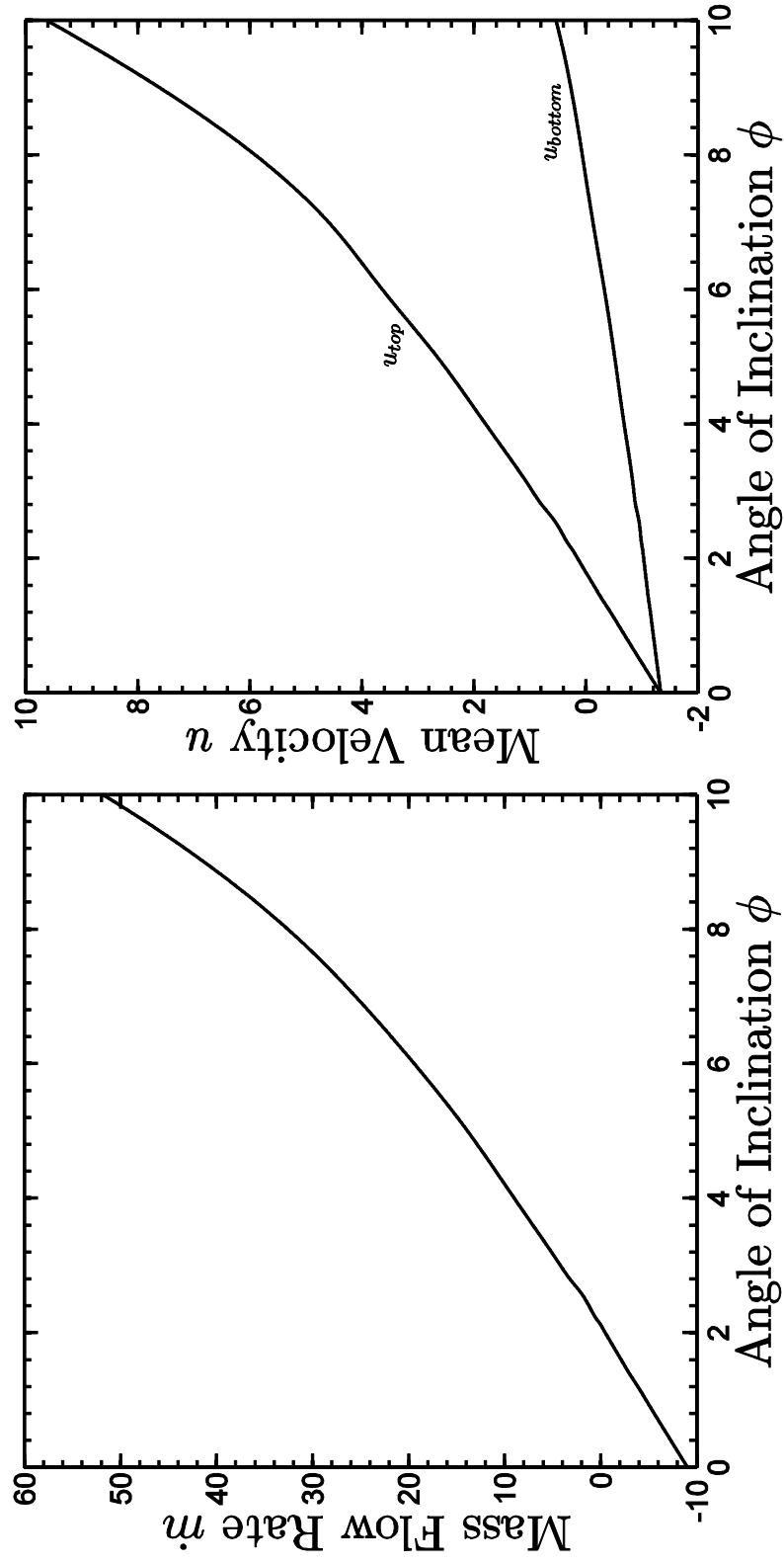
Figure 4.16: The variation of mass flow rate $\dot{m}$, the mean velocity u_{top} and u_{bottom} with angle of inclination ϕ when $\zeta = 180^0$, $\alpha = 2$, , $V_t^2 = V_n^2 = 1.5$, $m_t = 6.77$, $\theta = \pi/3$, $\sigma/d = 1$, and $e = e_w = .9$.

increases, the mass flow rate and the mean velocities u_{top} and u_{bottom} become less negative and eventually increasingly positive. Interestingly, when $\phi = 1.80^0$, the velocity u_{top} is exactly equal to zero, but the entire assembly is still moving up the slight incline. When ϕ is increased to 2.12^0, the *flow rate* is exactly equal to zero. In this case, u_{bottom} is still negative, but u_{top} is positive, so a lower portion of the assembly is moving up the incline and an upper portion is moving down the incline. Further increase in ϕ results in positive mass flow rates. However it is not until ϕ reaches 7.73^0 that u_{bottom} reaches zero and the assemblies start to flow entirely downward. In Figure 4.17, we show the profiles mean velocity u, granular temperature w, and solid fraction v for angle of inclinations $\phi = 0^0, 1.8^0, 2.12^0, 7.73^0,$ and 10^0 corresponding to Figure 4.16. When $\phi = 0$, the velocity is uniform because the shear stress is zero. As the angle of inclination increases, the effect of gravity penetrates to greater distances from the top of the flows. Consequently, for relatively low angles of inclination, the different portions of the assemblies can have velocities in opposite directions. For $\phi = 1.8$, the velocity at the surface is zero, and the flow is still moving up the hill. For $\phi = 2.12$, the mass flow rate reaches zero where the upper portion of the assembly is moving down and the lower half is moving up in such a way that the net flow rate $\dot{m}$ to cancels. When $\phi = 7.73$, there is no slip and the assemblies flow completely to the right, and for higher values of ϕ the slip is downward. In general, the flows become more thermalized and dilute as the angle of inclination increases.
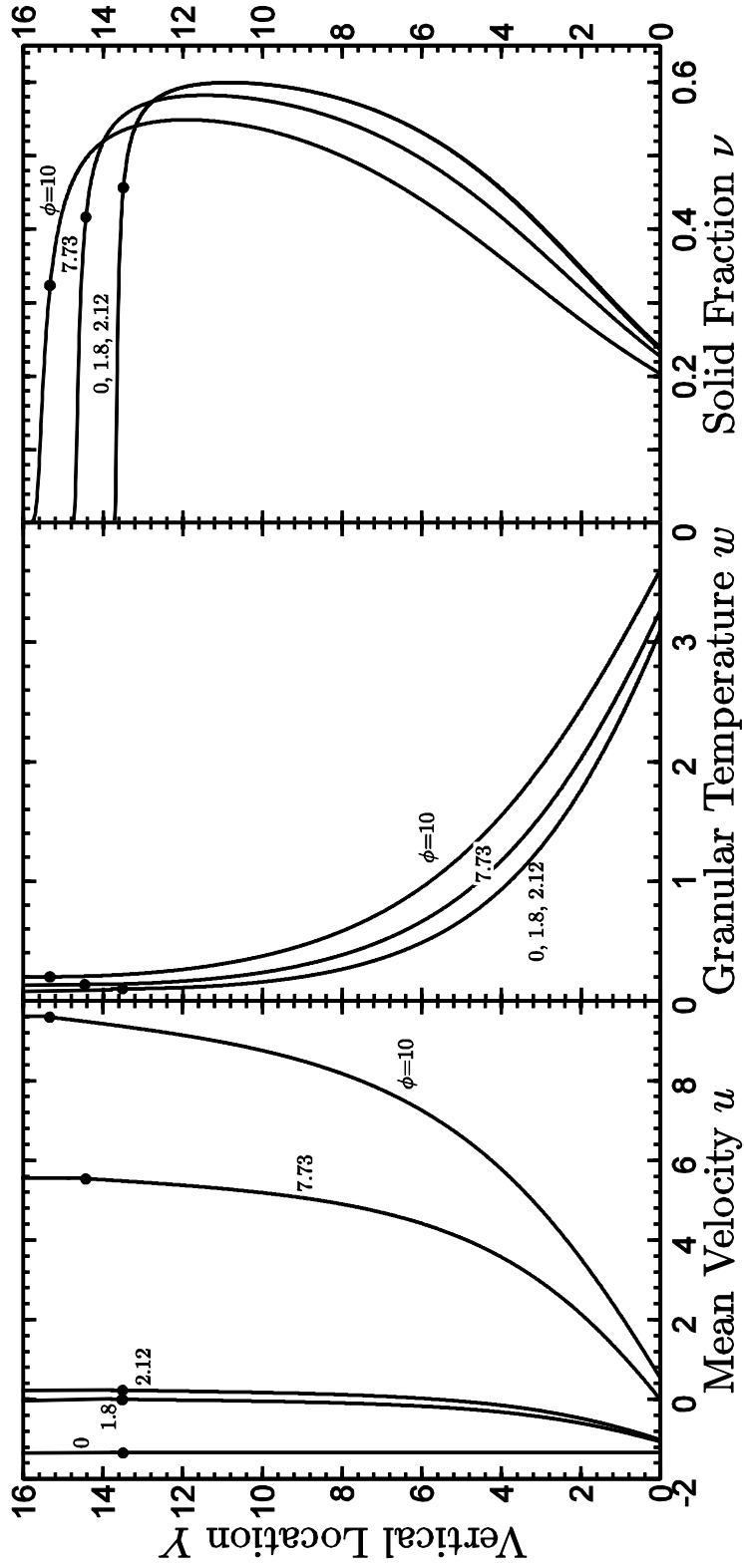
Figure 4.17: The profiles of mean velocity u, granular temperature w, and solid fraction ν for angle of inclinations $\phi = 0^0, 1.8^0, 2.12^0, 7.73^0, 10^0$ when $\zeta = 180^0$, $\alpha = 2$, $V_t^2 = V_n^2 = 1.5$, $m_t = 6.77$, $\sigma/d = 1$, and $e = e_w = .9$.

Chapter 5

Boundary Conditions for Binary Mixtures that Interact with Penetrable Boundaries that Vibrate with Three-Dimensional Anisotropy

5.1 Mean Fields for Binary Mixtures

In this chapter we consider the interactions between a binary granular mixture and a penetrable vibrating boundary (such as a sieve). The mixture consist of smooth, inelastic spheres of diameters σ_A and σ_B, masses m_A and m_B, and coefficients of restitution e_{AA} for collisions between two particles of species A, e_{BB} for collisions between two of species B, and e_{AB} for collisions between species.

For any species i = A or B, the particle's position r and velocity c_i are described statistically by a probability distribution function $f_i(c_i, r, t)$. The number density η_i of species i within the flow is then given by

$$\eta_i(r, t) = \int f_i(c_i, r, t) \, dc \quad , \tag{5.1}$$

where integration is over all velocities c_i, and i takes on the values of A and B. The mass density ρ_i for each species is then

$$\rho_i = m_i \eta_i \quad . \tag{5.2}$$

For the mixture, the total number density n is the sum,

$$\eta = \eta_A + \eta_B \quad , \tag{5.3}$$

and the total mass density ρ is the sum

$$\rho = \rho_A + \rho_B \quad . \tag{5.4}$$

For any physical property $\phi_i(\boldsymbol{c}_i)$ of a particle of species i, its mean value is calculated by:

$$\langle \phi_i \rangle \equiv \frac{1}{\eta_i} \int \phi_i(\boldsymbol{c}_i) f_i(\boldsymbol{c}_i, \boldsymbol{r}, t) \mathrm{d}\boldsymbol{c}_i \quad , \tag{5.5}$$

where integration is over all velocities. In this way, the mean velocity for species i is given by

$$\boldsymbol{u}_i = \langle \boldsymbol{c}_i \rangle \quad . \tag{5.6}$$

The barycentric velocity $\boldsymbol{u}$ for the mixture is defined as the mass weighted average,

$$\boldsymbol{u} = \frac{(\rho_A \boldsymbol{u}_A + \rho_B \boldsymbol{u}_B)}{\rho} \quad . \tag{5.7}$$

The fluctuation velocity $\boldsymbol{C}_i$ of a particle of species i is defined as the velocity of a particle of species i relative to the barycentric velocity of the mixture, so that

$$\boldsymbol{C}_i = \boldsymbol{c}_i - \boldsymbol{u} \quad . \tag{5.8}$$

The diffusion velocity $\langle \boldsymbol{C}_i \rangle$ of species i is simply $\boldsymbol{u}_i - \boldsymbol{u}.$

The granular temperature T_i of species i is defined as:

$$T_i = \frac{1}{3} m_i \langle C_i{}^2 \rangle \quad , \tag{5.9}$$

where $C_i{}^2 = \boldsymbol{C} \cdot \boldsymbol{C}$. Defined in this manner, T_i measures the mean kinetic energy of species i associated with its velocity fluctuations from $\boldsymbol{u}$. The granular temperature T of the entire mixture is defined as the number weighted average of granular temperatures for each species, and is given by

$$T = \frac{(\eta_A T_A + \eta_B T_B)}{n} \quad . \tag{5.10}$$

In what follows, we will employ a relatively simple flow theory based on a single temperature Maxwellian velocity distribution function $f_i(\boldsymbol{c}_i)$ given by,

$$f_i(\boldsymbol{c}_i, \boldsymbol{r}, t) \;=\; \eta_i \left(\frac{m_i}{2\pi T}\right)^{3/2} exp\left\{\frac{-m_i \boldsymbol{C}_i \cdot \boldsymbol{C}_i}{2T}\right\} \quad . \tag{5.11}$$

In order to maintain consistency with the theory, we will employ the same distribution function in deriving the boundary conditions.

5.2   Balance of Mass, Momentum, and Energy at the Boundary

We consider the interactions between a binary granular mixture described above and a penetrable boundary (such as a sieve) that fluctuates about its mean velocity $\boldsymbol{U}$. The unit inward normal to the boundary in $\boldsymbol{N}$. At the boundary, the slip velocity $\boldsymbol{v}_i$ for each species is defined as,

$$\boldsymbol{v}_i \equiv \boldsymbol{U} - \boldsymbol{u}_i \quad . \tag{5.12}$$
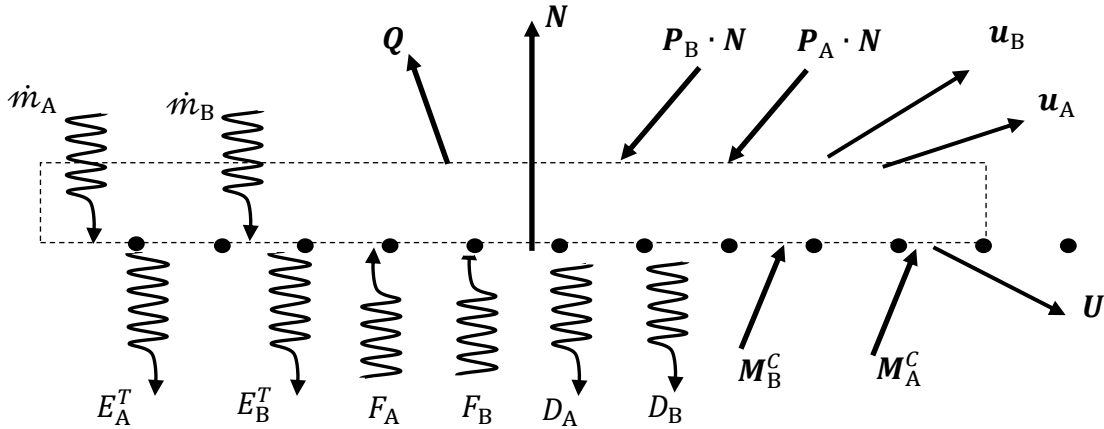
Figure 5.1: A fixed control volume at the boundary

Appropriate boundary conditions must guarantee that the flow of mass, momentum and energy are balanced at the interface, just as they are balanced everywhere within the flow. Consequently, we focus attention on a parallelepiped in the flow with two opposite faces of unit area; one face is in the flow and the other is coincident with the boundary (see Figure 5.1).

In the limit as the lateral sides shrink to zero, the balance of mass within the parallelepiped requires that

$$\dot{m}_i = \rho_i \boldsymbol{v}_i \cdot \boldsymbol{N} \qquad\qquad (i = A \text{ or } B) \quad, \qquad\qquad (5.13)$$

where $\dot{m}_i$ is the rate per unit area at which the mass of species i will pass from the inward side to the outward side through the vibrating sieve.

In the same limit, the balance of momentum for each species requires that

$$\boldsymbol{M}_i^C + \boldsymbol{M}_i^T = \boldsymbol{P}_i \cdot \boldsymbol{N} + \dot{m}_i \boldsymbol{u}_i \qquad\qquad (i = A \text{ or } B) \quad, \qquad\qquad (5.14)$$

where $\boldsymbol{M}_i^C$ is the rate per unit area of momentum transferred to species i due to collisions with the boundary, $\boldsymbol{M}_i^T$ is the rate per unit area of momentum transported by species i as it passes through the boundary, $\boldsymbol{P}_i$ is the pressure tensor associated with species i, $\boldsymbol{P}_i \cdot \boldsymbol{N}$ is the traction vector applied by species i, and $\dot{m}_i \boldsymbol{u}_i$ is the momentum transported by the mass of species i traveling with mean velocity $\boldsymbol{u}_i$ across the top surface of the parallelepiped. When the boundary is impenetrable, both $\dot{m}_i$ and $\boldsymbol{M}_i^T$ are equal to zero, and equation (5.13) reduces to impenetrable condition (3.1).

In order to express the balance of *total* energy at the boundary, we introduce F_i as the rate per unit area of energy supplied to species i by the boundary due its fluctuating motion, and D_i as the corresponding rate at which energy is dissipated by species i through inelastic collisions at the boundary, and E_i^T is the energy transported by species i as it passes through the boundary. In addition, $\boldsymbol{M}_i^C \cdot \boldsymbol{U}$ is the rate per unit area of energy transferred to the flow due to the collisional momentum exchange between species i and a boundary that moves with mean velocity $\boldsymbol{U}$. Then in the limit as the lateral sides of the parallelepiped shrink to zero, the balance of energy requires that

$$\sum_{i=A,B} \left(\boldsymbol{M}_i^C \cdot \boldsymbol{U} + F_i - D_i + E_i^T \right) = \boldsymbol{Q} \cdot \boldsymbol{N} + \sum_{i=A,B} \left[(\boldsymbol{P}_i \cdot \boldsymbol{N}) \cdot \boldsymbol{u}_i + \frac{1}{2} \dot{m}_i (\boldsymbol{u}_i \cdot \boldsymbol{u}_i) + \frac{3}{2} \dot{m}_i \frac{T}{m_i} \right],$$

$$(5.15)$$

where $\boldsymbol{Q}$ is the energy flux for the whole mixture. The term $(\boldsymbol{P}_i \cdot \boldsymbol{N}) \cdot \boldsymbol{u}_i$ is the rate per unit area at which the traction vector associated with species i does work by moving with mean velocity $\boldsymbol{u}_i$. The term $\dot{m}_i(\boldsymbol{u}_i \cdot \boldsymbol{u}_i)/2$ is the rate per unit area at which species i transports its mean kinetic energy, and the term $3\dot{m}_i T/2m_i$ is the rate per unit area at which species i transports its fluctuation energy measured by the mixture temperature T. When the boundary is impenetrable, both $\dot{m}_i$ and E_i^T are equal to zero, and equation (5.15) reduces to impenetrable condition (3.2).

The six transfer rates $\dot{m}_i$, $\boldsymbol{M}_i^T$, E_i^T, $\boldsymbol{M}_i^C$, F_i, and D_i depend on the boundary geometry and the boundary motion. The collisional transfer rates $\boldsymbol{M}_i^C$, F_i, and D_i also depend on the nature of a typical interaction between a flow particle and a boundary. In what follows, we first describe the geometry and the motion of the boundary, and then we calculate each transfer rate in succession.

5.3 The Vibrating Sieve: Geometry and Motion
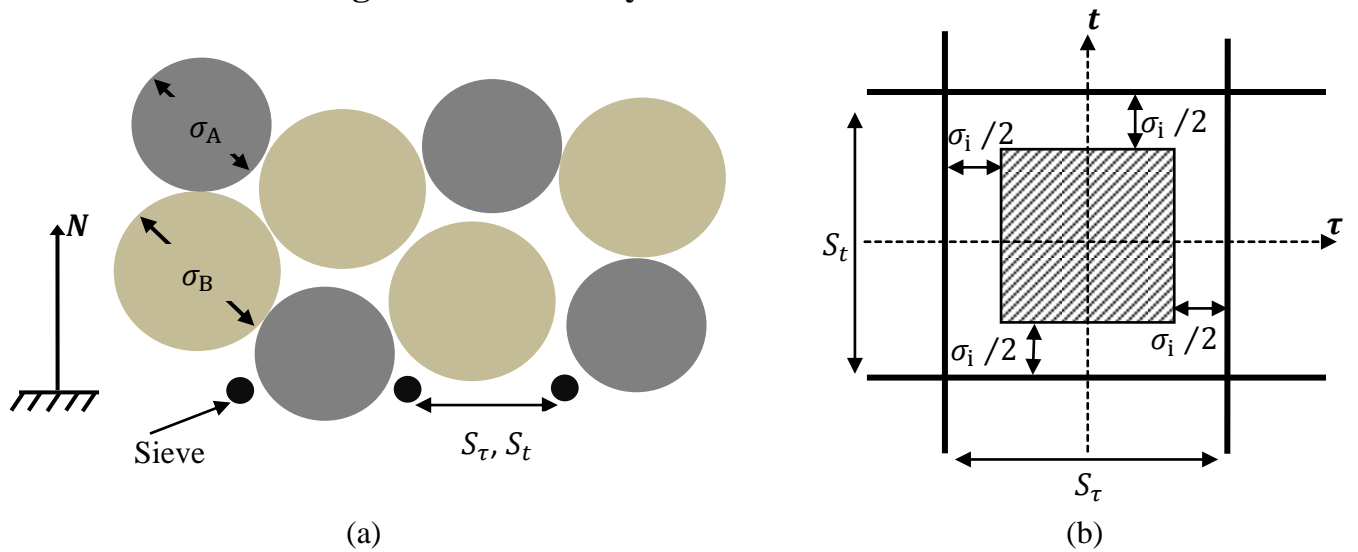
Figure 5.2: Side view and top view of the sieve

As shown in Figure 5.2, the sieve is a two-dimensional mesh with fibers in the t- and τ-perpendicular directions. The spacing between the fibers in the two directions are S_t and S_τ, respectively. The flow particle diameters are σ_i.

Like the bumpy boundary in Chapters 3 and 4, the sieve vibrates randomly with a velocity $\boldsymbol{\psi}$ governed by a probability distribution function $p(\boldsymbol{\psi})$ defined such that $p(\boldsymbol{\psi})d\boldsymbol{\psi}$ gives the probability that the sieve has a velocity $\boldsymbol{\psi}$ in the range $d\boldsymbol{\psi}$. The mean velocity $\boldsymbol{U}$ of the sieve is defined by equation (3.6), the fluctuation velocity of the sieve is $\boldsymbol{\Psi} \equiv \boldsymbol{\psi} - \boldsymbol{U}$, and the second moment $\boldsymbol{B}$ of its velocity fluctuations is defined by equation (3.7). The velocity distribution function $p(\boldsymbol{\psi})$ for the sieve is the anisotropic Maxwellian given by equation (3.10).
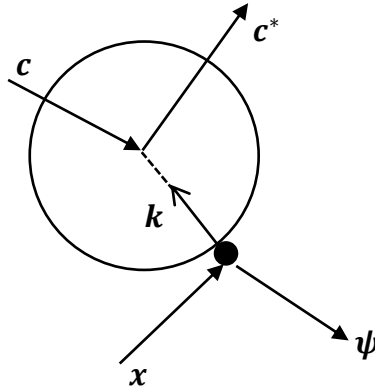
Figure 5.3: Particle-sieve collision geometry

The dynamics of a collision of species i (shown in Figure 5.3) at the boundary are described in terms of the pre-collisional velocities $\boldsymbol{c}_i$ of the flow particle and $\boldsymbol{\psi}$ of the boundary mesh, the unit vector $\boldsymbol{k}$ directed from the point of contact on the mesh to the center of the flow particle at impact, and the coefficient of restitution e_i which characterizes the energy dissipated in a collision between particle i and the boundary. If the velocity of the boundary is unaffected by the collision, then in terms of the relative velocity $\boldsymbol{g}_i \equiv \boldsymbol{\psi} - \boldsymbol{c}_i$, the change in linear momentum experienced by the flow particle is

$$m_i (c_i^* - c_i) = m_i (1 + e_i)(g_i \cdot k)k \quad , \tag{5.16}$$

where c_i^* the post-collisional velocity of the flow particle. The corresponding change in energy is

$$\frac{m_i}{2}(c_i^* \cdot c_i^* - c_i \cdot c_i) = m_i(1 + e_i)(g_i \cdot k)\left((U \cdot k) + (\Psi \cdot k) - \frac{1}{2}(1 - e_i)(g_i \cdot k)\right) \quad ,$$

$$\tag{5.17}$$

where $\Psi = \psi - U$ is the fluctuation velocity of the boundary particle.

The frequency of collisions per unit area of the boundary that involve flow particles of species i with velocities c_i in the range dc_i and wall particles with velocities ψ in the range $d\psi$, and occur within an element of solid angle dk centered about k on the surface of the wall particle is

$$\frac{\sigma_i \lambda_i}{2S_t S_\tau} f_i\left(c_i, x + \frac{\sigma_i}{2} k\right) p(\psi) (g_i \cdot k) \, dk dc_i d\psi \quad , \tag{5.18}$$

where the factor λ_i accounts for the effects excluded volume and shielding at the boundary on the likelihood of collisions with species i.

It remains to calculate the six transfer rates $\dot{m}_i$, M_i^T, E_i^T, M_i^C, F_i, and D_i.

5.4 Mass Transfer Through the Sieve

The integral $\dot{m}_i$ for the mass flow rate can be found by statistical averaging at the boundary (Richman and Wang [1995; 1996]). The number of flow particles of species i with velocity c_i in the range dc_i that are located in the volume element dr centered at r is $f_i(c_i) dr dc_i$; the probability of the boundary having velocity ψ in the range $d\psi$ is $p(\psi) d\psi$; and the probable number of such velocity pairs per unit volume is $f_i(c_i) p(\psi) dc_i d\psi$.
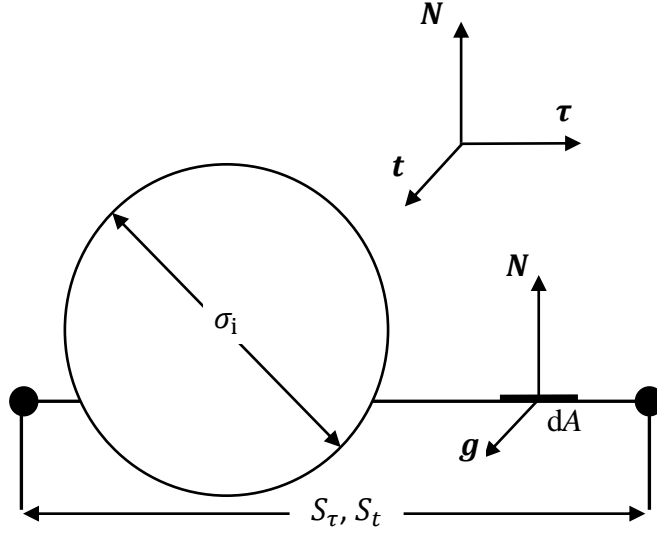
Figure 5.4: Flow through the sieve.

In Figure 5.4, we denote as dA a differential area element of the space between the fibers, N as the unit inward normal vector, and $\boldsymbol{g}_i = \boldsymbol{\psi} - \boldsymbol{c}_i$ as the velocity of the sieve relative to the flow particle. The number of flow particles with velocity $\boldsymbol{c}_i$ in the range $d\boldsymbol{c}_i$ that will pass through the sieve with velocity $\boldsymbol{\psi}$ in the range $d\boldsymbol{\psi}$ per unit time is $f_i(\boldsymbol{c}_i)p(\boldsymbol{\psi})(\boldsymbol{g}_i \cdot \boldsymbol{N})d\boldsymbol{c}_id\boldsymbol{\psi}$. A top view is given in Figure 5.3 b. The rate of mass $\dot{m}_i$ that will pass from the inward side to the outward side through the vibrating sieve per unit flat area is expressed by the integral:

$$\dot{m}_i = \frac{m_i}{S_t S_\tau} \int f_i(\boldsymbol{c}_i)\, p(\boldsymbol{\psi})(\boldsymbol{g}_i \cdot \boldsymbol{N})dAd\boldsymbol{c}_id\boldsymbol{\psi} \quad , \tag{5.19}$$

where the velocity integrations are carried out for $\boldsymbol{g}_i \cdot \boldsymbol{N} > 0$. The area element $dA = dtd\tau$, in which t- and τ- are scalar coordinates in the $\boldsymbol{t}$- and $\boldsymbol{\tau}$-directions. If they are measured from the center of a rectangular hole, then the integration is carried out on t between $-(S_t - \sigma_i)/2$ and $(S_t - \sigma_i)/2$, and on τ between $-(S_\tau - \sigma_i)/2$ and $(S_\tau - \sigma_i)/2$ when $\sigma_i < S_t$ and S_τ. Otherwise $\dot{m}_i$ is equal to zero.

In order to carry out the integration (5.19), we employ the anisotropic Maxwellian (3.11) for $p(\boldsymbol{\psi})$. Furthermore, we take the velocity distribution function $f_i(\boldsymbol{c}_i)$ for the flow particles to be the Maxwellian given by equation (5.11). We carry out the $\boldsymbol{c}_i$ and $\boldsymbol{\psi}$ velocity integrations in equation (5.19) by replacing $d\boldsymbol{c}_i d\boldsymbol{\psi}$ by $|J| d\boldsymbol{G} d\boldsymbol{Q}$, where $|J| = 8$, $\boldsymbol{Q} = (\boldsymbol{\Psi} + \boldsymbol{C}_i)/2$, and $\boldsymbol{G} = (\boldsymbol{\Psi} - \boldsymbol{C}_i)/2$. In this case, $\boldsymbol{C}_i = \boldsymbol{Q} - \boldsymbol{G}$, $\boldsymbol{\Psi} = \boldsymbol{Q} + \boldsymbol{G}$, and $\boldsymbol{g}_i = 2\boldsymbol{G} + \boldsymbol{v}_i$. We then write velocity vectors in terms of the unit vector $\boldsymbol{N}, \boldsymbol{t}$ and $\boldsymbol{\tau}$, and integrate Q_1, Q_2, Q_3, G_1, and G_3 between $-\infty$ and $+\infty$. The limits of integration of G_2 are between $-(1/2)v_2$ and $+\infty$, or alternatively on $\eta \equiv 2G_2 + v_2$ (so that $2dG_2 = d\eta$) from 0 and $+\infty$. In order to express the results of the integration compactly, we introduce two geometric parameters for the sieve: $r_{ti} = \sigma_i/S_t$ and $r_{\tau i} = \sigma_i/S_\tau$. In this manner, we find that,

$$\dot{m}_i = \frac{\rho_i}{(2\pi)^{1/2}} \left(\frac{T}{m_i} + V_2^2 \right)^{1/2} (1 - r_{ti})(1 - r_{\tau i})\left[\sqrt{\pi}\, \Phi_i\, erfc(-\Phi_i) + exp(-\Phi_i^2) \right] \quad , \quad (5.20)$$

where the quantity Φ_i is given by

$$\Phi_i = \frac{\boldsymbol{v}_i \cdot \boldsymbol{N}}{\sqrt{2\left(\frac{T}{m_i} + V_2^2 \right)}} \quad , \qquad\qquad (5.21)$$

where $\boldsymbol{v}_i$ is the slip velocity $\boldsymbol{U} - \boldsymbol{u}_i$, and the 2- direction is the $\boldsymbol{N}$- direction. Equation (5.20) applies provided that species i can pass through the sieve (i.e. when *both* $r_{ti} \equiv \sigma_i/S_t$ and $r_{\tau i} \equiv \sigma_i/S_\tau$ are less than 1), otherwise the mass flow rate $\dot{m}_i$ is equal to zero, and equation (5.20) does not apply.

The boundary condition for the mass balance of species i at the sieve is given by equation (5.13) in which $\dot{m}_i$ is given by (5.20).

5.5   Momentum Transfer at the Sieve

The integral M_i^T for the transport of momentum through the boundary is analogous to the integral for the corresponding mass flow $\dot{m}_i$ given by (5.19). In this case, we weigh the probability $f_i(c_i)p(\psi)(g_i \cdot N)dc_i d\psi$ by the momentum $m_i c_i$ to obtain,

$$M_i^T = \frac{m_i}{S_t S_\tau} \int c_i\, f_i(c_i)\, p(\psi)(g_i \cdot N)dAdc_i d\psi \quad , \tag{5.22}$$

where the limits of integrations are identical as those used in (5.19) for $\dot{m}_i$.

To decompose the integral (5.22), we replace c_i by $C_i + u_i$, and write M_i^T as the sum

$$M_i^T = \dot{m}_i u_i + \widetilde{M}_i^T \quad , \tag{5.23}$$

where $\widetilde{M}_i^T$ is given by

$$\widetilde{M}_i^T = \frac{m_i}{S_t S_\tau} \int C_i\, f_i(c_i)\, p(\psi)(g_i \cdot N)dAdc_i d\psi \quad . \tag{5.24}$$

Furthermore (5.23) may be used to rewrite the momentum boundary condition (5.14) for species

i as

$$M_i^C + \widetilde{M}_i^T \; = \; P_i \cdot N \qquad\qquad (i = A \text{ or } B) \quad . \tag{5.25}$$

The corresponding momentum boundary condition for the entire mixture is then

$$\sum_{i=A,B} \left(M_i^C + \widetilde{M}_i^T \right) \; = \; P \cdot N \quad . \tag{5.26}$$

where P is the pressure tensor for the whole mixture.

The integration (5.24) for the transport of momentum $\widetilde{M}_i^T$ is carried out in the same manner used to obtain equation (5.20) from integral (5.19), and yields

$$\widetilde{M}_i^T = -\frac{\rho_i T}{2m_i}(1 - r_{ti})(1 - r_{\tau i})erfc(-\Phi_i)N \tag{5.27}$$

The transfer rate $\boldsymbol{M}_i^C$ is a statistical average of the change in momentum $m_i(\boldsymbol{c}_i^* - \boldsymbol{c}_i)$ per collision weighted by collision frequency (5.18). According to equation (5.16), $m_i\,(\boldsymbol{c}_i^* - \boldsymbol{c}_i)$ is equal to $m_i(1 + e_i)(\boldsymbol{g}_i \cdot \boldsymbol{k})\boldsymbol{k}$, so $\boldsymbol{M}_i^C$ may be written compactly in integral form

$$\boldsymbol{M}_i^C = \frac{m_i(1 + e_i)\lambda_i}{2S_t S_\tau} \int (\boldsymbol{g}_i \cdot \boldsymbol{k})^2 \boldsymbol{k}\, f_i\left(\boldsymbol{c}_i, \boldsymbol{x} + \frac{\sigma_i}{2}\boldsymbol{k}\right) p(\boldsymbol{\psi})\, d\boldsymbol{k} d\boldsymbol{c}_i d\boldsymbol{\psi} \quad . \tag{5.28}$$

The integrations over velocities $\boldsymbol{c}$ and $\boldsymbol{\psi}$ in (5.28) are carried out by replacing $d\boldsymbol{c}_i d\boldsymbol{\psi}$ by $|J| d\boldsymbol{C}_i d\boldsymbol{\Psi}$ where $|J| = 1$, writing velocity vectors $\boldsymbol{C}_i$, $\boldsymbol{g}_i$, $\boldsymbol{v}_i$ and $\boldsymbol{\Psi}$ explicitly in terms of the unit vector $\boldsymbol{k}$ (in the 1-direction) and two additional arbitrary mutually perpendicular unit vectors (in the 2- and 3-directions), and first integrating over Ψ_2, Ψ_3, C_{i2}, and C_{i3} between $-\infty$ and $+\infty$. Then the fluctuation velocity C_{i1} is rewritten as $C_{i1} = \Psi_1 - g_{i1} + v_{i1}$, and $dC_{i1} d\Psi_1$ is replaced by by $|J| dg_{i1} d\Psi_1$ where $|J| = 1$. Finally, integration over Ψ_1 is carried out between $-\infty$ and $+\infty$, and integration over g_{i1} is carried out between 0 and $+\infty$. The intermediate result is

$$\boldsymbol{M}_i^C = \frac{(1 + e_i)\rho_i \lambda_i T}{2\pi^{1/2} S_t S_\tau} \int (\boldsymbol{k} \cdot \boldsymbol{\mathcal{B}} \cdot \boldsymbol{k})\boldsymbol{k}\left[\sqrt{\pi}\left(\frac{1}{2} + \Phi_i^2\right) erfc(-\Phi_i) + \Phi_i exp\left(-\Phi_i^2\right)\right] d\boldsymbol{k} \quad ,$$

$$\tag{5.29}$$

where $\boldsymbol{\mathcal{B}} \equiv \boldsymbol{I} + \boldsymbol{B}/T$, Φ_i is given by equation (5.21), and all the mean fields are evaluated at $\boldsymbol{x} + \sigma_i \boldsymbol{k}/2$.

We consider the case when the off-diagonal components of $\boldsymbol{B}$ are small compared to its diagonal components, the velocity $\boldsymbol{v}$ is small compared to the granular temperature T at the boundary, and the change $\sigma \nabla \boldsymbol{u}$ in velocity is small compared $T^{1/2}$. The small gradient assumption allows us to expand the mean fields in the integrand of equation (5.29) in two-term Taylor series about $\boldsymbol{x} + \sigma_i \boldsymbol{N}/2$ with respect to these small quantities.

In order to carry out the surface area integrations indicated by $d\boldsymbol{k}$, we must account for all the locations that the center of a flow particle can occupy when it makes contact anywhere on a periodic element of the sieve mesh. As shown in Figure 5.5, angle φ measures the positive
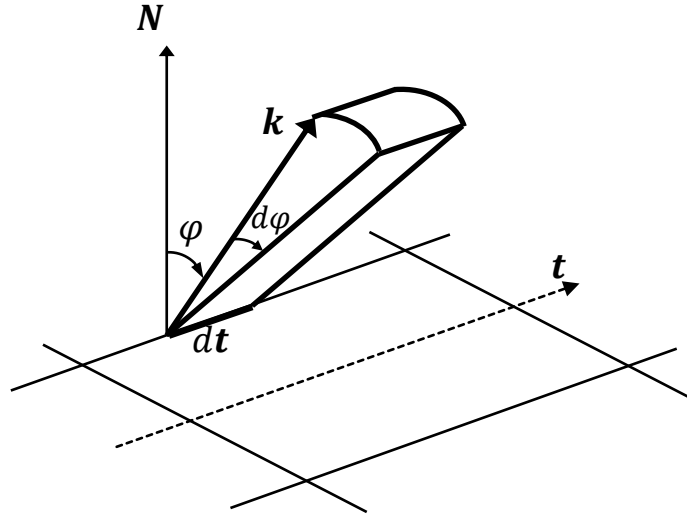
Figure 5.5: Angle-definition for integration over boundary particle surface

acute angle between vector $\boldsymbol{N}$ and the unit vector $\boldsymbol{k}$- directed from the point of contact to the center of the colliding particle at impact. When integrating along a fiber of the sieve in the $\boldsymbol{t}$- direction, $d\boldsymbol{k}$ is an area element $dS = \mathrm{d}\varphi\, dt$ on a unit cylinder whose axis coincides with the fiber. In this case, $k_i = \cos\varphi\, N_i + \sin\varphi\, \tau_i$. Similarly when integrating in the $\boldsymbol{\tau}$- direction, $d\boldsymbol{k} = dS = \mathrm{d}\varphi\, d\tau$ and $k_i = \cos\varphi\, N_i + \sin\varphi\, t_i$.

With the t-τ coordinate system centered as shown in Figure 5.2, the range of integration on t is from $-S_t/2$ to $+S_t/2$, and the range of integration on τ is from $-S_\tau/2$ to $+S_\tau/2$. In integrating along a fiber in the $\boldsymbol{t}$- direction, adjacent fibers in the τ- direction (and possibly adjacent fibers in the $\boldsymbol{t}$- direction) restrict the range of φ. The extent of the restriction can depend on the location t of the point of contact between a flow particle and the fiber. Consequently, the

limits of integration on φ depend on t. Similarly, integrating along a fiber in the τ- direction, the limits of integration on φ depend on τ. The limits on φ are derived in detail in the Appendix 1. There are two different cases. In the first case, the particles of species i can pass through the sieve (i.e. $\sigma_i < S_t$ and $\sigma_i < S_\tau$). In the second case, the particles of species i cannot pass through the sieve (i.e. $\sigma_i < S_t$ and $\sigma_i > S_\tau$; or $\sigma_i > S_t$ and $\sigma_i > S_\tau$). We can assume without loss in generality that $S_t \geq S_\tau$. As demonstrated in Appendix 1, in both cases, we can carry out the t- and τ- integrations in closed form.

The resulting integral expression for $\boldsymbol{M}_i^C$ is given by the sum

$$\boldsymbol{M}_i^C = \boldsymbol{M}_{it}^C + \boldsymbol{M}_{i\tau}^C \quad . \tag{5.30}$$

The two terms $\boldsymbol{M}_{it}^C$ and $\boldsymbol{M}_{i\tau}^C$ are the contributions from the collisions experienced by fibers in the t- and τ- directions, expressed in terms of quantities R_{1i} and R_{3i} defined by:

$$R_{1i} \equiv \frac{m_i(V_2^2 - V_1^2)}{(T + m_i V_1^2)} \quad , \tag{5.31}$$

and

$$R_{3i} \equiv \frac{m_i(V_2^2 - V_3^2)}{(T + m_i V_3^2)} \quad , \tag{5.32}$$

When species i _can_ pass through the sieve (i.e. $\sigma_i < S_t$ and $\sigma_i < S_\tau$), the x_l- components of $\boldsymbol{M}_{it}^C$ are given by

$$
\begin{aligned}
(\boldsymbol{M}_{it}^C)_l = {} & \frac{2(1 + e_i)\rho_i \lambda_i r_{\tau i}}{\sqrt{2}\pi^{3/2}} \left\{ \frac{\pi^{1/2}}{2\sqrt{2}} \left[\left(1 - \frac{r_{ti}}{2}\right)\frac{T}{m_i} + \left(\frac{2}{3}V_2^2 + \frac{V_3^2}{3}\right) - r_{ti}(V_2^2 + V_3^2) \right] N_l \right. \\
& + \frac{\pi^{1/2}}{3\sqrt{2}}\left(1 - \frac{r_{ti}}{2}\right)(\boldsymbol{\tau} \cdot \boldsymbol{B} \cdot \boldsymbol{N})\tau_l \\
& + (\boldsymbol{v}_i)_k \left(\frac{T}{m_i} + V_3^2\right)^{1/2} \int_0^{\pi/2} (1 + R_{3i}\cos^2\varphi)^{1/2}(1 - r_{ti}\sin\varphi)\mathfrak{T}_{lk}(\boldsymbol{\tau})d\varphi
\end{aligned}
$$

$$+\frac{\sigma_i}{2}\frac{\partial (u_i)_k}{\partial x_j}\left[\left(\frac{T}{m_i}+V_3^2\right)^{1/2}\int_0^{\pi/2}(1+R_{3i}cos^2\varphi)^{1/2}(1-r_{ti}sin\varphi)\left(\mathfrak{T}_{lk}(\boldsymbol{\tau})N_j-\mathfrak{T}_{ljk}(\boldsymbol{\tau})\right)d\varphi\right]\Bigg\},$$

$$(5.33)$$

in which the tensors $\mathfrak{T}_{lk}(\boldsymbol{\tau})$ and $\mathfrak{T}_{ljk}(\boldsymbol{\tau})$ are given by,

$$\mathfrak{T}_{lk}(\boldsymbol{\tau})=cos^2\varphi N_l N_k+sin\varphi cos\varphi(N_l\tau_k+N_k\tau_l)+sin^2\varphi\tau_l\tau_k \quad , \qquad (5.34)$$

and

$$\mathfrak{T}_{ljk}(\boldsymbol{\tau})=cos^3\varphi\,N_lN_j\,N_k+sin^3\varphi\tau_l\tau_j\tau_k+cos^2\varphi sin\varphi\left(N_lN_j\,\tau_k+N_lN_k\,\tau_j+N_jN_k\,\tau_l\right)$$

$$+sin^2\varphi cos\varphi\left(N_l\tau_j\,\tau_k+N_j\tau_k\,\tau_l+N_k\tau_j\,\tau_l\right), \quad (5.35)$$

and where the x_l- components of $\boldsymbol{M}_{i\tau}^C$ in (5.30) are given by (5.33) in which r_{ti}, $r_{\tau i}$, R_{3i}, V_3, $\mathfrak{T}_{lk}(\boldsymbol{\tau})$, and $\mathfrak{T}_{ljk}(\boldsymbol{\tau})$ are replaced by $r_{\tau i,}$, r_{ti}, R_{1i}, V_1, $\mathfrak{T}_{lk}(\boldsymbol{t})$, and $\mathfrak{T}_{ljk}(\boldsymbol{t})$, respectively. The two geometric parameters for the sieve that appear in (5.33) are $r_{ti}\equiv\sigma_i/S_t$ and $r_{\tau i}\equiv\sigma_i/S_\tau$. The mean fields that appear in (5.33) are evaluated at $\boldsymbol{x}+\sigma_i\boldsymbol{N}/2$.

When species i *cannot* pass through the sieve (i.e. $\sigma_i<S_t$ and $\sigma_i>S_\tau$; or $\sigma_i>S_t$ and $\sigma_i>S_\tau$ where we can assume without loss in generality that $S_t\ge S_\tau$), the x_l- components of $\boldsymbol{M}_{it}^C$ are given by

$$(\boldsymbol{M}_{it}^C)_l=\frac{2(1+e_i)\rho_i\lambda_ir_{\tau i}}{\sqrt{2}\pi^{3/2}}\left\{\frac{\pi^{1/2}}{2\sqrt{2}}\left[(C_1+C_2)\frac{T}{m_i}+(C_1V_2^2+C_2V_3^2)\right]N_l+\frac{B\pi^{1/2}}{\sqrt{2}}(\boldsymbol{\tau}\cdot\boldsymbol{B}\cdot\boldsymbol{N})\tau_l\right.$$

$$+(v_i)_k\left(\frac{T}{m_i}+V_3^2\right)^{1/2}\int_0^{sin^{-1}\left(\frac{1}{r_{\tau i}}\right)}(1+R_{3i}cos^2\varphi)^{1/2}(1-r_{ti}sin\varphi)\mathfrak{T}_{lk}(\boldsymbol{\tau})d\varphi$$

$$+\frac{\sigma_i}{2}\frac{\partial (u_i)_k}{\partial x_j}\left[\left(\frac{T}{m_i}+V_3^2\right)^{1/2}\int_0^{sin^{-1}\left(\frac{1}{r_{\tau i}}\right)}(1+R_{3i}cos^2\varphi)^{1/2}(1-r_{ti}sin\varphi)\left(\mathfrak{T}_{lk}(\boldsymbol{\tau})N_j-\mathfrak{T}_{ljk}(\boldsymbol{\tau})\right)d\varphi\right],$$

$$(5.36)$$

in which the tensors $\mathfrak{T}_{lk}(\tau)$ and $\mathfrak{T}_{ljk}(\tau)$ are given by equations (5.34) and (5.35), and the constants C_1 and C_2 are given by

$$C_1 = \left(1 - \frac{r_{ti}}{r_{\tau i}}\right)\left[\frac{3}{4r_{\tau i}} + \frac{1}{12}\sin\left[3\sin^{-1}\left(\frac{1}{r_{\tau i}}\right)\right]\right] + \frac{r_{ti}}{2r_{\tau i}^2}\left(\frac{3}{4} + \frac{r_{\tau i}}{4} - \frac{1}{6r_{\tau i}^2}\right) \quad , \tag{5.37}$$

and

$$C_2 = \left(1 - \frac{r_{ti}}{r_{\tau i}}\right)\frac{1}{3r_{\tau i}^3} + \frac{r_{ti}}{12r_{\tau i}^4} \quad . \tag{5.38}$$

The x_l- components of $\boldsymbol{M}_{i\tau}^C$ are given by

$$(\boldsymbol{M}_{i\tau}^C)_l = \frac{2(1+e_i)\rho_i\lambda_i r_{ti}}{\sqrt{2}\pi^{3/2}}\left\{\frac{\pi^{1/2}}{2\sqrt{2}}\left[\left(\frac{3}{8}\frac{r_{ti}}{r_{\tau i}^2} + \frac{1}{8}\frac{r_{ti}}{r_{\tau i}}\right)\frac{T}{m_i} + \frac{r_{ti}}{2r_{\tau i}^2}\left(\frac{3}{4} + \frac{r_{\tau i}}{4} - \frac{1}{6r_{\tau i}^2}\right)V_2^2\right.$$

$$\left. + \left(\frac{1}{12}\frac{r_{ti}}{r_{\tau i}^4}\right)V_1^2\right]N_i + \frac{1}{12}\frac{r_{ti}}{r_{\tau i}^4}\frac{\pi^{1/2}}{\sqrt{2}}(\boldsymbol{t}\cdot\boldsymbol{B}\cdot\boldsymbol{N})t_l$$

$$+ (\boldsymbol{\nu}_i)_k\left(\frac{T}{m_i} + V_1^2\right)^{1/2}\int_0^{\sin^{-1}\left(\frac{1}{r_{\tau i}}\right)}(1 + R_{1i}\cos^2\varphi)^{1/2}(1 - r_{ti}\sin\varphi)\mathfrak{T}_{lk}(\boldsymbol{t})d\varphi$$

$$+ \frac{\sigma_i}{2}\frac{\partial(u_i)_k}{\partial x_j}\left[\left(\frac{T}{m_i} + V_1^2\right)^{1/2}\int_0^{\sin^{-1}\left(\frac{1}{r_{\tau i}}\right)}(1 + R_{1i}\cos^2\varphi)^{1/2}(1 - r_{ti}\sin\varphi)\left(\mathfrak{T}_{lk}(\boldsymbol{t})N_j - \mathfrak{T}_{ljk}(\boldsymbol{t})\right)d\varphi\right].$$

$$\tag{5.39}$$

The two geometric parameters for the sieve that appear in (5.36) and (5.39) are $r_{ti} = \sigma_i/S_t$ and $r_{\tau i} = \sigma_i/S_\tau$. Its easily verified that expressions (5.36) and (5.39) are identical when $S_t = S_\tau$. The mean fields that appear in (5.36) and (5.39) are evaluated at $\boldsymbol{x} + \sigma_i \boldsymbol{N}/2$.

The boundary condition for the momentum balance of species i at the sieve is given by equation (5.30) in which $\boldsymbol{M}_{it}^C$ and $\boldsymbol{M}_{i\tau}^C$ are given by either (5.33) and its τ- direction counterpart when species i can pass through the sieve, and by (5.36) and (5.39) when it cannot pass.

5.6   Energy Transfer at the Sieve

The integral E_i^T for the transport of energy through the boundary is analogous to the integral for the corresponding mass flow $\dot{m}_i$ given by (5.19) and the momentum flow $\boldsymbol{M}_i^T$ given by (5.22). In this case, we weigh the probability $f_i(\boldsymbol{c}_i)p(\boldsymbol{\psi})(\boldsymbol{g}_i \cdot \boldsymbol{N})d\boldsymbol{c}_id\boldsymbol{\psi}$ by the kinetic energy $m_i\boldsymbol{c}_i \cdot \boldsymbol{c}_i/2$ to obtain,

$$E_i^T = \frac{m_i}{S_tS_\tau} \int \left(\frac{1}{2}\boldsymbol{c}_i \cdot \boldsymbol{c}_i\right) f_i(\boldsymbol{c}_i)\, p(\boldsymbol{\psi})(\boldsymbol{g}_i \cdot \boldsymbol{N})dAd\boldsymbol{c}_id\boldsymbol{\psi} \tag{5.40}$$

where the limits of integrations are identical as those used in (5.19) and (5.22).

To decompose the integral (5.40), we replace $\boldsymbol{c}_i$ by $\boldsymbol{C}_i + \boldsymbol{u}_i$, and write E_i^T as the sum

$$E_i^T = \frac{1}{2}\dot{m}_i(\boldsymbol{u}_i \cdot \boldsymbol{u}_i) + \widetilde{\boldsymbol{M}}_i^T \cdot \boldsymbol{u}_i + \tilde{E}_i^T \tag{5.41}$$

where $\tilde{E}_i^T$ is given by

$$\tilde{E}_i^T = \frac{m_i}{S_tS_\tau} \int \left(\frac{1}{2}\boldsymbol{C}_i \cdot \boldsymbol{C}_i\right) f_i(\boldsymbol{c}_i)\, p(\boldsymbol{\psi})(\boldsymbol{g}_i \cdot \boldsymbol{N})dAd\boldsymbol{c}_id\boldsymbol{\psi} \tag{5.42}$$

Furthermore (5.41) and (5.26) may be used to rewrite the balance of energy (5.15) as

$$\sum_{i=A,B} \left(\boldsymbol{M}_i^C \cdot \boldsymbol{v}_i + F_i - D_i + \tilde{E}_i^T\right) = \boldsymbol{Q} \cdot \boldsymbol{N} + \sum_{i=A,B} \left(\frac{3}{2}\dot{m}_i\frac{T}{m_i}\right) \tag{5.43}$$

The integration (5.42) for the transport of momentum $\tilde{E}_i^T$ is carried out in the same manner used to obtain both the rate of mass transport (5.20) from integral (5.19), and the rate of momentum transport (5.27) from (5.24). In this manner we find

$$\tilde{E}_i^T = \frac{\rho_i T(1 - r_{ti})(1 - r_{\tau i})}{2(2\pi)^{1/2}m_i}\left(\frac{T}{m_i} + V_2^2\right)^{1/2}\left\{\frac{3}{2}\left[\sqrt{\pi}\ \Phi_i erfc(-\Phi_i)\right]\right.$$

$$\left. + exp\left(-\Phi_i{}^2\right)\left(1 + \frac{(2\,T/m_i + V_2^2)}{(T/m_i + V_2^2)}\right)\right\} . \tag{5.44}$$

The collisional rate F_i at which energy is supplied to species i due to the fluctuating motion of the boundary, and the collisional rate D_i at which energy absorbed from species i due to dissipative interactions at the boundary are, respectively statistical averages weighted by collision frequency (5.18) of the second term $m_i(1 + e_i)(\boldsymbol{g}_i \cdot \boldsymbol{k})(\boldsymbol{\Psi} \cdot \boldsymbol{k})$ and the third term $m_i(1 - e_i^2)(\boldsymbol{g}_i \cdot \boldsymbol{k})^2/2$ in equation (5.17) for the change in energy $m_i(\boldsymbol{c}_i^* \cdot \boldsymbol{c}_i^* - \boldsymbol{c}_i \cdot \boldsymbol{c}_i)/2$ per collision. Consequently, F_i and D_i may be written compactly in integral form

$$F_i = \frac{m_i(1 + e_i)\lambda_i}{2S_t S_\tau} \int (\boldsymbol{g}_i \cdot \boldsymbol{k})^2 (\boldsymbol{\Psi} \cdot \boldsymbol{k}) f_i\left(c_i, x + \frac{\sigma_i}{2}k\right) p(\psi)\, d\boldsymbol{k} dc_i d\psi \quad , \tag{5.45}$$

and

$$D_i = \frac{m_i(1 + e_i)\lambda_i}{2S_t S_\tau} \int \frac{1}{2}(1 - e_i)(\boldsymbol{g}_i \cdot \boldsymbol{k})^3 f_i\left(c_i, x + \frac{\sigma_i}{2}k\right) p(\psi)\, d\boldsymbol{k} dc_i d\psi \quad . \tag{5.46}$$

The integrations over velocities $\boldsymbol{c}$ and $\boldsymbol{\psi}$ in (5.45) and (5.46) are carried out in the same manner as (5.28), and are written as,

$$F_i = \frac{\sqrt{2}(1 + e_i)\rho_i \lambda_i T^{3/2}}{2\pi^{1/2}S_t S_\tau} \int (\boldsymbol{k} \cdot \boldsymbol{\mathcal{B}} \cdot \boldsymbol{k})^{1/2}(\boldsymbol{k} \cdot \boldsymbol{\mathcal{B}} \cdot \boldsymbol{k} - 1)\left[\sqrt{\pi}\,\Phi_i\, erfc(-\Phi_i) + exp(-\Phi_i^2)\right] d\boldsymbol{k},$$
$$\tag{5.47}$$

and

$$D_i = \frac{(1 - e_i^2)\rho_i \lambda_i T^{3/2}}{2\pi^{1/2}S_t S_\tau} \int (\boldsymbol{k} \cdot \boldsymbol{\mathcal{B}} \cdot \boldsymbol{k})^{3/2}\left[\sqrt{\pi}\,\Phi_i\left(\frac{3}{2} + \Phi_i^2\right)erfc(-\Phi_i)\left(1 + \Phi_i^2\right)exp\left(-\Phi_i^2\right)\right] d\boldsymbol{k}.$$
$$\tag{5.48}$$

The integrations over $\boldsymbol{k}$ in (5.47) and (5.48) are carried out in the same manner as (5.29) and may be written as sums of the contributions from integrations along the fibers in the t- and τ-directions:

$$F_i = F_{it} + F_{i\tau} \quad \text{and} \quad D_i = D_{it} + D_{i\tau} \quad . \tag{5.49}$$

Regardless of whether or not species i can pass through the sieve, the integral expressions for F_{it} and D_{it} are:

$$F_{it} = \frac{2(1 + e_i)\rho_i \lambda_i r_{\tau i}}{\sqrt{2}\pi^{3/2}} \left(\frac{T}{m_i} + V_3^2\right)^{1/2} \int_0^{\varphi_{max}} (1 + R_{3i}cos^2\varphi)^{1/2}$$

$$\times \left[\left(\frac{T}{m_i} + V_3^2\right)(1 + R_{3i}cos^2\varphi) - \frac{T}{m_i}\right](1 - r_{ti}sin\varphi)d\varphi , \quad (5.50)$$

and

$$D_{it} = \frac{2(1 - e_i^2)\rho_i \lambda_i r_{\tau i}}{2\sqrt{2}\pi^{3/2}} \left(\frac{T}{m_i} + V_3^2\right)^{3/2} \int_0^{\varphi_{max}} (1 + R_{3i}cos^2\varphi)^{3/2}(1 - r_{ti}sin\varphi)d\varphi \quad , \quad (5.51)$$

where R_{3i} is given by equation (5.31), and φ_{max} depends on whether or not species i can pass through the sieve. If species i *can* pass through the sieve (i.e. $\sigma_i < S_t$ and $\sigma_i < S_\tau$), then $\varphi_{max} = \pi/2$. If species i *cannot* pass through the sieve (i.e. $\sigma_i < S_t$ and $\sigma_i > S_\tau$; or $\sigma_i > S_t$ and $\sigma_i > S_\tau$ regardless of whether $S_t > S_\tau$ or $S_t < S_\tau$), then $\varphi_{max} = \sin^{-1}(1/r_{\tau i})$. The two geometric parameters for the sieve that appear in (5.50) and (5.51) are $r_{ti} = \sigma_i/S_t$ and $r_{\tau i} = \sigma_i/S_\tau$. The mean fields that appear in (5.50) and (5.51) are evaluated at $x + \sigma_i N/2$.

The expressions for $F_{i\tau}$ and $D_{i\tau}$ in equations (5.49) are obtained by integrating along a fiber in the τ-direction, and are identical to (5.50) and (5.51) in which r_{ti}, $r_{\tau i}$, R_{3i}, and V_3 are replaced by $r_{\tau i}$, r_{ti}, R_{1i}, and V_1, respectively, and when $r_{\tau i}$ is replaced by r_{ti} in φ_{max}.

The boundary condition for the energy balance of the mixture at the sieve is given by equation (5.43). The terms M_{it}^C and $M_{i\tau}^C$ are given by either (5.33) and its τ- direction counterpart when species i can pass through the sieve, and by (5.36) and (5.39) when it cannot pass. The contributions of F_{it} and D_{it} are given by (5.50) and (5.51) in which φ_{max} is chosen appropriately, and the contributions of $F_{i\tau}$ and $D_{i\tau}$ are given by the τ- direction counterparts of (5.50) and (5.51).

Chapter 6

Vibratory Sieving of Monosized Assemblies

In this chapter, in order to isolate several elements of the basic physics of sieving, we focus attention on the assemblies of *monosized* granular materials and determine how and why they evolve as they flow through vibrating sieves. For given sieve geometry, vibrational energy, vibrational direction, and the initial mass on the sieve, we wish to predict the time variations of the mass on the sieve, the flow rate through the sieve, and the profiles of the solid volume fraction, mean velocity normal to the vibrating sieve, and the granular temperature. For simplicity, the granular materials consist of identical, smooth, inelastic spheres of diameter σ, mass m. The energy dissipated in collisions between any two flow particles is described by the coefficient of restitution e, and the energy dissipated in collisions between any flow particles and the sieve is described by the coefficient of restitution e_w.

For these materials we combine the boundary conditions derived in Chapter 5 (specialized for monosized assemblies) with the constitutive theory outlined in Chapter 2.

6.1   Governing Equations

The assemblies are unconfined from above, thermalized from below by a horizontal vibrating sieve, and contained by a vertical acceleration g due to gravity. These flows are unsteady in the sense that each of these quantities varies with time, even though the vibratory motion of the sieve does not.

We consider sieves with dimensions that are much larger than the depths of the materials they support. If a x_1 - x_2 - x_3 Cartesian coordinate system is established such that x_1 and x_3 are

tangent to the plane of the sieve, and x_2 measures perpendicular distance from the sieve, then the solid volume fraction ν, the component u_2 of the mean velocity normal to the sieve, and the granular temperature T depend on the distance x_2 and time. The vibrations of the sieve induce no mean motion in the tangential directions. The dimensionless normal distance from the sieve is $Y \equiv x_2/\sigma$, the dimensionless normal velocity is $u \equiv u_2/(g\sigma)^{1/2}$, the dimensionless granular temperature is $w^2 \equiv \mathcal{T} \equiv T/g\sigma$, and t is time nondimensionalized by the factor $\sqrt{\sigma/g}$ Under these circumstances, the balance of mass (2.4) is given by

$$\frac{\partial \nu}{\partial t} + \frac{\partial(\nu u)}{\partial Y} = 0 \quad . \tag{6.1}$$

The momentum balance (2.5) is in the Y- direction is,

$$\nu\left(\frac{\partial u}{\partial t} + u\frac{\partial u}{\partial Y}\right) = -\frac{\partial P}{\partial Y} - \nu \quad , \tag{6.2}$$

where P is the dimensionless normal pressure $P \equiv P_{22}/\rho_p\, g\sigma$. The energy balance (2.6) is

$$\frac{3}{2}\nu\left(\frac{\partial \mathcal{T}}{\partial t} + u\frac{\partial \mathcal{T}}{\partial Y}\right) = -\frac{\partial Q}{\partial Y} - P\frac{\partial u}{\partial Y} - \Gamma \quad , \tag{6.3}$$

in which $Q \equiv Q_2/\rho_p(g\sigma)^{3/2}$ and $\Gamma \equiv \gamma/\rho_p\sigma^{3/2}g^{3/2}$ are the dimensionless energy flux and energy dissipation, respectively.

From equation (2.10), the constitutive relation for the pressure P has the form:

$$P = \nu(1 + 4G)\mathcal{T} - \frac{\mu}{3}(5 + 4E)\frac{\partial u}{\partial Y} \quad , \tag{6.4}$$

where $G(\nu)$ is given by (2.9), μ is given by (2.8), and $E(\nu) \equiv 1 + \pi[1 + 5/(8G)]^2/12$.

From equation (2.11), the energy flux is

$$Q = -k\frac{\partial \mathcal{T}}{\partial Y} \quad , \tag{6.5}$$

where the coefficient k is given by

$$k = \frac{4 \nu G \mathcal{M} \mathcal{T}^{1/2}}{\pi^{1/2}} \quad , \tag{6.6}$$

where $\mathcal{M}(\nu) = 1 + 9\pi[1 + 5/(12G)]^2/32$. From equation (2.7), the energy dissipation Γ is given by:

$$\Gamma = \frac{24(1-e)\nu G \mathcal{T}^{3/2}}{\pi^{1/2}} \quad . \tag{6.7}$$

6.2   Boundary Conditions

At the free surface $(Y = \beta)$, the normal pressure P, and the normal component of the energy flux Q are zero:

$$P(Y = \beta) = 0 \quad ; \tag{6.8}$$

and

$$Q(Y = \beta) = 0 \quad . \tag{6.9}$$

At the vibrating sieve $(Y = 0)$, we employ boundary conditions (5.13), (5.25), and (5.43) for mass, momentum, and energy. In this case, the conditions for binary mixtures can be simplified for assemblies of monosized particles and the ratio T/m_i in the theory for binary mixtures is replaced by T in the theory for monosized particles.

The balance of mass (5.13) at the boundary is

$$-\nu u = \dot{m} \quad , \tag{6.10}$$

where $\dot{m} \equiv \dot{m}/\rho_p(g\sigma)^{1/2}$. From (5.20) the integral expression for $\dot{m}$ is

$$\dot{m} = \frac{\nu \alpha (\Omega^2 + V_n^2)^{1/2}}{(2\pi)^{1/2}} (1 - r_t)(1 - r_\tau)\left[\sqrt{\pi} \, \Phi \, erfc(-\Phi) + \exp(-\Phi^2)\right] \quad , \tag{6.11}$$

where $\Omega \equiv w/\alpha$, $r_t = \sigma/S_t$, $r_\tau = \sigma/S_\tau$, and Φ is given by

$$\Phi = \frac{-u}{[2\alpha^2(\Omega^2 + V_n^2)]^{1/2}} \quad . \tag{6.12}$$

The balance of momentum at the boundary (5.25) is

$$P = M^C + \tilde{M}^T \quad , \tag{6.13}$$

where $M^C \equiv M_2^C/\rho_p g\sigma$ and $\tilde{M}^T \equiv \tilde{M}_2^T/\rho_p g\sigma$ (in which the subscript 2 refers to the N direction).

From (5.27) the integral expression for $\tilde{M}^T$ is

$$\tilde{M}^T = -\frac{v\alpha^2\Omega}{2}(1 - r_t)(1 - r_\tau)erfc(-\Phi) \quad . \tag{6.14}$$

From (5.30), M^C is the sum.

$$M^C = M_t^C + M_\tau^C \quad . \tag{6.15}$$

From (5.33) corresponding to the case where the particles can pass through the sieve, the integral expression for M_t^C is

$$M_t^C = \frac{(1 + e_w)v\lambda r_\tau}{\sqrt{2}\pi^{3/2}} \left\{ \frac{\pi^{1/2}\alpha^2}{2\sqrt{2}} \left[\left(1 - \frac{r_t}{2}\right)\Omega^2 + \left(\frac{2}{3}V_n^2 + \frac{V_\tau^2}{3}\right) - \frac{r_t}{4}(V_n^2 + V_\tau^2) \right] \right.$$

$$+ u\,\alpha(\Omega^2 + V_\tau^2)^{1/2} \int_0^{\pi/2} (1 + R_\tau \cos^2\varphi)^{1/2}(1 - r_t \sin\varphi)\cos^2\varphi \, d\varphi$$

$$\left. + \frac{1}{2}\frac{\partial u}{\partial Y}\left[\alpha(\Omega^2 + V_\tau^2)^{1/2} \int_0^{\pi/2} (1 + R_\tau \cos^2\varphi)^{1/2}(1 - r_t \sin\varphi)(\cos^2\varphi - \cos^3\varphi)d\varphi \right] \right\}, \tag{6.16}$$

where the ratios R_1 and R_3 are given respectively in dimensionless form by

$$R_t = \frac{(V_n^2 - V_t^2)}{(\Omega^2 + V_t^2)} \qquad \text{and} \qquad R_\tau = \frac{(V_n^2 - V_\tau^2)}{(\Omega^2 + V_\tau^2)} \quad . \tag{6.17}$$

M_τ^C is given by (8.16) in which r_t, r_τ, R_τ, and V_τ are replaced by r_τ, r_t, R_t, and V_t.

The balance of energy at the boundary (5.43) is

94

$$Q = -M^C u + \mathcal{F} - \mathcal{D} + \tilde{\mathcal{E}}^T - \frac{3}{2}\dot{m}a^2\Omega^2 \quad , \tag{6.18}$$

where M^C is given by (6.15), $\dot{m}$ is given by (6.11), $\mathcal{F} \equiv F/\rho_p(g\sigma)^{3/2}$, $\mathcal{D} \equiv D/\rho_p(g\sigma)^{3/2}$, and

$\tilde{\mathcal{E}}^T \equiv \tilde{\mathcal{E}}^T/\rho_p(g\sigma)^{3/2}$.

From (5.49), $\mathcal{F}$ and $\mathcal{D}$ are the sums

$$\mathcal{F} = \mathcal{F}_t + \mathcal{F}_\tau \quad \text{and} \quad \mathcal{D} = \mathcal{D}_t + \mathcal{D}_\tau \tag{6.19}$$

From (5.50) and (5.51) corresponding to the case where the particles can pass through the sieve, the integral expressions for $\mathcal{F}_t$ and $\mathcal{D}_t$ are

$$\mathcal{F}_t = \frac{(1 + e_w)\nu\lambda r_\tau a^3(\Omega^2 + V_\tau^2)^{1/2}}{\sqrt{2}\pi^{3/2}} \int_0^{\pi/2} (1 + R_\tau cos^2\varphi)^{1/2}$$

$$[(\Omega^2 + V_\tau^2)(1 + R_\tau cos^2\varphi) - \Omega^2](1 - r_t sin\varphi)d\varphi , \tag{6.20}$$

and

$$\mathcal{D}_t = \frac{(1 - e_w^2)\nu\lambda r_\tau a^3(\Omega^2 + V_\tau^2)^{3/2}}{2\sqrt{2}\pi^{3/2}} \int_0^{\pi/2} (1 + R_\tau cos^2\varphi)^{3/2}(1 - r_t sin\varphi)d\varphi . \tag{6.21}$$

The expressions for $\mathcal{F}_\tau$ and $\mathcal{D}_\tau$ in equation (6.19) are obtained by integrating along a fiber in the

τ- direction, and are obtained from (6.20) and (6.21) by replacing r_t, r_τ, R_τ, and V_τ with

r_τ, r_t, R_t, and V_t.

From (5.44) the expression for $\tilde{\mathcal{E}}^T$ is

$$\tilde{\mathcal{E}}^T = \frac{\nu a^3 \Omega^2}{(2\pi)^{1/2}}(1 - r_t)(1 - r_\tau)(\Omega^2 + V_n^2)^{1/2}\left\{\frac{3}{2}\left[\sqrt{\pi}\ \Phi_i erfc(-\Phi_i)\right]\right.$$

$$\left. + exp\left(-\Phi_i^2\right)\left(1 + \frac{(2\Omega^2 + V_n^2)}{(\Omega^2 + V_n^2)}\right)\right\} . \tag{6.22}$$

6.3 Quasi-Steady Solutions

In principle, balance equations (6.1), (6.2), and (6.3), and constitutive relations (6.4), (6.5), and (6.7) can be solved exactly subjected to boundary condition (6.8), (6.9) at $Y = \beta$, boundary conditions (6.10), (6.13), (6.18) at $Y = 0$, and appropriate initial conditions. However, in what follows we restrict our attention to cases in which the holes in the sieve are only slightly larger than the size of the particles that pass through them. Under these circumstances, the flow rates and the mean velocities are relatively small, and the mass hold-up m_t, defined by

$$m_t \equiv \int_0^\beta v \, dY \quad , \tag{6.23}$$

varies slowly in time. The thermalized states maintained on the sieve are nearly the steady states that would be maintained at the instantaneous value of mass hold-up without vertical flow through the sieve. These quasi-steady thermalized states depend on time only because the mass hold-up itself decreases gradually with time. In what follows, the quasi-steady solutions are denoted by subscript "0," so that the solid fraction is $\nu_0(Y; m_t)$, the granular temperature is $\mathcal{T}_0(Y; m_t)$ and $w_0 \equiv \sqrt{\mathcal{T}_0}$, the pressure is $P_0(Y; m_t)$, the energy flux is $Q_0(Y; m_t)$, and the energy dissipation is $\Gamma_0(Y; m_t)$.

In terms of these quantities, the momentum equation (6.2) is

$$\frac{dP_0}{dY} = -\nu_0 \quad , \tag{6.24}$$

and the energy equation (6.3) is

$$\frac{dQ_0}{dY} = -\Gamma_0 \quad , \tag{6.25}$$

where $\Gamma_0 \equiv \Gamma(\nu_0, \mathcal{T}_0)$, and Γ is given by equation (6.7).

The corresponding constitutive relations for pressure and energy flux are

$$P_0 = v_0(1 + 4G_0)\mathcal{T}_0 \quad , \tag{6.26}$$

in which $G_0 \equiv G(v_0)$ with $G(v) = v/(1 - v/v_m)^{5v_m/2}$ and

$$\frac{d\mathcal{T}_0}{dY} = -\frac{Q_0}{k_0} \quad , \tag{6.27}$$

in which $k_0 \equiv k(v_0, \mathcal{T}_0)$ with k is given by equation (6.6). Equations (6.24) through (6.27) determine the quasi-steady solutions $v_0(Y)$, $\mathcal{T}_0(Y)$, $P_0(Y)$, and $Q_0(Y)$ to within three constants of integration.

Following the manipulations described in section 4.1 for incline flows, these equations can be rewritten (for angle of inclination $\phi = 0$) in the following form:

$$\mathcal{T}_0^{'} \equiv 2\mathcal{T}_0 H_0 \quad , \tag{6.28}$$

which defines H_0 ;

$$H_0^{'} = \frac{(1 - 2h_0)H_0}{(4G_0 + 1)\mathcal{T}_0} - (4h_0 + 1)H_0^2 - \frac{3(1 - e)}{\mathcal{M}_0} \quad , \tag{6.29}$$

where $h_0 \equiv h(v_0)$ is given by (4.11); and

$$v_0^{'} = \frac{-v_0 - 8G_0 F_0 H_0 v_0 \mathcal{T}_0}{\mathcal{T}_0(1 + 4G_0 + 4v_0\, dG_0/dv_0)} \quad . \tag{6.30}$$

The boundary conditions at the free "surface" (at $Y = \beta$) require that the normal stress and the energy flux vanish there

$$P_0(Y = \beta) = 0 \text{ and } Q_0(Y = \beta) = 0 \quad . \tag{6.31}$$

At the sieve $(Y = 0)$, the momentum boundary condition (6.13) requires that

$$P_0 = \frac{(1 + e_w)v_0\lambda_0\alpha^2}{2\pi}\left\{\Omega_0{}^2 r_\tau(1 - r_t) + \Omega_0{}^2 r_t(1 - r_\tau) + r_\tau\left(\frac{2}{3}V_n^2 + \frac{V_\tau^2}{3}\right)\right.$$

$$\left. +r_t\left(\frac{2}{3}V_n^2 + \frac{V_t^2}{3}\right) - \frac{r_t r_\tau}{4}(2V_n^2 + V_\tau^2 + V_t^2)\right\} - \frac{v_0\Omega_0\alpha^2}{2}(1 - r_t)(1 - r_\tau) \quad , \tag{6.32}$$

where we used integrals expressions (6.14) and (6.16). Equation (6.32) determines the unknown factor λ_0 in terms of P_0, ν_0, and $\Omega_0 \equiv \sqrt{\mathcal{T}_0}/\alpha$.

At the sieve $(Y = 0)$, the energy boundary condition (6.18) requires that

$$Q_0 = \mathcal{F}_0 - \mathcal{D}_0 + \tilde{\mathcal{E}}_0^T \quad , \tag{6.33}$$

where $\mathcal{F}_0 = \mathcal{F}(\nu_0, \Omega_0, \lambda_0)$, $\mathcal{D}_0 = \mathcal{D}(\nu_0, \Omega_0, \lambda_0)$, and $\tilde{\mathcal{E}}_0^T = \tilde{\mathcal{E}}^T(\nu_0, \Omega_0, \lambda_0, \Phi = 0)$. The functional forms of $\mathcal{F}$, $\mathcal{D}$ and $\tilde{\mathcal{E}}^T$ are given, respectively, in first and second equations in (6.19) and in equation (6.22).

The solution procedure for $\nu_0(Y; m_t)$, $w_0(Y; m_t)$ and $H_0(Y; m_t)$ is identical to that described in section 4.3 for ν, w and H in inclined flows when the angle of inclination is $\phi = 0$.

With ν_0 and Ω_0 $(\equiv w_0/\alpha)$ known, the flow rate is obtained from the lowest order approximation of expression (6.11) with $\Phi = 0$:

$$\dot{m}_1 = \frac{\nu_0\,\alpha(\Omega_0^2 + V_n^2)^{1/2}}{(2\pi)^{1/2}}(1 - r_t)(1 - r_\tau) \quad , \tag{6.34}$$

where the subscript on $\dot{m}_1$ indicates that the flow rate is of higher order than terms with subscript "0." With the flow rate known, we can prescribe a small increment δt in time and update the mass hold up according to:

$$m_t(t + \delta t) = m_t(t) - \dot{m}_1\delta t \quad . \tag{6.35}$$

The solution procedure for $\nu_0(Y; m_t)$, $w_0(Y; m_t)$ and $H_0(Y; m_t)$ can then be carried out for successive values of m_t to obtain the quasi-steady variations of solid fraction and granular temperature profiles.

At any value of m_t, with the flow rate calculated from (6.34), the mean velocity $u_1(Y)$ normal to the sieve is determined from the balance of mass (6.1)

$$\dot{m}_1 \frac{\partial v_0}{\partial m_t} + \frac{d(v_0 u_1)}{dY} = 0 \quad , \tag{6.36}$$

where the time derivative $\partial(\ )/\partial t$ has been replaced by $\dot{m}_1 \partial(\ )/\partial m_t$. Integrating equation (6.35) and combining the result with the integrated form of equation (6.24) yields the velocity:

$$u_1(Y) = \frac{\dot{m}_1}{v_0(Y)} \frac{\partial P_0}{\partial m_t} \quad . \tag{6.37}$$

We anticipate that the solutions obtained here will serve as good approximations to the actual flow profiles provided that the diameter σ of the flow particles is only slightly less than less than at least one of the two spacings S_t and S_τ. In this case, either the quantity $(1 - r_t)$ or the quantity $(1 - r_\tau)$ or both are small, equation (6.34) shows that the flow rates will also be small.

6.4   Improved Solutions

The solutions obtained so far may be used as the zeroth order solutions to initiate a systematic perturbation scheme to obtain corrections to the solid fraction, granular temperature, and mean velocity. In order to formalize this perturbation scheme, the mean fields of solid fraction v and granular temperature $\mathcal{T}$ are written as the sums:

$$v(Y,t) = v_0(Y; m_t(t)) + v_1(Y; v_0, \mathcal{T}_0, u_1) \quad , \tag{6.38}$$

and

$$\mathcal{T}(Y,t) = \mathcal{T}_0(Y; m_t(t)) + \mathcal{T}_1(Y; v_0, \mathcal{T}_0, u_1) \quad , \tag{6.39}$$

where the subscript "0" denotes the zeroth order (quasi-steady) contribution, and the subscript "1" denotes first order corrections that are small compared to their zeroth order counterparts. The mean velocity $u(Y,t)$ has no zeroth order contribution, so that its lowest order term is $u_1(Y; v_0, \mathcal{T}_0, m_t)$ given by equation (6.37). Similar decompositions can be made for the pressure, energy flux, and energy dissipation:

$$P(Y,t) = P_0\big(y; m_t(t)\big) + P_1(Y; v_0, \mathcal{T}_0, u_1) \quad , \tag{6.40}$$

$$Q(Y,t) = Q_0\big(Y; m_t(t)\big) + Q_1(Y; v_0, \mathcal{T}_0, u_1) \quad , \tag{6.41}$$

and

$$\Gamma(Y,t) = \Gamma_0\big(Y; m_t(t)\big) + \Gamma_1(Y; v_0, \mathcal{T}_0, u_1) \quad , \tag{6.42}$$

The quasi-steady zeroth-order solutions depend implicitly on time through their dependence on mass hold-up m_t.

The equations governing the correction terms are obtained by first employing sums (6.38) through (6.42), in balance equations (6.1), (6.2), and (6.3), constitutive relations (6.4), (6.5) and (6.7), and by balancing the first order terms in each. The first order terms in the balance of momentum (6.2) and balance of energy (6.3) are

$$\frac{dP_1}{dY} = -v_1 \quad , \tag{6.43}$$

and

$$\frac{3}{2}v_0\left(\dot{m}_1 \frac{\partial \mathcal{T}_0}{\partial m_t} + u_1 \frac{d\mathcal{T}_0}{dY}\right) = -\frac{dQ_1}{dY} - P_0 \frac{du_1}{dY} - \Gamma_1 \quad , \tag{6.44}$$

respectively. The time derivative $\partial(\ \ )/\partial t$ has been replaced by $\dot{m}_1 \, \partial(\ \ )/\partial m_t$

The first order constitutive relation for the correction pressure P_1 is:

$$P_1 = \mathcal{T}_0\left[(1 + 4G_0) + 4v_0 \frac{dG_0}{dv_0}\right]v_1 + v_0(1 + 4G_0)\mathcal{T}_1 - \frac{\mu_0}{3}(5 + 4E)\frac{du_1}{dY} \quad , \tag{6.45}$$

where $\mu_0 \equiv \mu(v_0, \mathcal{T}_0)$ and μ is given by equation (2.8). Solving for v_1 yields

$$v_1 = \frac{3[P_1 - v_0(1 + 4G_0)\mathcal{T}_1] + \mu_0(5 + 4E){u_1}'}{3\mathcal{T}_0\left[(1 + 4G_0) + 4v_0 \frac{dG_0}{dv_0}\right]} \quad , \tag{6.46}$$

The corresponding constitutive relation for the correction energy flux Q_1

$$Q_1 = -k_1 \frac{d\mathcal{T}_0}{dY} - k_0 \frac{d\mathcal{T}_1}{dY} \quad . \tag{6.47}$$

Solving for $\mathcal{T}_1'$ gives

$$\mathcal{T}_1' = \frac{(-2k_1\mathcal{T}_0 H_0 - Q_1)}{k_0} \quad , \tag{6.48}$$

where we used equation (6.28) to eliminate $\mathcal{T}_0'$. where $k_0 \equiv k(v_0, \mathcal{T}_0)$ in which k is given by

equation (6.6), and

$$k_1 = \frac{4\mathcal{T}_0^{1/2}}{\pi^{1/2}} \left[\left(G_0 \mathcal{M}_0 + v_0 \frac{dG_0}{dv_0} \mathcal{M}_0 + v_0 G_0 \frac{d\mathcal{M}_0}{dG_0} \frac{dG_0}{dv_0} \right) v_1 + \frac{v_0 G_0 \mathcal{M}_0}{2T_0} \mathcal{T}_1 \right] \quad , \tag{6.49}$$

in which $\mathcal{M}_0 \equiv \mathcal{M}(G_0)$ where $G(v) = v/(1 - v/v_m)^{5v_m/2}$ and $\mathcal{M}(v) = 1 + 9\pi[1 +$

$5/(12G)]^2/32$; We can write and Q_1' respectively as

$$Q_1' = -\frac{3}{2}v_0 \left(\dot{m}_1 \frac{\partial \mathcal{T}_0}{\partial m_t} + 2u_1 \mathcal{T}_0 H_0 \right) - P_0 u_1' - \Gamma_1 \quad , \tag{6.50}$$

and Γ_1 is given by

$$\Gamma_1 = \frac{24(1-e)\mathcal{T}_0^{1/2}}{\pi^{1/2}} \left[\left(G_0 + v_0 \frac{dG_0}{dv_0} \right) \mathcal{T}_0 v_1 + \frac{v_0 G_0 \mathcal{M}_0}{2T_0} \mathcal{T}_1 \right] \quad . \tag{6.51}$$

First order equations (6.43), (6.48), and (6.50) combined with algebraic equations (6.46), (6.49),

and (6.51) determine P_1, $\mathcal{T}_1$, Q_1 and v_1 to within three constants of integration.

In order to apply boundary conditions at the top of the assemblies, it is necessary to

distinguish between the actual (as yet undetermined) height L and the distance h from the sieve

to the location at which the downward integrations were initiated (i.e. where $Q_0 = 0$ and

$v_0 = 10^{-6}$). The zeroth-order solution did not include a prediction for L. Because h can be made

arbitrarily large by taking $v_0(Y = h)$ to be arbitrarily small, in what follows we assume that h is

greater than L. With L and h defined in this way, the mass hold-up is given by two integrals:

$$m_t = \int_0^L v \, dY = \int_0^h v_0 \, dY \quad . \tag{6.52}$$

These integrals insure that both the total solution and the zeroth-order solution correspond to the same value of mass hold-up. Taking $v = v_0 + v_1$ and employing the zeroth- and first-order momentum balances (6.24) and (6.43) in equation (6.52) yields

$$P_1(0) = P_0(L) + P_1(L) \quad . \tag{6.53}$$

Because the total pressure $P_0 + P_1$ at $Y = L$ is equal to zero,

$$P_1(L) = -P_0(L) \quad , \tag{6.54}$$

and equations (6.53) then shows that

$$P_1(0) = 0 \quad . \tag{6.55}$$

Finally, because the total energy flux $Q_0 + Q_1$ at $Y = L$ is also equal to zero,

$$Q_1(L) = -Q_0(L) \quad . \tag{6.56}$$

At the bottom sieve $(Y = 0)$, the first order terms of momentum boundary condition (6.13) requires that

$$P_1 = M_1^C + \widetilde{M}_1^T \quad , \tag{6.57}$$

where M_1^C and $\widetilde{M}_1^T$ are the first order corrections to M^C and $\widetilde{M}^T$. The first order terms in energy balance (6.18) at the sieve are:

$$Q_1 = -P_0 u_1 + \mathcal{F}_1 - \mathcal{D}_1 + \widetilde{\mathcal{E}}_1^T - \frac{3}{2} \dot{m} \mathcal{J}_0 \quad , \tag{6.58}$$

where $\mathcal{F}_1$, $\mathcal{D}_1$, and $\widetilde{\mathcal{E}}_1^T$ are the first order corrections to $\mathcal{F}$, $\mathcal{D}$ and $\widetilde{\mathcal{E}}^T$. The momentum transfer rates M_1^C and $\widetilde{M}_1^T$, and the energy transfer rates $\mathcal{F}_1$, $\mathcal{D}_1$, and $\widetilde{\mathcal{E}}_1^T$ are given by (A2.7), (A2.9), the first and second of (A2.10), and (A2.13) in Appendix 2. The collisional integrals each depend on the first order correction λ_1 to the shielding factor λ that appears in (6.16), (6.20), and (6.21).

First order equations (6.43), (6.48), and (6.50) combined with algebraic equations (6.46), (6.49), and (6.51) determine P_1, $\mathcal{T}_1$, Q_1 and v_1 to within three constants of integration. The three constants of integration and the depth L are determined by condition (6.54) and (5.56) at $Y = L$, condition (6.55) at $Y = 0$, and energy condition (6.58). The factor λ_1 is determined in terms of P_1, v_1, and $\mathcal{T}_1$ from momentum boundary condition (6.57) at $Y = 0$. The solution procedure is as follows. Integrations are initiated from $Y = 0$, where P_1 vanishes. We guess at the value of $\mathcal{T}_1(0)$, use constitutive relation (6.46) to compute $v_1(0)$, and use the energy boundary condition (6.58) to compute $Q_1(0)$. The integrations proceed upward until P_1 satisfies condition (6.54). In order to find the actual solution, we use Newton-Raphson iteration on the value of $\mathcal{T}_1(0)$ until the energy flux condition (6.56) is satisfied at the same height $Y = L$.

The corrected solution for v, T, P, and Q are then given by sums (6.38), (6.39), (6.40), and (6.41). The corrected flow rate $\dot{m}$ is given by equation (6.11) evaluated at $v = v_0 + v_1$ and $\mathcal{T} = \mathcal{T}_0 + \mathcal{T}_1$. The corrected mean velocity is given by the analogy to equation (6.37):

$$u(Y) = \frac{\dot{m}}{v(Y)} \frac{\partial P}{\partial m_t} \quad , \tag{6.59}$$

where $P = P_0 + P_1$.

6.5 Results and Discussion

The spacing between the fibers in the t- and τ-directions of the sieve are specified by two ratios:

$$\Delta_t \equiv \frac{S_t}{\sigma} = \frac{1}{r_t} \qquad \text{and} \qquad \Delta_\tau \equiv \frac{S_\tau}{\sigma} = \frac{1}{r_\tau} \quad , \tag{6.60}$$

respectively. Unless otherwise specified, we consider the case of equal spacing $\Delta \equiv \Delta_t = \Delta_\tau$.

In Figures 6.1 and 6.2, we evaluate the importance of the first order corrections described in the previous section by showing the profiles of solid fraction ν, granular temperature $w \equiv \sqrt{\mathcal{T}}$, and mean velocity u for different spacings $\Delta = 1.05, 1.1, 1.15, 1.2, 1.25, 1.3$ (when $m_t = 4$, $\alpha = 1$, $V_n^2 = V_t^2 = V_\tau^2 = 1$, and $e = e_w = .9$). The zeroth order solutions are dashed curves and the corrected solutions are solid. Whereas the zeroth order solutions are of infinite height, the solution procedure for the corrected solutions determines a finite height L (indicated by horizontal dashed line across the panels). The flow rates and therefore the velocities throughout the assemblies increase significantly as the spacing increases. The zeroth order solutions are based on the assumption that the flow rates are small. Consequently, the differences between the uncorrected and the corrected solutions increases as the spacings increase. Figures 6.1 and 6.2 suggest that the uncorrected solutions are quite adequate for spacings Δ that are less than about 1.2. For these values of Δ, therefore, we show results based on the uncorrected solutions unless otherwise specified.

The profiles in Figures 6.1 and 6.2 are typical. The region near the sieve is the most thermalized and most dilute. The granular temperature decreases monotonically from the bottom to the top of the assembly because energy must be conducted into the region above any prescribed location. As the temperature decreases, the solid fraction increases from its value at the sieve to a its maximum value somewhere within the flow after which it decreases to it free surface value. The assembly behaves like a molecular gas at nonuniform pressure. In this case, the pressure decreases as the distance away from the sieve increases. The density and solid fraction vary inversely nearer to the base where the decrease in pressure is relatively gradual. However they decrease together near the top where the decrease in pressure is more rapid.
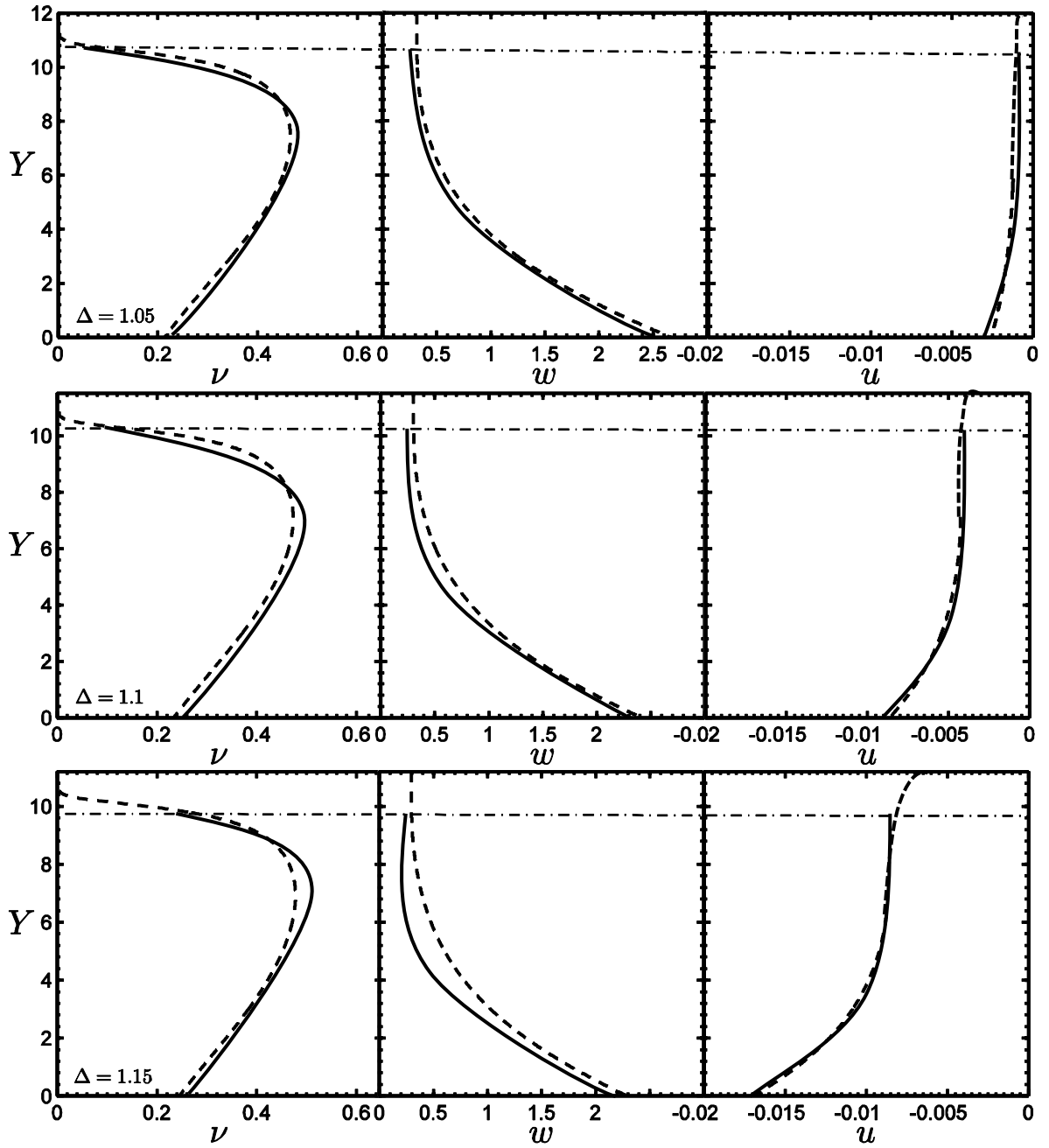
Figure 6.1: The profiles of solid fraction ν, granular temperature w, and mean velocity u for spacings $\Delta = 1.05, 1.1, 1.15$ when $\alpha = 1, V_n^2 = V_t^2 = V_\tau^2 = 1$, $m_t = 4$, and $e = e_w = .9$.

105
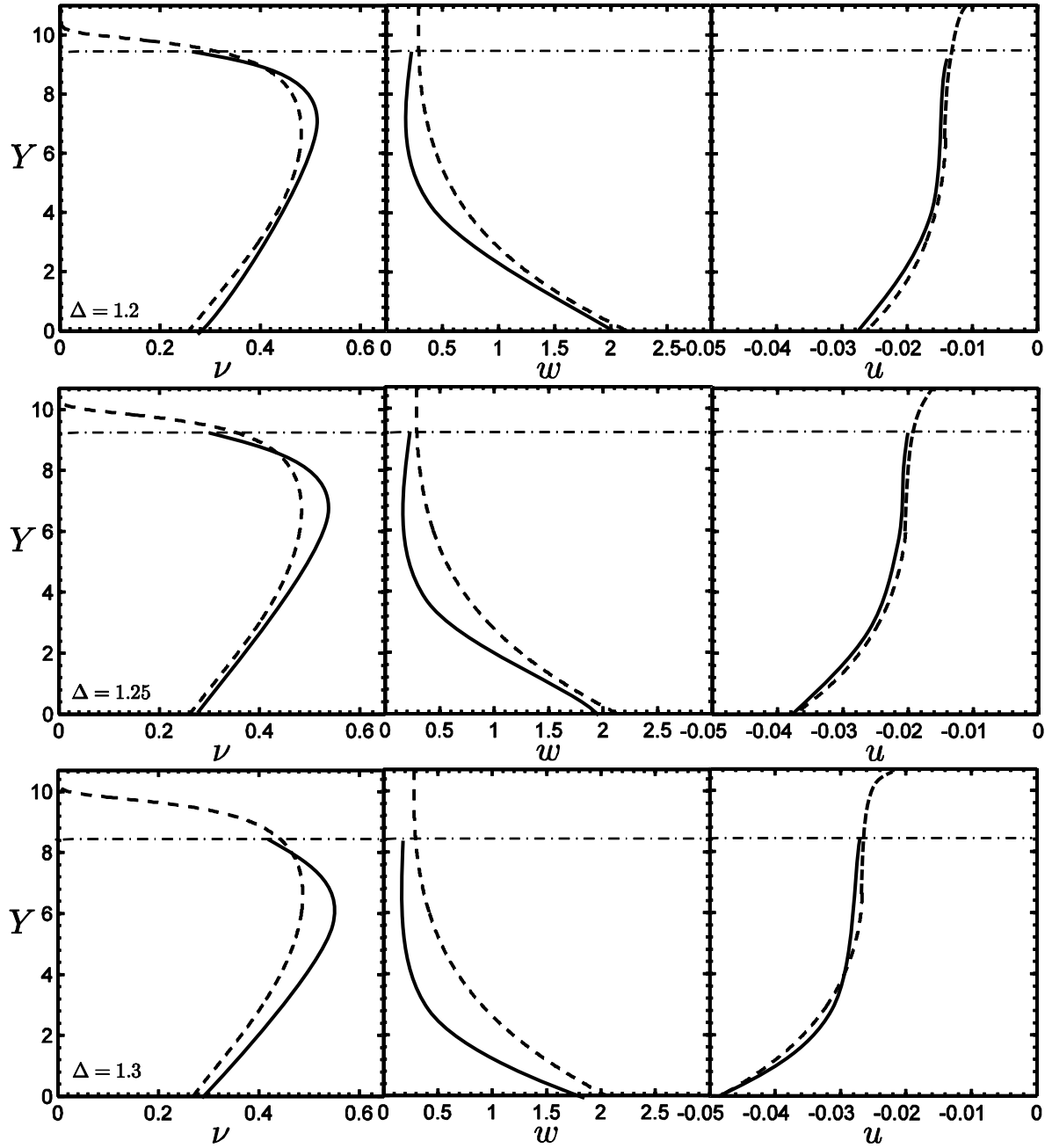
Figure 6.2: The profiles of solid fraction ν, granular temperature w, and mean velocity u for spacings $\Delta = 1.2, 1.25, 1.3$ when, $\alpha = 1, V_n^2 = V_t^2 = V_\tau^2 = 1$, $m_t = 4$, and $e = e_w = .9$.

Figure 6.3 shows how the (corrected) profiles of solid fraction v, granular temperature w, and mean velocity u evolve as the mass hold-up decreases from 16 to 2 at five values $m_t = 16, 12, 8, 4, 2$ (when $\alpha = 1$, $V_n^2 = V_t^2 = V_\tau^2 = 1$, $\Delta = 1.1$, and $e = e_w = .9$). At relatively high a values of mass hold-up, the assembly is relatively deep, and only a small region near the sieve is thermalized. The upper regions are unthermalized and move downward as a uniform closed-packed solid. At relatively low values of mass hold-up, the assemblies are much shallower. Consequently they are thermalized (and relatively dilute) throughout the depth. In these cases, there is no solid-like region and the mean velocity is non-uniform through the depth.

Figures 6.4 through 6.6 describe overall bulk flow behavior through the sieve and how it is affected by changing the fiber spacing. In Figure 6.4 we show the variation of mass flow rate $\dot{m}$ with mass hold-up m_t (from $m_t = 20$ to $m_t = 2$) for spacings $\Delta = 1.05, 1.1, 1.15$ (when $\alpha = 1$, $V_n^2 = V_t^2 = V_\tau^2 = 1$, and $e = e_w = .9$). For any fixed Δ, the mass flow rate decreases as the mass hold-up decreases, and for any value of mass hold-up m_t, the mass flow rate increases with spacing. Figure 6.5 shows the corresponding explicit time variations of mass hold-up m_t and mass flow rate $\dot{m}$. These variations demonstrate that the time to reach the final value $m_t = 2$ of mass hold-up increases dramatically as the holes on the sieve get very small. In Figure 6.6, we explore this in more detail by focusing on a case in which the initial value of mass hold-up is $m_t = 20$ and by showing explicitly how the time t^* to reach a specified (lower) value of mass hold-up varies with spacing Δ (when $\alpha = 1$, $V_n^2 = V_t^2 = V_\tau^2 = 1$, and $e = e_w = .9$). Naturally, the time required to reach a prescribed value of m_t increases as the size of the holes decreases. Interestingly, the time t^* becomes much more sensitive to changes in the spacing as the holes become increasingly close to the size of the particles.
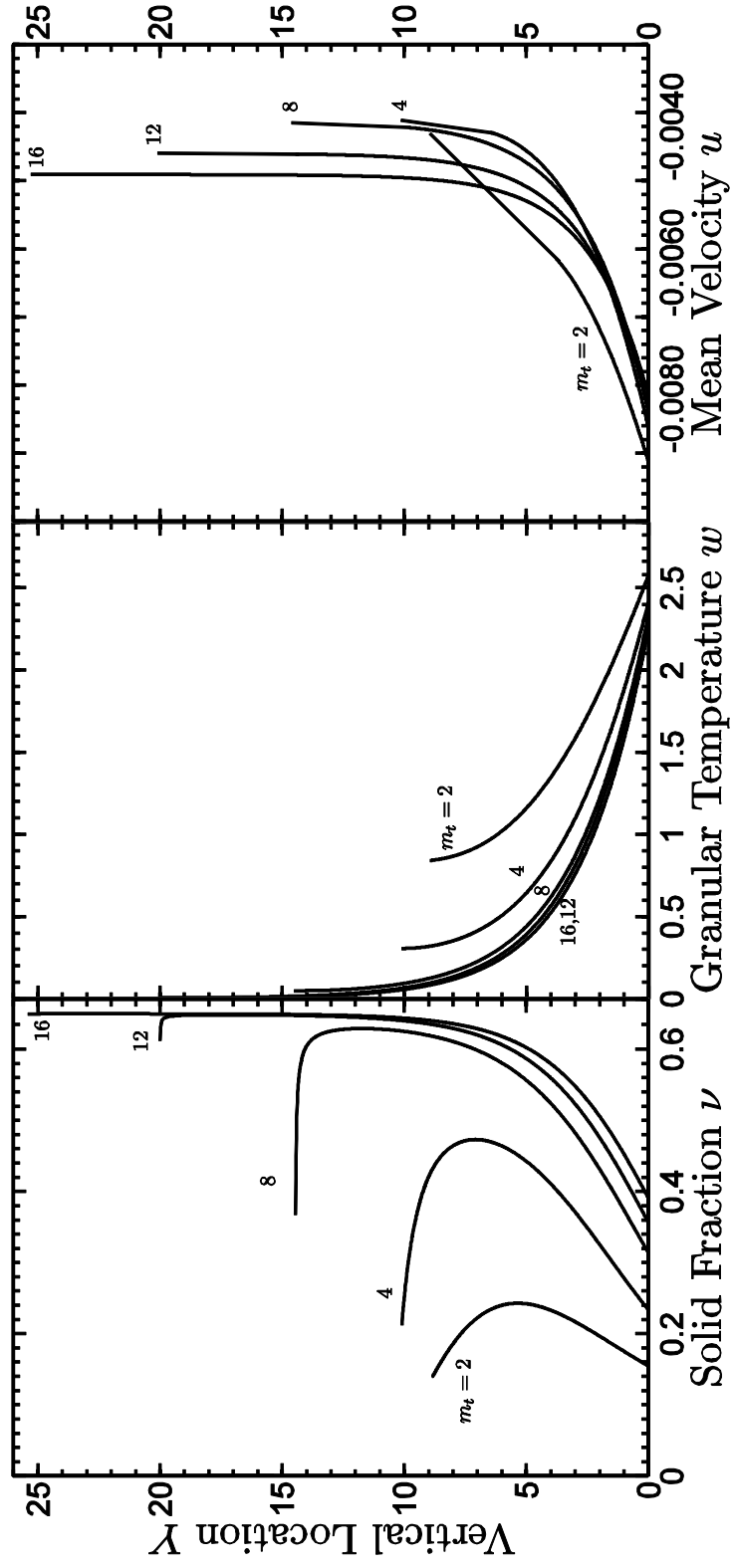
Figure 6.3: The profiles of solid fraction v, granular temperature w, and mean velocity u for mass hold-up $m_t = 2, 4, 8, 12, 16$ when $\alpha = 1$, $V_n^2 = V_t^2 = V_\tau^2 = 1$, $\Delta = 1.1$, and $e = e_w = .9$.
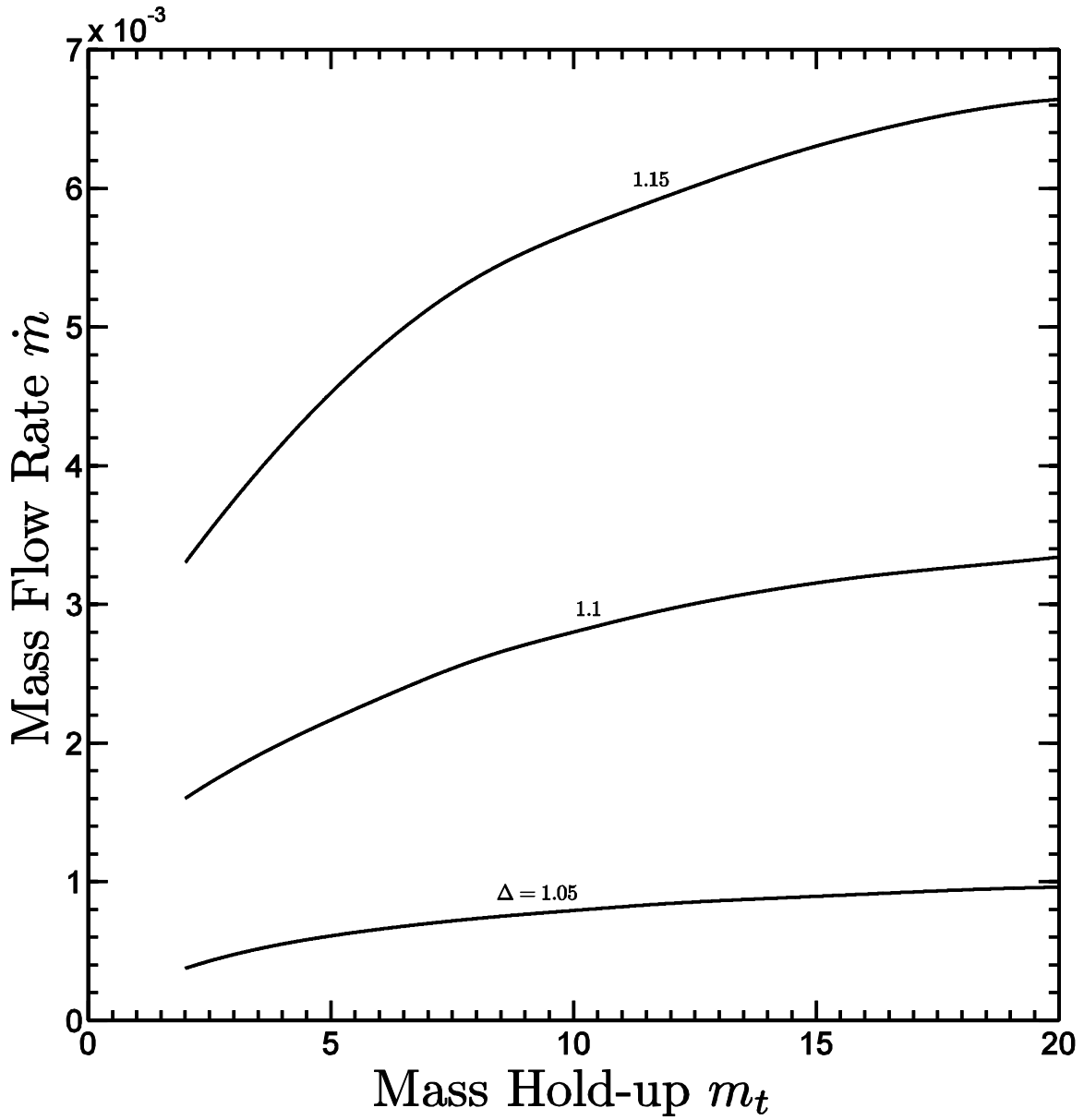
Figure 6.4: The variation of mass flow rate $\dot{m}$ with mass hold-up m_t for spacings $\Delta = 1.05$, $1.1, 1.15$ when $m_t(t = 0) = 20$, $\alpha = 1$, $V_n^2 = V_t^2 = V_\tau^2 = 1$, and $e = e_w = .9$.
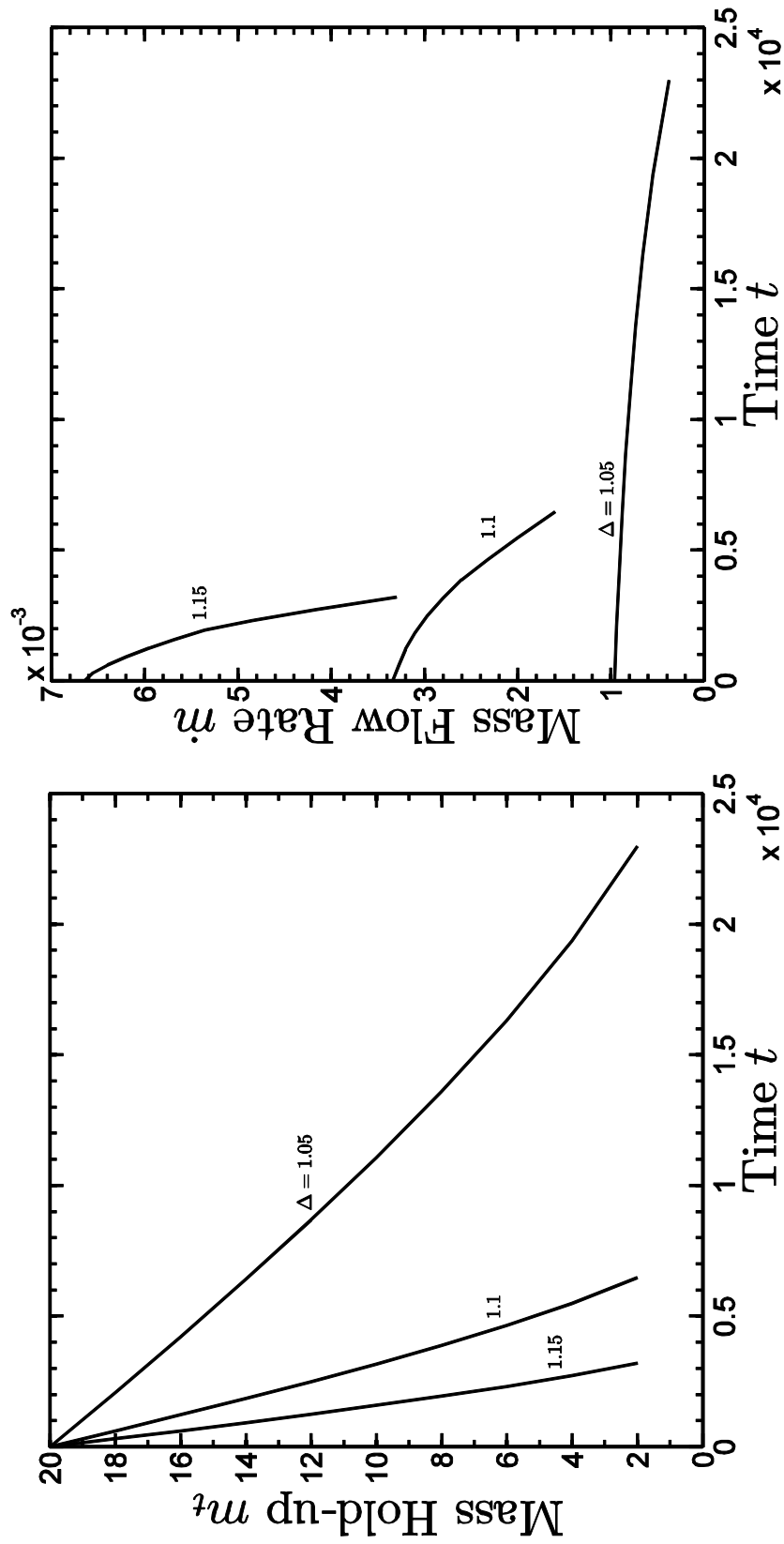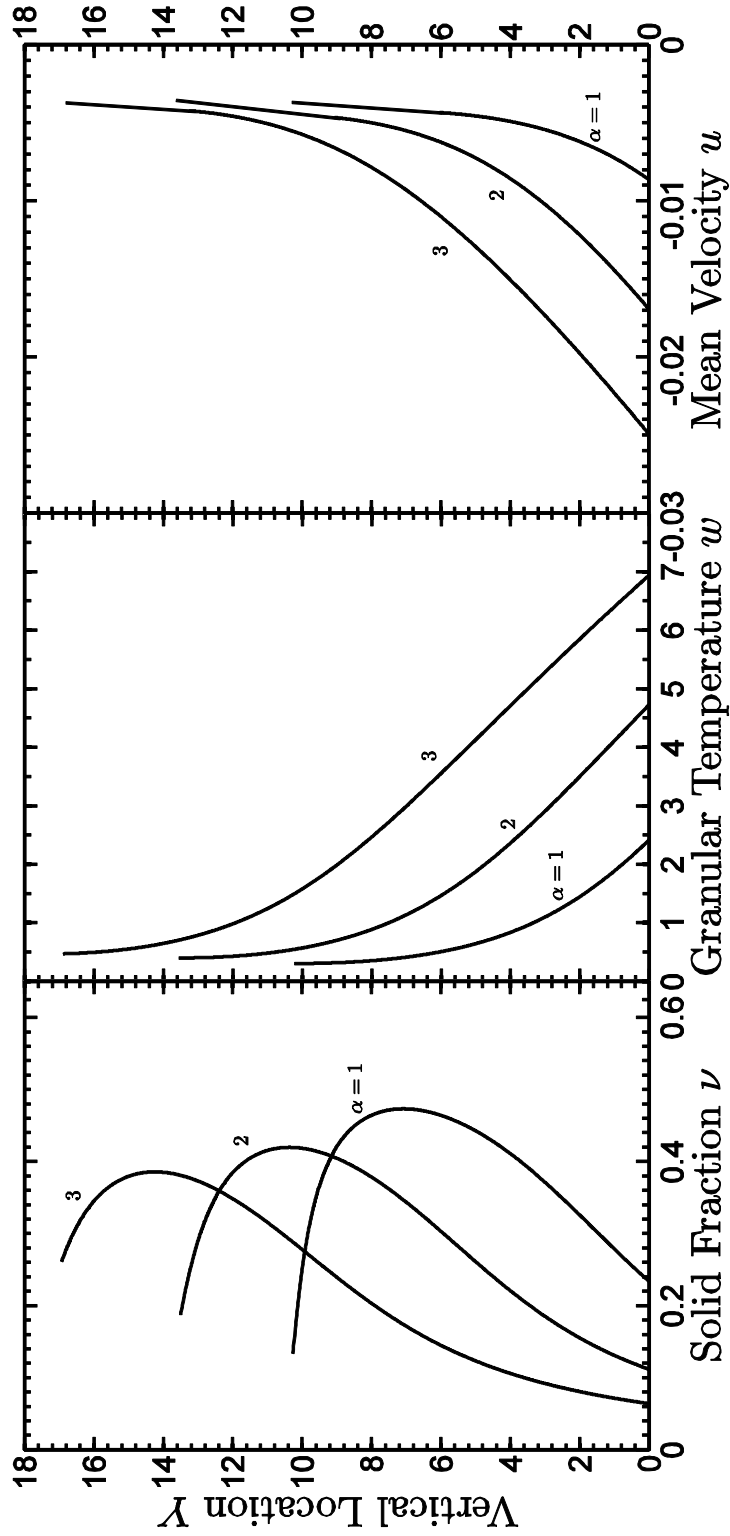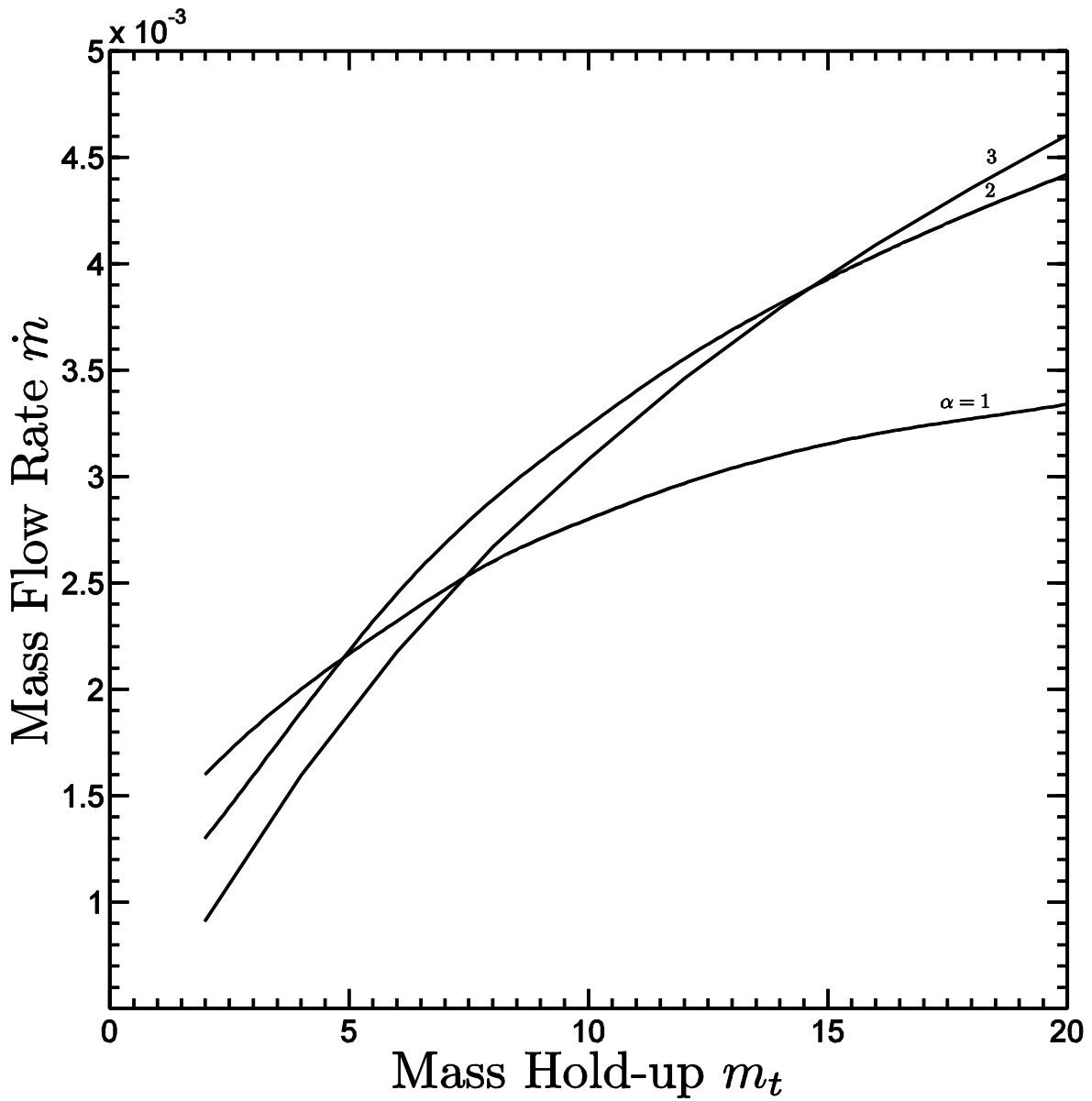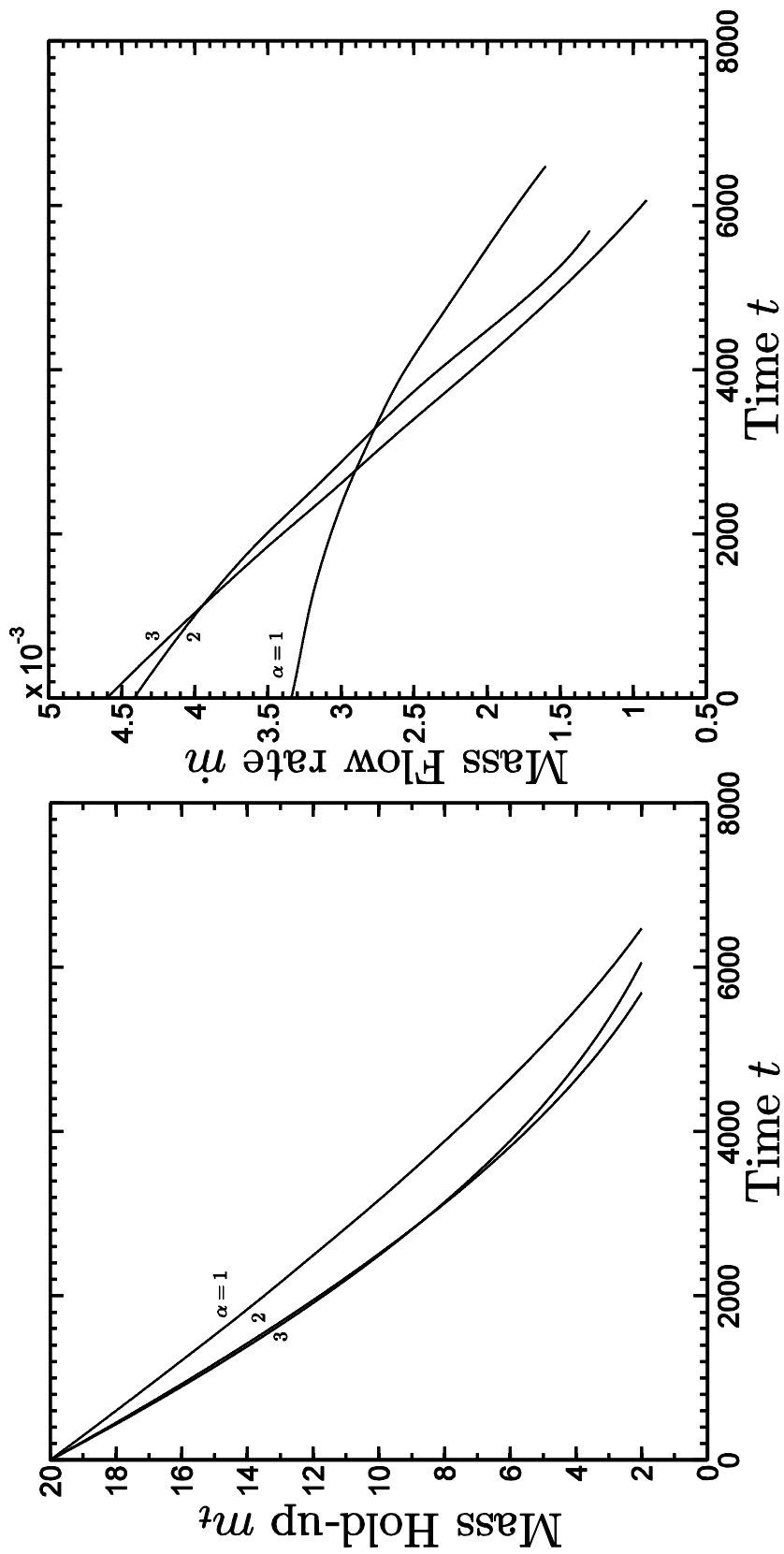
Figure 6.5: The variation of mass hold-up m_t and mass flow rate $\dot{m}$ with time t for spacings $\Delta = 1.05, 1.1, 1.15$ when $m_t(t = 0) = 20$, $\alpha = 1$, $V_n^2 = V_t^2 = V_\tau^2 = 1$, and $e = e_w = .9$.
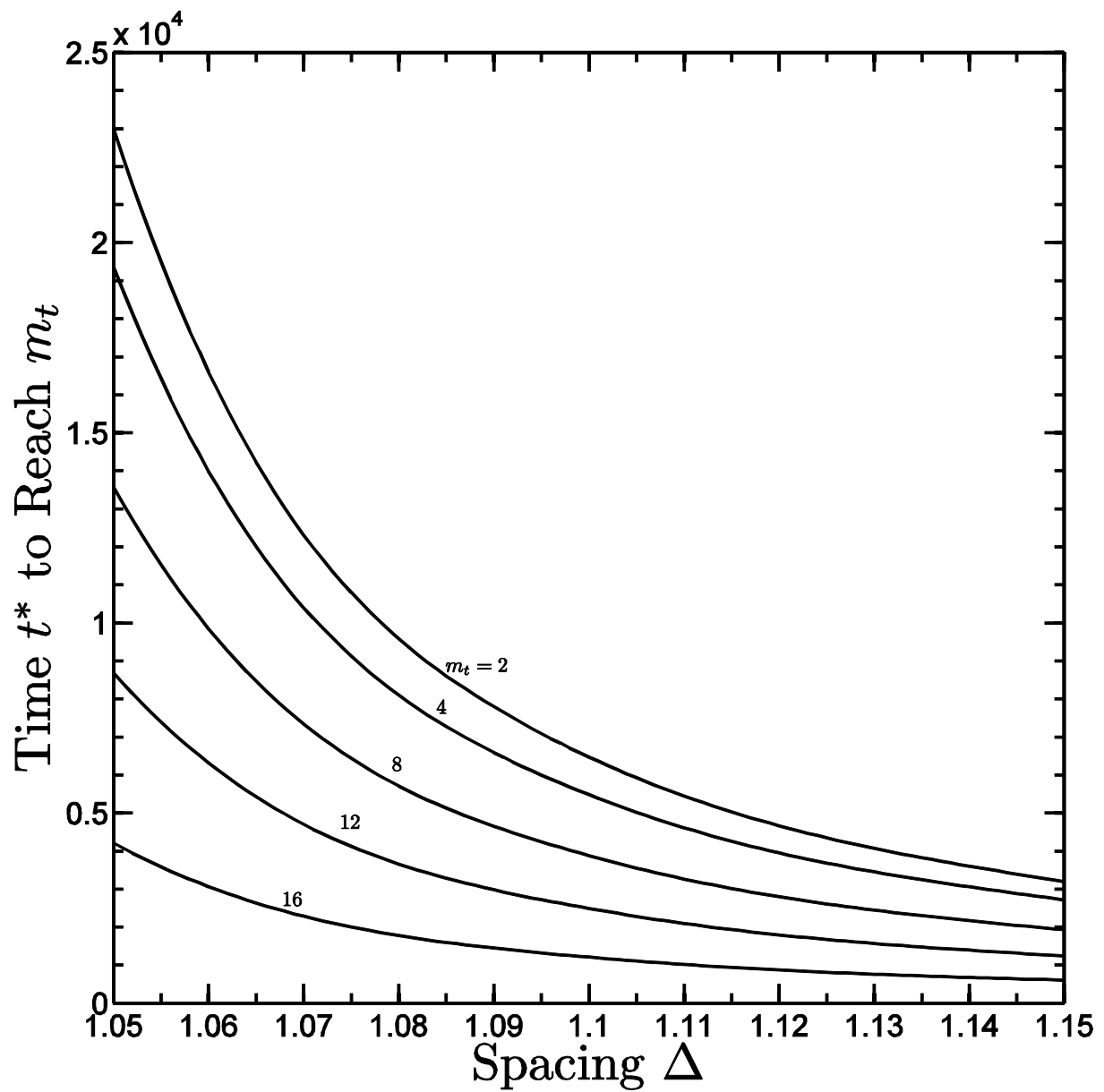
Figure 6.6: The variation of time t^* to reach a prescribed m_t with spacing Δ for mass hold-up $m_t = 2, 4, 8, 12\ 16$ when $m_t(t=0) = 20$, $\alpha = 1$, $V_n^2 = V_t^2 = V_\tau^2 = 1$, and $e = e_w = .9$.

Of particular interest is the effect that different sieve vibrations have on the flows. In Figures 6.7 to 6.12, we explore in a variety of ways how changes in the total vibrational energy α affect the flows. Figure 6.7, for example, shows the (corrected) profiles of solid fraction v, granular temperature w, and mean velocity u for $\alpha = 1, 2,$ and 3 (when $m_t = 4$, $V_n^2 = V_t^2 = V_\tau^2 = 1$, $\Delta = 1$, and $e = e_w = .9$). As might be expected, increasing the total vibrational energy α makes the flows more thermalized, more dilute, and faster. The corresponding variation of the net flow rates is not as clear because decreasing the solid fraction and increasing the mean velocity influence the flow rates in opposite ways.

To explore this further, in Figure 6.8 we show the variation of mass flow rate $\dot{m}$ with mass hold-up m_t (from $m_t = 20$ to $m_t = 2$) for total vibrational energies $\alpha = 1, 2, 3$ (when $V_n^2 = V_t^2 = V_\tau^2 = 1$, $\Delta = 1.1$, and $e = e_w = .9$). For fixed values of α, the flow rates decrease with decreasing mass hold-up. As Figure 6.3 suggests this is because, as the mass hold up decreases from 20 to 2, the decrease in the solid fraction at the sieve is far more dramatic than the corresponding increase in the mean velocity. Perhaps most interestingly, sieves with higher vibrational energies yield higher mass flow rates when the mass hold-up is relatively large, but they yield lower mass flow rates when the mass hold-up is relatively low. These lower flow rates are a result of the very high granular temperatures (and therefore very low solid fractions) that occur on a sieve with high vibrational energy when the mass remaining on the sieve is small. Figure 6.9 shows the corresponding explicit time variations of mass hold-up m_t and mass flow rate $\dot{m}$. Interestingly, of the three values of $\alpha = 1, 2, 3$ chosen, the intermediate value $\alpha = 2$ requires the shortest time reach the final value $m_t = 2$ of mass hold-up. This is another indication that the flow rates are not always enhanced by increasing the vibrational energy of the sieve.

Figure 6.7: The profiles of solid fraction v, granular temperature w, and mean velocity u for vibrational energy $\alpha = 1, 2, 3$ when $V_n^2 = V_t^2 = V_\tau^2 = 1$, $m_t = 4$, $\Delta = 1.1$, and $e = e_w = .9$.

113

Figure 6.8: The variation of mass flow rate $\dot{m}$ with mass hold-up m_t for vibrational energy $\alpha = 1, 2, 3$ when $V_n^2 = V_t^2 = V_\tau^2 = 1$, $m_t(t = 0) = 20$, $\Delta = 1.1$ and $e = e_w = .9$.
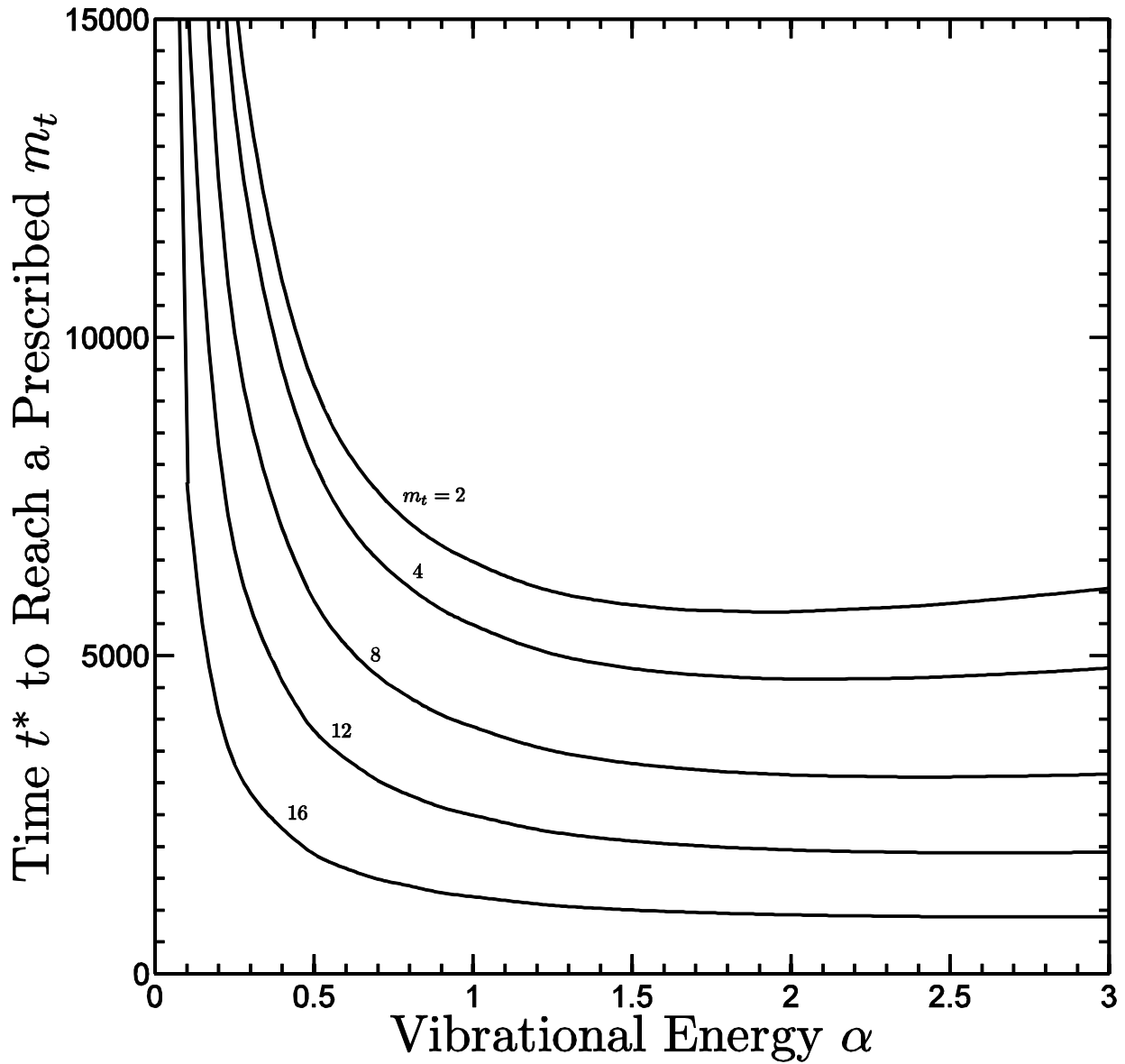
Figure 6.9: The variation of mass hold-up m_t and mass flow rate $\dot{m}$ with time t for vibrational energy $\alpha = 1, 2, 3$ when $V_n^2 = V_t^2 = V_\tau^2 = 1$, $m_t(t = 0) = 20$, $\Delta = 1.1$, and $e = e_w = .9$.

In Figure 6.10, we explore this in more detail by focusing on a case in which the initial value of mass hold-up is $m_t = 20$, and by showing explicitly how the time t^* to reach a specified (lower) value of mass hold-up varies with total vibrational energy α (when $V_n^2 = V_t^2 = V_\tau^2 = 1$, $\Delta = 1.1$, and $e = e_w = .9$). For relatively low values of α, as the total vibrational energy increases from zero, the times required to reach a prescribed value of m_t decrease dramatically. As α continues to increase, the times decrease at much lower rate, and for relatively low values of m_t, the times actually increase with increasing α. This indicates that when sieving at fixed levels of vibrational energy, there is a value of α that will minimize the time to complete the process, however there is an even lower value of α beyond which there will be no appreciable decrease in time required to complete the process.

Interestingly, based on the physics that we have already described, the value of vibrational energy α that maximizes the flow rates at any instant during the sieving process changes with decreasing mass hold-up. In Figure 6.11 we show the variation of mass flow rate $\dot{m}$ with total vibrational energy α for mass hold-ups $m_t = 20, 16, 12, 8, 4$ and 2 (when $V_n^2 = V_t^2 = V_\tau^2 = 1$, $\Delta = 1.1$, and $e = e_w = .9$). For each fixed value of m_t, the dots on the curves correspond to the optimum value α_{opt} of vibrational energy that maximizes the mass flow rate. Below these values, the flows are more dense but slower, and above them, the flows are faster but more dilute.
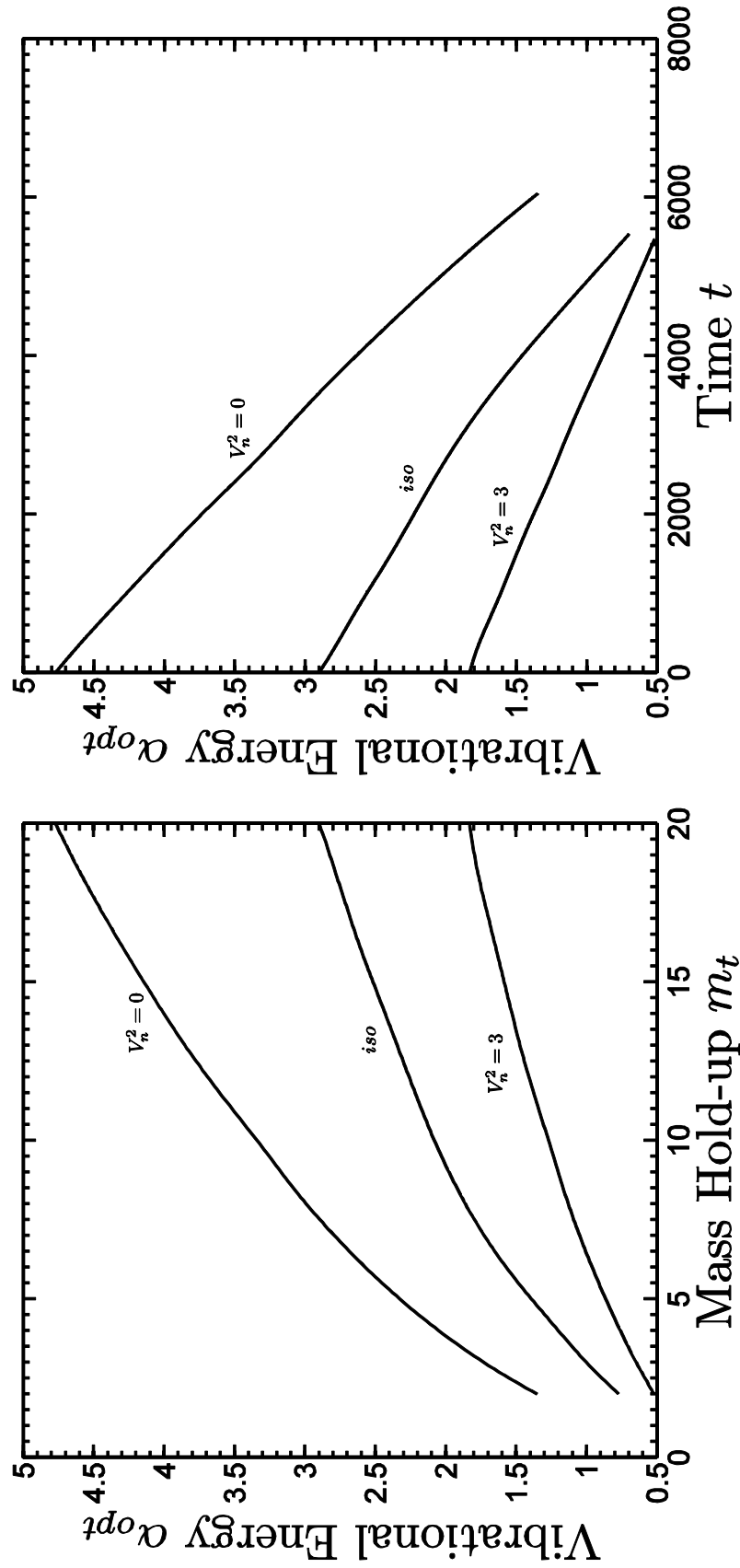
In Figure 6.12 we show the variation of optimum vibrational energy α_{opt} with mass hold-up m_t (left panel) and explicitly with time t (right panel). The three cases shown are for entirely normal vibrations $V_n^2 = 3$, entirely tangential vibrations $V_n^2 = 0$ parallel to one of the fiber directions, and isotropic vibrations $V_n^2 = V_t^2 = V_\tau^2 = 1$ (when m_t is initially 20 and finally 2,

Figure 6.10: The variation of time t^* to reach a prescribed m_t with vibrational energy α for mass hopld-up $m_t = 2, 4, 8, 12\ 16$ when $m_t(t = 0) = 20$, $V_n^2 = V_t^2 = V_\tau^2 = 1$, $\Delta = 1.1$ and $e = e_w = .9$.
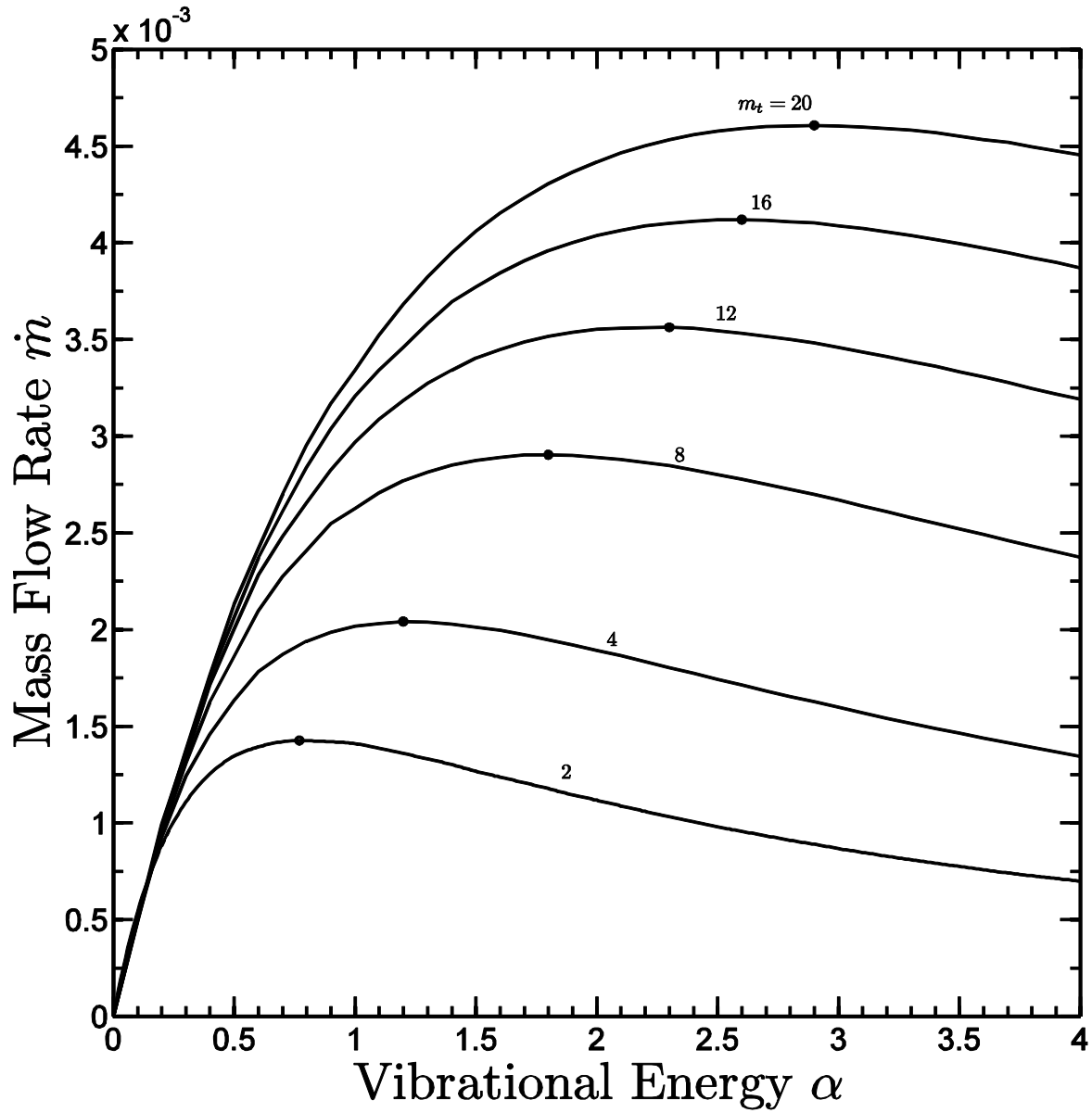
Figure 6.11: The variation of mass flow rate $\dot{m}$ with vibrational energy α for mass hold-up $m_t = 4, 8, 12, 16, 20$ when $V_n^2 = V_t^2 = V_\tau^2 = 1$, $\Delta = 1.1$, and $e = e_w = .9$.
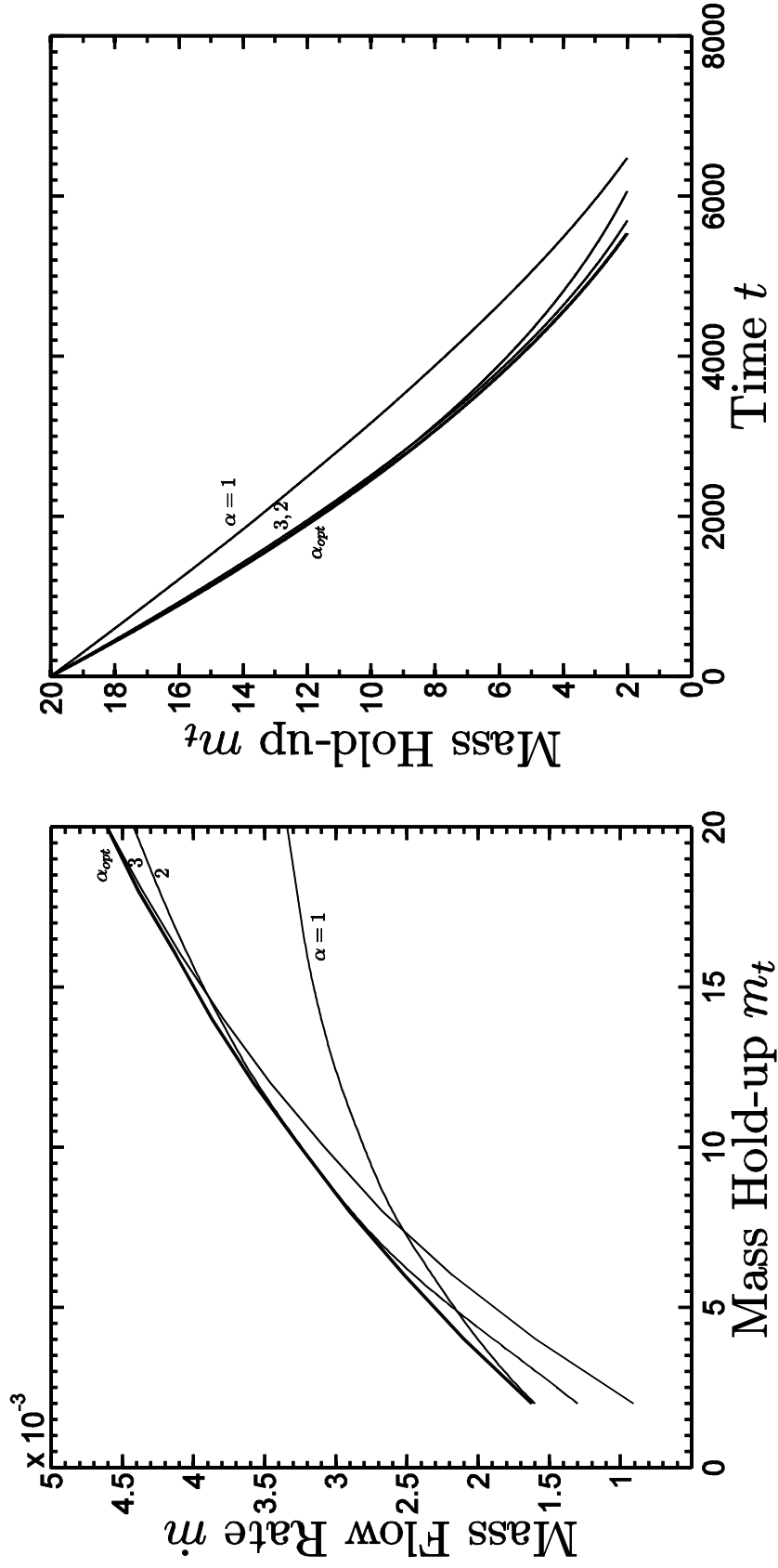
Figure 6.12: The variation of optimum vibrational energy α_{opt} with mass hold-up m_t and time t for degree of normal vibration $V_n^2 = 0, 3$ and for $V_n^2 = V_s^2 = V_t^2 = V_\tau^2 = 1$ when $m_t(t = 0) = 20$, $\Delta = 1$, and $e = e_w = .9$.

119

$\Delta= 1.1$, and $e = e_w = .9$). In all cases, the value of α_{opt} decreases as the mass hold-up decreases (and time increases). If the vibrational energy were not reduced as the mass on the sieve decreased, the assemblies would become overly thermalized and dilute. Figure 6.12 also demonstrates that the total energy required to optimize the flow rates decreases as the vibrational energy is converted from tangential to normal. This is because (on these relatively flat sieves) normal vibrations transfer energy to the flows more effectively than do tangential vibrations.

For completeness, in Figure 6.13, we demonstrate explicitly the advantages (and disadvantages) of vibrating with the optimum energy. In the left panel of Figure 6.13, the curve corresponding to α_{opt} is superposed on a reproduction of Figures 6.8, and in the right panel of Figure 6.13 the curve corresponding to α_{opt} is superposed on a reproduction of the left panel Figure 6.9. At every intermediate value of mass hold-up, the mass flow rate corresponding to vibration energies α_{opt} are highest, and therefore at every intermediate time the remaining mass hold-up is lowest.

We are also interested in predicting how changes in the direction of vibrations affect the sieve flows. In Figures 6.14 to 6.19, we explore in a variety of ways how, for a fixed total vibrational energy, changes in the decomposition of vibrational energy in different directions affect the flows. Figure 6.14, for example, shows the (corrected) profiles of solid fraction ν, granular temperature w, and mean velocity u for $V_n^2 = 0, 1, 2, 3$ (when $\alpha = 1$, $V_\tau^2 = 0$, $m_t = 4$, $m_t = 4$, $\Delta= 1.1$, and $e = e_w = .9$). As the vibrational energy evolves from purely tangential ($V_n^2 = 0$), to purely normal ($V_n^2 = 3$), the flow becomes more dilute, more thermalized, and faster. These effects are similar to those observed when α increases while the directional distribution of energy is fixed, and indicate that normal vibrations are more effective than tangential vibrations at transferring energy to the flow. The corresponding variation of the net

Figure 6.13: The variation of mass flow rate $\dot{m}$ with mass hold-up m_t (left panel), the variation of mass hold-up m_t with time t (right panel) for vibrational energy $\alpha = 1, 2, 3, \alpha_{opt}$ when $V_n^2 = V_t^2 = V_\tau^2 = 1$, $m_t(t = 0) = 20$, $\Delta = 1.1$ and $e = e_w = .9$.
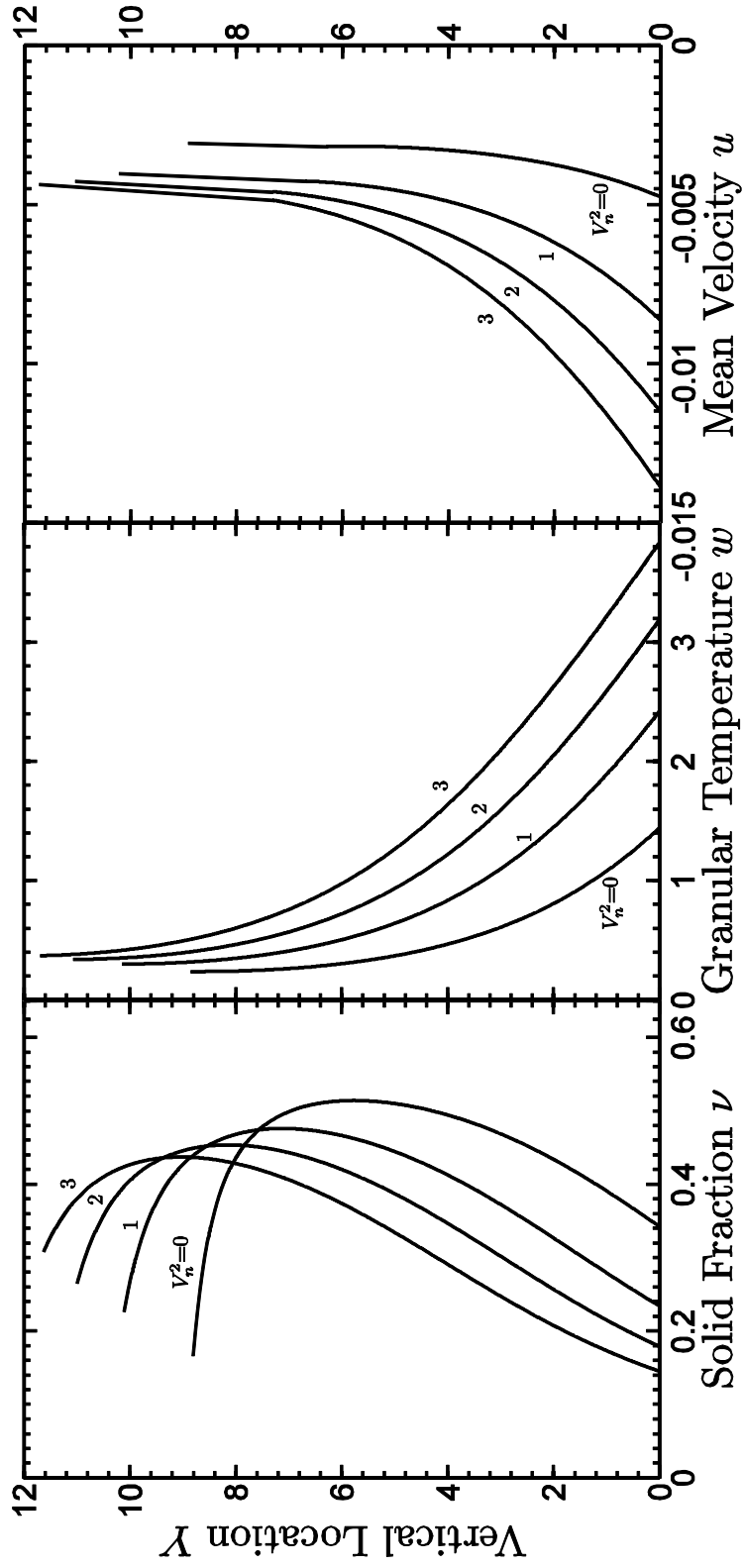
Figure 6.14: The profiles of solid fraction ν, granular temperature w, and mean velocity u for degree of normal vibration $V_n^2 = 0, 1, 2, 3$ when $\alpha = 1$, $V_\tau^2 = 0$, $m_t = 4$, $\Delta = 1.1$, and $e = e_w = .9$.

flow rates is not as clear because decreasing the solid fraction and increasing the mean velocity influence the flow rates in opposite ways.

To explore the flow rates further, in Figure 6.15 we show the variation of mass flow rate $\dot{m}$ with mass hold-up m_t (from $m_t = 20$ to $m_t = 2$) for degree of vertical vibrations $V_n^2 = 0, 1, 2, 3$ (when $\alpha = 1$, $V_\tau^2 = 0$, $\Delta = 1.1$, and $e = e_w = .9$). As we have already seen in Figure 6.8, the flow rates decrease with decreasing mass hold-up. Perhaps most interestingly, sieves with higher vibrational components in the normal direction yield higher mass flow rates when the mass hold-up is relatively large, but this effect diminishes as the mass hold up decreases, and even reverses at the lowest values of m_t. This is because the normal vibrations more effectively transfer energy to the flow. Consequently, at lower values of mass hold-up, they induce relatively high granular temperatures, relatively low solid fractions at the sieve, and correspondingly low flow rates. This indicates that for a fixed total energy of vibration, the flow rates are not always maximized by purely normal vibrations. Figure 6.16 shows the corresponding explicit time variations of mass hold-up m_t and mass flow rate $\dot{m}$.
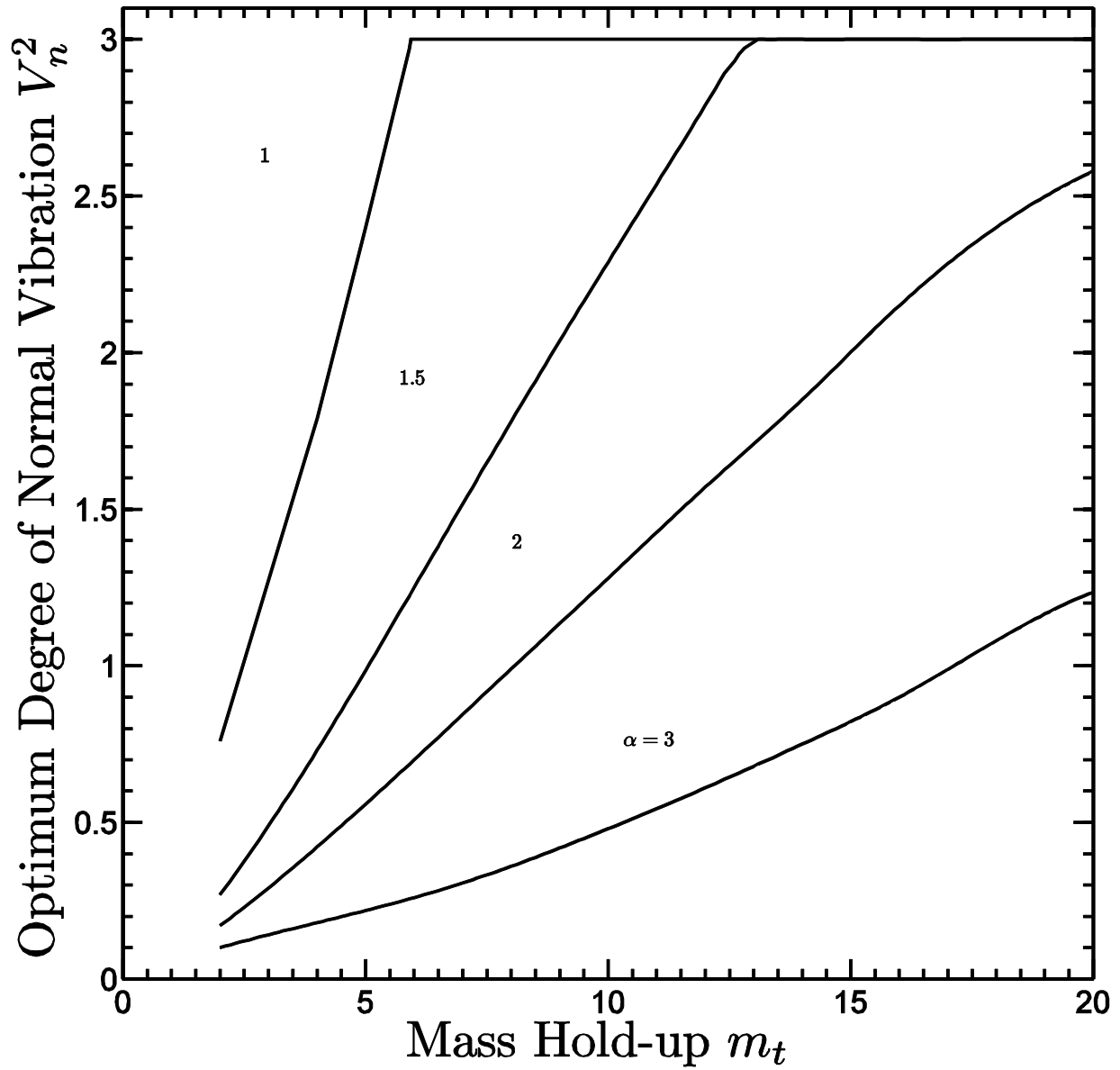
In Figure 6.17 we show the variation with mass hold-up m_t of *optimum* degree of normal vibrations V_n^2 that instantaneously maximizes the flow rate for $\alpha = 1, 1.5, 2,$ and 3 (when $V_\tau^2 = 0$, $\Delta = 1.1$, and $e = e_w = .9$). When the mass hold-up is relatively high and the total vibrational energy is relatively low, the flow rates are enhanced by increasing the energy transferred to them. In these cases, the flow rates are maximized by purely normal vibrations ($V_n^2 = 3$). However, as either the mass hold-up decreases or the total vibrational energy increases, the flows are already quite thermalized and dilute. Under these circumstances, the flow rates are no longer enhanced by more energy transferred to them. Therefore they are maximized
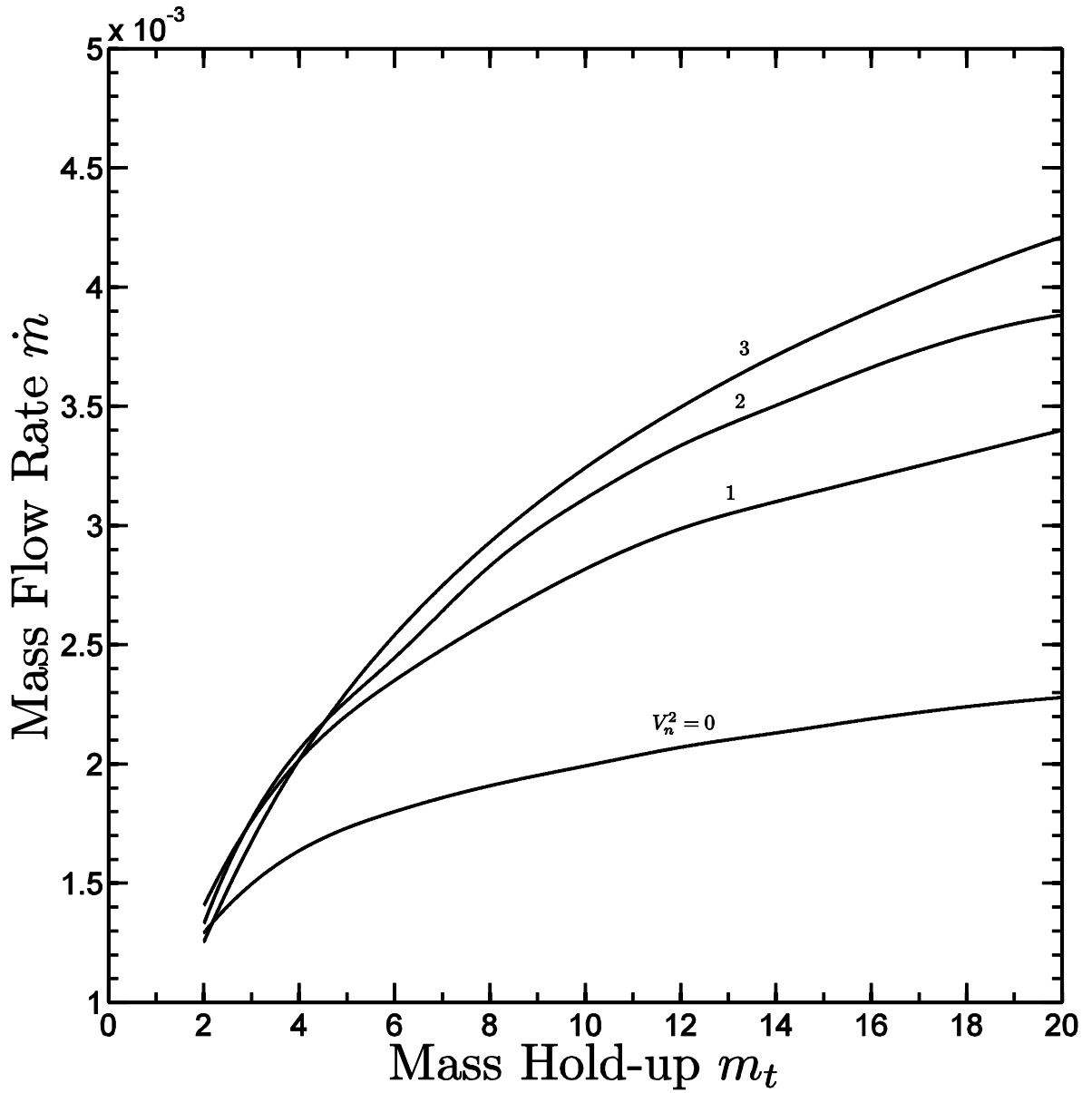
Figure 6.15: The variation of mass flow rate $\dot{m}$ with mass hold-up m_t for degree of normal vibration $V_n^2 = 0, 1, 2, 3$ when $\alpha = 1$, $m_t(t=0) = 20$, $\Delta = 1$, and $e = e_w = .9$.
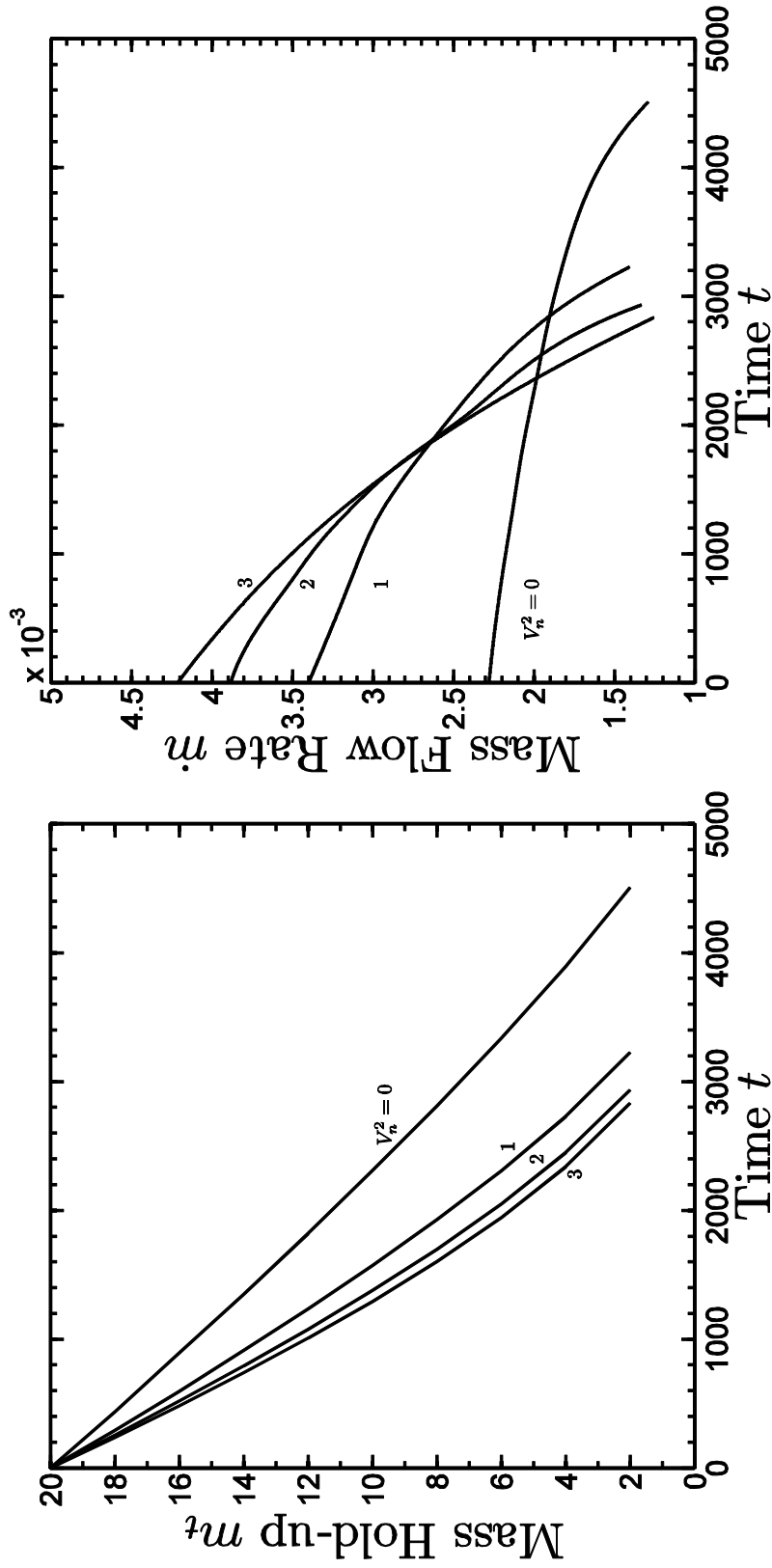
Figure 6.16: The variation of mass hold-up m_t and mass flow rate $\dot{m}$ with time t for degree of normal vibration $V_n^2 = 0, 1, 2, 3$ when $\alpha = 1$, $m_t(t = 0) = 20$, $\Delta = 1$, and $e = e_w = .9$.
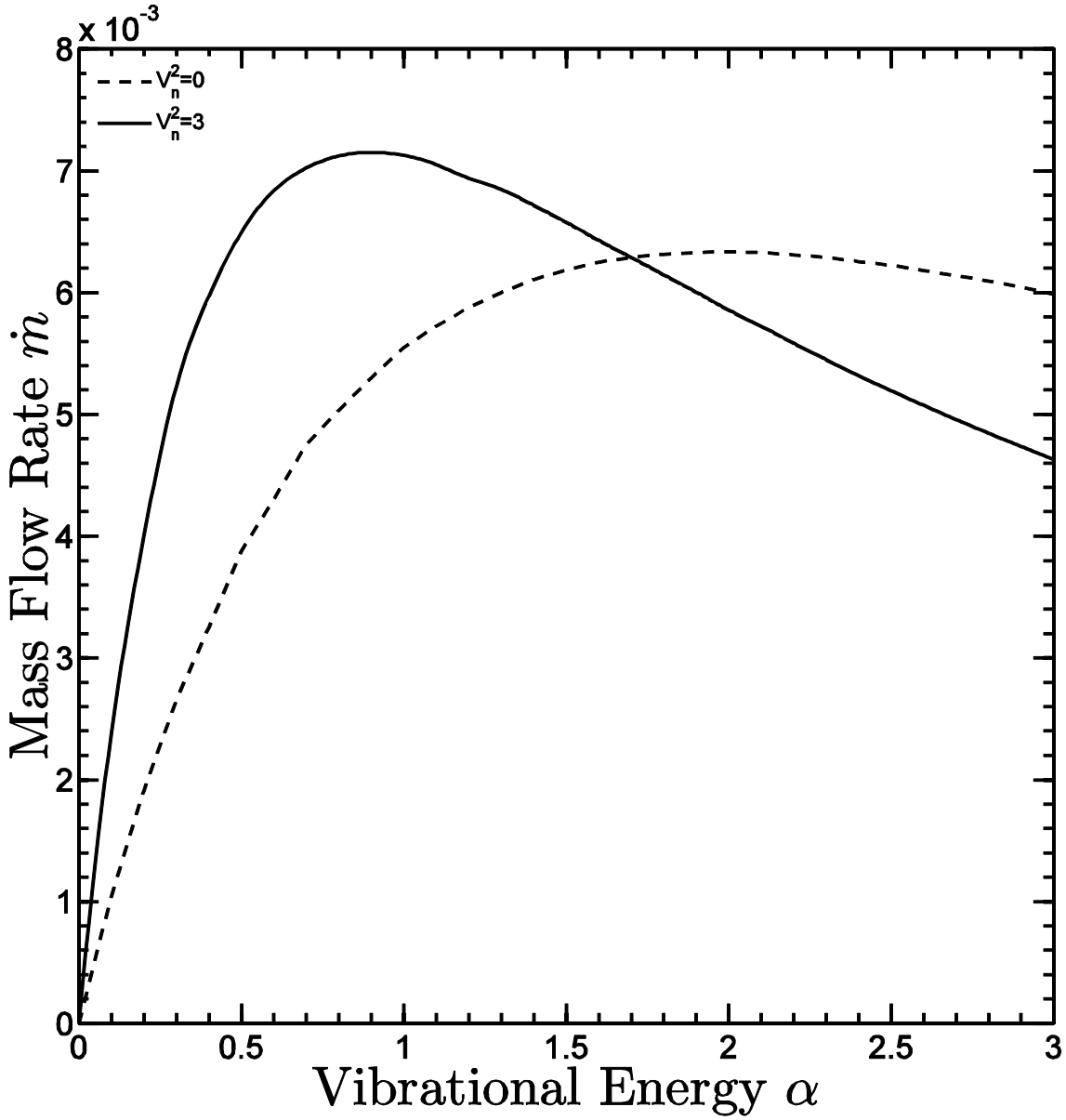
Figure 6.17: The variation of optimum degree of normal vibration V_n^2 with mass hold-up m_t for vibrational energy $\alpha = 1, 1.5, 2, 3$ when $\Delta = 1.1$, $m_t(t = 0) = 20$, and $e = e_w = .9$.

126

by converting some of the normal vibrational energy to tangential energy, and the optimum value of V_n^2 is less than 3.

To examine this phenomenon more closely, in Figure 6.18 we focus on the moment at which $m_t = 4$ and show the variation of mass flow rate $\dot{m}$ with total vibrational energy α for degree of vertical vibrations $V_n^2 = 3$ and $V_n^2 = 0$ (when $V_\tau^2 = 0$, $\Delta = 1.2$, and $e = e_w = .9$). When α is relatively low, the flows are enhanced by adding energy so that purely normal vibrations result in higher mass flow rate. But at higher values of α, the flows are already highly thermalized and dilute so that purely tangential vibrations result in higher mass flow rates.

In Figure 6.19, we focus on a case in which the initial value of mass hold-up is $m_t = 20$ and show explicitly how the time t^* to reach a specified (lower) value of mass hold-up varies with normal vibrational energy V_n^2 (when $\alpha = 1, V_\tau^2 = 0, \Delta_t = \Delta_\tau = 1.1$, and $e = e_w = .9$). Although converting tangential vibrational energy to normal energy does not necessarily maximize flow rates at all times, the *overall* time required to reach a lower value of mass hold-up decreases with increasing normal component V_n^2.

As a final study, in Figures 6.20 to Figures 6.22 we demonstrate how the effects of tangential vibrations in the t- and τ-directions differ when the corresponding spacings Δ_t and Δ_τ are unequal. In Figure 6.20, for example, we consider the hypothetical case in which $\Delta_t = 1.1$ and $\Delta_\tau = 1.2$ and show the (corrected) profiles of solid fraction v, granular temperature w, and mean velocity u in eight different cases of two-dimensional vibrations: the solid curves correspond to tangential vibrations $V_t^2 = 0, 1, 2, 3$ while $V_\tau^2 = 0$ (so that $V_n^2 = 3 - V_t^2$); and dashed curves correspond to tangential vibrations $V_\tau^2 = 0, 1, 2, 3$ while $V_t^2 = 0$ (so that $V_n^2 = 3 - V_\tau^2$). In all cases, $\alpha = 1$, $m_t = 4$, $e = e_w = .9$. Because the spacing Δ_t in the t-direction is *smaller* than the spacing Δ_τ in the τ-direction, more collisions between the flow particles and the sieve are

Figure 6.18: The variation of mass flow rate $\dot{m}$ with vibrational energy α for degree of normal vibration $V_n^2 = 0, 3$ when $\Delta = 1.2$, $m_t = 4$, and $e = e_w = .9$.
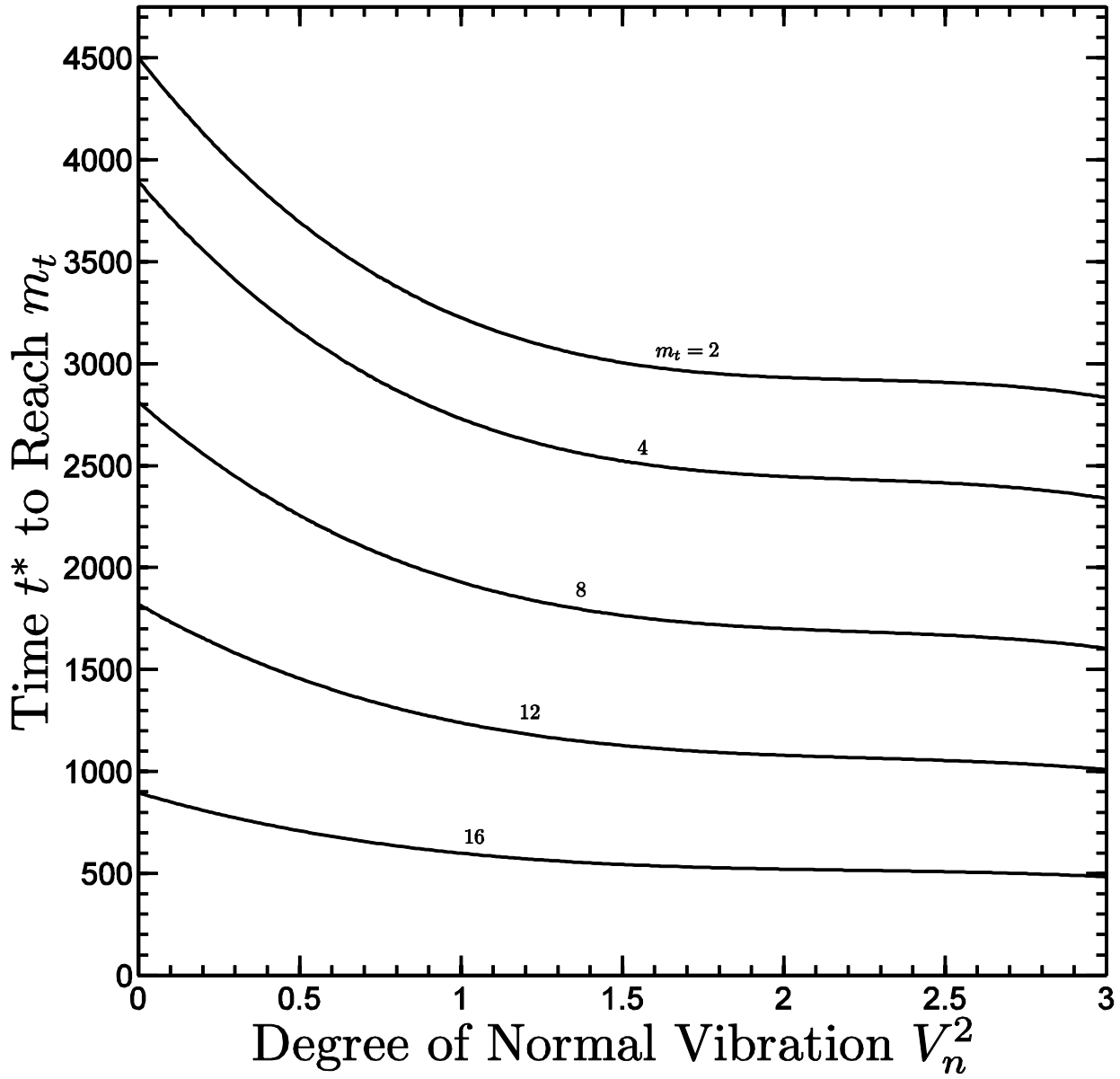
Figure 6.19: The variation of time t^* to reach a prescribed m_t with degree of normal vibration V_n^2 for mass hold-up $m_t = 2, 4, 8, 12 \ 16$ when $m_t(t=0) = 20$, $\alpha = 1$, $\Delta = 1$, and $e = e_w = .9$.
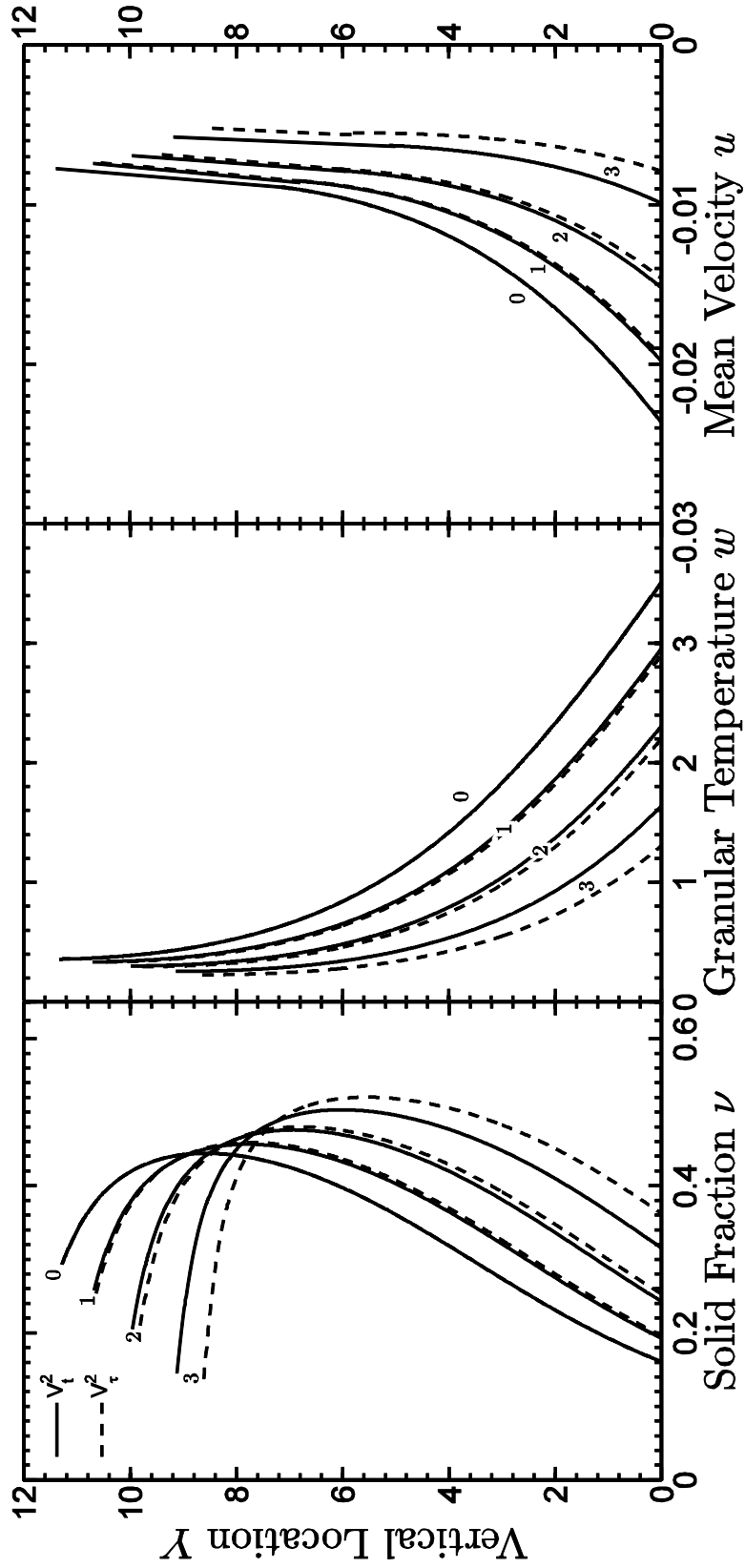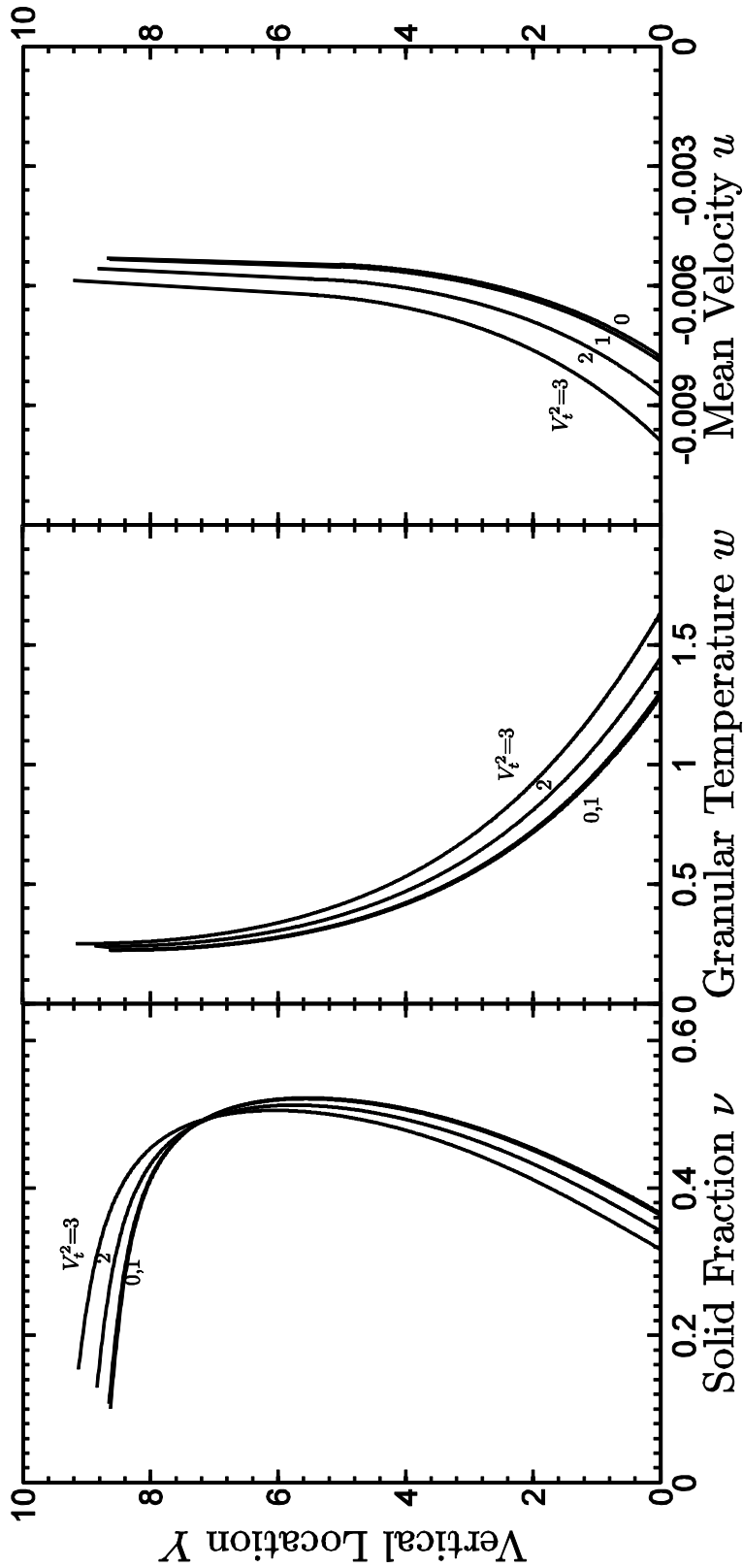
Figure 6.20: The profiles of solid fraction v, granular temperature w, and mean velocity u for degree of tangential vibration $V_t^2 = 0, 1, 2, 3$, and $V_\tau^2 = 0, 1, 2, 3$ when $\Delta_t = 1.1$, $\Delta_\tau = 1.2$, $m_t = 4$, $\alpha = 1$, and $e = e_w = .9$.

induced by vibrations in the t-direction than by vibrations of the same intensity in the τ-direction. Consequently, the flows for tangential vibrations $V_t^2 = 1, 2, 3$ in the t-direction are more thermalized, more dilute, faster, and deeper than the corresponding flows for tangential vibrations $V_\tau^2 = 1, 2, 3$ in the τ-direction. (When $V_\tau^2 = V_t^2 = 0$, the vibrations are entirely normal and the flows in both cases are identical.) These effects are not extremely pronounced because the difference between Δ_t and Δ_τ is small and the sieve is not very bumpy. Of course, both the solid and dashed set of profiles demonstrate that when the vibrational energy evolves from purely tangential to purely normal, the flow becomes deeper, more dilute, more thermalized, and faster.

In Figure 6.21, we again focus on the case of unequal spacing in which $\Delta_t = 1.1$ and $\Delta_\tau = 1.2$ (when $\alpha = 1$, $m_t = 4$, $e = e_w = .9$). The (corrected) profiles of solid fraction ν, granular temperature w, and mean velocity u are shown in four different cases of purely tangential (i.e. $V_n^2 = 0$) vibrations in which the vibrations in one tangential direction are gradually converted to the other: $V_t^2 = 0, 1, 2, 3$ (while in each case $V_\tau^2 = 3 - V_t^2$). Because the spacing Δ_t is *smaller* than Δ_τ, more collisions between the flow particles and the sieve are induced by vibrations in the t-direction than by vibrations of the same intensity in the τ-direction. Consequently, as the energy of vibration is converted from the t-direction to the τ-direction, the flows become less thermalized, less dilute, slower, and more shallow. These effects are not extremely pronounced because the difference between Δ_t and Δ_τ is small and the sieve is not very bumpy.

Finally, in the same case of unequal spacing ($\Delta_t = 1.1$ and $\Delta_\tau = 1.2$), Figure 6.22 compares how the resulting mass flow rates $\dot{m}$ vary with total vibrational energy α for two purely one-dimensional cases of tangential vibrations: $V_t^2 = 3$ and $V_\tau^2 = 3$ (when $m_t = 4$, and

Figure 6.21: The profiles of solid fraction v, granular temperature w, and mean velocity u for degree of tangential vibration $V_t^2 = 0, 1, 2, 3$ when $V_n^2 = 0$, $\Delta_t = 1.1$, $\Delta_\tau = 1.2$, $m_t = 4$, $\alpha = 1$, and $e = e_w = .9$.
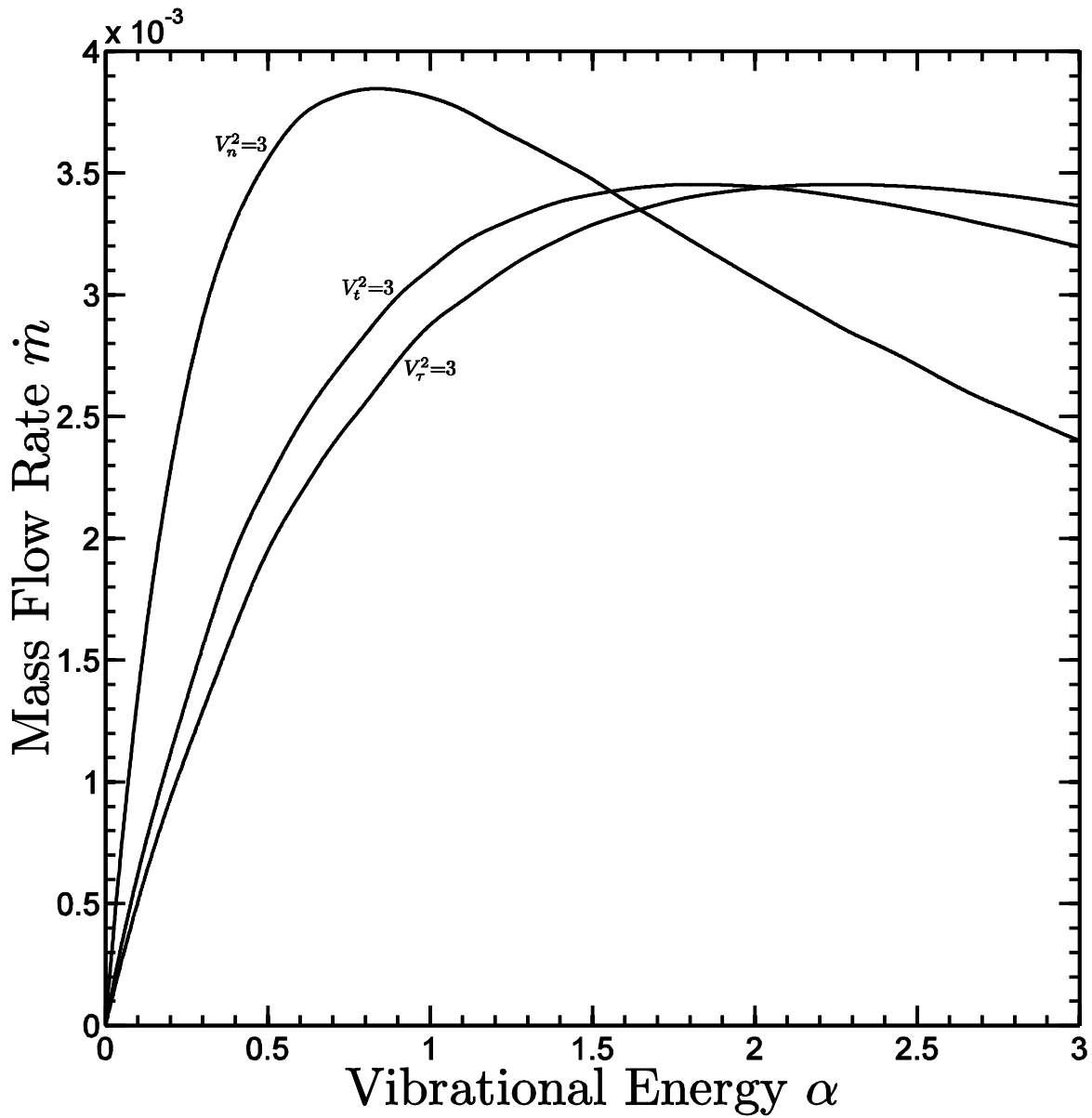
Figure 6.22: The variation of mass flow rate $\dot{m}$ with vibrational energy α for direction of vibration $V_n^2 = 3$, $V_\tau^2 = 3$, and $V_t^2 = 3$ when $\Delta_t = 1.1$, $\Delta_\tau = 1.2$ $m_t = 4$, and $e = e_w = .9$

$e = e_w = .9$ in both cases). For low values of vibrational energy α, the flows are relatively slow and unthermalized, and are more efficiently enhanced by the vibrations that more effectively transfer energy to the flow. For high values of α, the flows are highly thermalized and dilute, and are less efficiently enhanced by the vibrations that more effectively transfer energy to the flow. Consequently, when α is low the flow rates are higher due to shaking in the direction in which the spacing is smallest ($V_t^2 = 3$), and when α is high the flow rates are higher due to shaking in the direction in which the spacing is largest ($V_\tau^2 = 3$). Also shown for reference is the corresponding flow rates induced by purely normal vibrations $V_n^2 = 3$, which (for the same reasons) enhance the flows more effectively (than tangential vibrations) when α is low, and less effectively when α is high.

Chapter 7

Vibratory Sieving and Segregation of Binary Mixtures

In this chapter we focus attention on assemblies of binary granular mixtures that are thermalized by and flow through vibrating sieves. The goal is to use the boundary conditions derived in Chapter 5 for such mixtures in combination with the relatively simple flow theory of Jenkins and Mancini [1987] to predict the behavior of the mixture as it passes through the sieve. Of particular interest is the dependence of this behavior on the vibrations of the sieve. As a special case, when the holes in the sieve are too small to allow any particles to pass through, we will focus entirely on particle segregation induced by boundary vibrations. This case is important in sieving, because even when the holes are large enough to allow particles through, the assemblies that remain on the sieve at any time are segregated in much the same way.

7.1 Governing Equations

The mixtures consist of smooth, inelastic spheres of diameters σ_A and σ_B, masses m_A and m_B, and coefficients of restitution e_{AA} for collisions between two particles of species A, e_{BB} for collisions between two of species B, and e_{AB} for collisions between species. Generally, subscript A refers to the smaller particles and subscript B refers to the larger particles. The important size ratios are defined by

$$r_i \equiv \frac{\sigma_i}{\sigma_A} \qquad \text{and} \qquad r \equiv \frac{\sigma_B}{\sigma_A} \qquad (i = A, B) \qquad (7.1)$$

The mass density of each particle are given by ρ_{pA} and ρ_{pB}. The definitions of the mean fields relevant to such mixtures are given in Section 5.1.

The mixtures are confined from above by the downward force of gravity, and thermalized from below a horizontal vibrating sieve. The vibrating boundaries have no mean velocity. The vibrations induce flow normal to (and through) the sieve, but the phase of the vibrations is taken such that no tangential velocities are induced. We introduce an $x_1 - x_2 - x_3$ Cartesian coordinate system in which the x_2- direction is in the normal N-direction, and x_1- and x_3- directions are parallel to the fibers of the sieve in the t- and τ-directions. The right-handed triad $N - t - \tau$ is shown on the sieve in Figures 5.2/7.1.
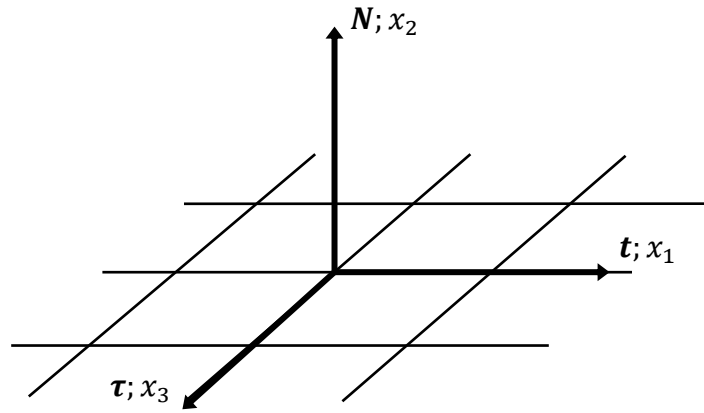
Figure 7.1: Cartesian coordinate system

In what follows we focus on number densities rather than on solid fractions, and introduce dimensionless number densities $n_A \equiv \eta_A \pi \sigma_A^3/6$ and $n_B \equiv \eta_B \pi \sigma_A^3/6$, which are *both* scaled by the volume $\pi \sigma_A^3/6$ of the *smaller* particles. The corresponding solid fractions for each species are $v_A = n_A$ and $v_B = r^3 n_B$. In addition, we introduce the characteristic velocity a and define the dimensionless normal velocities $u_A \equiv u_{2A}/a$, and $u_B \equiv u_{2B}/a$, the dimensionless granular temperature T as its dimensional counterpart (defined by equation (5.10)) scaled by $m_A a^2$, the dimensionless normal pressure $P \equiv P_{22}/(\rho_{pA} a^2)$, the dimensionless energy flux $Q \equiv q_2/(\rho_{pA} a^3)$, and dimensionless energy dissipation $\Gamma \equiv \sigma_A \gamma/(\rho_{pA} a^3)$. The dimensionless

coordinate Y is defined as x_2/σ_A. In this chapter we take the characteristic velocity to be $a = (\sigma_A g)^{1/2}$.

We focus on cases in which the holes on the sieve are sufficiently small to yield flow rates and mean velocities that are also small. Under these circumstances, the results of Chapter 6 demonstrate that the number densities and granular temperature are quasi-steady in the sense that they can be calculated as steady solutions based on the instantaneous values of the mass hold-ups m_{tA} and m_{tB} for each species, which themselves varies gradually in time. The mean velocities do not affect these solutions, and are calculated to satisfy the higher order balance of mass based on the lower order approximations for the number densities and solid fraction. Under these circumstances n_A, n_B, and T depend explicitly only on Y and implicitly on time through m_{tA} and m_{tB}. The mean velocities u_A and u_B then depend on n_A, n_B, and T.

The simple flow theory of Jenkins and Mancini [1987] consists of mass balances for each species, momentum balances for each species, and a single energy balance for the entire mixture. The corresponding mean fields are n_A, n_B, u_A, u_B, and T. The balance of mass for each species is satisfied identically at lowest order.

The momentum equations are written as the sum (for the whole mixture) and the difference of the corresponding equations for each species. With no mean motion in the tangential direction, the x_1- components of the momentum balances are identically satisfied. The x_2- component for the whole mixture is

$$P' = -\tilde{g}(n_A + n_B r^3) \quad , \tag{7.2}$$

where the prime denote differentiation with respect to Y, and $\tilde{g} \equiv \sigma_A g/a^2$ is equal to 1 when $a = (\sigma_A g)^{1/2}$. The x_2- component of the difference in momentum equations for each species can be written as,

$$\frac{n_B r^3}{(n_A + n_B r^3)T} \left[T(n_A + K_{AA} + K_{AB}) \right]' - \frac{n_A}{(n_A + n_B r^3)T} \left[T(n_B + K_{AB} + K_{BB}) \right]'$$

$$+ K_{AB} \left[\left(\frac{1 - r^3}{1 + r^3} \right) (lnT)' + \left(ln\frac{n_B}{n_A} \right)' \right] = 0 \quad , \tag{7.3}$$

where the terms K_{ik} are defined by,

$$K_{ik} \equiv \frac{(1 + e_{ik})}{4} g_{ik} \frac{(\sigma_i + \sigma_k)^3}{\sigma_A^3} n_i n_k \qquad (i = A, B \text{ and } k = A, B) \quad , \tag{7.4}$$

in which g_{ik} is given in terms of the solid volume fraction v for the mixture,

$$v \equiv n_A + n_B r^3 \quad , \tag{7.5}$$

by

$$g_{ik} = -\frac{1}{1 - v} + 3\frac{r_i r_k}{(r_i + r_k)} \cdot \frac{(n_A + n_B r^2)}{(1 - v)^2} + 2\left(\frac{r_i r_k}{r_i + r_k} \right)^2 \cdot \frac{(n_A + n_B r^2)^2}{(1 - v)^3} \quad . \tag{7.6}$$

Equation (7.3) is Fick's Law for the mixture. The constitutive relation for the normal pressure P for the whole mixture is

$$P = (n_A + n_B + K_{AA} + 2K_{AB} + K_{BB}) T \quad . \tag{7.7}$$

In order to write equation (7.2) and (7.3) in a form more easily used for numerical integration, we employ equation (7.7) to eliminate P from momentum equation (7.2), and write the result in the form:

$$\chi_{11} n_A' + \chi_{12} n_B' = \beta_1 \quad , \tag{7.8}$$

where the coefficients χ_{11} and χ_{12} depend on n_A and n_B according to

$$\chi_{11} = 1 + \frac{\partial K_{AA}}{\partial n_A} + 2\frac{\partial K_{AB}}{\partial n_A} + \frac{\partial K_{BB}}{\partial n_A} \quad , \tag{7.9}$$

and

$$\chi_{12} = 1 + \frac{\partial K_{AA}}{\partial n_B} + 2\frac{\partial K_{AB}}{\partial n_B} + \frac{\partial K_{BB}}{\partial n_B} \quad , \tag{7.10}$$

in which K_{ik} are given by equation (7.4), and where the coefficient β_1 depends on n_A, n_B, and T' according to

$$\beta_1 = -\frac{1}{T}[(n_A + n_B + K_{AA} + 2K_{AB} + K_{BB})\, T' + \tilde{g}(n_A + n_B r^3)] \quad . \tag{7.11}$$

In addition, we employ the momentum balance (7.2) to rewrite Fick's Law (7.3) in the from

$$\chi_{21} n'_A + \chi_{22} n'_B = \beta_2 \quad , \tag{7.12}$$

where the coefficients χ_{21} and χ_{22} depend on n_A and n_B according to

$$\chi_{21} = 1 + \frac{\partial K_{AA}}{\partial n_A} + \frac{\partial K_{AB}}{\partial n_A} - \frac{K_{AB}}{n_A} \quad , \tag{7.13}$$

and

$$\chi_{22} = \frac{\partial K_{AA}}{\partial n_B} + \frac{\partial K_{AB}}{\partial n_B} + \frac{K_{AB}}{n_B} \quad . \tag{7.14}$$

In which K_{ik} are given by equation (7.4), and where the coefficient β_2 depends on n_A, n_B, and T' according to

$$\beta_2 = -\frac{1}{T}\left[(n_A + K_{AA} + K_{AB})\, T' + K_{AB}\left(\frac{1 - r^3}{1 + r^3}\right) T' + \tilde{g} n_A\right] \quad . \tag{7.15}$$

Equation (7.8) and (7.12) determine n'_A and n'_B as the following explicit functions of n_A, n_B, and T' :

$$n'_A = \frac{\chi_{22}\beta_1 - \chi_{12}\beta_2}{\chi_{11}\chi_{22} - \chi_{12}\chi_{21}} \quad , \tag{7.16}$$

and

$$n'_B = \frac{\chi_{11}\beta_2 - \chi_{21}\beta_1}{\chi_{11}\chi_{22} - \chi_{12}\chi_{21}} \quad . \tag{7.17}$$

The balance of energy for the whole mixture is

$$Q' = -\Gamma \quad . \tag{7.18}$$

The constitutive relation for the energy flux Q of the whole mixture is,

$$Q = -kT' \quad , \tag{7.19}$$

where the thermal conductivity k is given by

$$k = \frac{1}{\pi^{1/2}} \left[K_{AA} + 2K_{AB} \left(\frac{1+r}{1+r^3} \right) \left(\frac{2r^3}{1+r^3} \right)^{1/2} + \frac{K_{BB}}{r^{5/2}} \right] T^{1/2} \quad . \tag{7.20}$$

The constitutive relation for the energy dissipation Γ for the whole mixture is,

$$\Gamma = \frac{6}{\pi^{1/2}} \left[K_{AA}(1 - e_{AA}) + 2 \frac{K_{AB}(1 - e_{AB})}{(1+r)} \left(\frac{2 + 2r^3}{r^3} \right)^{1/2} + \frac{K_{BB}}{r^{5/2}}(1 - e_{BB}) \right] T^{3/2} . \tag{7.21}$$

Equation (7.16), (7.17), (7.18), and (7.19) determine n_A, n_B, T, and Q within four constants of integrations. The conditions required to carry out the integrations are discussed in Section 7.2.

The mean velocities u_A and u_B are then determined from the first order approximations to the balance of mass for species A and species B:

$$\dot{m}_A \frac{\partial n_A}{\partial m_{tA}} + \dot{m}_B \frac{\partial n_A}{\partial m_{tB}} + \frac{\partial (n_A u_A)}{\partial Y} = 0 \quad ; \tag{7.22}$$

and

$$\dot{m}_B \frac{\partial n_B}{\partial m_{tB}} + \dot{m}_A \frac{\partial n_B}{\partial m_{tA}} + \frac{\partial (n_B u_B)}{\partial Y} = 0 \quad , \tag{7.23}$$

where the dimensionless flow rates $\dot{m}_i$ are given in terms of dimensional flow rate $\dot{m}_i$ by $\dot{m}_i \equiv \dot{m}_i / \rho_{pA} a$, the mass hold-up for each species is defined by

$$m_{ti} \equiv \int_0^\beta v_i dy \qquad (v_i = r_i^3 n_i) \quad , \tag{7.24}$$

and the derivative with respect to time has been replaced by $\dot{m}_A \partial(\ )/\partial m_{tA} + \dot{m}_B \partial(\ )/\partial m_{tB}$. Integrating equations (7.22) and (7.23) yields

$$u_A(Y) = \frac{\dot{m}_A \frac{\partial}{\partial m_{tA}}\left(\int_Y^\beta n_A dy\right) + \dot{m}_B \frac{\partial}{\partial m_{tB}}\left(\int_Y^\beta n_A dy\right)}{n_A} \quad , \tag{7.25}$$

and

$$u_B(Y) = \frac{\dot{m}_A \frac{\partial}{\partial m_{tA}}\left(\int_Y^\beta n_B dy\right) + \dot{m}_B \frac{\partial}{\partial m_{tB}}\left(\int_Y^\beta n_B dy\right)}{n_B} \quad . \tag{7.26}$$

The integrals at the boundary required to determine $\dot{m}_A$ and $\dot{m}_B$ are discussed in Section 5.4.

7.2 Boundary Conditions

The boundary conditions are as follows. At the free surface ($Y = \beta$), the normal pressure P, and the energy flux Q are zero:

$$P(Y = \beta) = 0 \qquad \text{and} \qquad Q(Y = \beta) = 0 \quad . \tag{7.27}$$

The momentum balance (5.26) at the sieve in the Y direction gives:

$$P = \sum_{i=A,B} \left(M_i^C + \tilde{M}_i^T\right) \quad , \tag{7.28}$$

where $M_i^C \equiv M_{2i}^C/\rho_{pA}a^2$ and $\tilde{M}_i^T \equiv \tilde{M}_{2i}^T/\rho_{pA}a^2$ are the rates of momentum transfer due to collisions and transport of species i. From equation (5.30), the collision terms M_i^C are written as the sum

$$M_i^C = M_{it}^C + M_{i\tau}^C \quad , \tag{7.29}$$

in which M_{it}^C and $M_{i\tau}^C$ are the contributions from the collisions experienced by fibers in the t- and τ- directions.

When species i *can* pass through the sieve (i.e. $\sigma_i < S_t$ and $\sigma_i < S_\tau$), M_{it}^C (from (5.33)) is

$$M_{it}^C = \frac{2(1 + e_i)r_i^3 \lambda_i n_i r_{\tau i}}{\sqrt{2}\pi^{3/2}} \left\{\frac{\pi^{1/2}\alpha^2}{2\sqrt{2}}\left[\left(1 - \frac{r_{ti}}{2}\right)\frac{\Omega^2}{r_i^3} + \left(\frac{2}{3}V_n^2 + \frac{V_\tau^2}{3}\right) - r_{ti}(V_n^2 + V_\tau^2)\right]\right\} \quad , \tag{7.30}$$

141

where $r_{ti} \equiv \sigma_i/S_t$ and $r_{\tau i} \equiv \sigma_i/S_\tau$. The term $M_{i\tau}^C$ in (7.29) is given by (7.30) in which r_{ti}, $r_{\tau i}$,

and V_τ are replaced by $r_{\tau i}$, r_{ti}, and V_n, respectively. The transport term $\widetilde{M}_i^T$ (from (5.27)) is

$$\widetilde{M}_i^T = -\frac{n_i \alpha^2 \Omega^2}{2}(1 - r_{ti})(1 - r_{\tau i}) \quad . \tag{7.31}$$

When species i *cannot* pass through the sieve (i.e. $\sigma_i < S_t$ and $\sigma_i > S_\tau$; or $\sigma_i > S_t$ and

$\sigma_i > S_\tau$ where we can assume without loss in generality that $S_t > S_\tau$), M_{it}^C (from (5.36)) is

$$M_{it}^C = \frac{2(1 + e_i)r_i^3 \lambda_i n_i r_{\tau i}}{\sqrt{2}\pi^{3/2}} \left\{ \frac{\pi^{1/2}}{2\sqrt{2}} \left[(C_1 + C_2)\frac{\Omega^2}{r_i^3} + (C_1 V_2^2 + C_2 V_3^2) \right] \right\} \quad , \tag{7.32}$$

where C_1 and C_2 are given by (5.37) and (5.38), respectively. In the same case, $M_{i\tau}^C$ (from (5.39))

is

$$M_{i\tau}^C = \frac{2(1 + e_i)r_i^3 \lambda_i n_i r_{\tau i}}{\sqrt{2}\pi^{3/2}} \left\{ \frac{\pi^{1/2}}{2\sqrt{2}} \left[\left(\frac{3}{8}\frac{r_{ti}}{r_{\tau i}^2} + \frac{1}{8}\frac{r_{ti}}{r_{\tau i}} \right)\frac{\Omega^2}{r_i^3} + \frac{r_{ti}}{2r_{\tau i}^2}\left(\frac{3}{4} + \frac{r_{\tau i}}{4} - \frac{1}{6r_{\tau i}^2} \right) V_2^2 + \left(\frac{1}{12}\frac{r_{ti}}{r_{\tau i}^4} \right)V_1^2 \right] \right\}. \tag{7.33}$$

In this case the transport term $\widetilde{M}_i^T$ is equal to zero.

The energy balance (5.43) at the sieve is:

$$Q = \sum_{i=A,B} \left(\mathcal{F}_i - \mathcal{D}_i + \widetilde{\mathcal{E}}^T \right) \quad , \tag{7.34}$$

where $\mathcal{F}_i \equiv \mathcal{F}_i/\rho_{pA}a^3$, $\mathcal{D}_i \equiv \mathcal{D}_i/\rho_{pA}a^3$, and $\widetilde{\mathcal{E}}^T \equiv \mathcal{E}^T/\rho_{pA}a^3$ are the rates of energy transfer

due to collisions and transport of species i. From equation (5.49), the collision terms $\mathcal{F}_i$ and $\mathcal{D}_i$

are written as the sums

$$\mathcal{F}_i = \mathcal{F}_{it} + \mathcal{F}_{i\tau} \quad \text{and} \quad \mathcal{D}_i = \mathcal{D}_{it} + \mathcal{D}_{i\tau} \quad , \tag{7.35}$$

from collisions with the fibers in the t- and τ- directions. From (5.50) and (5.51), the integral

expressions for $\mathcal{F}_{it}$ and $\mathcal{D}_{it}$ are:

$$\mathcal{F}_i = \frac{2(1 + e_{iw})r_i{}^3\lambda_i n_i r_{\tau i}\alpha^3(\Omega^2/r_i{}^3 + V_\tau^2)^{1/2}}{\sqrt{2}\pi^{3/2}} \int_0^{\varphi_{Max}} (1 + R_{\tau i}\cos^2\varphi)^{1/2}$$

$$[(\Omega^2/r_i{}^3 + V_\tau^2)(1 + R_{\tau i}\cos^2\varphi) - \Omega^2/r_i{}^3](1 - r_{ti}\sin\varphi)d\varphi \quad , \quad (7.36)$$

and

$$\mathcal{D}_i = \frac{2(1 - e_{iw}^2)r_i{}^3\lambda_i n_i r_{\tau i}\alpha^3(\Omega^2/r_i{}^3 + V_\tau^2)^{3/2}}{2\sqrt{2}\pi^{3/2}} \int_0^{\varphi_{Max}} (1 + R_{\tau i}\cos^2\varphi)^{3/2}(1 - r_{ti}\sin\varphi)d\varphi$$

$$(7.37)$$

where the ratios R_{ti} and $R_{\tau i}$ are defined by

$$R_{ti} \equiv \frac{r_i{}^3(V_n^2 - V_t^2)}{(\Omega^2 + r_i{}^3 V_t^2)} \quad , \quad\quad\quad (7.38)$$

and

$$R_{\tau i} \equiv \frac{r_i{}^3(V_n^2 - V_\tau^2)}{(\Omega^2 + r_i{}^3 V_\tau^2)} \quad . \quad\quad\quad (7.39)$$

The angle φ_{Max} in integrals (7.36) and (7.37) depends on whether or not species i can pass through the sieve. If species i *can* pass through the sieve (i.e. $\sigma_i < S_t$ and $\sigma_i < S_\tau$), then $\varphi_{Max} = \pi/2$. If species i *cannot* pass through the sieve (i.e. $\sigma_i < S_t$ and $\sigma_i > S_\tau$; or $\sigma_i > S_t$ and $\sigma_i > S_\tau$ regardless of whether $S_t > S_\tau$ or $S_t < S_\tau$), then $\varphi_{Max} = \sin^{-1}(1/r_{\tau i})$. The geometric parameters that appear in (7.36) and (7.37) are $r_{ti} \equiv \sigma_i/S_t$ and $r_{\tau i} \equiv \sigma_i/S_\tau$.

When species i *can* pass through the sieve, the transport of energy $\tilde{\mathcal{E}}^T$ (from (5.44)) is

$$\tilde{\mathcal{E}}^T = \frac{n_i\alpha^3\Omega^2}{(2\pi)^{1/2}}(1 - r_{ti})(1 - r_{\tau i})(\Omega^2/r_i{}^3 + V_n^2)^{1/2}\left(1 + \frac{(2\Omega^2 + V_n^2)}{(\Omega^2 + V_n^2)}\right) \quad . \quad (7.40)$$

When species i *cannot* pass through the sieve, the transport of energy $\tilde{E}_i^T$ is equal to zero.

Finally the first order contribution to the flow rate is obtained from the lowest order approximation of expression (5.20):

$$\dot{m}_i = -\frac{n_i \alpha r_i^3 (\Omega^2/r_i^3 + V_n^2)^{1/2}}{(2\pi)^{1/2}}(1 - r_{ti})(1 - r_{\tau i}) \quad . \tag{7.41}$$

7.3 Solution Procedure

Equations (7.16), (7.17), (7.18), and (7.19) determine n_A, n_B, T, and Q within four constants of integrations. The temperature gradient T' is replaced by $-Q/k$ wherever it appears implicitly in (7.16) and (7.17) through β_1 and β_2. The energy dissipation Γ in equation (7.18) is given by (7.21), and the coefficient of thermal conductivity k in equation (7.19) is given by (7.20). We restrict attention to mixtures in which the particles are close in size, so that the difference between the shielding factors λ_i can be ignored.

The four constants of integration, the shielding factor $\lambda_A = \lambda_B$, and the height β of the flow are determined by momentum condition (7.28) and energy condition (7.34) at the sieve $(Y = 0)$, the conditions (7.27) that $P = 0$ and $Q = 0$ at the top $(Y = \beta)$, and the requirements that the solid fractions ν_A and ν_B give prescribed mass hold-ups m_{tA} and m_{tB} according to integral (7.24).

As in the case of monosized assemblies (see Section 4.3) the theory predicts that the condition $P = 0$ and $Q = 0$ can be satisfied only at infinite distance from the bottom boundary. To avoid this difficulty, we keep $Q = 0$ but pick a an arbitrarily small value for P (i.e. $P = 10^{-4}$) at the top of the assembly, and guess values for n_A and n_B there. The corresponding granular temperature T is computed from equation (7.7). We then integrate equations (7.16), (7.17), (7.18), and (7.19) downward. At every step, momentum condition (7.28) is used to eliminate $\lambda_A = \lambda_B$ from energy condition (7.34). The integrations proceed until the energy condition (7.34) is satisfied. The solid volume fractions $\nu_A = n_A$ and $\nu_B = n_B r^3$ are then

integrated to calculate the mass hold-ups m_{tA} and m_{tB} according to equation (7.24). If the mass hold-ups calculated in this manner do not agree with their prescribed values, then the values of n_A and n_B at the top surface are iterated using Newton-Raphson until all requirements are satisfied.

With n_A, n_B, and $\Omega\left(\equiv \sqrt{T}/\alpha\right)$ known, the flow rates are obtained from (7.41). With the flow rates known, we can prescribe a small increment δt in time and update the mass hold up according to:

$$m_{ti}(t + \delta t) = m_{ti}(t) - \dot{m}_i \delta t \qquad . \tag{7.42}$$

The solution procedure for n_A, n_B, T, and Q can then be carried out for successive pairs m_{tA} and m_{tB} to obtain the quasi-steady variations of solid fraction and granular temperature profiles.

At each successive time, the corresponding velocity profiles $u_A(Y)$ and $u_B(Y)$ are calculated according to (7.25) and (7.26).

In obtaining results, we restrict attention to typical cases in which the spacings S_t between fibers in the t-direction, and S_τ between fibers in the τ-direction are equal to a common value S. In this special case,

$$r_{ti} = r_{\tau i} = \frac{\sigma_i}{S} \qquad (i = A, B) \quad , \tag{7.43}$$

and two different measures of the same spacing are

$$\Delta_i \equiv \frac{S}{\sigma_i} \qquad (i = A, B) \quad . \tag{7.44}$$

When Δ_i is greater than 1, species i can pass through the sieve. Because the fiber spacing S is the same in both directions, the two values of Δ_i are related by,

$$\Delta_B = \frac{\Delta_A}{r} \qquad , \tag{7.45}$$

where r is the size ratio r_B/r_A. In addition, unless otherwise specified, we take the coefficient of restitution e_i between a particle of species i and the sieve to be the same as the coefficient of restitution e_{ii} between two particles of species i, and we take the coefficient of restitution e_{AB} between a particle of species A and a particle of species B to be equal to the average value $(e_{AA} + e_{BB})/2$.

7.4 Segregation Induced by Horizontal *Impenetrable* Vibrating Boundaries

In order to study particle segregation at impenetrable vibrating surfaces, we apply the solution procedure described in Section 7.3 to the special cases in which the vibrating boundaries are sieve-like (i.e. mesh) surfaces with equal spacings that are *less* than the diameters of both particles: i.e. $\Delta_i < 1$. In this case, the mean velocities u_A and u_B, and therefore the flow rates $\dot{m}_A$ and $\dot{m}_B$ are zero.

The phenomenon of particle segregation (at impenetrable surfaces) is important by itself. But we are interested in it here as a preliminary study primarily because, even before particles of one size (or even both) eventually pass through a vibrating sieve, they segregate as they migrate downward much as they would if the sieve were impenetrable.

In order to see how the mixtures segregate due to differences in particle size, in Figure 7.2 we show the solid fraction profiles ν_A and ν_B for the individual species, as well as the corresponding mixture temperature $w \equiv \sqrt{T}$ for size ratio $r \equiv r_B/r_A = 1, 1.05, 1.1,$ and 1.15 (when $\alpha = 1,$ $V_n^2 = V_t^2 = V_\tau^2 = 1,$ $\Delta_A = 0.72,$ $e_{AA} = e_{BB} = 0.95,$ and $m_{tA} = m_{tB} = 1.5.$) When $r = 1$, the particles are identical (both in size and inelasticity), and the solid fraction profiles are the same. As the size ratio r increases (so that particles of species B become gradually larger than the particles of species A), the larger particles settle in greater numbers
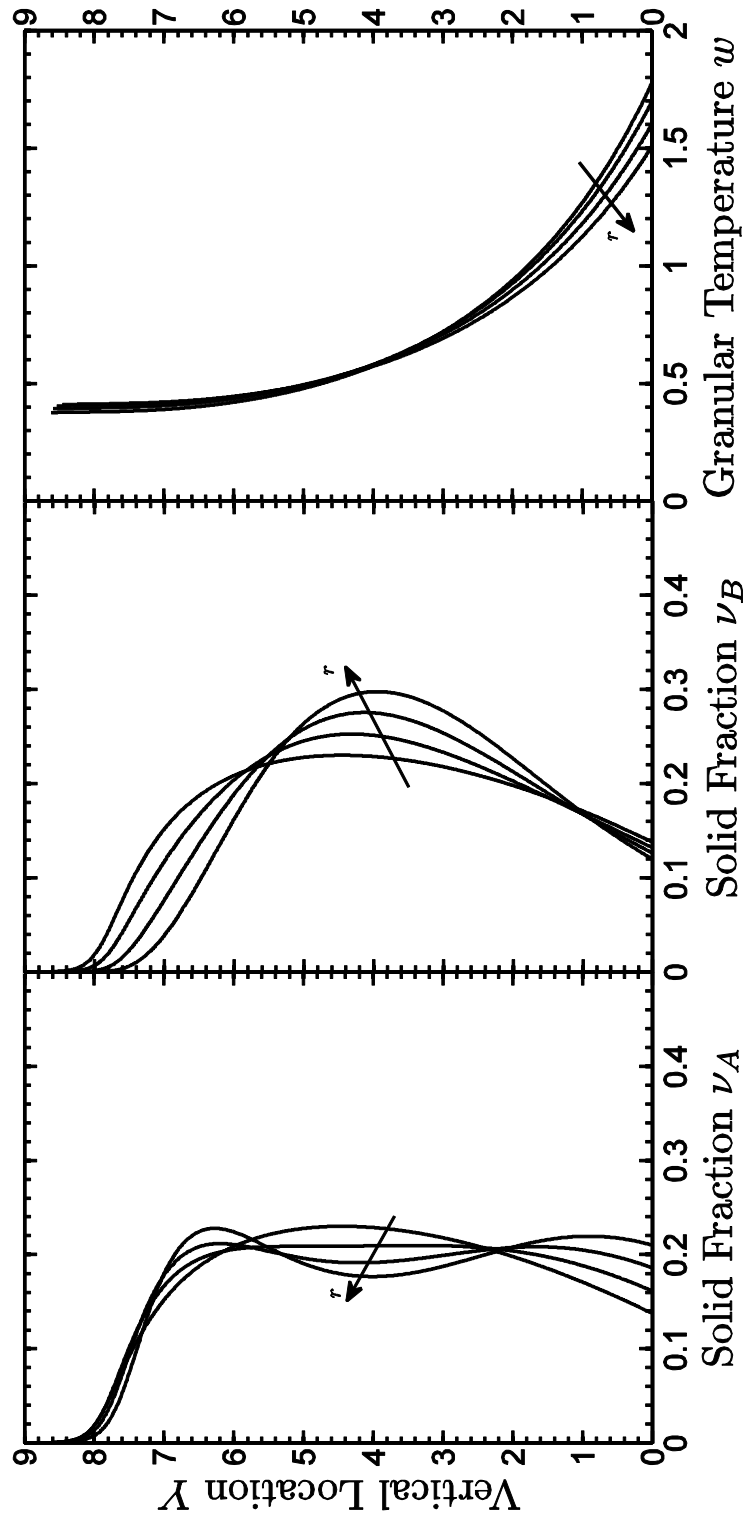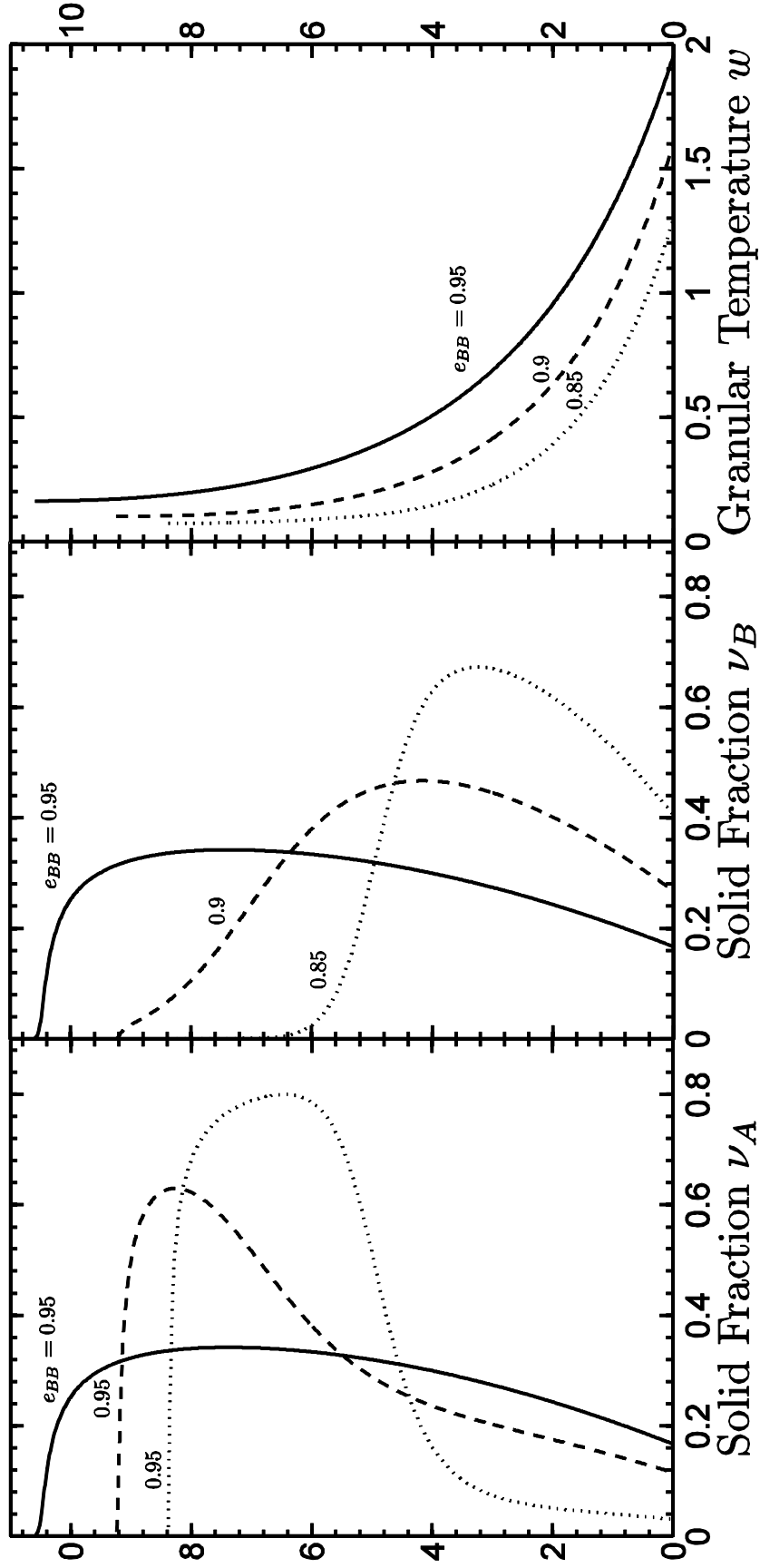
Figure 7.2: The profiles of solid fraction ν_A and ν_B for the individual species, and the mixture temperature w for size ratio $r = 1$, 1.05, 1.1, and 1.15 when $\alpha = 1$, $V_n^2 = V_t^2 = V_\tau^2 = 1$, $\Delta_A = 0.72$, $e_{AA} = e_{BB} = 0.95$, and $m_{tA} = m_{tB} = 1.5$.

away from the boundaries toward the middle region of the assemblies, whereas the smaller particles are most densely packed near the vibrating surface (and near the free surface, as well). Based on energy considerations the relatively high density of smaller particles near the vibrating may be explained as follows. A greater number of small particles than large particles can be fit into any fixed volume, so at the same granular temperature and solid fraction, an assembly of smaller particles will experience more collisions and dissipate more energy than an assembly of larger particles. Consequently, a particle arrangement with more particles in the high-temperature region near the boundary more efficiently dissipates the energy supplied by the vibrating boundary. The region near the free surface where the small particles also seem to congregate may be due to fact that the region of larger particles in middle region (at relatively lower temperatures) behaves like an increasingly impenetrable boundary for the small particles trapped above it.

The common kinematic argument for the high densities of small particles near the vibrating boundary is as follows. Just as particles fluctuate about their positions during vibration, complementary void spaces between the particles also fluctuate as the system is oscillated. For example, at the end of the upward stroke, spaces open between the boundary and the assembly as the particles gain kinetic energy and separate from boundary as it slows down and reverses direction. Then, as the particles collide and fall in gravity, there is a greater probability that smaller particles rather than larger particles will fill the temporary voids. Thus, on average the smaller particles will move slightly down and the larges particle will slightly up at the end of each stroke, until steady state is reached. This idea, which does not apply to the high density region of small particles trapped above the dense region, can be traced back to almost every early discussion on size separation in the presence of gravity.

In order to isolate the effects on segregation due to differences in particle inelasticity, we consider cases in which the particles are the same (i.e. $r = 1$) but have different coefficients of restitution. Figure 7.3, for example, shows the solid fraction profiles ν_A and ν_B for the individual species, as well as the corresponding mixture temperature $w \equiv \sqrt{T}$ for three different coefficients of restitution $e_{BB} = 0.95, 0.9$, and 0.85 while $e_{AA} = 0.95$ remains the same (when $\alpha = 1$, $V_n^2 = V_t^2 = V_\tau^2 = 1$, $\Delta_A = 0.9$, and $m_{tA} = m_{tB} = 3$). When $e_{BB} = 0.95$ the particles are identical (both in size and inelasticity), and the solid fraction profiles are the same. As the particles of species B become more dissipative than those of species A, the middle panel of Figure 7.3 demonstrates that they increasingly concentrate in a region of higher temperatures near the vibrating boundary, while the left panel shows that the more elastic particles of species A migrate to a region of lower temperature much further away from the boundary. This arrangement more efficiently dissipates the energy supplied by the boundary. In the extreme case when the differences in inelasticity are greatest (when $e_{AA} = 0.95$ and $e_{BB} = 0.85$), a slightly thermalized block consisting almost entirely of the more elastic speices A is supported from below by a highly thermalized region near the boundary that consists almost entirely by the relatively dissipative species B. The striking conclusion is that, in the absence of size differences, disparities in coefficients of restitution alone can induce significant segregation in a binary mixture.

We are interested in assessing the relative strengths of the mechanisms responsible for segregation due to differences in both size and inelasticity. Figure 7.4 shows the solid fraction profiles ν_A and ν_B for the individual species, as well as the corresponding mixture temperature $w \equiv \sqrt{T}$ for two cases in which species A ($e_{AA} = 0.95$) is much more elastic than species B ($e_{BB} = 0.85$) when $\alpha = 1$, $V_n^2 = V_t^2 = V_\tau^2 = 1$, $\Delta_A = 0.9$, and $m_{tA} = m_{tB} = 3$. When the

Figure 7.3: The profiles of solid fraction ν_A and ν_B for the individual species, and the mixture temperature w for coefficient of restitution $e_{AA} = 0.95$, $e_{BB} = 0.95, 0.9$, and 0.85 when $r = 1$, $\alpha = 1$, $V_n^2 = V_t^2 = V_\tau^2 = 1$, $\Delta_A = 0.9$, and $m_{tA} = m_{tB} = 3$.
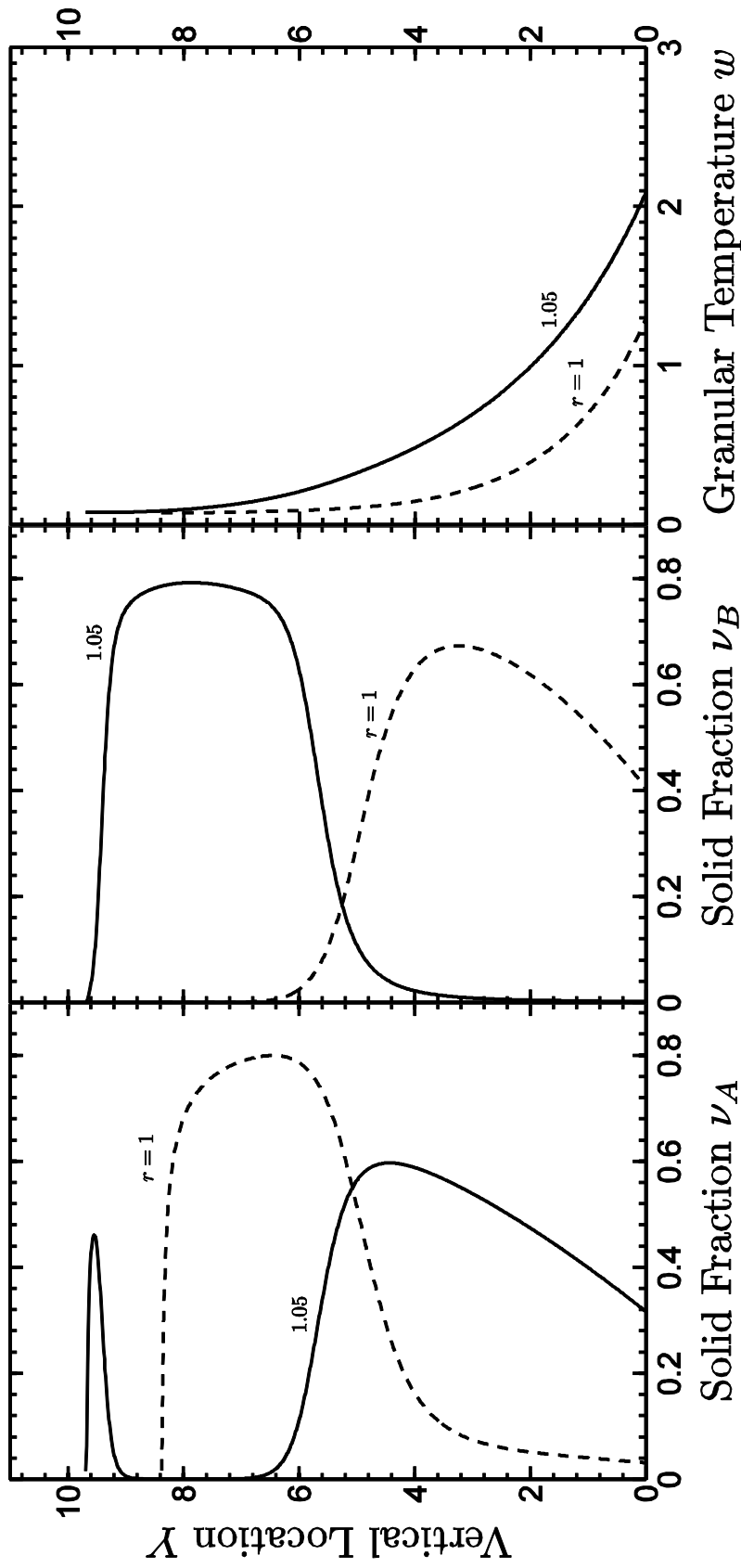
Figure 7.4 The profiles of solid fraction ν_A and ν_B for the individual species, and the mixture temperature w for size ratio $r = 1, 1.05$ when $e_{AA} = 0.95$, $e_{BB} = 0.85$, $\alpha = 1$, $V_n^2 = V_t^2 = V_\tau^2 = 1$, $\Delta_A = 0.9$, and $m_{tA} = m_{tB} = 3$.

species are of the same size ($r = 1$), the more dissipative particles (species B) settle at the bottom while the more elastic particles (species A) settle at the top. (This is the extreme case show in Figure 7.3). However, when the more dissipative particles B become just five percent larger than the more elastic particles A (so that $r = 1.05$), the assembly rearranges itself with the larger particles B on the top and the smaller particles A on the bottom. This demonstrates that the mechanism responsible for segregation due to differences in size is dominant over that due to differences in inelasticity.

Finally, we introduce the following quantity D that gives a depth-averaged measure of the degree of segregation that characterizes an entire assembly:

$$D = \frac{1}{2h} \int_0^h \left| \frac{\nu_A}{\bar{\nu}_A} - \frac{\nu_B}{\bar{\nu}_A} \right| dY \quad , \tag{7.46}$$

where h is the finite height of the assembly and $\bar{\nu}_A$ and $\bar{\nu}_B$ are the depth-averaged values of the solid fractions ν_A and ν_B. Defined in this way, D can take values from 0 to 1 in such a way that in the extremes, when $D = 0$ the assembly is perfectly mixed and when $D = 1$ it is perfectly segregated.

In Figure 7.5, we show three variations of the degree of segregation D. In the left panel the variation is with mass hold-up $m_{tA} = m_{tB}$ (when $\alpha = 1$ and $V_n^2 = V_t^2 = V_\tau^2 = 1$); in the middle panel the variation is with total vibrational energy α (when $V_n^2 = V_t^2 = V_\tau^2 = 1$ and $m_{tA} = m_{tB} = 1.5$); and in the right panel the variation is with V_n^2 (when $\alpha = 1$, $V_\tau^2 = 0$, and $m_{tA} = m_{tB} = 1.5$). All three cases are for $e_{AA} = e_{BB} = 0.95$, $r = 1.15$, and $\Delta_A = 0.72$. The three curves demonstrate that for the limited range of parameters explored here, the degree of segregation decreases as the effect of boundary vibrations increases. This is an indication that while vibrations have a segregating effect on assemblies, they also have a mixing effect.
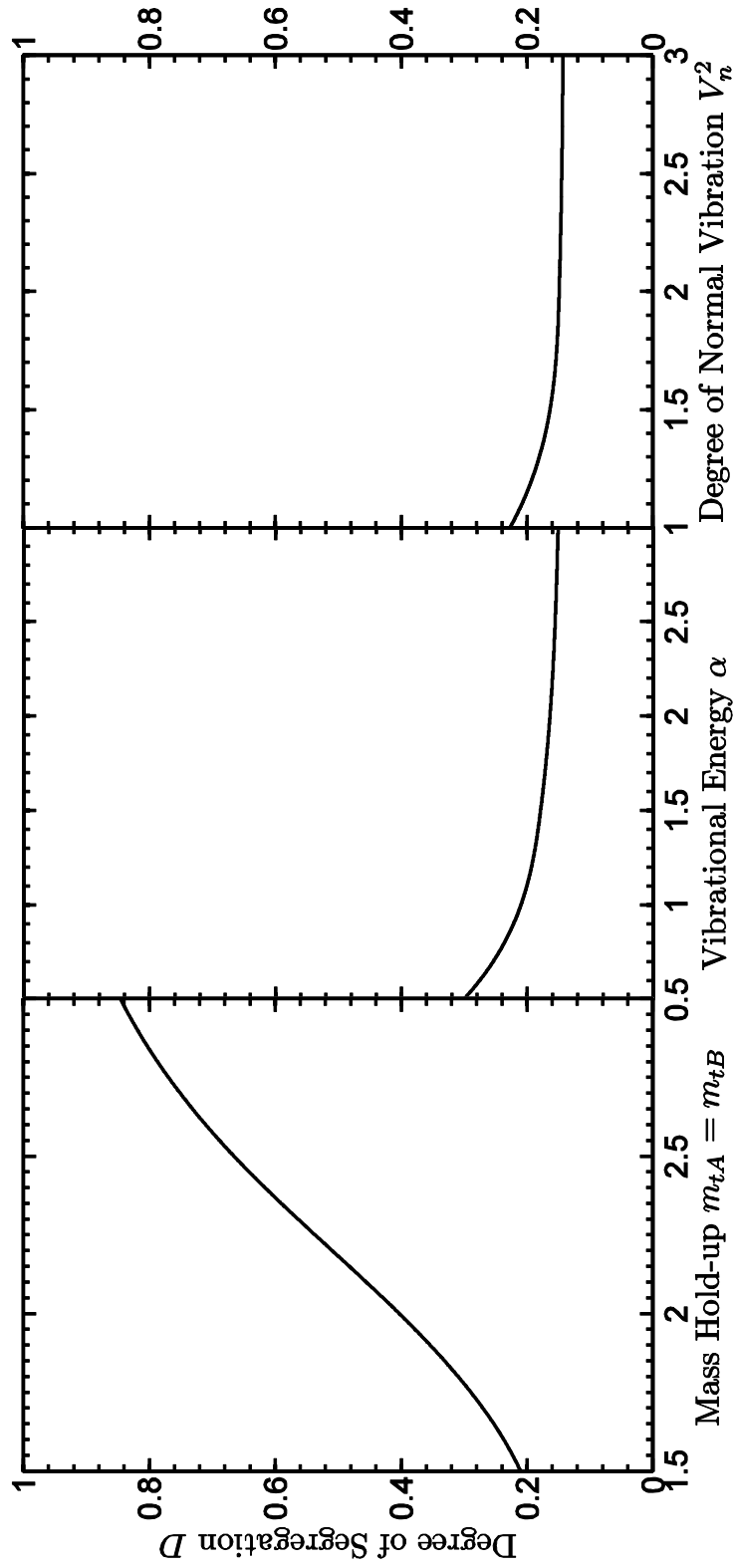
Figure 7.5: The variations of mass hold-up $m_{tA} = m_{tB}$ (when $\alpha = 1$ and $V_n^2 = V_t^2 = V_\tau^2 = 1$), vibrational energy α (when $V_n^2 = V_t^2 = V_\tau^2 = 1$ and $m_{tA} = m_{tB} = 1.5$), and degree of normal vibration V_n^2 (when $\alpha = 1$, $V_t^2 = 0$, and $m_{tA} = m_{tB} = 1.5$) with degree of segregation D. All three cases are for $e_{AA} = e_{BB} = 0.95$, $r = 1.15$, and $\Lambda_\circ = 0.72$.

So segregation might be best achieved by low intensity vibrations (over long durations), while mixing might be achieved by high intensity vibrations (perhaps over far shorter durations).

In the left panel of Figure 7.5, although the total vibrational energy and the direction of vibration are fixed, the effect of the vibrations felt in the assemblies actually increases as the mass hold-up decreases, and the degree of segregation decreases dramatically as the mass hold-ups $m_{tA} = m_{tB}$ decrease from 3 to 1.5. In the middle and right panels, as either the total vibrational energy α increases (for fixed vibration direction) or as the normal component V_n^2 of vibrational motion increases (for fixed total vibrational energy α), the energy transferred to the assemblies from the boundary increases and the assemblies become less segregated and more mixed. These two effects are not very dramatic, but (as the left panel suggest) that is because for the relatively small values of mass hold-up $m_{tA} = m_{tB} = 1.5$ considered here, even at the lowest values of α (in the middle panel) and V_n^2 (in the right panel) the effects of vibrations are already strong enough to mix the assemblies quite well.

## 7.5   Flows through Horizontal Vibrating Sieves

In this section, we employ the full solution procedure described in Section 7.3 to calculate the profiles of solid fraction profiles ν_A and ν_B for the individual species, the temperature $w \equiv \sqrt{T}$ of the whole mixture, and mean velocities u_A and u_B for each species as the material flows through the sieve. Of particular importance are the resulting mass flow rates $\dot{m}_A$ (if only one species passes through the sieve) and $\dot{m}_B$ (if both pass through the sieve) and how these flow rates are influenced by the geometry and vibratory motion of the boundary. In most cases, we consider the case in which the small particles A can pass through the sieve while the large particles B cannot.

As a first example, we track the details of the flows as the small particles A pass through the sieve while the large particles do not. In Figure 7.6, we show the profiles of the solid fraction ν_A and ν_B for the individual species, as well as the profiles of the corresponding temperature $w \equiv \sqrt{T}$ the solid fraction $\nu = \nu_A + \nu_B$ of the whole mixture for a series of successively decreasing mass hold-ups $m_{tA} = 3.0, 2.5, 2.0, 1.5, 1.0, 0.5,$ and 0.1 (when $\Delta_A = 1.1, r = 1.222,$ $\alpha = 1.5,$ $V_n^2 = V_t^2 = V_\tau^2 = 1,$ $m_{tB} = 3,$ and $e_{AA} = e_{BB} = 0.95$). Figure 7.7 shows the corresponding mean velocity profiles u_A and u_B. Initially (at $m_{tA} = 3$), the assembly is segregated with a region of small particles A near the sieve, a region of larger particles away from the boundary, and a thin layer of trapped small particles near the free surface. As the particles of species A pass through the sieve, the mass hold-up m_{tA} and the solid fraction ν_A decrease to zero, and species B rearranges itself until its solid fraction profile ν_A takes the familiar shapes seen (in Section 4.4) in monosized assemblies thermalized by impenetrable horizontal vibrating boundaries. The shape of the granular temperature profiles does not change, but the temperatures themselves increase everywhere in the remaining assembly because increasingly fewer particles must dissipate the same energy supplied by the vibrations of the sieve.

The velocity profile u_A in Figure 7.7 evolves in a complicated manner. At first, although most of the small particles A move downward, there is a region (in this case between about 6 to 8 particle diameters from the sieve) at which the small particles A actually move away from the sieve to join the trapped small particles at the top of the flow. However, for times after which the mass hold-up $m_{tA} = 1.5$ decreases to about half its initial value, the larger particles B are no longer sufficiently densely packed to trap any small particles, and the small particles move downward everywhere throughout the assembly. The mean velocities u_A of the small particles at the sieve increase as the sieving proceeds, but because the solid fraction ν_A of small particles at the sieve

155
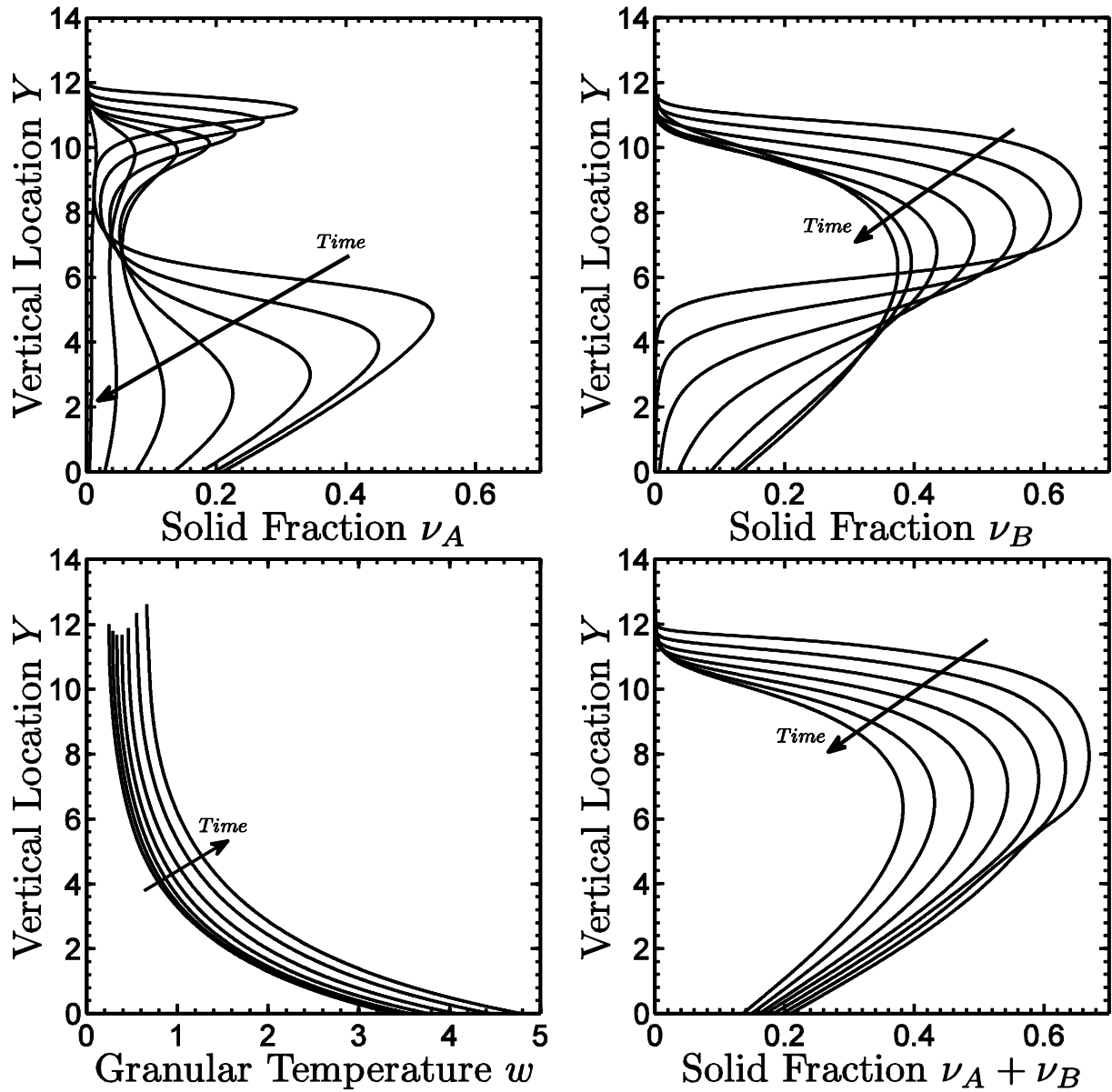
Figure 7.6: The profiles of solid fraction ν_A and ν_B for the individual species, the mixture temperature w, and the mixture solid fraction $\nu = \nu_A + \nu_B$ for mass hold-up $m_{tA} = 0.1, 0.5, 1, 1.5, 2, 2.5, 3$ when $\Delta_A = 1.1$, $r = 1.222$, $\alpha = 1.5$, $V_n^2 = V_t^2 = V_\tau^2 = 1$, $m_{tB} = 3$, and $e_{AA} = e_{BB} = 0.95$.
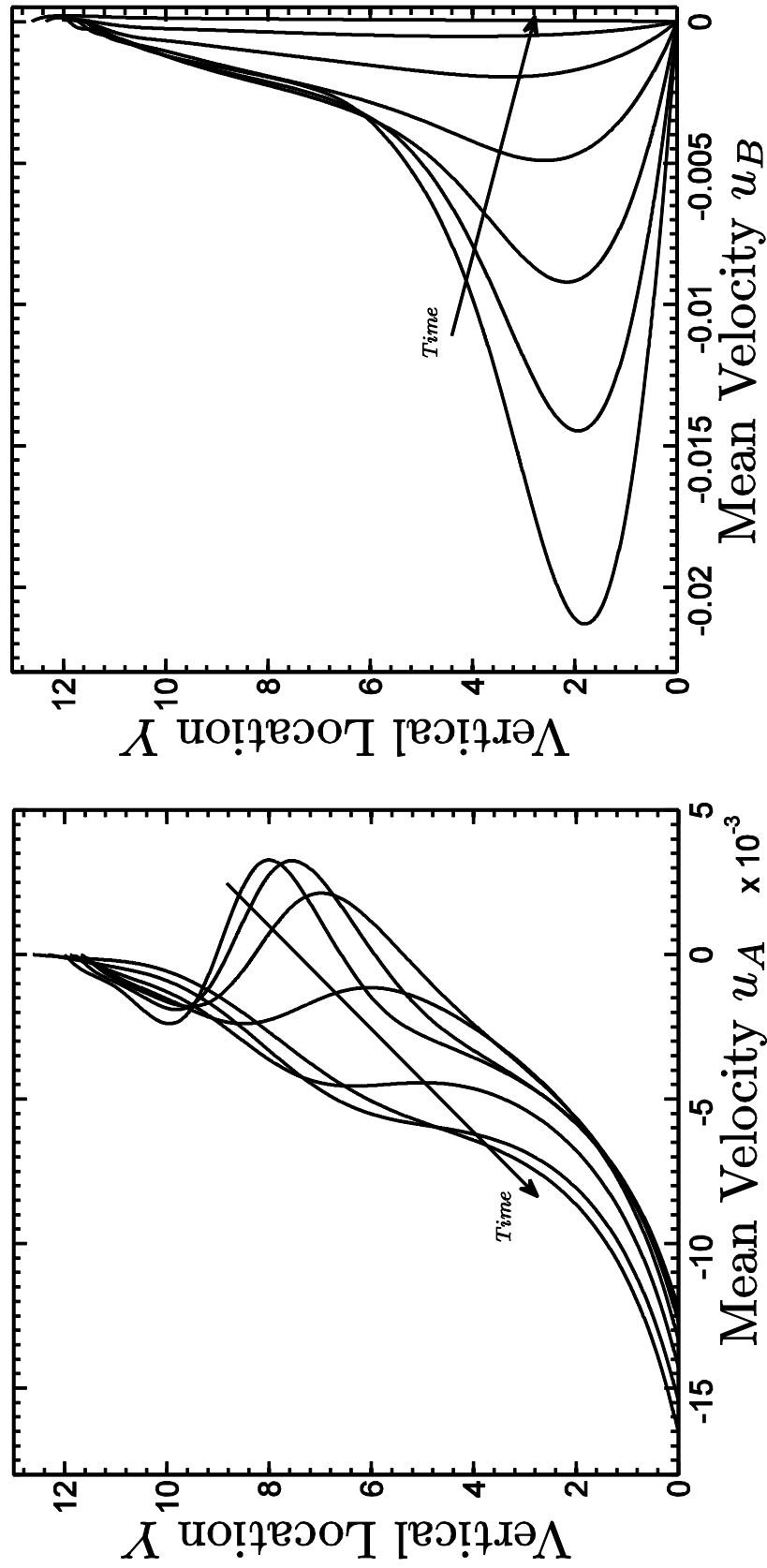
Figure 7.7: The profiles of mean velocities u_A and u_B for mass hold-up $m_{tA} = 0.1, 0.5, 1, 1.5, 2, 2.5, 3$ when $\Delta_A = 1.1$, $r = 1.222$, $\alpha = 1.5$, $V_n^2 = V_t^2 = V_\tau^2 = 1$, $m_{tB} = 3$, and $e_{AA} = e_{BB} = 0.95$.

also decreases, the effect of the flow rates are not clear from these results. Throughout the process, the mean velocities u_B of the larger particles B are downward at all locations at all times, indicating that the larger particles B replace the small particles A that were initially segregated near the boundary. Of course, the velocity u_B at the sieve must vanish because the larger particles B cannot pass through the sieve. Although the theory predicts, at least at the earliest times, that the large particles B move with much higher velocities near the sieve, the fact is that the solid fraction ν_B in this region at those times is very small. Consequently, even at high velocities, the corresponding flow rates of the large particles B are very small there. For completeness, in what follows we will show several more sets of velocity profiles in several more cases, but we will not describe them in any detail because they are all qualitatively similar to those shown in Figure 7.7.

Figures 7.8 through 7.10 describe overall bulk flow behavior through the sieve and how it is affected by changing the fiber spacing Δ_A. In Figure 7.8 we show the variation of mass flow rate $\dot{m}_A$ of the small particles A with mass hold-up m_t (from $m_{tA} = 3$ to $m_{tA} = .1$) for spacings $\Delta_A = 1.05, 1.1, 1.15$ (when $r = 1.222$, $\alpha = 1$, $V_n^2 = V_t^2 = V_\tau^2 = 1$, $m_{tB} = 3$, and $e_{AA} = e_{BB} = 0.95$). These figures are similar to Figures 6.4 to 6.6 generated for the case of sieving of monosized assemblies. For any fixed Δ_A, the mass flow rate decreases as the mass hold-up decreases, and for any value of mass hold-up m_t, the mass flow rate increases with spacing. Figure 7.9 shows the corresponding explicit time variations of mass hold-up m_{tA} and mass flow rate $\dot{m}_A$. In Figure 7.10, we focus on the case in which the initial value of mass hold-up is $m_{tA} = 3$ and show explicitly how the time t^* to reach a specified (lower) value of mass hold-up varies with spacing Δ_A (when $r = 1.222$, $\alpha = 1$, $V_n^2 = V_t^2 = V_\tau^2 = 1$, $m_{tB} = 3$ and
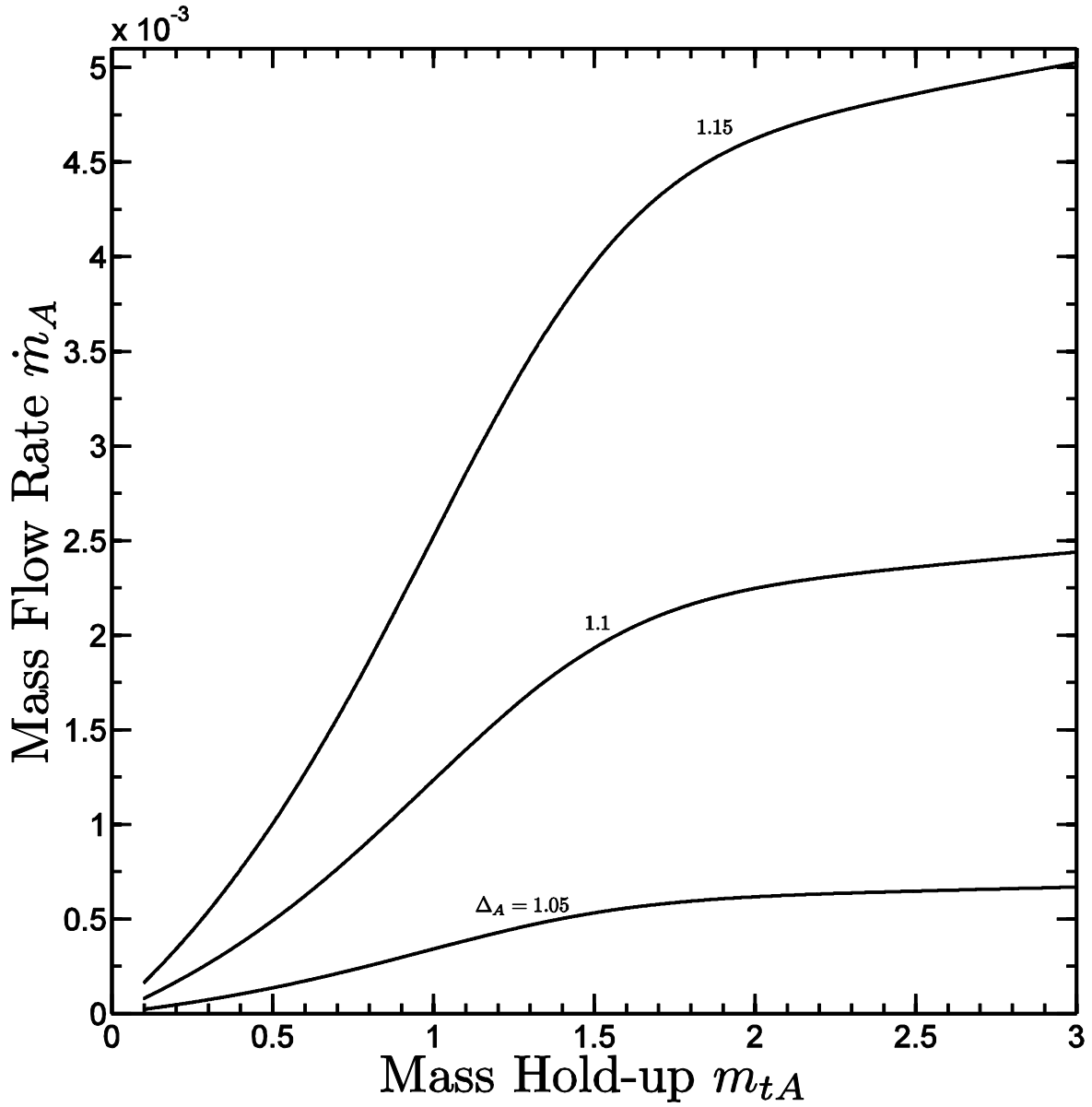
Figure 7.8: The variation of mass flow rate $\dot{m}_A$ with mass hold-up m_{tA} for spacing $\Delta_A = 1.05, 1.1, 1.15$ when $r = 1.222$, $\alpha = 1$, $V_n^2 = V_t^2 = V_\tau^2 = 1$, $m_{tB} = 3$, and $e_{AA} = e_{BB} = 0.95$.
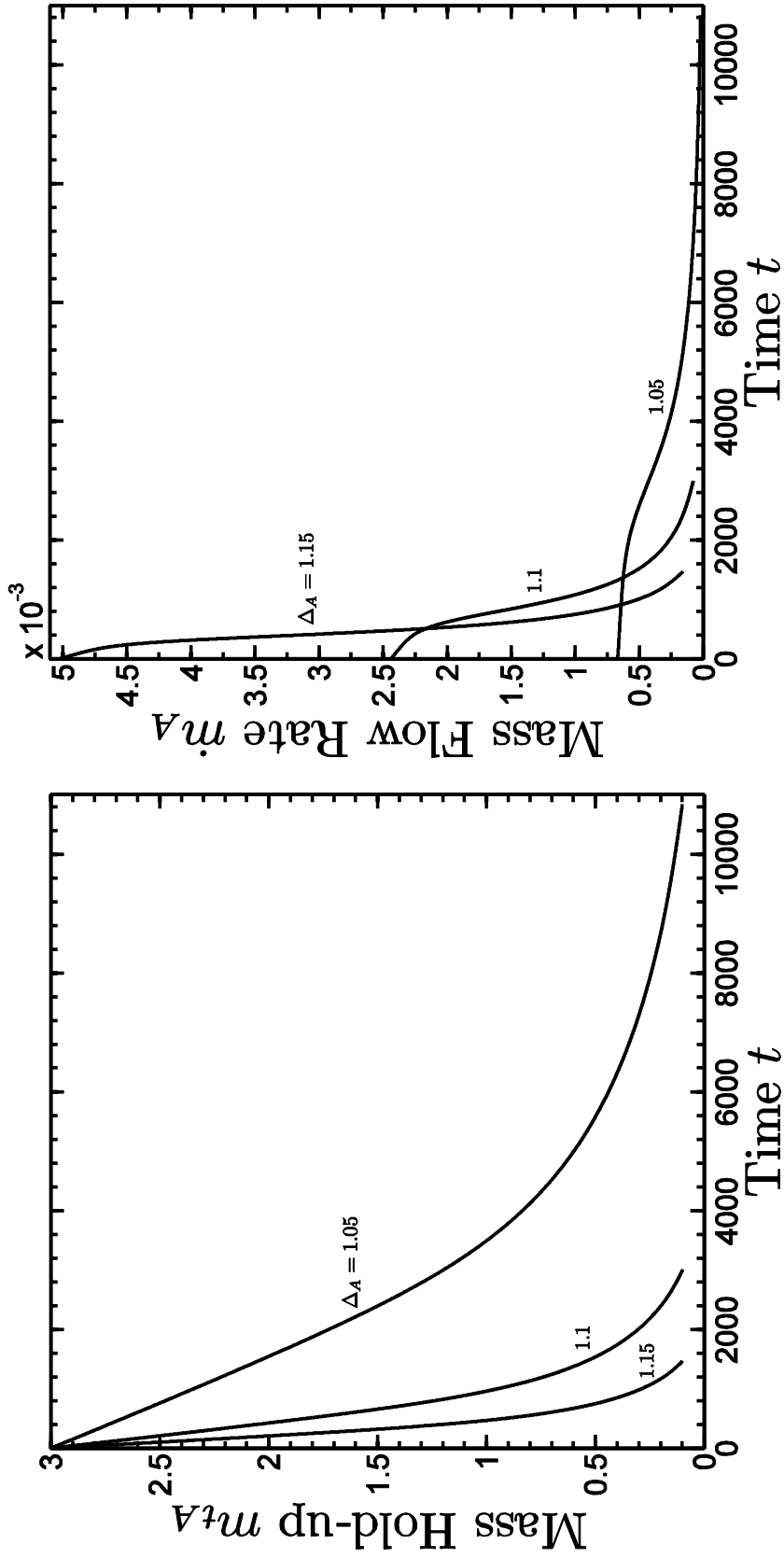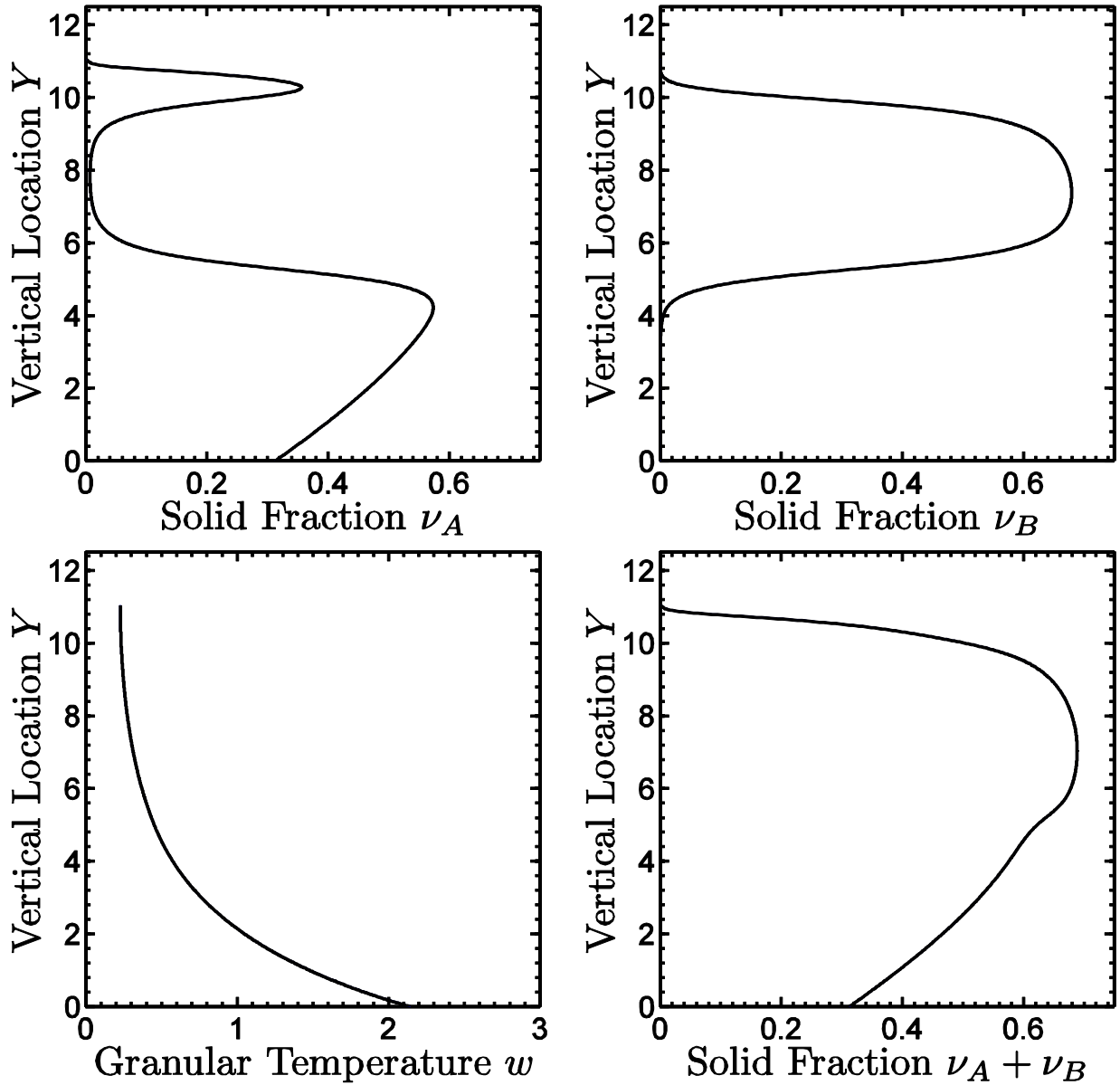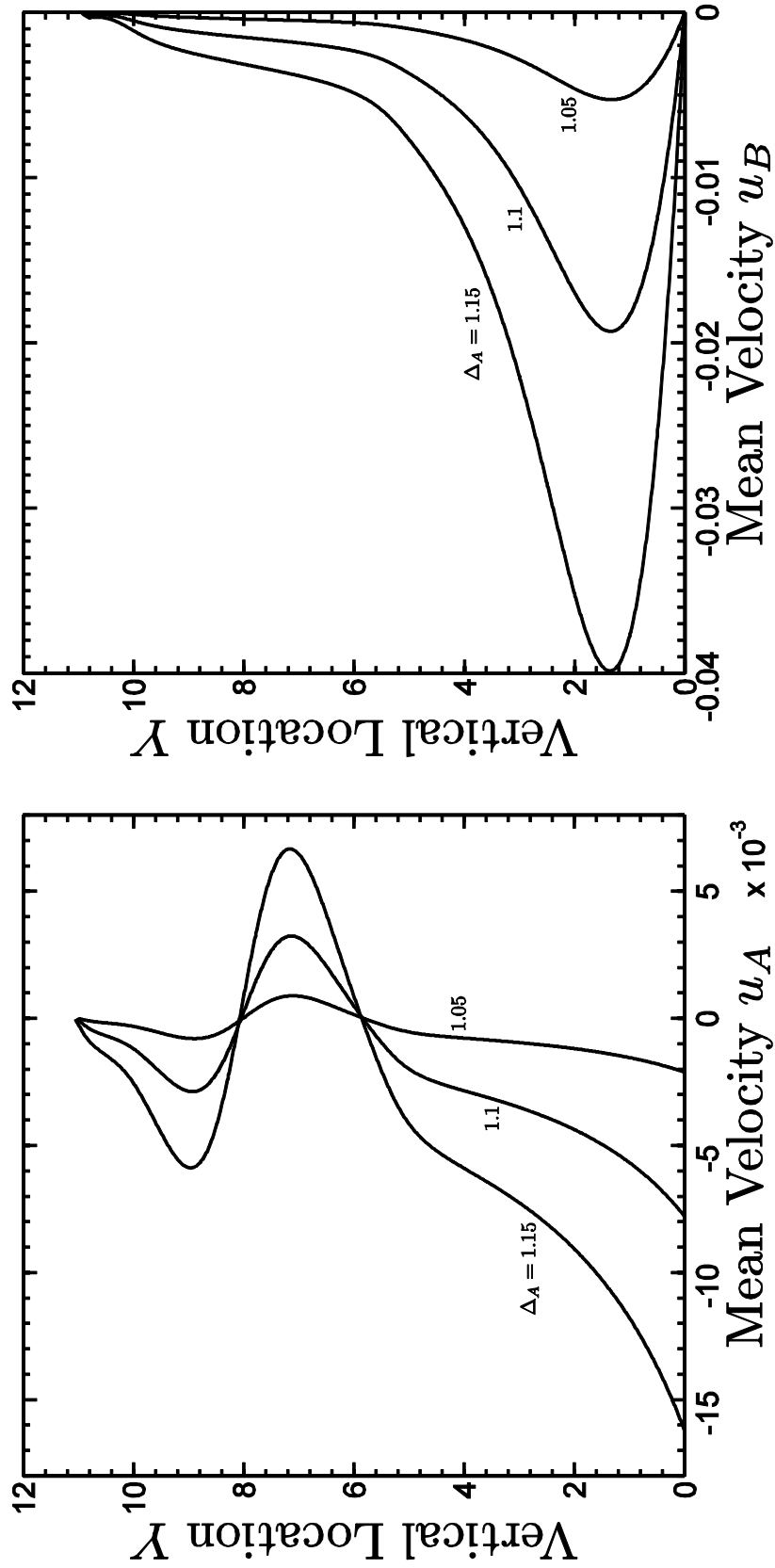
Figure 7.9: The variations of mass hold-up up m_{tA} and mass flow rate $\dot{m}_A$ with time t for spacing $\Delta_A = 1.05, 1.1, 1.15$ when $r = 1.222$, $\alpha = 1$, $V_n^2 = V_t^2 = V_\tau^2 = 1$, $m_{tB} = 3$, and $e_{AA} = e_{BB} = 0.95$.
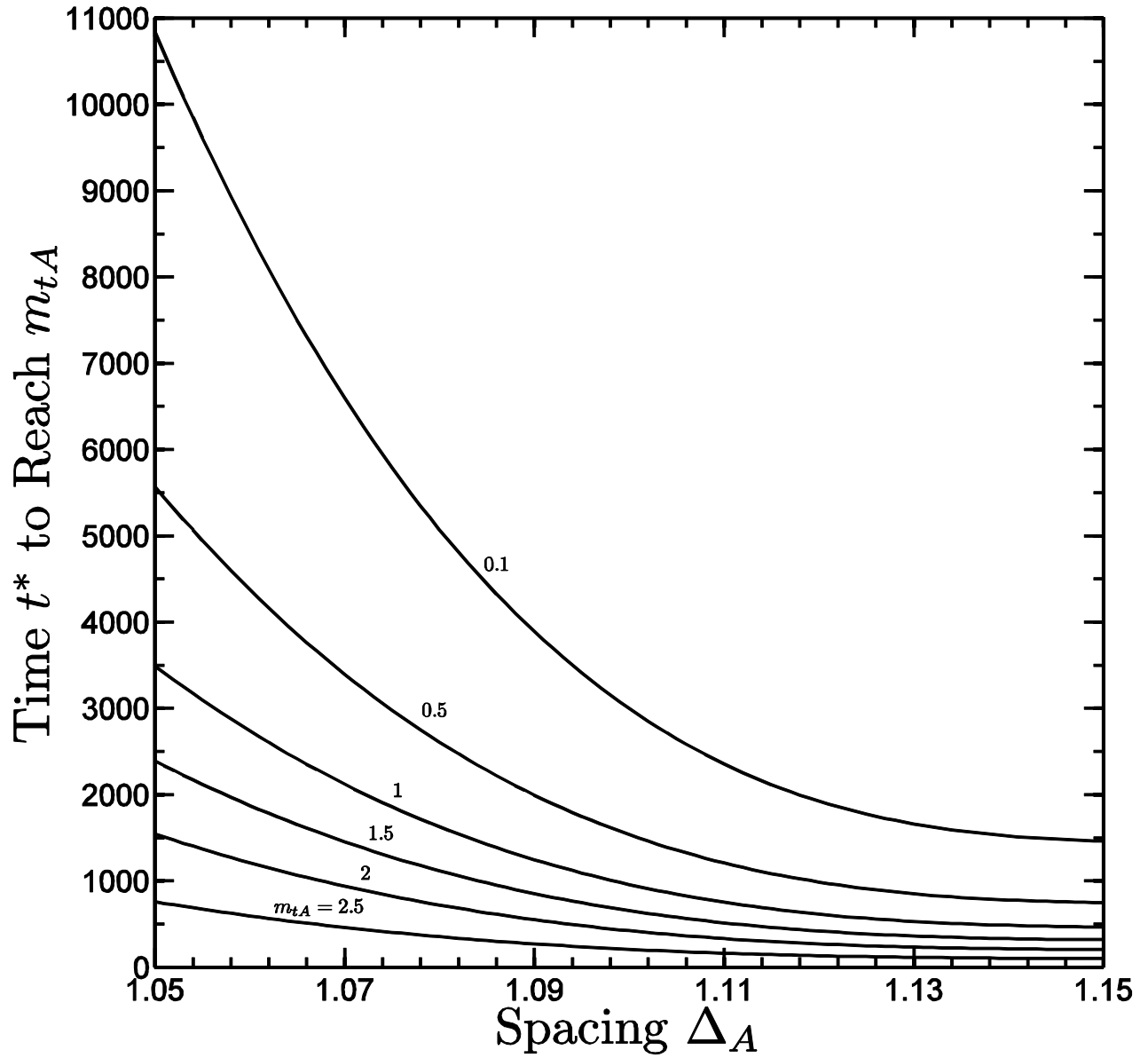
Figure 7.10: The variation of time t^* to reach a prescribed value of m_{tA} with spacing Δ_A for mass hold-up $m_{tA} = 0.1, 0.5, 1, 1.5, 2, 2.5$ when $r = 1.222$, $\alpha = 1$, $V_n^2 = V_t^2 = V_\tau^2 = 1$, $m_{tB} = 3$, and $e_{AA} = e_{BB} = 0.95$.

$e_{AA} = e_{BB} = 0.95$). The time t^* required to reach a prescribed value of m_t increases as the size of the holes decreases, and becomes much more sensitive to changes in the spacing as the holes become increasingly close to the size of the particles. Figure 7.11 shows the corresponding profiles of the solid fraction v_A and v_B for the individual species, as well as the profiles of the corresponding temperature $w \equiv \sqrt{T}$ the solid fraction $v = v_A + v_B$ of the whole mixture at the initial time (i.e. when $m_{tA} = 3.0$) for the three spacings $\Delta_A = 1.05, 1.1, 1.15$. The qualitative features of these curves have already been described elsewhere, and because of the relatively small changes in Δ_A, the curves are quantitatively indistinguishable from one another. Figure 7.12 shows the corresponding mean velocity profiles u_A and u_B with shapes similar to those shown in Figure 7.7. The both the downward (and upward) velocities increase with increased spacing.

Just as in sieving of monosized assemblies of Chapter 6, we are interested in the effect that different sieve vibrations have on the flows. In Figures 7.13 to 7.16, we demonstrate how changes in the total vibrational energy α affect the flows. The results are similar to those obtained in Figures 6.8 to 6.10. In Figure 7.13 we show the variation of the mass flow rate $\dot{m}_A$ of the smaller particles A with their mass hold-up m_{tA} (from $m_{tA} = 3$ to $m_t = .1$) for total vibrational energies $\alpha = .5, 1, 2,$ and 3 (when $r = 1.222$, $V_n^2 = V_t^2 = V_\tau^2 = 1$, $m_{tB} = 3$, and $e_{AA} = e_{BB} = 0.95$). For fixed values of α, the flow rates decrease with decreasing mass hold-up. Initially, when the mass hold-up $m_{tA} = 3$, for example, the flow rates $\dot{m}_A$ increase with increasing vibrational energy for values of α less than about 1.5 and decrease with further increases in α. The same variation is observed at intermediate values of mass-hold-up in Figure 6.8. However, as in Figure 6.8, for relatively low mass hold-ups, the flow rates decrease

Figure 7.11: The profiles of solid fraction ν_A and ν_B for the individual species, the mixture temperature w, and the mixture solid fraction $\nu = \nu_A + \nu_B$ for spacing $\Delta_A = 1.05, 1.1, 1.15$ when $r = 1.222$, $\alpha = 1$, $V_n^2 = V_t^2 = V_\tau^2 = 1$, $m_{tA} = m_{tB} = 3$, and $e_{AA} = e_{BB} = 0.95$.

Figure 7.12: The profiles of mean velocities u_A and u_B for spacing $\Delta_A = 1.05, 1.1, 1.15$ when $r = 1.222$, $\alpha = 1$, $V_n^2 = V_t^2 = V_\tau^2 = 1$, $m_{tA} = m_{tB} = 3$, and $e_{AA} = e_{BB} = 0.95$.
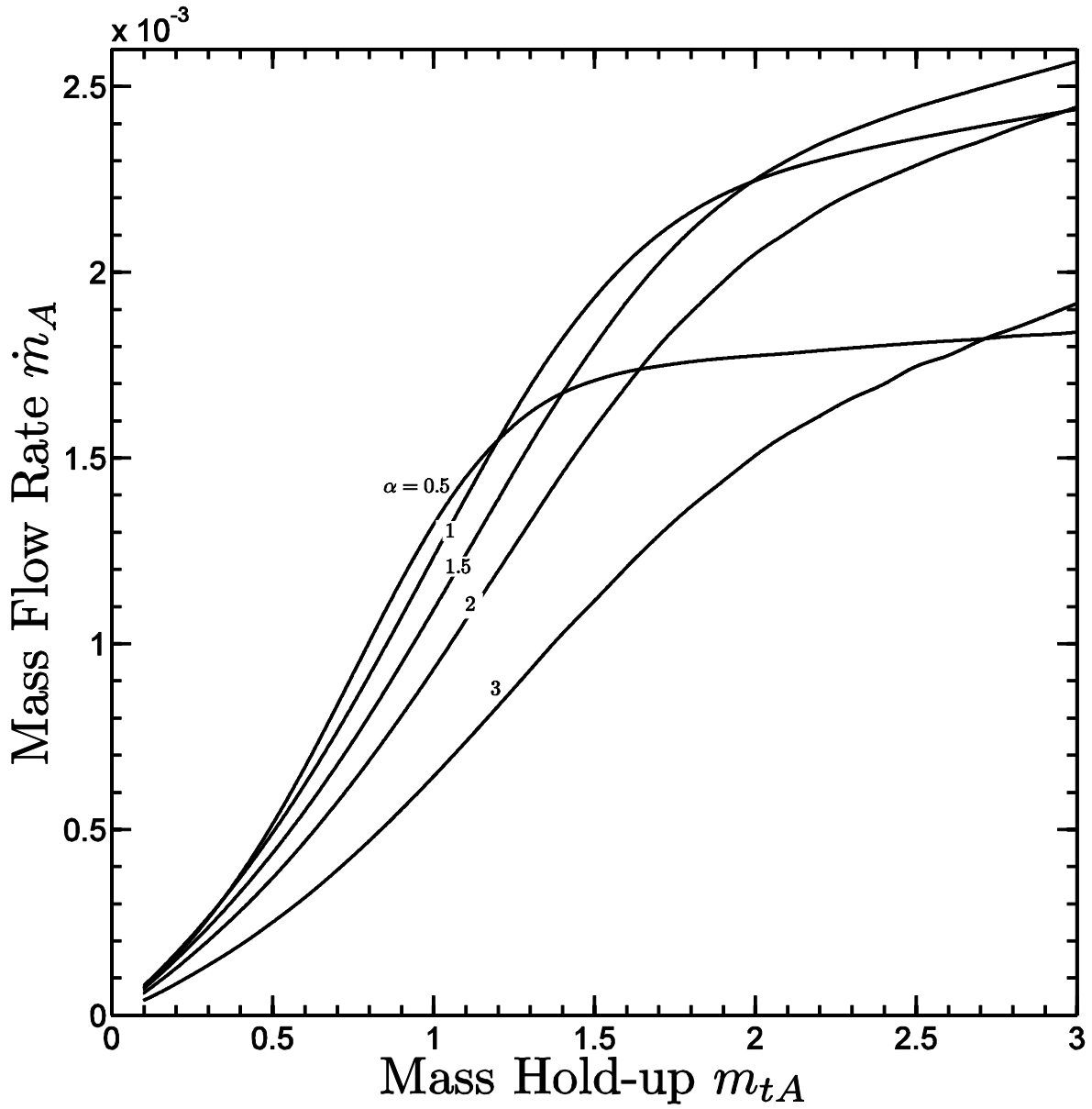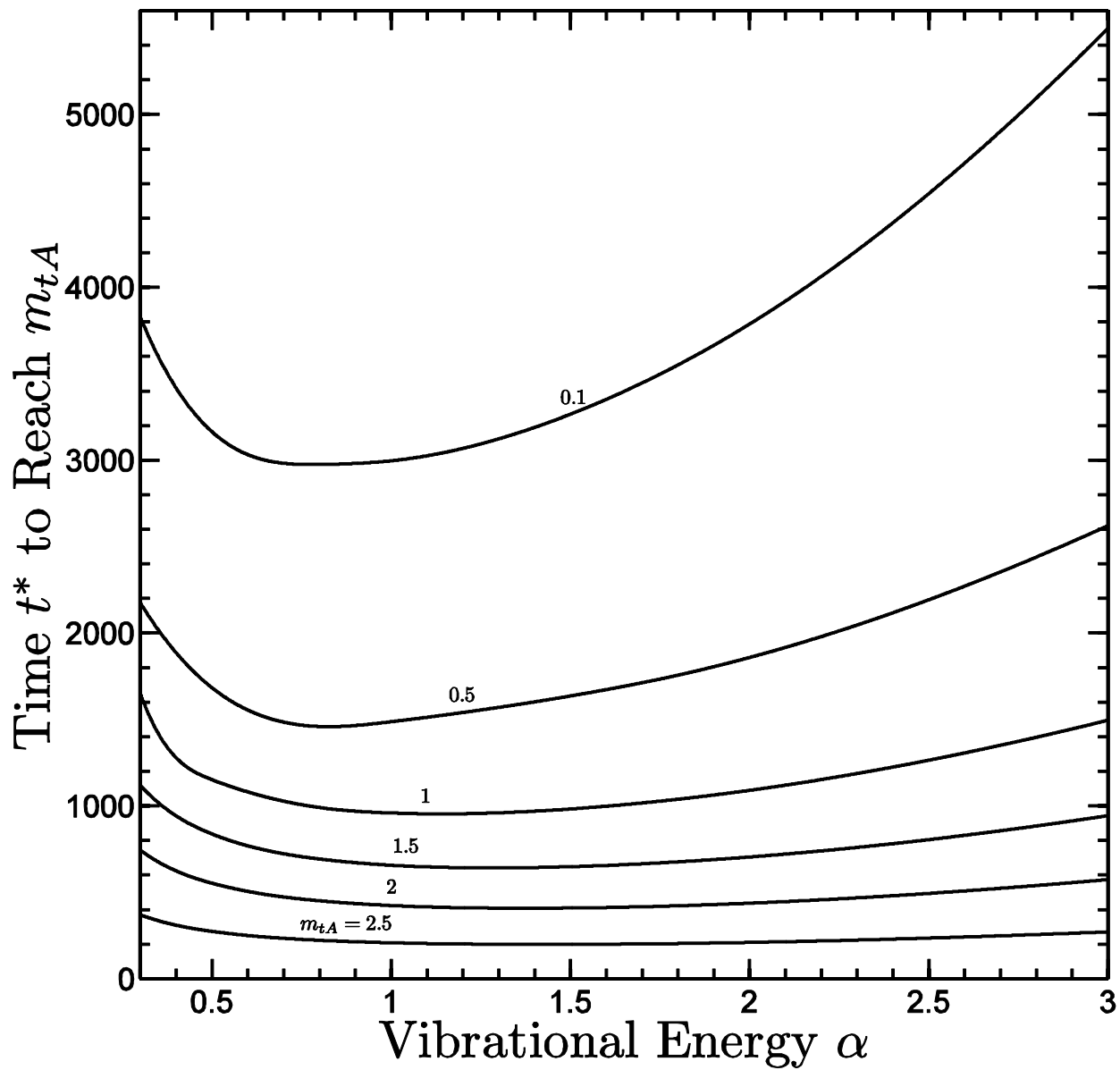
Figure 7.13: The variation of mass flow rate $\dot{m}_A$ with mass hold-up m_{tA} for vibrational energy $\alpha = 0.5, 1, 1.5, 2, 3$ when $r = 1.222$, $V_n^2 = V_t^2 = V_\tau^2 = 1$, $m_{tB} = 3$, and $e_{AA} = e_{BB} = 0.95$.

monotonically with increasing values of α. Figure 7.14 shows the corresponding explicit time variations of mass hold-up m_{tA} and mass flow rate $\dot{m}_A$. Interestingly, sieving at the highest value ($\alpha = 3$) requires the longest time reach the final value $m_{tA} = .1$ of mass hold-up of species A . This is an indication that the flow rates may actually be impeded by increasing the vibrational energy of the sieve. In Figure 7.15, we explore this in more detail by focusing on a case in which the initial value of mass hold-up is $m_{tA} = 3.0$, and by showing explicitly how the time t^* to reach a specified (lower) value of mass hold-up varies with total vibrational energy α. For relatively low values of α, as the total vibrational energy increases, the times required to reach a prescribed value of m_t decreases, and the decrease is more substantial as the final value of m_{tA} decreases. However, there is a value of α that minimizes the time to reach any intermediate value of m_{tA}, and further increases in α actually increase the time required. For $\alpha = .5, 1, 2,$ and 3. Figure 7.16 shows the corresponding profiles of the solid fraction v_A and v_B for the individual species, as well as the profiles of the corresponding temperature $w \equiv \sqrt{T}$ the solid fraction $v = v_A + v_B$ of the whole mixture at the initial time (i.e. when $m_{tA} = 3.0$), and Figure 7.17 shows the corresponding mean velocity profiles u_A and u_B with shapes similar to those shown in Figure 7.7. These profiles have the same qualitative features as those shown in Figures 7.6 and 7.7 (at the early stages of sieving) and Figures 7.11 and 7.12. As we have already observed in several other contexts, increasing the total vibrational energy α makes the flows more thermalized, more dilute, and faster.

In Figures 7.18 to 7.22, we show the results of a similar study to demonstrate how, for a fixed total vibrational energy, changing the distribution of vibrational energy in different directions affects the flows. In Figure 7.18, for example, we show the variation of mass flow rate $\dot{m}_A$ with mass hold-up m_{tA} (from $m_{tA} = 3$ to $m_{tA} = .1$) for degree of vertical vibrations $V_n^2 = 0, 1, 2, 3$
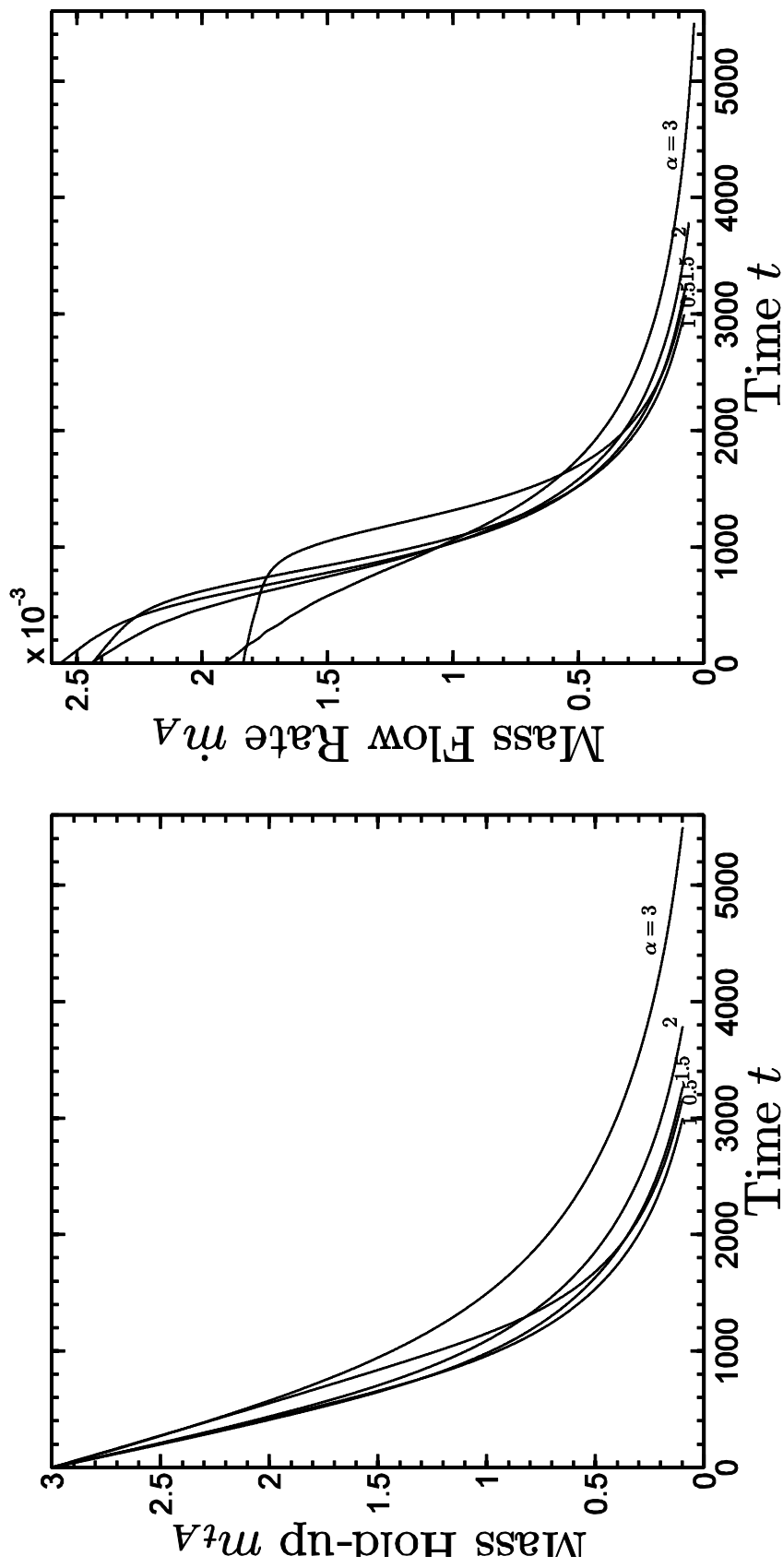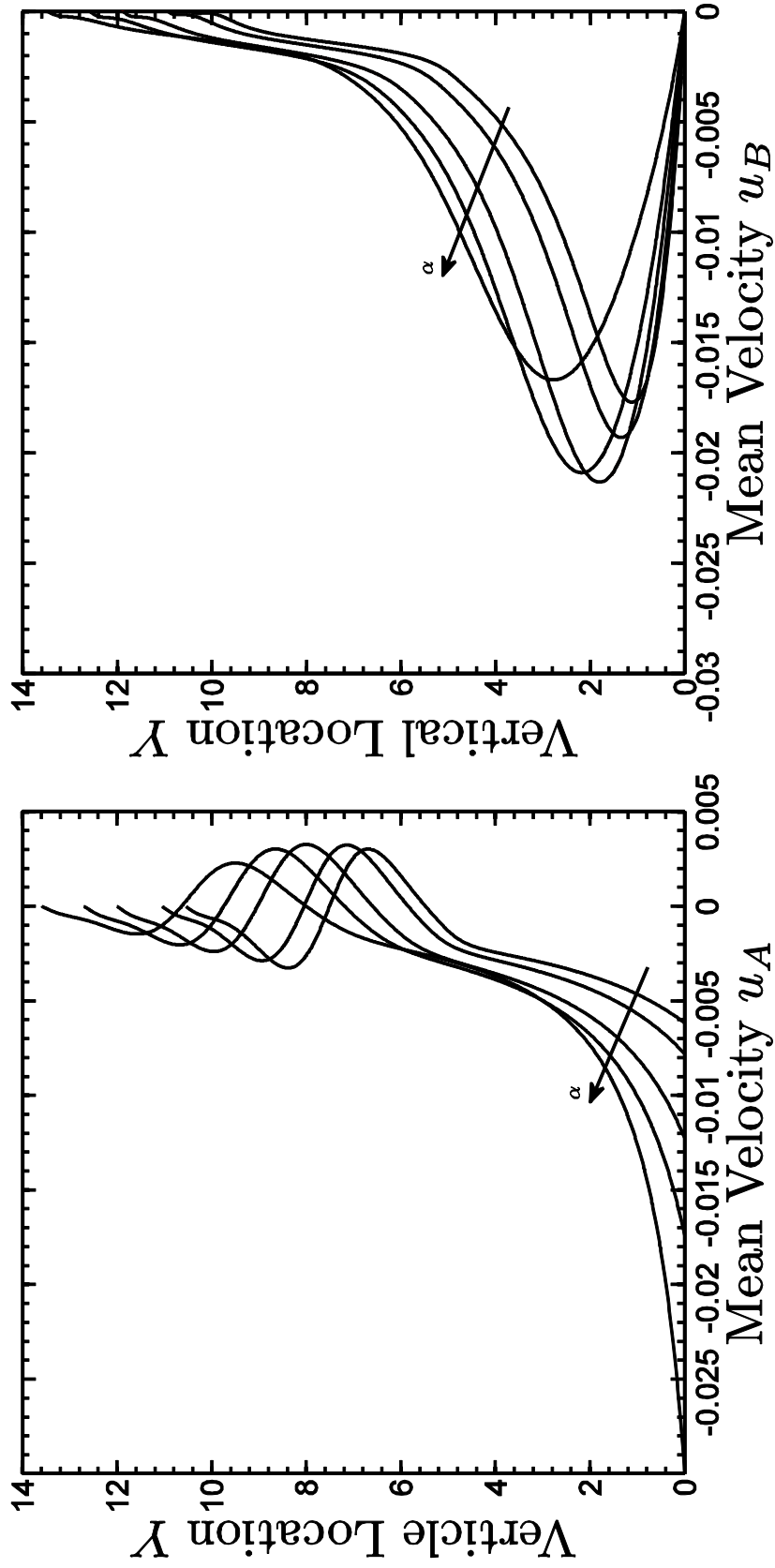
Figure 7.14: The variations of mass hold-up m_{tA} and mass flow rate $\dot{m}_A$ with time t for vibrational energy $\alpha =$ 0.5, 1,, 1.5, 2, 3 when $r = 1.222$, $V_n^2 = V_t^2 = V_\tau^2 = 1$, $m_{tB} = 3$, and $e_{AA} = e_{BB} = 0.95$.

Figure 7.15: the variation of time t^* to reach a prescribed value of m_{tA} with vibrational energy α for mass hold-up $m_{tA} = 0.1, 0.5, 1, 1.5, 2, 2.5$ when $r = 1.222$, $V_n^2 = V_t^2 = V_\tau^2 = 1$, $m_{tB} = 3$, and $e_{AA} = e_{BB} = 0.95$.
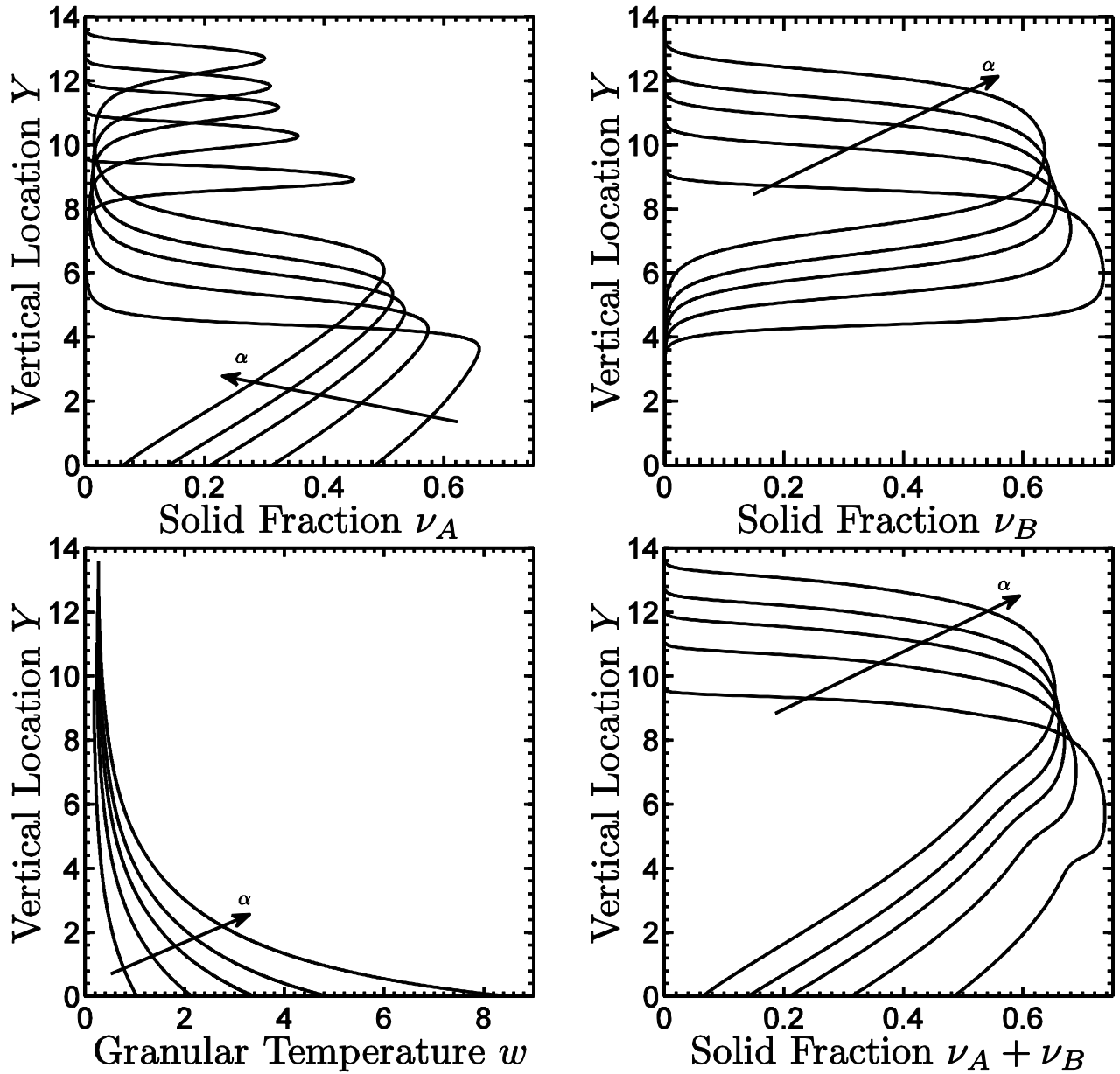
Figure 7.16: The profiles of solid fraction ν_A and ν_B for the individual species, the mixture temperature w, and the mixture solid fraction $\nu = \nu_A + \nu_B$ for vibrational energy $\alpha = 0.5, 1, 1.5, 2, 3$ when $r = 1.222$, $V_n^2 = V_t^2 = V_\tau^2 = 1$, $m_{tA} = m_{tB} = 3$, and $e_{AA} = e_{BB} = 0.95$.

**Figure 7.17:** The profiles of mean velocities u_A and u_B for vibrational energy $\alpha = 0.5, 1, 1.5, 2, 3$ when $V_n^2 = V_t^2 = V_\tau^2 = 1$, $m_{tA} = m_{tB} = 3$, $r = 1.222$, and $e_{AA} = e_{BB} = 0.95$.
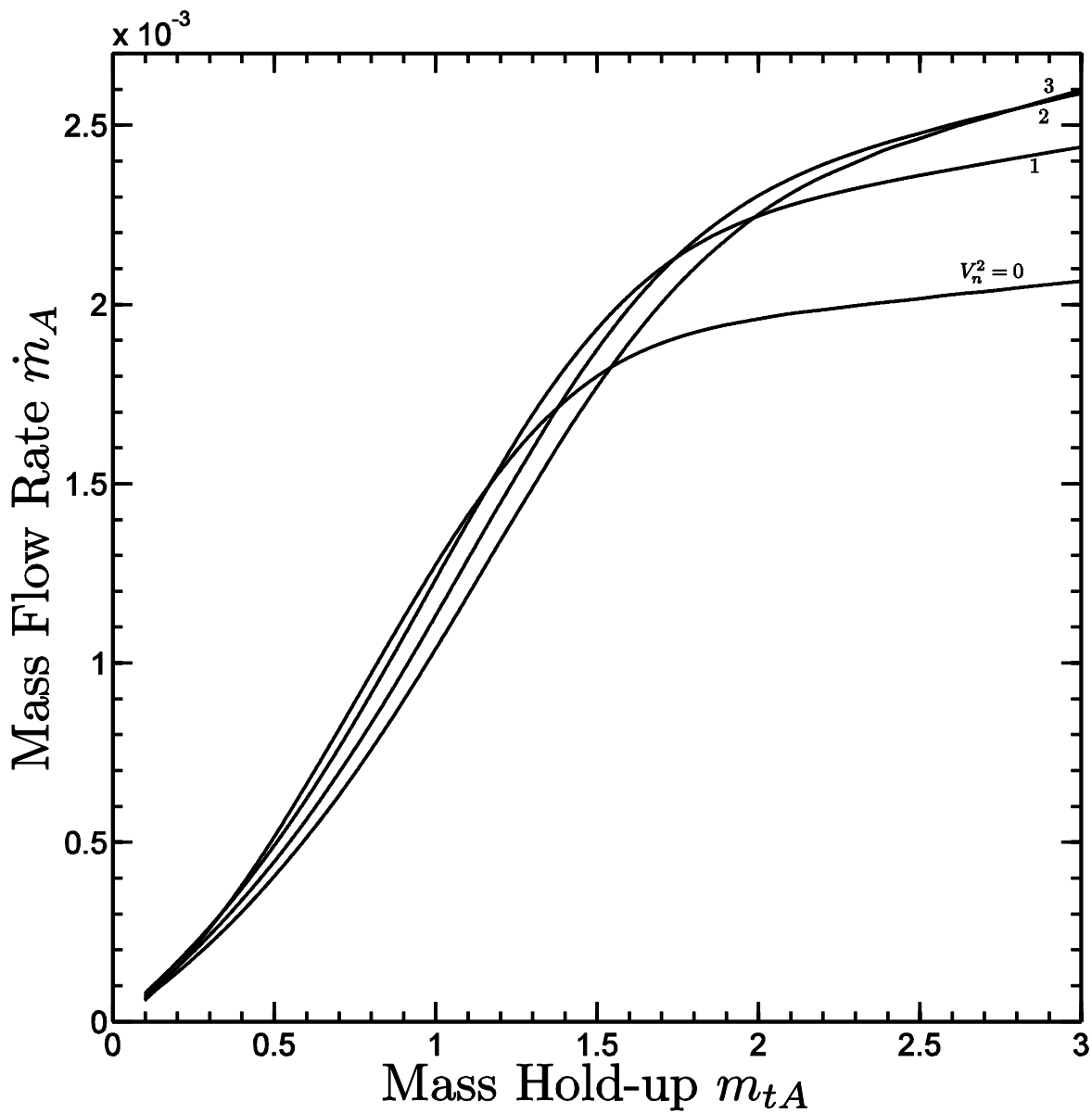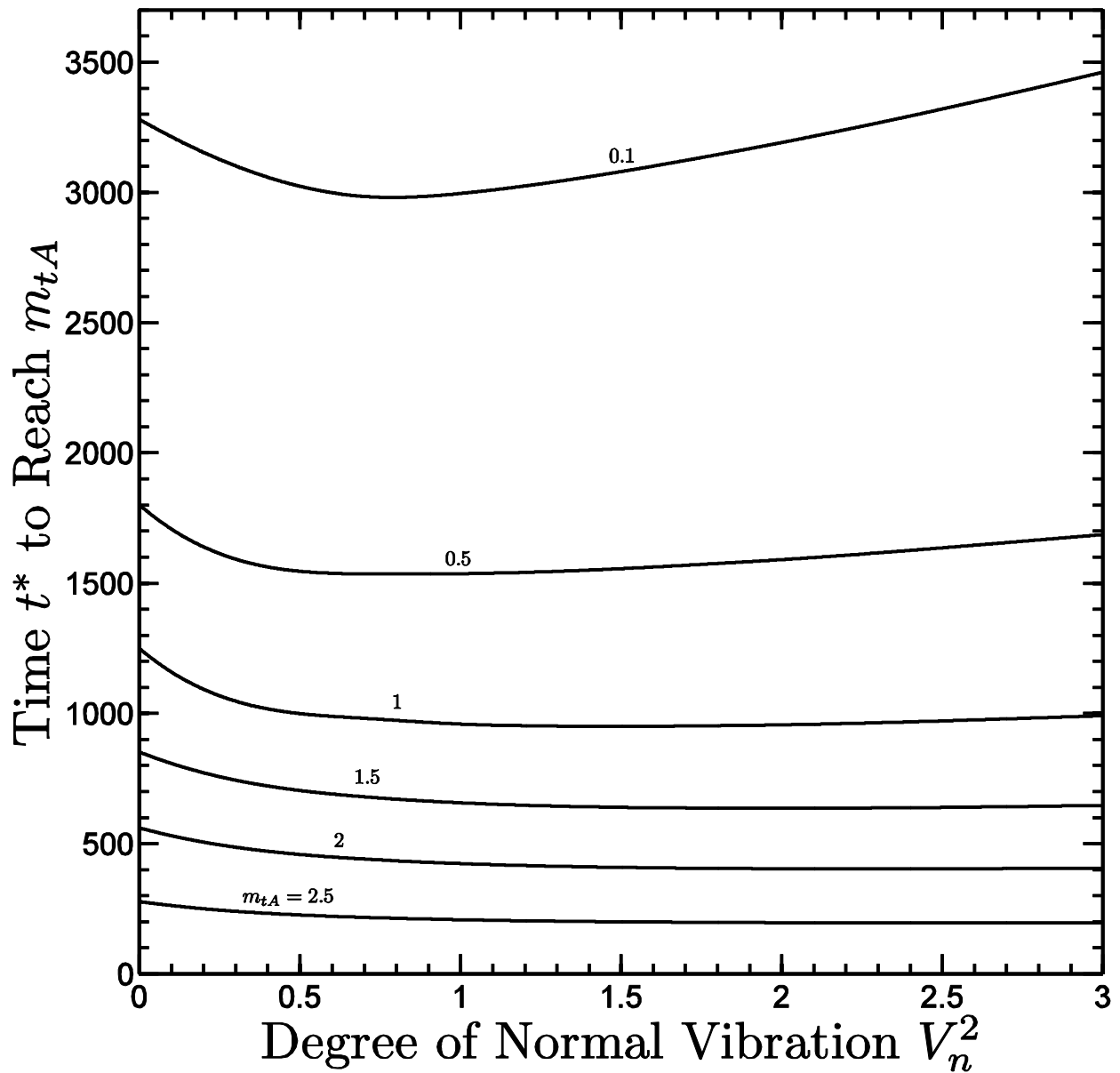
Figure 7.18: The variation of mass flow rate $\dot{m}_A$ with mass hold-up m_{tA} for degree of normal vibration $V_n^2 = 0, 1, 2, 3$ when $r = 1.222$, $\alpha = 1$, $V_\tau^2 = 0$, $m_{tB} = 3$, and $e_{AA} = e_{BB} = 0.95$.

171

(when $r = 1.222$, $\alpha = 1$, $V_\tau^2 = 0$, $m_{tB} = 3$, and $e_{AA} = e_{BB} = 0.95$). This corresponds to a study in which the vibrational energy is converted in three separate increments from entirely tangential (in the t-direction) to entirely normal. As we have already seen in Figures 7.8 and 7.13, the flow rates decrease with decreasing mass hold-up. Figure 7.18 demonstrates that a sieve vibrating with more of its energy distributed in the normal direction produces higher mass flow rates $\dot{m}_A$ when the mass hold-up m_{tA} is relatively large, but lower mass flow rates $\dot{m}_A$ when the mass hold-up m_{tA} is small. This same phenomenon was observed when discussing Figure 6.15 for sieving of monosized materials. Figure 7.19 shows the corresponding explicit time variations of mass hold-up m_{tA} and mass flow rate $\dot{m}_A$. In Figure 7.20, we focus on a case in which the initial value of mass hold-up is $m_{tA} = 3.0$ and show explicitly how the time t^* to reach a specified (lower) value of mass hold-up varies with normal vibrational energy V_n^2. Typically there is an optimum value of V_n^2 that minimizes the time to reach a prescribed intermediate value of m_{tA}. This indicates that for lower values (of V_n^2), the flows are under-thermalized, more dense but slower; and for higher values (of V_n^2), the flows are over-thermalized, more dilute and faster. However, according to Figure 7.20 the time required to reach any intermediate value of mass hold-up m_{tA} depends only modestly on the value of V_n^2.

This seems to indicate that, while we anticipate that varying V_n^2 from 0 (purely tangential vibrations) to 3 (purely normal vibrations) will significantly change the individual profiles of solid fraction and mean normal velocity within the flows, the competing effects of density and velocity very nearly cancel. Figure 7.21 shows the corresponding profiles of the solid fraction ν_A and ν_B for the individual species, as well as the profiles of the corresponding temperature $w \equiv \sqrt{T}$ the solid fraction $\nu = \nu_A + \nu_B$ of the whole mixture at the initial time (i.e. when $m_{tA} = 3.0$), and Figure 7.22 shows the corresponding mean velocity profiles u_A and u_B with
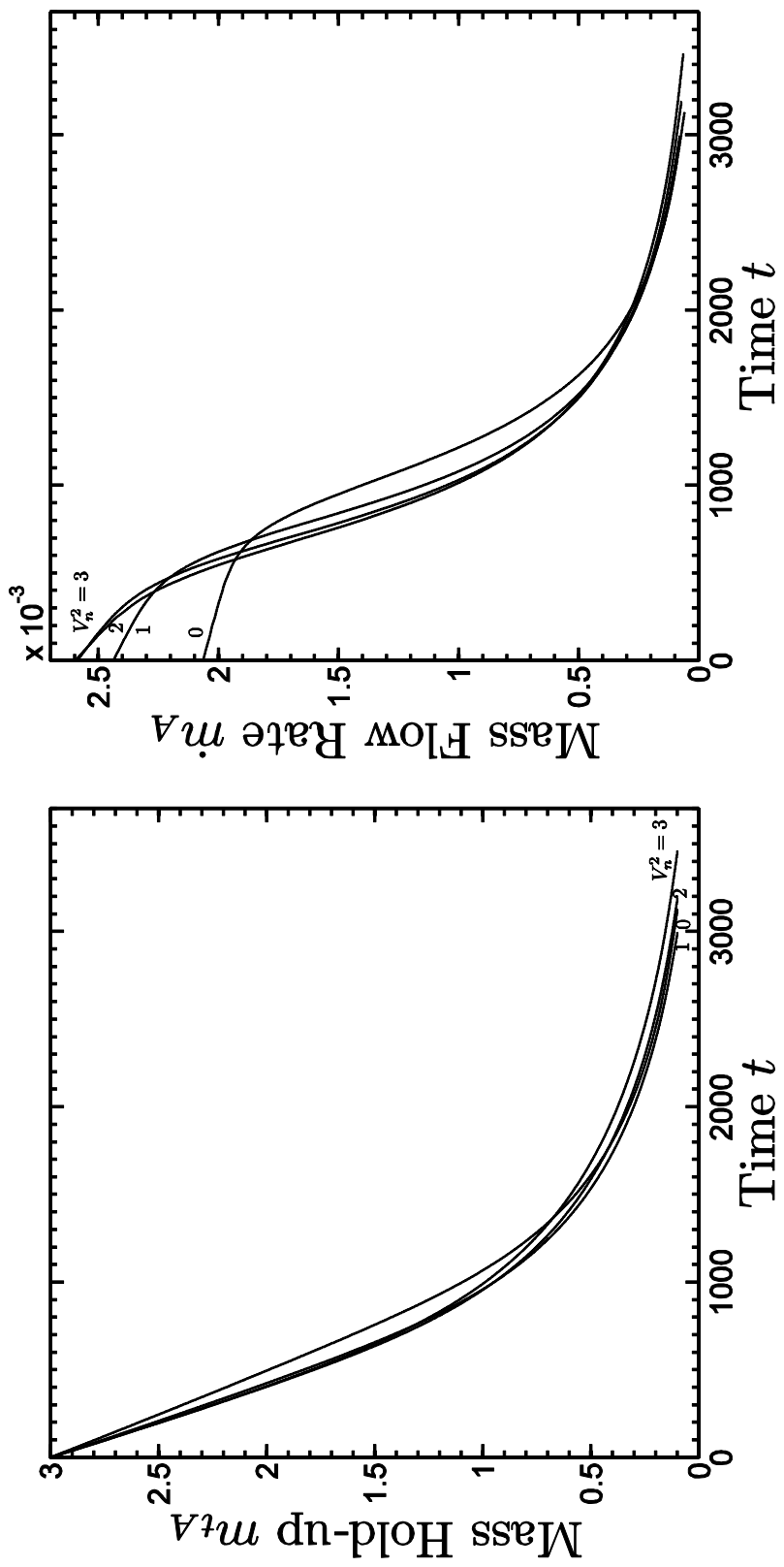
Figure 7.19: The variations of mass hold-up m_{tA} and mass flow rate $\dot{m}_A$ with time t for degree of normal vibration $V_n^2 = 0, 1, 2, 3$ when $r = 1.222$, $\alpha = 1$, $V_\tau^2 = 0$, $m_{tB} = 3$, and $e_{AA} = e_{BB} = 0.95$.

Figure 7.20: the variation of time t^* to reach a prescribed value of m_{tA} with degree of normal vibration V_n^2 for mass hold-up $m_{tA} = 0.1, 0.5, 1, 1.5, 2, 2.5$ when $r = 1.222$, $\alpha = 1$, $V_\tau^2 = 0$, $m_{tB} = 3$, and $e_{AA} = e_{BB} = 0.95$.
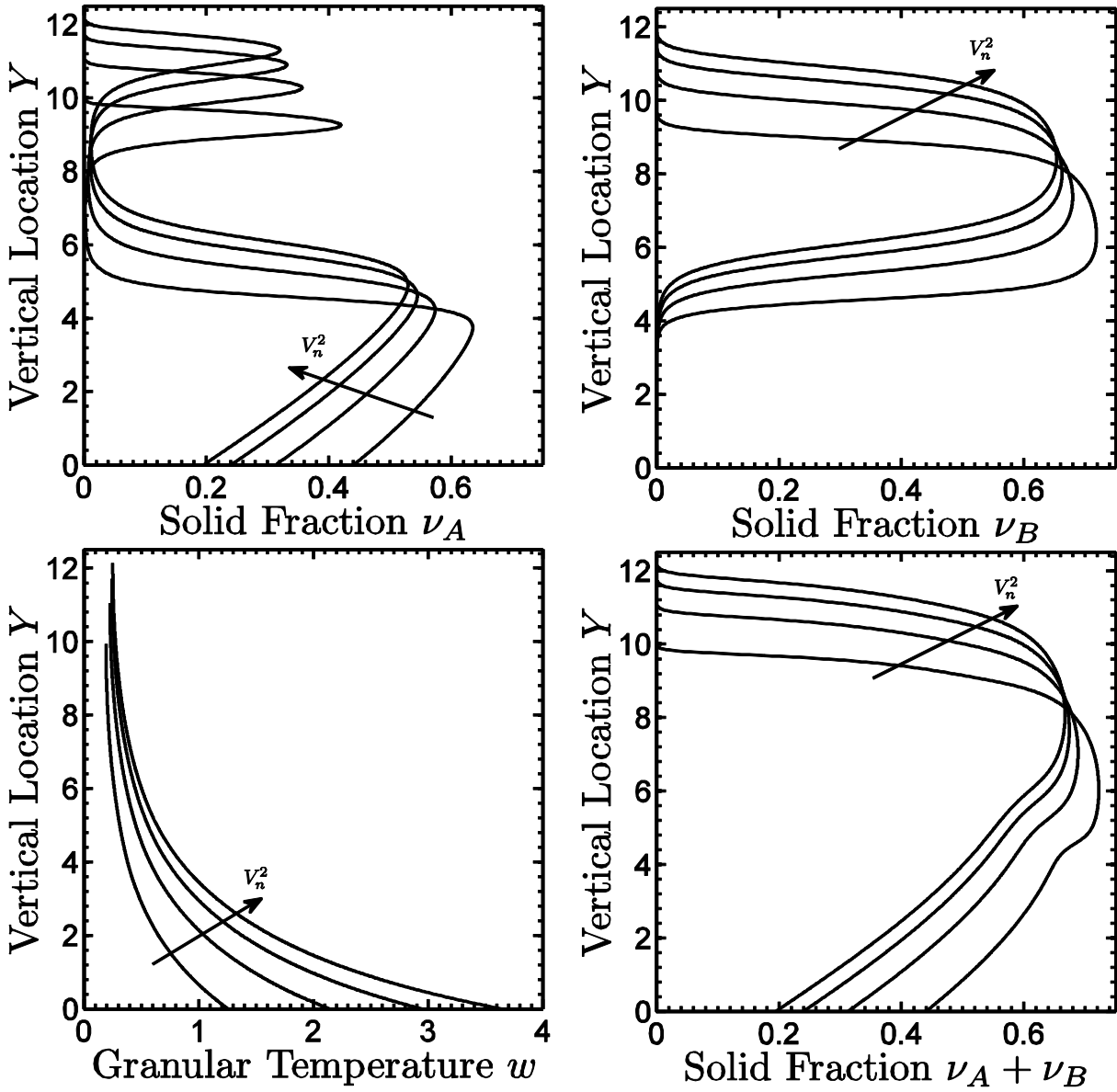
Figure 7.21: The profiles of solid fraction ν_A and ν_B for the individual species, the mixture temperature w, and the mixture solid fraction $\nu = \nu_A + \nu_B$ for degree of normal vibration $V_n^2 = 0, 1, 2, 3$ when $r = 1.222$, $\alpha = 1$, $V_\tau^2 = 0$, $m_{tA} = m_{tB} = 3$, and $e_{AA} = e_{BB} = 0.95$.
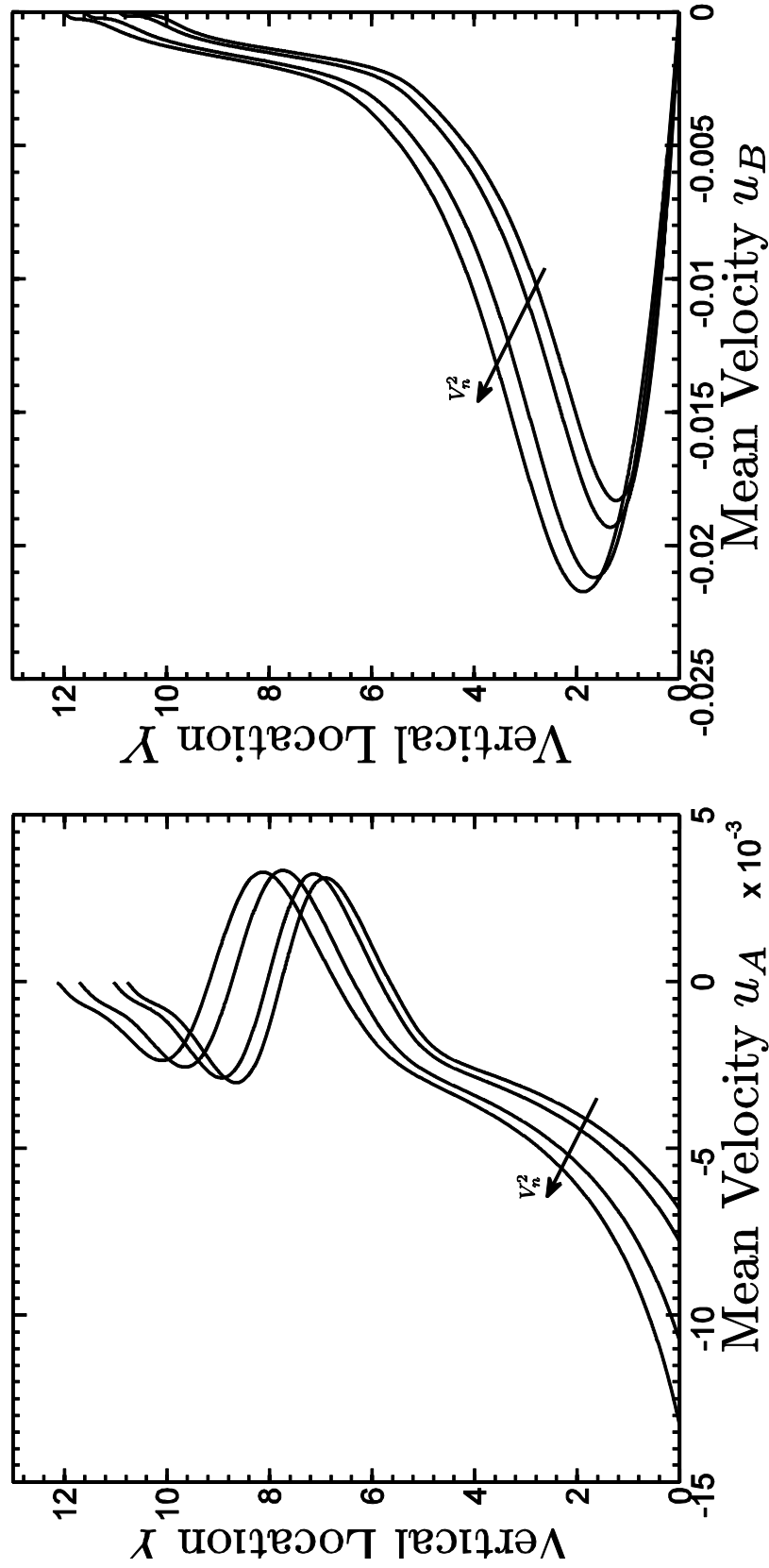
Figure 7.22: The profiles of mean velocities u_A and u_B for degree of normal vibration $V_n^2 = 0, 1, 2, 3$ when $r = 1.222$, $\alpha = 1$, $V_\tau^2 = 0$, $m_{tA} = m_{tB} = 3$, and $e_{AA} = e_{BB} = 0.95$.

shapes similar to those shown in Figure 7.7. Both figures include results for $V_n^2 = 0, 1, 2, 3$. These profiles have the same qualitative features as those shown in Figures 7.6 and 7.7 (at the early stages of sieving) and Figures 7.11 and 7.12, as well as in Figure 7.16 and 7.17. In all cases, there is a region of several particle diameters within the sieve that is occupied entirely by small particles A, as well as a layer of small particles trapped at the top of the assembly. For purely tangential vibrations the flows are only slightly thermalized and relatively slow. In this case, there is a region of several particle diameters within the sieve that is occupied entirely by small particles A, a sharp transition to a region in which the only larger particles B reside, and a layer of small particles trapped at the top of the assembly. As the tangential vibrations are converted to normal vibrations, the assemblies become significantly more thermalized and faster. The region populated only by small particles immediately above the sieve becomes deeper and more dilute; the transition to the region of large particles becomes more mixed; and the trapped layer of small particles at the top of the assemblies remains. Of interest also is how the flows of a fixed initial mass of small particles A through the sieves are influenced by the presence of different amounts of species B. In Figure 7.23, for example, we show the variation of mass flow rate $\dot{m}_A$ of species A with mass hold-up m_{tA} of species A for three different values of the mass hold-up $m_{tB} = 2, 3, 4$ of speices B when m_{tA} is initially equal to 3 (and when $\Delta_A = 1.1$, $r = 1.222$, $\alpha = 1$, $V_n^2 = V_t^2 = V_\tau^2 = 1$, and $e_{AA} = e_{BB} = 0.95$). As has already been observed several times (e.g. in Figures 7.8, 7.13, and 7.18), the flow rates $\dot{m}_A$ diminish as the mass hold-up m_{tA} decreases. However, interestingly Figure 7.23 shows that, for a fixed instantaneous value of m_{tA}, the corresponding mass flow rate $\dot{m}_A$ increases with increasing m_{tB}. This somewhat counterintuitive result indicates that the flow of the small particles A through the sieve are actually enhanced by increasing amount of species B. This is due to two effects. First, once
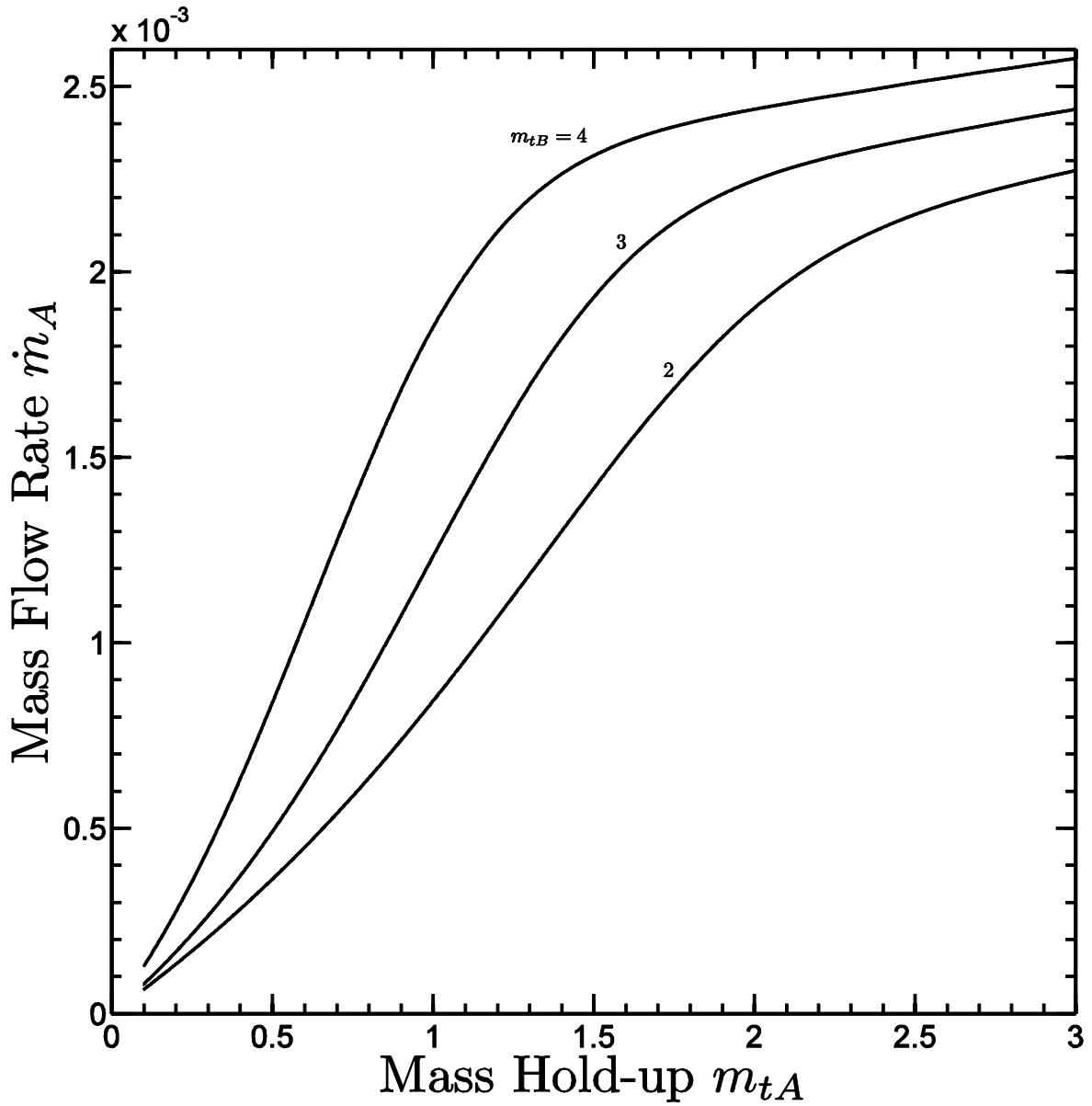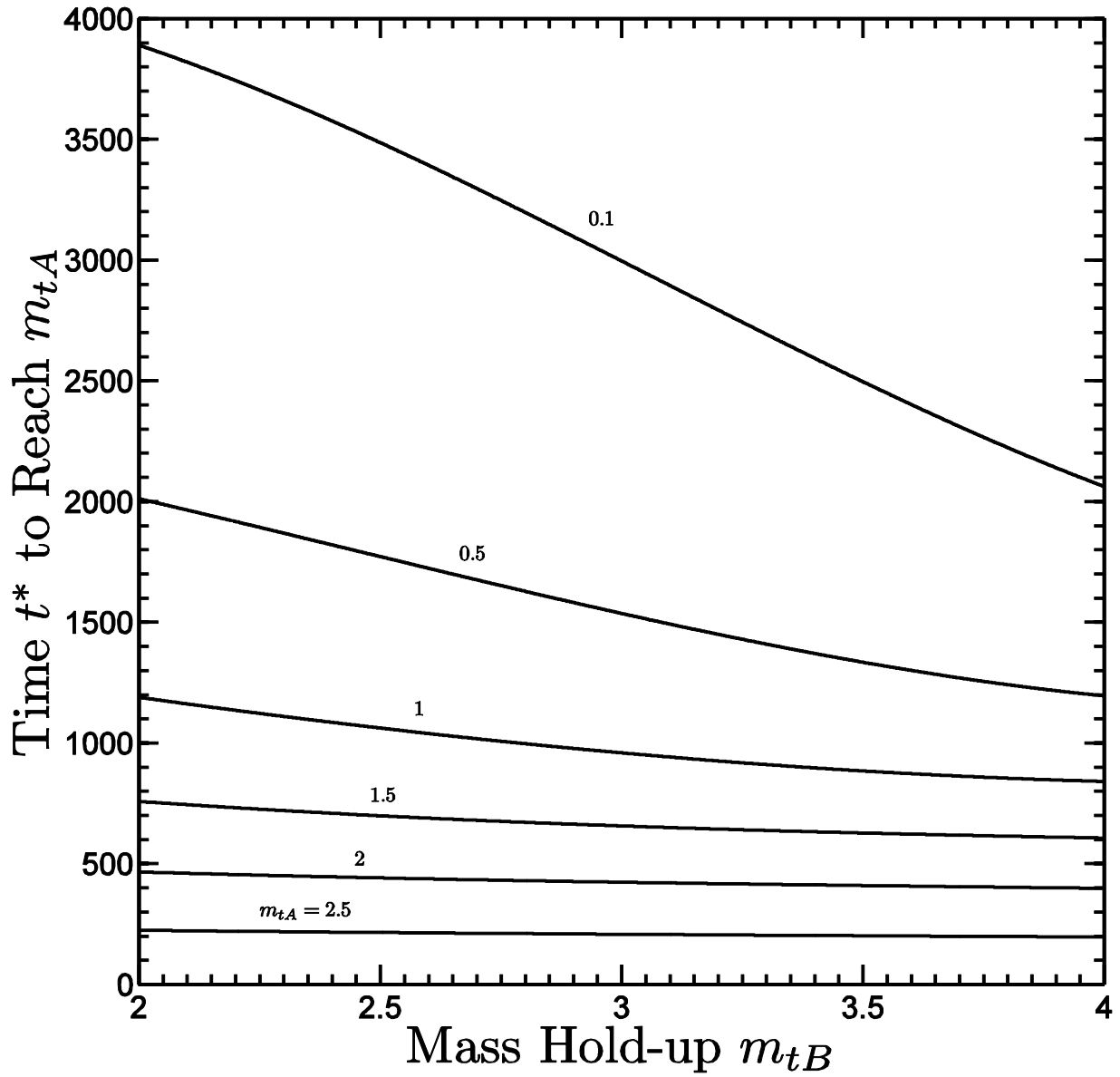
Figure 7.23: The variation of mass flow rate $\dot{m}_A$ with mass hold-up m_{tA} for mass hold-up $m_{tB} = 2, 3, 4$ when $\Delta_A = 1.1$, $r = 1.222$, $\alpha = 1$, $V_n^2 = V_t^2 = V_\tau^2 = 1$, and $e_{AA} = e_{BB} = 0.95$.

the assembly is segregated, the presence of a region of larger particles B away from the sieve creates an overburden resting on the region of smaller particles A immediately adjacent to the sieve. This in turn increases the downward pressure on the small particles near the sieve. Second, in this range of m_{tB}, the degree of segregation actually increases as m_{tB} increases so the lower layer dominated by smaller particles is impeded by the presence of fewer larger particles. Figure 7.24 shows the corresponding explicit time variations of mass hold-up m_{tA} and mass flow rate $\dot{m}_A$. The right panel actually shows that beyond a certain *time* the flow rates $\dot{m}_A$ are smaller for larger values of m_{tB}. However, the cumulative effect of higher flow rates before that time is sufficient to ensure that the total time required to reach $m_{tA} = .1$ decreases with increasing m_{tB}. In Figure 7.25 we focus on the case in which the initial value of mass hold-up is $m_{tA} = 3.0$ and show explicitly how the time t^* to reach a specified (lower) value of mass hold-up varies with mass hold-up m_{tB}. In all cases, the time to reach a prescribed value of m_{tA} decreases as the total mass hold-up m_{tB} increases. In Figures 7.26, we show the corresponding profiles of solid fraction v_A and v_B for species A and B, mixture temperature w, and solid fraction $v = v_A + v_B$ of the whole mixture for the three cases $m_{tB} = 2, 3, 4$ (when $m_{tA} = 3.0$). Figure 7.27 shows the corresponding mean velocity profiles u_A and u_B with shapes similar to those shown in Figure 7.7. As m_{tB} increases, the region dominated by the presence of small particles A (near the sieve) and the region dominated by large particles B (above it) become more segregated, and the transition between the two regions becomes more distinct. Interestingly, at this value of $m_{tA}(= 3.0)$, adding more large particles B does not lower the granular temperature of the mixture significantly because they settle in a relatively unthermalized region where the rate at which they dissipate energy due to collisions is relatively low. In the last study of a case in which only one species can pass through the sieve, we demonstrate in Figures 7.28 to 7.32 how the size
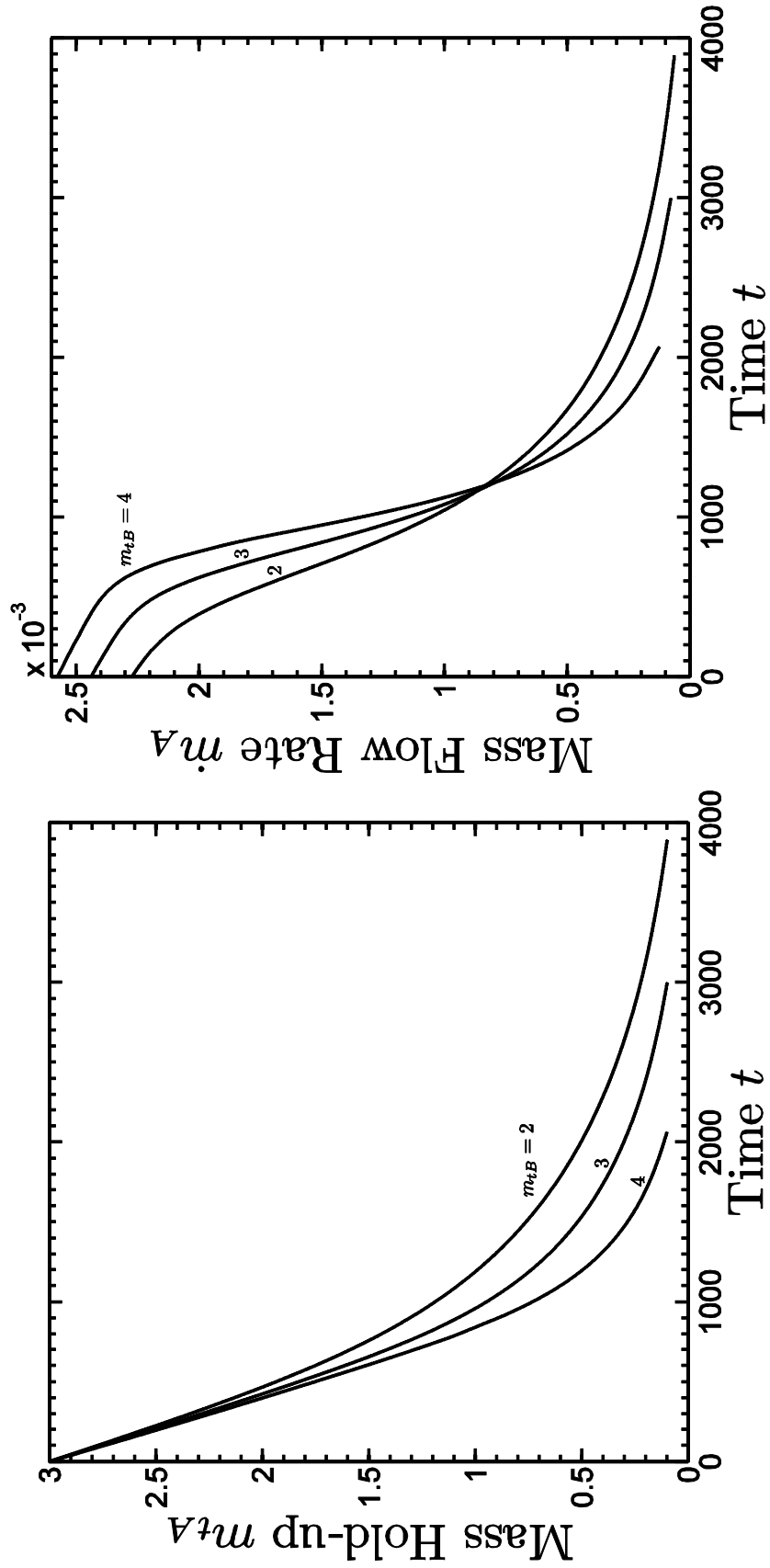
Figure 7.24: The variations of hold-up m_{tA} and mass flow rate $\dot{m}_A$ with time t for mass hold-up $m_{tB} = 2, 3, 4$ when $\Delta_A = 1.1$, $r = 1.222$, $\alpha = 1$, $V_n^2 = V_t^2 = V_\tau^2 = 1$, and $e_{AA} = e_{BB} = 0.95$.

Figure 7.25: The variation of time t^* to reach a prescribed value of $m_{t\mathrm{A}}$ with mass hold-up $m_{t\mathrm{B}}$ for mass hold-up $m_{t\mathrm{A}} = 0.1, 0.5, 1, 1.5, 2, 2.5$ when $\Delta_{\mathrm{A}} = 1.1$, $r = 1.222$, $\alpha = 1$, $V_n^2 = V_t^2 = V_\tau^2 = 1$, and $e_{\mathrm{AA}} = e_{\mathrm{BB}} = 0.95$.
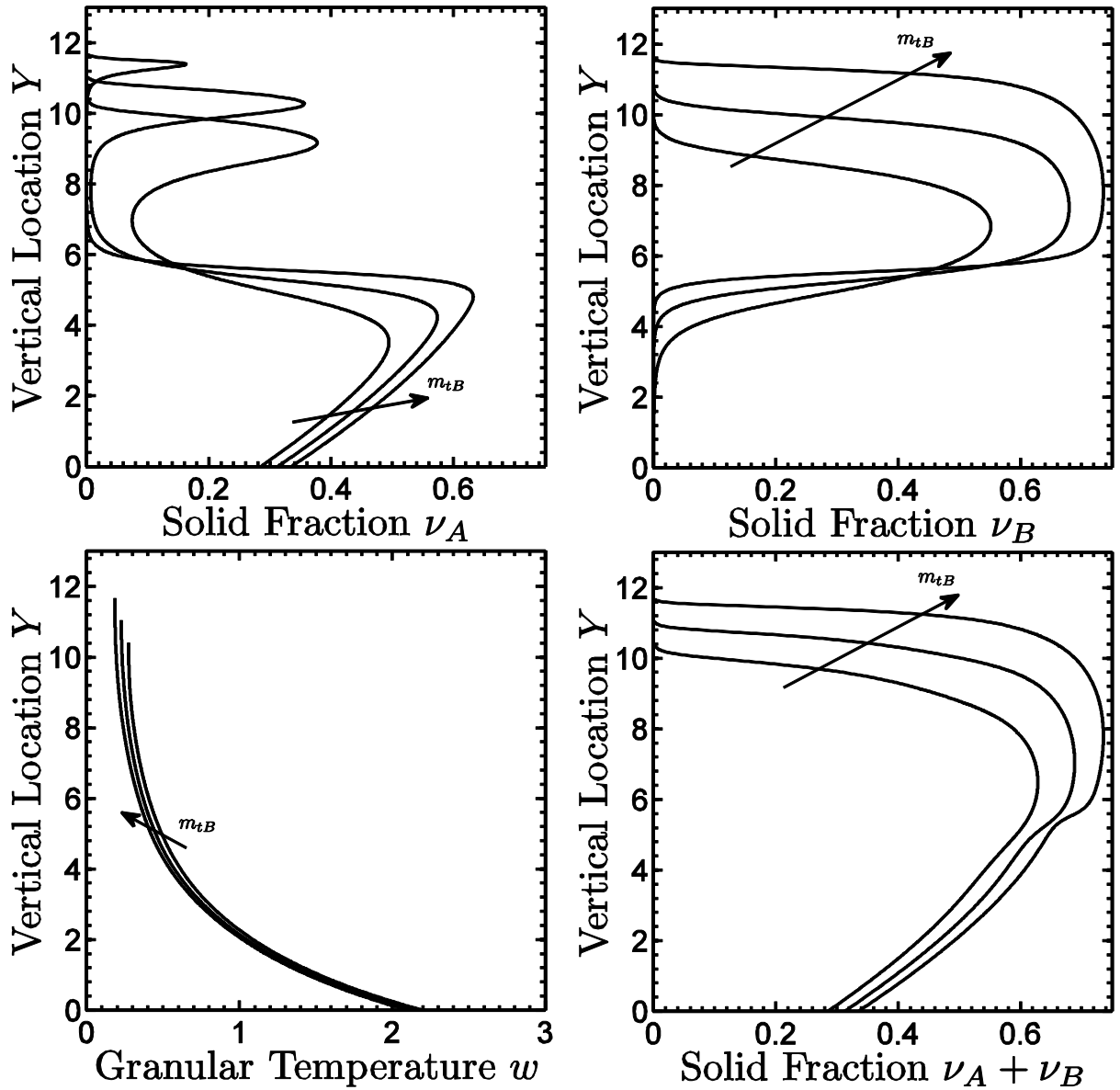
Figure 7.26: The profiles of solid fraction ν_A and ν_B for the individual species, the mixture temperature w, and the mixture solid fraction $\nu = \nu_A + \nu_B$ for mass hold-up $m_{tB} = 2, 3, 4$ when $\Delta_A = 1.1$, $r = 1.222$, $\alpha = 1$, $V_n^2 = V_t^2 = V_\tau^2 = 1$, $m_{tA} = 3$, and $e_{AA} = e_{BB} = 0.95$.
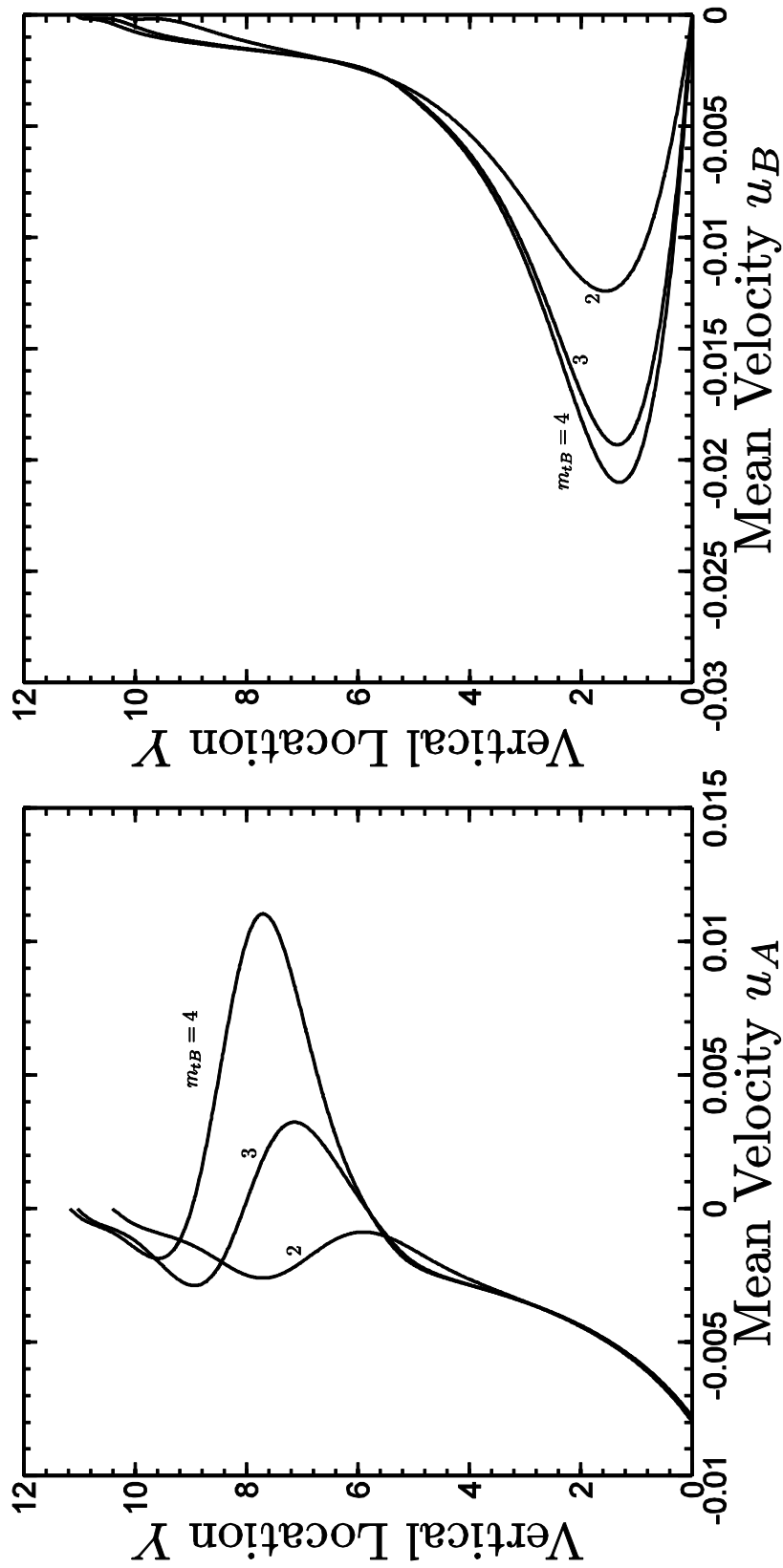
Figure 7.27: The profiles of u_A and u_B for mass hold-up $m_{tB} = 2, 3, 4$ when $\Delta_A = 1.1$, $r = 1.222$, $\alpha = 1$, $V_n^2 = V_t^2 = V_\tau^2 = 1$, $m_{tA} = 3$, and $e_{AA} = e_{BB} = 0.95$.

disparity between the two species affects the flows. In Figure 7.28 we show the variation of mass flow rate $\dot{m}_A$ with mass hold-up m_{tA} for diameter ratios $r = 1.15, 1.2,$ and 1.3 (and when $\Delta_A = 1.1,$ $m_{tB} = 3,$ $\alpha = 1,$ $V_n^2 = V_t^2 = V_\tau^2 = 1,$ and $e_{AA} = e_{BB} = 0.95$). Figure 7.29 shows the corresponding explicit time variations of mass hold-up m_{tA} and mass flow rate $\dot{m}_A$. Initially, when $m_{tA} = 3$, the mixture is highly segregated for all values of r shown. The region near the sieve is populated entirely by small particles A and is therefore identical in all three cases. Consequently Figure 7.28 indicates that the flow rates are identical. As m_{tA} decreases, the degree of segregation in the mixtures decreases more slowly in those mixtures with larger size ratios r. Consequently, at any intermediate value of m_{tA}, both the degree of segregation and the flow rates increase with increasing values of r. However, this effect is quite small in all cases shown because a large fraction of the small particles A in the initially segregated region near the sieve pass through before the mixing of species occurs. This fact is demonstrated in Figure 7.30, where we focus on the case in which the initial value of mass hold-up is $m_{tA} = 3.0$ and show explicitly how the time t^* to reach a specified (lower) value of mass hold-up varies with size ratio r. For the reasons described here, the times t^* decrease, but only very slightly with increasing r. In Figures 7.31, we show the corresponding profiles of solid fraction ν_A and ν_B for species A and B, mixture temperature w, solid fraction $\nu = \nu_A + \nu_B$ of the whole mixture for the three cases $r = 1.15, 1.2,$ and 1.3 (when $m_{tA} = 3.0$). Figure 7.32 shows the corresponding mean velocity profiles u_A and u_B with shapes similar to those shown in Figure 7.7. At this initial stage of the sieving process, the species are almost perfectly segregated. The profiles of solid fraction ν_A and ν_B and granular temperature w, as well as the mean normal velocity u_A at

Figure 7.28: The variation of mass flow $\dot{m}_A$ with mass hold-up m_{tA} for size ratio $r = 1.15, 1.2, 1.3$ when $\Delta_A = 1.1$, $m_{tB} = 3$, $\alpha = 1$, $V_n^2 = V_t^2 = V_\tau^2 = 1$, and $e_{AA} = e_{BB} = 0.95$.
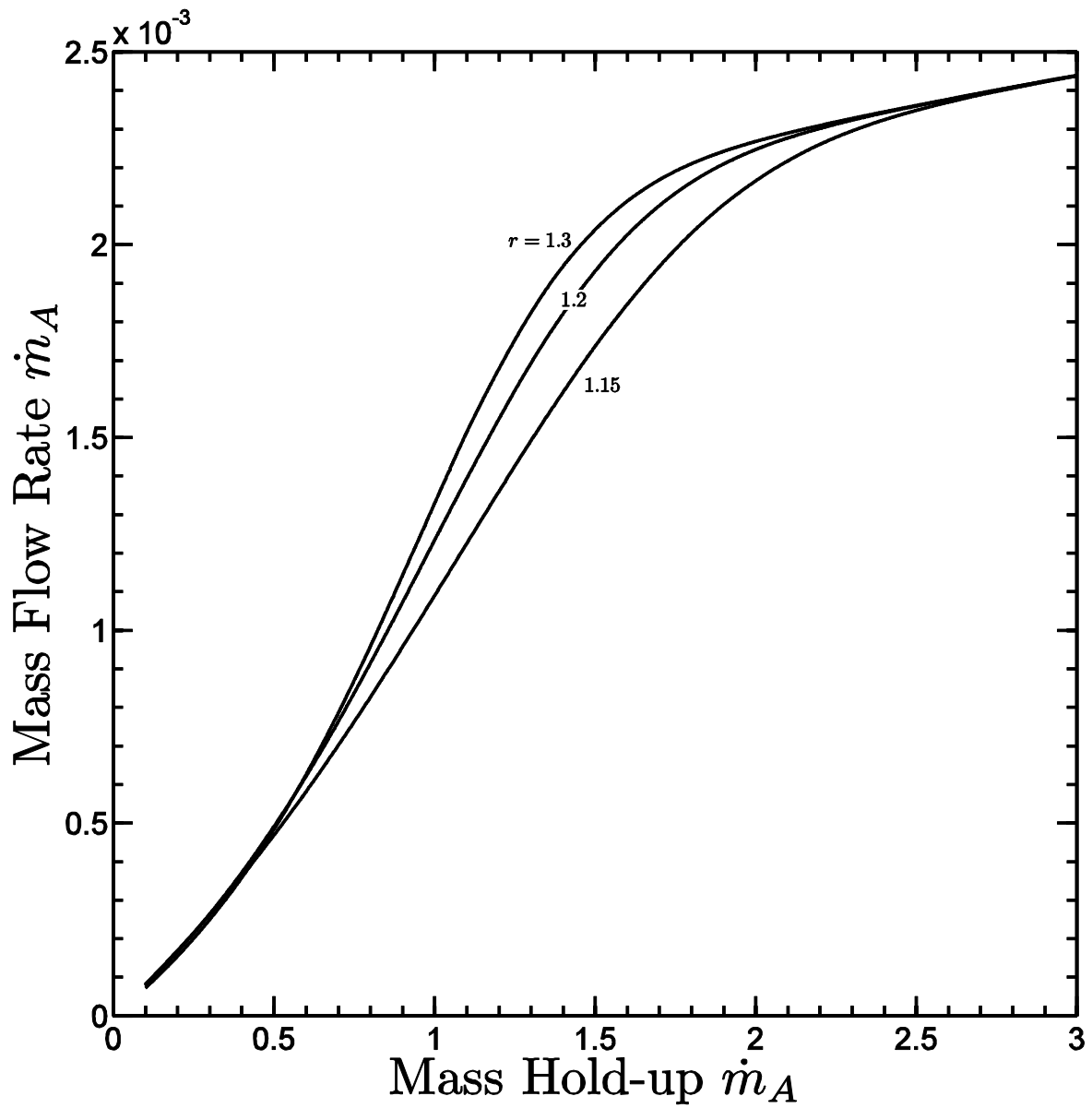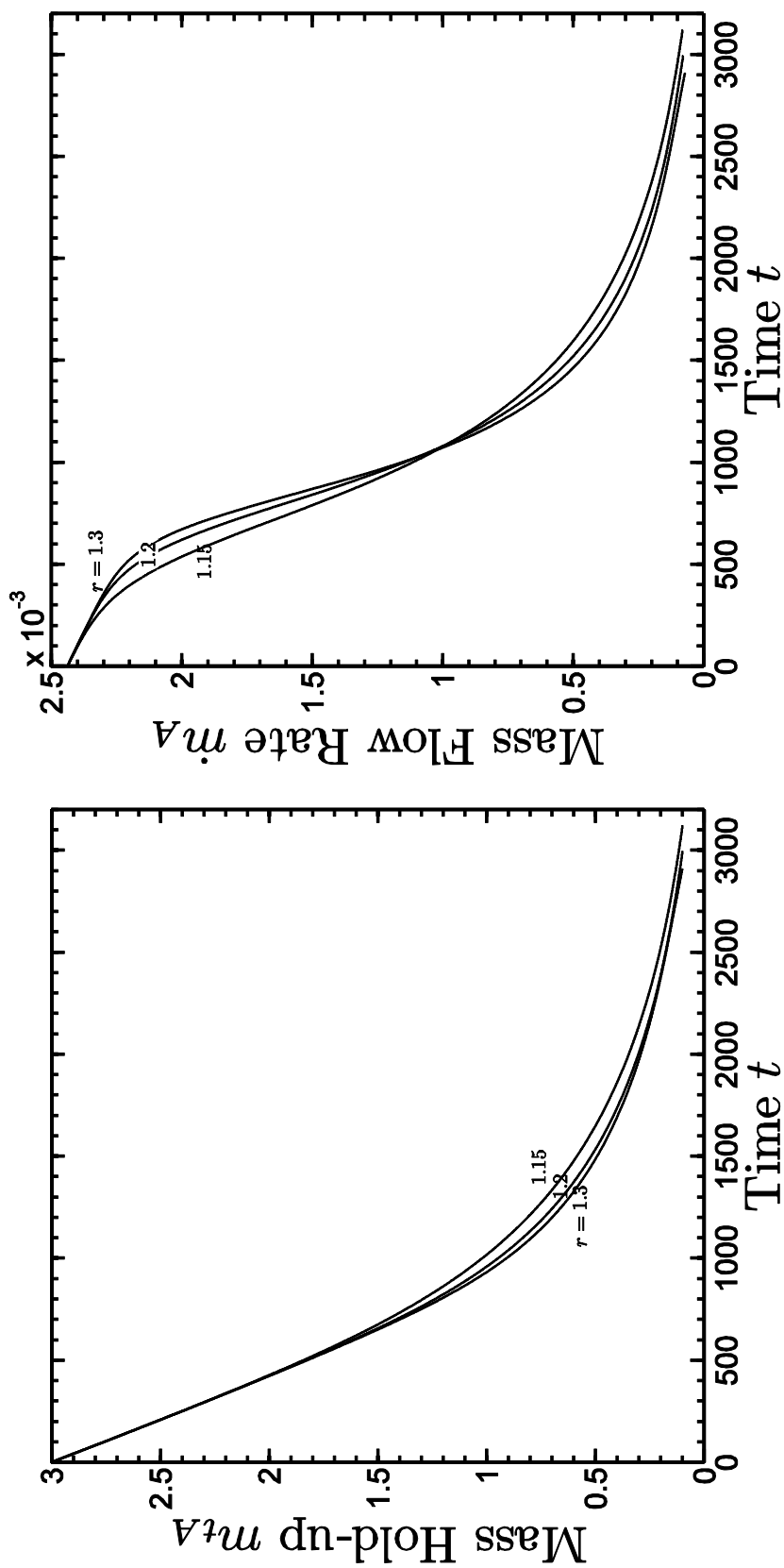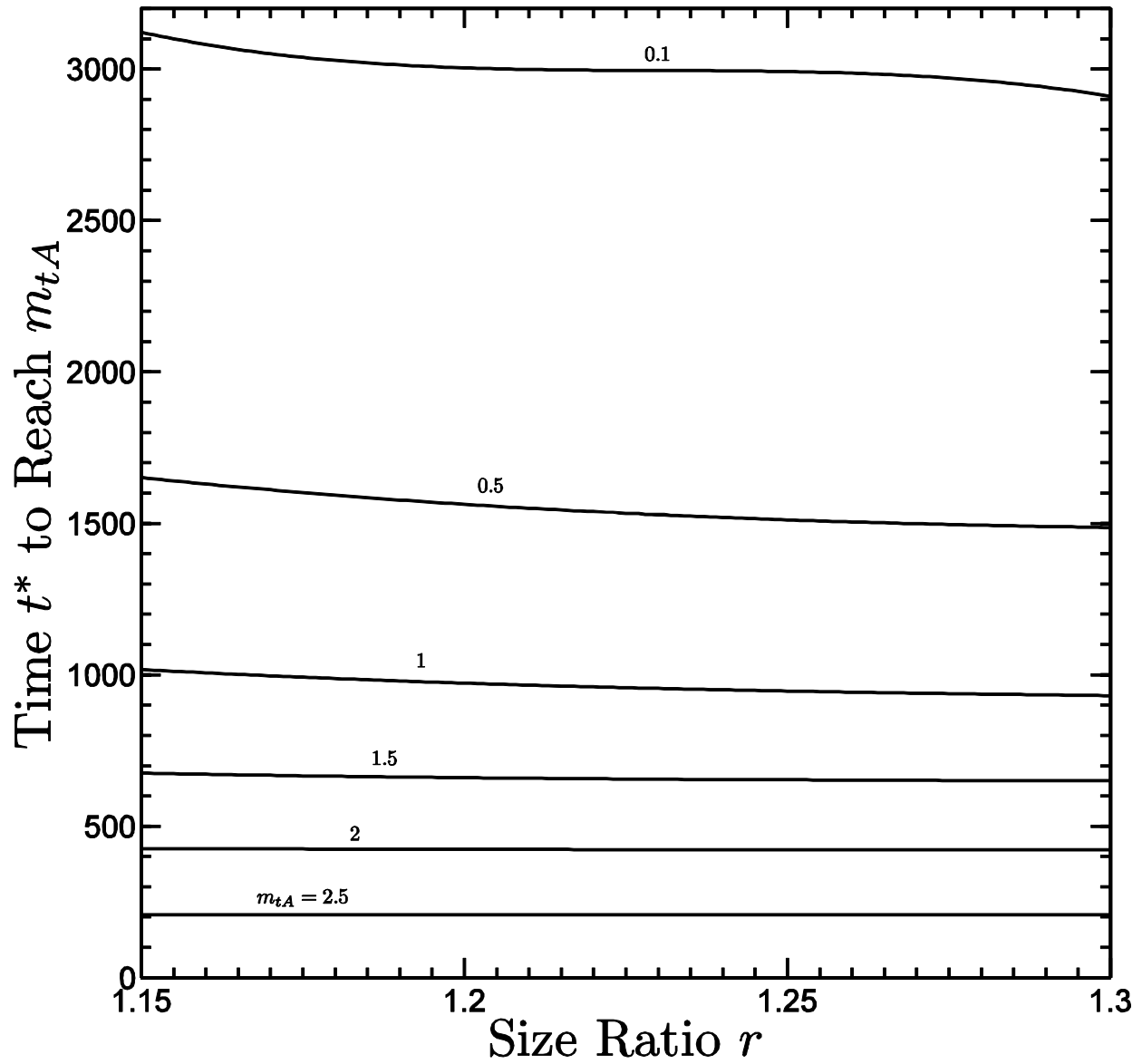
Figure 7.29: The variations of mass hold-up m_{tA} and mass flow rate $\dot{m}_A$ with time t for size ratio $r = 1.15, 1.2, 1.3$ when $\Delta_A = 1.1$, $m_{tB} = 3$, $\alpha = 1$, $V_n^2 = V_t^2 = V_\tau^2 = 1$, and $e_{AA} = e_{BB} = 0.95$.

Figure 7.30: The variation of time t^* to reach a prescribed value of m_{tA} with size ratio r for mass hold-up $m_{tA} = 0.1, 0.5, 1, 1.5, 2, 2.5$ when $\Delta_A = 1.1$, $m_{tB} = 3$, $\alpha = 1$, $V_n^2 = V_t^2 = V_\tau^2 = 1$, and $e_{AA} = e_{BB} = 0.95$.
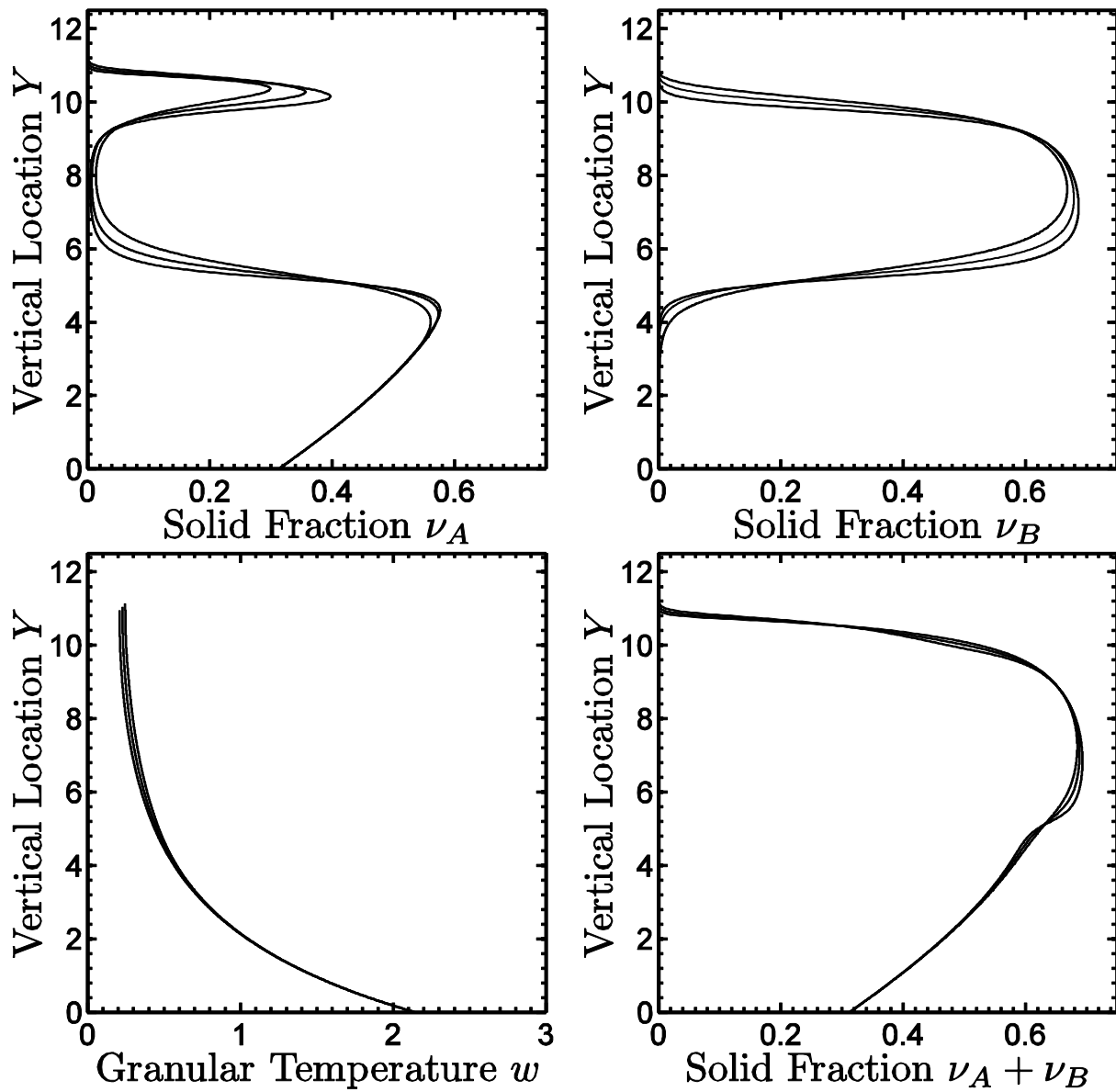
Figure 7.31: The profiles of solid fraction ν_A and ν_B for the individual species, the mixture temperature w, and the mixture solid fraction $\nu = \nu_A + \nu_B$ for size ratio $r = 1.15, 1.2, 1.3$ when $\Delta_A = 1.1$, $r = 1.222$, $\alpha = 1$, $V_n^2 = V_t^2 = V_\tau^2 = 1$, $m_{tB} = m_{tA} = 3$, and $e_{AA} = e_{BB} = 0.95$.

Figure 7.32: The profiles of mean velocity u_A and u_B for size ratio $r = 1.15, 1.2, 1.3$ when $\Delta_A = 1.1$, $m_{tA} = m_{tB} = 3$, $\alpha = 1$, $V_n^2 = V_t^2 = V_\tau^2 = 1$, and $e_{AA} = e_{BB} = 0.95$.
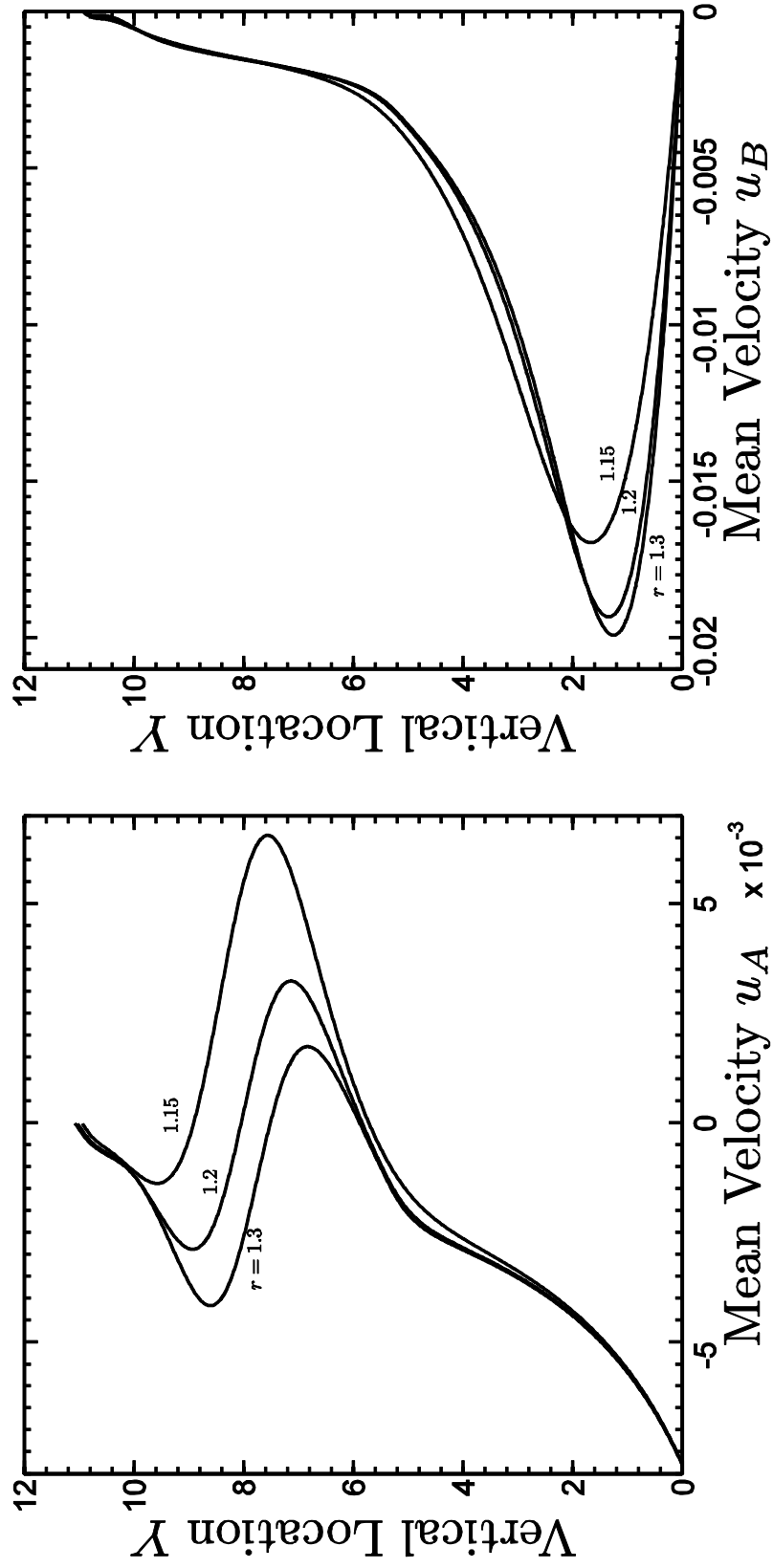
189

the sieve corresponding to different values of r are nearly identical. Consequently the flow rates $\dot{m}_A$ for $m_{tA} = 3.0$ (that may be read from Figure 7.28) are identical as well.

As a final example, we consider the case in which the holes on the sieve are large enough to allow *both* the small particles A and the large particles B to pass through. In Figure 7.33 we show the variation of flow rates (right panel) $\dot{m}_A$ (of the smaller particles) and $\dot{m}_B$ (of the larger particles) with time t when the size ratio between the particles is $r = 1.02$ and the spacing on the sieve is $\Delta_A = 1.07$ (for $\alpha = 1$, $V_n^2 = V_t^2 = V_\tau^2 = 1$, and $e_{AA} = e_{BB} = 0.95$). The initial values of the two mass hold-up are $m_{tA} = m_{tB} = 3$ for both the smaller and larger particles. In Figure 7.32 we show the corresponding time variations of the mass hold-ups (left panel) m_{tA} (of the smaller particles) and m_{tB} (of the larger particles). Due to even the slight size disparity, the smaller particles are more concentrated near the sieve than are the larger particles, and they fit somewhat more easily through the holes in the sieve. So initially the flow rate $\dot{m}_A$ for species A is significantly higher than the corresponding flow rate $\dot{m}_B$ for species B. Flow rates $\dot{m}_A$ decrease monotinically with time. However, because the size disparity is small, the region near the sieve is populated (but at lower concentration) by larger particles as well. Consequently, even at the earliest times, the flow rates $\dot{m}_B$ are non-zero. Moreover, during these early times the flow rate $\dot{m}_B$ actually increases with time as shielding due to the presence of species A rapidly diminishes. For all times after approximately two-thirds of species A but only about one-third of species B has passes through the sieve, the flow rate $\dot{m}_B$ is greater than $\dot{m}_A$, and both decrease to zero asymptotically.
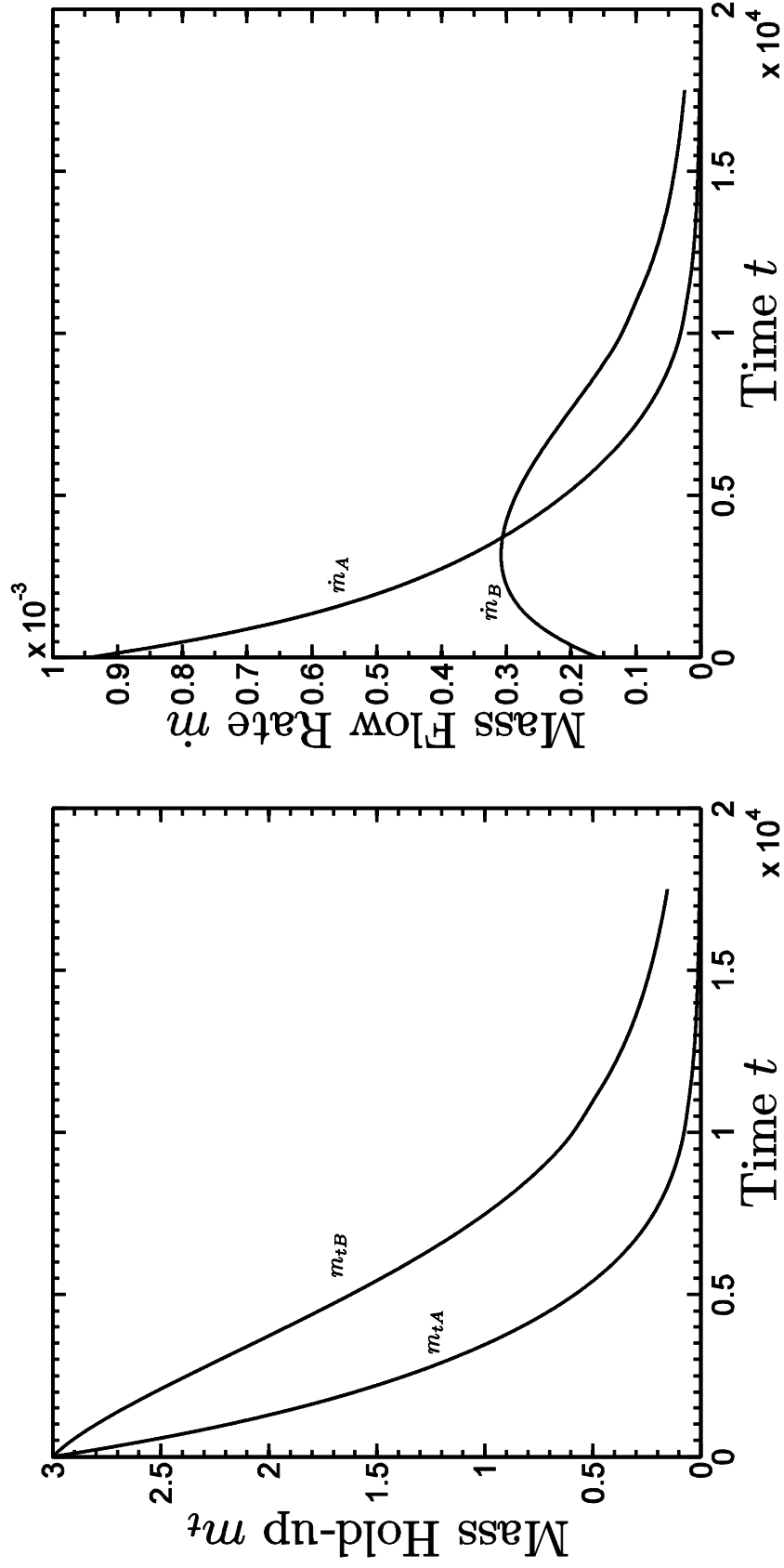
Figure 7.33: The variations of mass hold-up m_{tA} and m_{tB}, mass flow rate $\dot{m}_A$ and $\dot{m}_B$ with time t when $r = 1.02$, $\alpha = 1$, $V_\tau^2 = 0$, $m_{tB}(t = 0) = m_{tA}(t = 0) = m_{tA}(t = 0) = 3$, and $e_{AA} = e_{BB} = 0.95$.

Chapter 8

Conclusion

In this work, we have studied three granular flow applications: inclined flows; particle segregation; and particle sieving. The common thread in each is the influence that vibrating boundaries have on the results. In the case of inclined flows, even without vibrations, gravity would drive the flows, and the relative slip between the granular material and the bumpy boundaries would provide a mechanism to thermalize the assemblies. In this case, vibrations modify the flows. By contrast, in the cases of segregation and sieving studied here, boundary vibrations are the primary drivers of the processes. However, in all cases, our approach was the same: derive appropriate boundary conditions; combine the conditions with an already existing but relatively simple constitutive theory; and formulate the resulting well posed boundary value problem. In obtaining results, our interest is always in how the parameters that describe the boundary geometry and the boundary vibrations affect the results. In the case of the bumpy boundaries on the inclines, the geometry is described by the size of the bumps and the spacing between them relative to the size of the particles. In the case of flat mesh sieves (which were also used in our study of segregation with holes that were too small for the particles to pass through), the geometry is described by the spacings between adjacent parallel fibers. Each sieve can have different spacings for each set of perpendicular fibers. In all cases, the vibratory motion of the vibrating boundaries is described statistically by the full second moment of its velocity fluctuations around its mean velocity. We have provided a simple way to relate these statistical parameters to the amplitudes, frequencies, and phase angles of the boundaries' vibrations in three independent directions.

As a special case of inclined flows, we first considered the thermalization of a granular assembly resting on a horizontal bumpy vibrating boundary. This case isolates the effects of vibrations from the driving force of gravity, and shows very clearly how that under most circumstances normal vibrations are more effective than tangential vibrations at transferring energy to the flows, but that this effect is diminished (and eventually slightly reversed) as the bumpiness of the boundary increases. In addition, the results indicate that the phase angle of the vibrations can be adjusted to induce mean motion tangent to the boundary, and that the velocities induced can be optimized by adjusting the fraction of the total vibrational energy that is expended in the normal and tangential directions.

For inclined flows, the theory predicts that increasing either the total energy of vibration or the degree of normal vibration makes the flows deeper, faster, more dilute, and more thermalized. Although there is a competing effect between increased speeds and decreased volume fraction, the mass flow rates increase, as well. By adjusting the phase angle of the vibrations, it is possible (at least for small angles of inclination) for the boundary to drive the flows entirely or partially uphill. However, these possibilities only occur for small angles of inclination, indicating that the force exerted due to the choice of phase angle is small compared to the driving force of gravity, and that the overwhelming influence on the flows is due to the energy transferred from the boundary vibrations.

Vibratory sieving combines the physics of energy transfer with the phenomenon of particle segregation. We isolated the effects of energy transfer by studying the sieving of monosized assemblies. As for thermalization of horizontal assemblies, the results demonstrate that energy is best transferred to the assemblies by normal vibrations. However, because more highly thermalized assemblies are more dilute, the flow rates can actually decrease if too much

energy is supplied to the flows. Consequently, when the direction of vibration is fixed, there is an optimum value of vibrational energy that maximizes the flow rates through the sieve, and that value decreases as the mass on the sieve decreases and increases as the normal vibrations are converted to tangential vibrations.

We separately isolated the effects of segregation by considering binary mixtures that are thermalized by vibrating mesh surfaces with holes that are too small to allow any particles to pass through. The theory predicts dramatic segregation by size and by inelasticity of particles of the same size. When the particles differ only by size, a region of small particles forms near the boundary and a region of larger particles forms further away. When the particles differ only by their inelasticity, a region of the more inelastic particles forms near the boundary, and a region of the more elastic particles forms further away. When the particles differ in both respects, size differences dominate the segregation process. In this case, the smaller particles will collect near the boundary even if they are more elastic than the larger ones.

Finally, we considered sieving of binary mixtures and observed how the effects of energy transfer and segregation combine to affect the flows. Most results were for the case in which only the small particles could pass through the sieve.   Not surprisingly, because in many instances the region nearest the boundary is, especially for early times, dominated by particles of only one size, the observations concerning the effect of energy transfer on the flow rates of monosized assemblies apply to the binary mixtures as well. This includes the occurrence of an optimum level of vibrational energy that minimizes the time for the small paricles to pass through. Typically, by the time the larger particles migrate to the boundary, a large fraction of the smaller particles have already passed through, and as a result the effects of shielding of the small particles by the large particles is relatively small.

For sieving of binary mixtures, we also examined how changing the total mass of the large particles affects the flows of a fixed mass of small particles. The results indicate that increasing the presence of larger particles actually increases the flow rates of the small particles. This somewhat counter intuitive result is another demonstration that the segregated nature of the assemblies limits the interactions between the two species, and limits the negative effects that the shielding of smaller particles by larger particles would otherwise impose. In this case, then, increasing the mass of the larger particles serves primarily to increase the overburden on the region of smaller particles, which in turn increases the pressures with which they are forced through the sieve. Finally, the theory predicts that flow rates through the sieve also increase as the size disparity between the particles increases. This is due to fact that the degree of particle segregation increases with increasing size disparities, the mixing between the two species is delayed for longer times, and the large particles do not ever significantly shield the small particles from passing through the sieve.

A straightforward extension of this work, requiring no further theoretical development, would be to apply the theory and boundary conditions (presented here) for binary mixtures to predict segregation phenomena on bumpy vibrating inclines can be incorporated with the boundary condition on an inclined bumpy boundary to study the segregation between different properties. In a similar fashion, a systematic application of the theory could be used to predict the segregation of confined assemblies of binary mixtures induced by both shearing and anisotropic boundary vibrations.

Because the focus of this research was on developing appropriate *form* of the boundary conditions, in all applications we used the simplest kinetic flow theories available. The rates of mass, momentum, and energy transferred at the boundary must be calculated in a manner that is

consistent with the assumptions of the flow theory employed. As a result, the choice of a simple flow theory also simplified the statistical averaging at the boundary. In principle, the theories employed could, for example, be modified to include frictional (i.e. rough) spheres. Also, the particles can be considered soft, in which the contacting particles undergo a small overlap so that collisions occur over a finite duration.

Sphericity has been assumed in most studies for many reasons. In theoretical work and computer simulations it is easy to detect a collision of round particles, as particles are in contact whenever their centers are two radii apart. For out-of-round particles, the contact decision becomes much more complicated, as the orientation of the particle (which changes as the particle rotates) must be taken into account. Large-aspect-ratio particles may have preferred orientations of their principal axes within a given flow field. Also, from an experimental point of view, aspherical particles are difficult because of particle breakage as the experiment proceeds, causing a slow degradation of the particle properties.

Even if particle roughness and non-spherical particle geometries are ignored, however, there is a need to develop a kinetic theory framework for polydispersed systems which, at the very least, contain particles of many sizes. Such efforts would more closely model real granular systems that contain a range of different particles with a range of different properties.

References

Ahn, H., Brennen, C.E., Sabersky, R.H., [1988]. Experiments on chute flows of granular materials. <u>Micromechanics of Granular Materials</u>, 339-348.

Ahn, H., Brennen, C.E., Sabersky, R.H., [1991]. Measurements of velocity, velocity fluctuation, density, and stresses in chute flows of granular materials. <u>Journal of Applied Mechanics</u>, 58, 792-803.

Ahn, H., Brennen, C.E., Sabersky, R.H., [1992]. Analysis of the fully developed chute flow of granular materials. <u>Journal of Applied Mechanics</u>, 59, 109-119.

Alam, M., Luding, S., [2002]. How good is the equipartition assumption for the transport properties of a granular mixture?. <u>Granular Matter</u>, 4, 3, 139–142.

Alam, M., Luding, S., [2003]. Rheology of bi-disperse granular mixtures via event driven simulations. <u>Journal of Fluid Mechanics</u>, 476, 69-103.

Allen, T., [2003]. Particle size analysis by sieving, Powder Sampling and Particle Size Determination. <u>Elsevier</u>, 208-250, Ch.4.

Anderson, K. G., Jackson, R., [1992]. A comparison of the solutions of some proposed equations of motion of granular materials for fully developed flow down inclined planes. <u>Journal of Fluid Mechanics</u>, 241, 145-168.

Apling, A.C., [1984]. Blinding of screens by sub-sieve sized particles. Transactions of the Institution of Mining and Metallurgy, Section C, <u>Mineral Processing and Extractive Metallurgy</u> 93,C92-C94.

Arnarson, B.O., Jenkins, J.T., [2004]. Binary mixtures of inelastic spheres: Simplified constitutive theory. <u>Physics of Fluids</u>, 16, 12, 4543-4550.

Azanza, E., Chevoir, F., Moucheront, P., [1999]. Experimental study of collisional granular flows down an inclined plane. <u>Journal of Fluid Mechanics</u>, 400, 199-227.

Baran, O., Ertas, D., Halsey, T.C., Grest, G.S., Lechman, J.B., [2006]. Velocity correlations in dense gravity-driven granular chute flow. <u>Physical Review E</u>, 74, 5, 051302-051312.

Behringer, R.P., [1993]. The dynamics of flowing sand. <u>Nonlinear Science Today</u>, 3, 1-15.

Bideau, D., Hansen, A., [1993]. Disorder and Granular Media. Elsevier, North-Holland, Amsterdam.

Brennen, C.E., Ghosh, S., Wassgren, C., [1993]. Vertical oscillation of a bed of granular material. . Journal of Applied Mechanics, 63, 1, 156-161.

Brey,. J.J., Ruiz-Montero, M.J., Moreno, F., [2000]. Boundary conditions and normal state for a vibrated granular fluid. Physical Review E, 62, 4, 5339-5326.

Brilliantov, N.V., Poschel, T., [2004]. Kinetic Theory of Granular Gases. Oxford University Press.

Brito, R., Enriquez, H., Godoy, S., Soto1, R., [2008]. Segregation induced by inelasticity in a vibrofluidized granular mixture. Physical Review E, 77, 061301-061307.

Campbell, C.S., [1990]. Rapid granular flows. Annual Review of Fluid Mechanics, 22, 57-90.

Ciamarra, M.P., De Vizia, M.D., Fierro, A., Tarzia, M., Coniglio, A., Nicodemi, M., [2006]. Granular species segregation under vertical tapping: Effects of size, density, friction, and shaking amplitude. Physical Review Letters, 96, 5, 058001-058005.

Clelland, R., Hrenya, C.M., [2002]. Simulations of a binary-sized mixture of inelastic grains in rapid shear flow. Physical Review E, 65, 3, 031301-031311.

Clement, E., Rajchenbach, J., [1991]. Fluidization of a bidimensional powder. Europhysics Letters, 16, 2, 133-138.

Clement, E., Vanel, L., Rajchenbach, J., Duran, J., [1996]. Pattern formation in a vibrated two-dimensional granular layer. Physical Review E, 53, 3, 2972-2975.

Daerr, A., Douady, S., [1999]. Two types of avalanche behaviour in granular media. Nature, 399, 241-243.

De Silva, S.R., Dyroy, A., Enstad, G.G., [2000]. Segregation mechanisms and their quantification using segregation testers. In IUTAM Symposium on Segregation in Granular Flows, ed. By Rosato, A.D, Blackmore, D.L., Boston: Kluwer Academic Publishers. 11-29.

Dippel, S., Luding, S., [1995]. Simulations on size segregation: geometrical effects in the absence of convection. Journal de Physique I (France), 5, 1527-1537.

Douady, S., Fauve, S., Larouche, C., [1989]. Subharmonic instabilities and defects in a granular layer under vertical vibrations. Europhysics Letters, 8, 7, 621-627.

Drake, T.G., [1991]. Granular flow: Physical experiments and their implications for microstructural theories. Journal of Fluid Mechanics, 225, 121–152.

Duran, J., [1996]. Sand, Power, and Grains. Springer, New York.

Ennis, B.J., Green, J., Davis, R., [1994]. The legacy of neglect in the US. Chemical Engineering Progress, 90, 32-43.

Evesque, P., Rajchenbach, J., [1989]. Instability in a sand heap. Physical Review Letters, 62, 1, 44-46.

Faraday, M., [1831]. On a peculiar class of acoustical figures; and on certain forms assumed by groups of particles upon vibrating elastic surfaces, Phil. Trans. Roy. Soc. London, 52, 299-340.

Farrell, M., Lun, C.K.K., Savage, S.B., [1986]. A simple kinetic theory for granular flow of binary mixtures of smooth, inelastic, spherical particles. Acta Mechanica, 63, 1-4, 45 -60.

Felix, G., Thomas, N., [2004]. Relation between dry granular flow regimes and morphology of deposits: formation of levees in pyroclastic deposits. Earth and Planetary Science Letters, 221, 1-4, 197–213.

Forterre, Y., Pouliquen, O., [2001]. Longitudinal vortices in granular flows. Physical Review Letters, 86, 26, 5886-5889.

Forterre, Y., Pouliquen, O., [2002]. Stability analysis of rapid granular chute flows: formation of longitudinal vortices. Journal of Fluid Mechanics, 467, 361-387.

Forterre, Y., Pouliquen, O., [2008]. Flows of dense granular media. Annual Review of Fluid Mechanics, 40, 26, 1-24.

Gallas, J.A.C., Herrmann, H.J., Sokolowski, S., [1992]. Convection cells in vibrating granular media. Physical Review Letters, 69, 9, 1371-1374.

Goldhirsch , I., [2003]. Rapid granular flows. Annual Review of Fluid Mechanics, 35, 267-293. Goldhirsch, I., Tan, M.L., [1996]. The single-particle distribution function for rapid granular shear flows of smooth inelastic disks. Physics of Fluids, 8, 7, 1752-1763.

Hanes, D.M., Walton, O.R., [2000]. Simulations and physical measurements of glass spheres flowing down a bumpy incline. Powder Technology, 109, 1-3, 133-144.

Hong, D.C., Quinn, P.V., Luding, S., [2001]. Reverse Brazil nut problem: Competition between percolation and condensation Physical Review Letters, 86, 15, 3423-3426.

Hopkins, M.A., [1985]. Collisional stresses in a rapidly deforming granular flow. M.S. thesis, Clarkson University, Potsdam, New York.

Hsiau, S.S., Hunt, M.L., [1996]. Granular thermal diffusion in flows of binary-sized mixtures. Acta Mechanica, 114, 1-4, 121-137.

Hsiau. S.S, Wang, J.I., [1999]. Segregation process of a binary granular mixture in a shaker. Advanced Powder Technology, 10, 3, 245-253.

Hsiau, S.S., Yang, S.C., [2003]. Numerical simulation of self-diffusion and mixing in a vibrated granular bed with the cohesive effect of liquid bridge, Chemical Engineering Science, 58, 2, 339-351.

Hui, K., Half, P.K., Ungar, J.E., Jackson, R., [1984]. Boundary conditions for high shear grain flows. Journal of Fluid Mechanics, 145, 223-233.

Huilin, L., Wenti, L., Rushan, B., Lidan, Y., Gidaspow, D., [2000]. Kinetic theory of fluidized binary granular mixtures with unequal granular temperature Physica A, 284, 1-4, 265-276.

Hunt, M.L., Hsiau, S.S., Hong, K.T., [1994]. Particle mixing and volumetric expansion in a vibrated granular bed. Journal of Fluids Engineering, 116, 4, 785-791.

Jackson, R. [1991], Aerated and vibrated chute feeders for particulate materials. Final Project Report, US Departmenr of Energy, DOE Contract DE-FG22-86PC90518.

Jaeger, H.M., Knight, J.B., Liu, C.H., Nagel, S.R., [1994]. What is shaking in the sandbox. Material Research Society Bulletin, 19, 5, 25-31.

Jaeger, H.M., Nagel, S.R., [1992]. Physics of the granular state. Science, 255, 5051, 1523–1531. Jenkins, J.T., [1992]. Boundary conditions for rapid granular flows: flat, frictional walls. Journal of Applied Mechanics, 59, 1, 120–127.

Jenkins, J.T., [1994]. Rapid granular flow down inclines. Applied Mechanics Reviews, 47, 6 s, S240–S244.

Jenkins, J.T., [2001]. Boundary conditions for collisional grain flows at bumpy, frictional walls. Physics and Astronomy, 564, 125-139.

Jenkins, J.T., [2006]. Dense shearing flows of inelastic disks. Physics of Fluids, 18, 10, 103307-103316.
Jenkins, J.T., [2007]. Dense inclined flows of inelastic spheres. Granular Matter, 10, 1, 47-52.

Jenkins, J.T., Louge M.Y., [1997]. On the flux of fluctuation energy in a collisional grain flow at a flat, frictional wall. Physics of Fluids, 9, 10, 2835-2841.

Jenkins, J.T., Mancini, F., [1989]. Kinetic theory for binary mixtures of smooth, nearly elastic spheres. Physics of Fluids A, 1, 12, 2050-2058.

Jenkins, J.T., Richman M.W., [1985a]. Grad's 13-moment system for a dense gas of inelastic spheres. Archieve for Rational Mechanics and Analysis, 87, 4, 355-377.

Jenkins, J.T., Richman M.W., [1985b]. Kinetic theory for plane flows of a dense gas of identical, rough, inelastic, circular disks. Physics of Fluids, 28, 12, 3485-3494.

Jenkins, J.T., Richman M.W., [1986]. Boundary conditions for plane flows of smooth nearly elastic, circular disks. . Journal of Fluid Mechanics, 171, 53-69.

Johnson, P.C., Nott, P., Jackson, R., [1990]. Frictional–collisional equations of motion for particulate flows and their applications to chutes. Journal of Fluid Mechanics, 210, 501-535.

Jullien, R., Meakin, P., Pavlovitch, A., [1992]. Three-dimensional model for particle size segregation by shaking. Physical Review Letters, 69, 4, 640-643.

Khakhar, D.V., McCarthy, J.J., Ottino, J.M., [1999]. Mixing and segregation of granular materials in chute flows. Chaos, 9, 3, 594-610.

Knight, J.B., Jaeger, H.M., Nagel, S.R., [1993]. Vibration-induced size separation in granular media: the convection connection, Physical Review Letters, 70, 24, 3728-3731.

Knowlton, T.M., Carson, J.W., Klinzing, G.E., Yang, W.C, [1994]. The importance of storage, transfer, and collection. Chemical Engineering Process, 90, 44-54.

Kudrolli, A., [2004]. Size separation in vibrated granular matter. Reports on Progress in Physics, 67, 3, 209-247.

Kumaran, V., [2006a]. The constitutive relations for the granular flow of rough particles, and its application to the flow down an inclined plane. Journal of Fluid Mechanics, 561, 1-42.

Kumaran, V., [2006b]. Kinetic theory for the density plateau in the granular flow down an inclined plane. Europhysics Letters, 73, 2, 232-238.

Kumaran, V., [2008]. Dense granular flow down an inclined plane: from kinetic theory to granular dynamics. Journal of Fluid Mechanics, 599, 121–168.

Kumaran, V., [2009]. Dynamics of dense, sheared granular flows. Part I: Structure and diffusion Journal of Fluid Mechanics, 632, 109-144.

Lan, Y., Rosato, A.D., [1995]. Macroscopic behavior of vibrating beds of smooth inelastic spheres. Physics of Fluids, 7, 8, 1818-1831.

Lan, Y., Rosato, A.D., [1997]. Convection related phenomena in granular dynamics simulations of vibrated beds. Physics of Fluids, 9, 12, 3615-3624.

Leschonski, K., [1979]. Sieve analysis, the Cinderella of particle size analysis methods. Powder Technology, 24, 115-124.

Liu, K.S., [2009]. Some factors affecting sieving performance and efficiency. Powder Technology, 193, 208-213.

Lopez de Haro, M., Cohen, E.G.D., Kincaid, J.M., [1983]. The Enskog theory for multicomponent mixtures. I. Linear transport theory. Journal Chemical Physics, 78, 5, 2746-2760.

Louge, M.Y., [2003]. Model for dense granular flows down bumpy surfaces. Physical Review Letters, 67, 6, 061303-061313.

Louge, M.Y., Keast, S.C., [2001]. On dense granular flows down flat frictional inclines. Physics of Fluids, 13, 5, 1213-1233.

Lun, C.K.K., [1991]. Kinetic theory for granular flow of dense, slightly inelastic, slightly rough spheres. Journal of Fluid Mechanics, 223, 539-559.

Lun, C.K.K., Bent, A. A., [1994]. Numerical simulations of inelastic frictional spheres in simple shear flow. Journal of Fluid Mechanics, 258, 335-353.

Lun, C.K.K., Savage, S.B., [1987]. A simple kinetic theory for granular flow of rough, inelastic, spherical particles. Journal of Applied Mechanics, 54, 1, 47-53.

McNamara, S., Barrat, J-L., [1997]. Energy flux into a fluidized granular medium at a vibrating wall. Physical Review E, 55, 7767-7770.

Mehta, A., Barker, G.C., [1994]. The dynamics of sand. Physics of Fluids, 57, 4, 383-416.

Melo, F., Umbanhowar, P.B., Swinney, H.L., [1995]. Hexagons, kinks, and disorder in oscillated granular layers. Physical Review Letters, 75, 21, 3838-3841.

Mitarai, N., Nakanishi, H., [2004]. Linear stability analysis of rapid granular flow on a slope and density wave formation. Journal of Fluid Mechanics, 507, 309-334.

Mitarai, N., Nakanishi, H., [2005]. Bagnold scaling, density plateau, and kinetic theory analysis of dense granular flow. Physical Review Letters, 94, 12, 128001-128005.

Moon, B.Y., Kim, K.H., Kwak, K.H., Kang, G.J., Hong, C.H., [2008]. Dynamic analysis and design of separation screen mechanism in a plant of moisturized wastes. International Journal of Modern Physics B, 22, 1449-1454.

Nedderman, R.M., [1992]. Statics and Kinematics of granular Materials. Cambridge University Press, UK.

Nott, P., Jackson, R., [1992]. Frictional–collisional equations of motion for granular materials and their application to flow in aerated chutes. Journal of Fluid Mechanics, 241, 125-144.

Ogawa, S., [1978]. Multitemperature theory of granular materials. [edited by Cowin, S.C., and Satake, M.] . Proceedings of U.S.-Japan Symposium On Continuum Mechanics and Statistical Approaches to the Mechanics of Granular Media, page 208. Gakujutsu Bunken Fukyu-kai, Japan.

Poschel, T., Luding, S., [2001]. Lecture Notes in Physics Berlin and Heidelberg: Springer, 125-139.

Pouliquen, O., [1999]. Scaling laws in granular flows down a bumpy inclined plane. Physics of Fluids, 11, 3, 542-549.

Prescott, J.K., Carson, J.W., [2000]. Analyzing and overcoming industrial blending and segregation problems. IUTAM Symposium on Segregation in Granular Flows. [edited by Rosato, A.D., and Blackmore, D. L.]. Kluwer Academic Publishers, 89-101.

Rericha, E.C., Bizon, C., Shattuck, M.D., Swinney, H.L., [2001]. Shocks in supersonic sand. Physical Review Letters, 88, 1, 014302-014306.

Richman, M.W., [1988]. Boundary conditions based upon a modified Maxwellian velocity distribution for flows of identical, smooth, nearly elastic spheres. Acta Mechanica, 75, 1-4, 227-240.

Richman, M.W., [1992]. Boundary conditions for granular flows at randomly fluctuating bumpy boundaries. Mechanics of Materials, 16, 205-210.

Richman, M.W., Chou, C.S., [1988]. Boundary effects on granular shear flows of smooth disks. Journal of Applied Mathematics and Physics (ZAMP), 39, 6, 885-901

Richman, M.W., Marciniec, R.P., [1988]. Gravity-driven granular flows of smooth inelastic spheres down bumpy inclines. Journal of Applied Mechanics.

Richman, M.W., Martin, R.E., [1992]. The effects of anisotropic boundary vibrations on confined, thermalized, granular assemblies. Proc. of the 9th ASCE engineering conference [ed. Lutes, Niedzwedki], 900-903.

Richman, M.W., Martin, R.E., [1993]. Confined granular flows induced by identical, parallel, vibrating boundaries. Proc. of symposium on developments in Non-Newtonian flows, ASME winter annual meeting.

Richman, M.W., Wang, L., [1995]. Granular flows through vibrating surfaces with holes. SES 32th Annual Technical Meeting, Oct. 1995.

Richman, M.W., Wang, L., [1996]. Thermalized states of granular material flowing through vibrating sieves. ASCE Engineering Mechanics Conference, May. 1996.

Rosato, A. D., Strandburg, K.J., Prinz, F.B., Swendsen, R.H. [1987]. Why the Brazil nuts are on top: Size segregation of particulate matter by shaking. Physical Review Letters, 58, 10, 1038-1041.

Savage, S.B., [1979]. Gravity flow of cohesionless granular materials in chutes and channels. Journal of Fluid Mechanics, 92, 1, 53-96.

Savage, S.B., [1988]. Streaming motions in a bed of vibrationally fluidized dry granular material. Journal of Fluid Mechanics, 194, 457-478.

Savage, S.B., [1992]. Numerical simulation of couette flow of granular materials: Spatio-temporal coherence and 1/f noise. In Physics of Granular Media, 343-362.

Savage, S.B., Jeffrey, D.J., [1981]. The stress tensor in a granular flow at high shear rates. Journal of Fluid Mechanics, 110, 255-272.

Savage, S.B., Sayed, M., [1984]. Stresses developed by dry cohensionless granular materials in an annular shear cell. Journal of Fluid Mechanics, 142, 391-430.

Sela, N., Goldhirsch, I., [1998]. Hydrodynamic equations for rapid flows of smooth inelastic spheres to Burnett order. Journal of Fluid Mechanics, 361, 41-74.

Shaviv, G., [2004]. Numerical experiments in screening theory. Astron. Astrophys, 418, 801-811.

Shinbrot, T., Muzzio, F.J., [1998]. Reverse Buoyancy in Shaken Granular Beds. Physical Review Letters, 81, 20, 4365-4368.

Silbert, L.E., Ertas, D., Grest, G.S., Halsey, T.C., Levine. D., Plimpton. S.J., [2001]. Granular flow down an inclined plane: Bagnold scaling and rheology. Physical Review E, 64, 5, 51302-51316.

Silbert, L.E., Grest, G.S., Plimpton S.J., Levine, D., [2002]. Boundary effects and self-organization in dense granular flows. Physics of Fluids, 14, 8, 2637–2646.

Silbert, L.E., Landry, J., Grest, G., [2003]. Granular flow down a rough inclined plane: Transition between thin and thick piles. Physics of Fluids, 15, 1-10.

Standish, N., Bharadwaj, A.K., Hariri-Akbari, G., [1986]. A study of the effect of operating variables on the efficiency of a vibrating screen. Powder Technology, 48, 161-172.

Staron, L., [2008]. Correlated motion in the bulk of dense granular flows. Physical Review E, 77, 5, 051304-051310.

Sultanabawa, F.M., Owens, W.G., Pandiella, S.S., [2001]. A new approach to the prediction of particle separation by sieving in flour milling. Transaction of IChemE, 79 (Part C), 211-218.

Swinney, H.L., Rericha, E.C., [2004]. Pattern formation and shock waves in granular gases. In The Physics of Complex Systems [New Advances and Perspectives]: Proc. Int. School Phys. Enrico Fermi, Course CLV 155, 173, 1-34. Amsterdam: IOS Press.

Taguchi, Y.H., [1992]. New origin of convective motion: elastically induced convection in granular materials. Physical Review Letters, 69, 9, 1367-1370.
Tang, P., Puri, V.M., [2004]. Methods for minimizing segregation: A review. Particulate Science and Technology: An International Journal, 22, 4, 321-337.

Thomas, B., Mason, M.O., Liu, Y.A., Squires, A.M., [1989]. Identifying states in shallow vibrated beds. Powder Technology, 57, 4, 267-280.

Tsai, P.H., Chang, T.S., [2009]. Effects of open trench siding on vibration-screening effectiveness using the two-dimensional boundary element method. Soil Dyn.Earthq. Eng, 29 865-873.

Utsumi, R., Hata, T., Hirano, T., Mori, H., Tsubaki, J., Maeda, T.,. [2001]. Attrition testing of granules with a tapping sieve. Powder Technology, 119, 128-133.

Warr, S., Huntley, J.M., Jacques, G.T.H., [1995]. Fluidization of a two-dimensional granular system: Experimental study and scaling behavior. Physical Review E, 52, 5, 5583-1995.

Wassgren, C.R., Brennen, C.E., Hunt, M.L., [1996]. Vertical vibration of a bed of granular material in a container. Journal of Applied Mechanics, 63, 3, 712-719.

Wildman, R.D., Jenkins, J.T., Krouskop, P.E, Talbot, J., [2006]. A comparison of the predictions of a simple kinetic theory with experimental and numerical results for a vibrated granular bed consisting

Williams, J.C., [1963]. The segregation of powders and granular materials. Fuel Society Journal, 14, 29-34.

Williams, J.C., [1976]. The segregation of particulate materials. A review. Powder Technology, 15, 245–251

Wodzinski, P., [2003]. Screening of fine granular material. Coal Prep, 23, 185-213.

Xu, H., [2003]. Collisional Granular Flows With and Without Gas Interactions in Microgravity. Ph.D. Dissertation, Cornell University, Ithaca, NY.

Xu, H., Louge, M., Reeves, A., [2003]. Solutions of the kinetic theory for bounded collisional granular flows. Continuum Mechanics and Thermodynamics, 15, 4, 321-349.

Yang, S.C., Hsiau, S.S., [2000]. Simulation study of the convection cells in a vibrated granular bed. Chemical. Engineering Science, 55, 18, 3627-3637.

Appendix 1

Limits of Integrations for the Rates of Collisional Transfer at the Sieve

With the t-τ coordinate system centered as shown in Figure 5.2, the range of integration on t is from $-S_t/2$ to $+S_t/2$, and the range of integration on τ is from $-S_\tau/2$ to $+S_\tau/2$. From symmetry, we can integrate on t from 0 to $+S_t/2$, and on τ from 0 to $+S_\tau/2$. The result of each integration are multiplied by two.

In integrating along a fiber in the t-direction, adjacent fibers in the τ-direction (and possibly adjacent fibers in the t-direction) restrict the range of φ. The extent of the restriction can depend on the location t of the point of contact between a flow particle and the fiber. Consequently, the limits of integration on φ depend on t. Similarly, integrating along a fiber in the τ- direction, the limits of integration on φ depend on τ. The limits of integration on φ are

$$-\varphi_m < \varphi < +\varphi_m \quad , \tag{A1.1}$$

where φ_m must be calculated in two different cases. In the first case, the particles of species i can pass through the sieve (i.e. $\sigma_i < S_t$ and $\sigma_i < S_\tau$). In the second case, the particles of species i cannot pass through the sieve (i.e. $\sigma_i < S_t$ and $\sigma_i > S_\tau$; or $\sigma_i > S_t$ and $\sigma_i > S_\tau$). We can assume without loss in generality that $S_t \geq S_\tau$. In both cases, we can carry out the t- and τ- integrations in closed form. In what follows, we explain the limits of integration in those two cases.

Case #1: When species i *can* pass through the sieve (i.e. $\sigma_i < S_t$ and $\sigma_i < S_\tau$):
The t-integrations must be broken into two segments. In the first range of t,

$$0 < t < \frac{1}{2}(S_t - \sigma_i) \quad , \tag{A1.2}$$

a particle that collides with a fiber in the t-direction will not make contact with the adjacent fiber
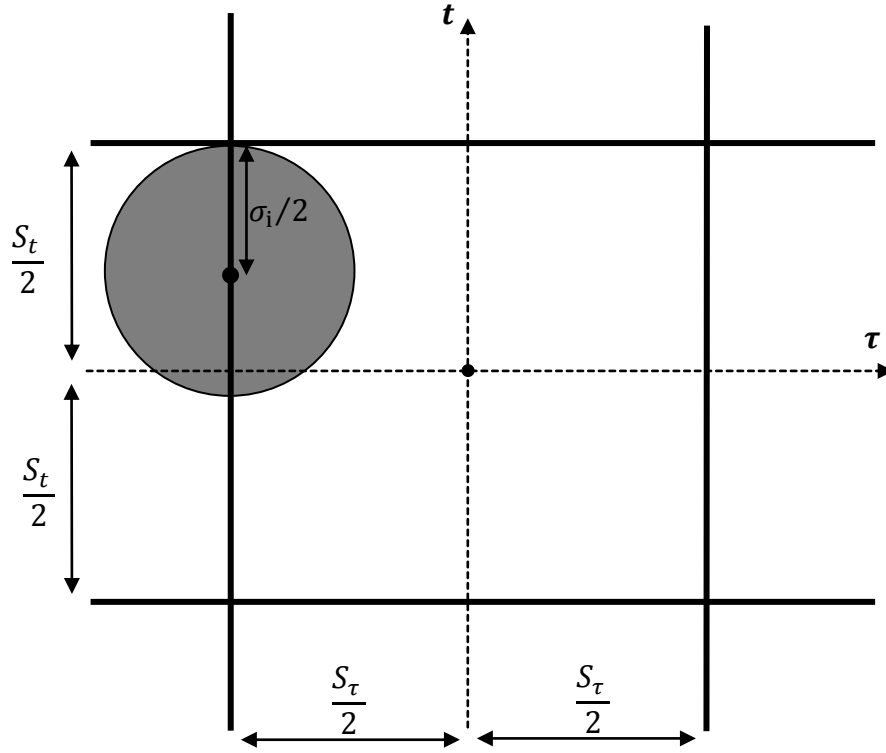
Figure 1: Top view when the particle just makes contact with a fiber in the τ- direction

in t-direction as it is rotated cylindrically about the t-fiber with which it collides. In this range of t, the limits of integration given by (A1.1) where on φ are:

$$\varphi_m = \frac{\pi}{2} \quad .$$
(A1.3)

However, for the values of t in the range

$$\frac{1}{2}(S_t - \sigma_i) < t < \frac{S_t}{2} \quad ,$$
(A1.4)

the particle will make contact with a fiber in the τ-direction at a cylindrical angle of rotation φ_m that depends on the location t. The angle φ_m is calculated as follows:

From the right triangle shown in Figure 2a, the distance $D(t)$, which is the diameter of the circular slice of the particle directly above the fiber in the τ- direction:

$$D(t) = \sqrt{\sigma_i{}^2 - (S_t - 2t)^2} \quad .$$
(A1.5)
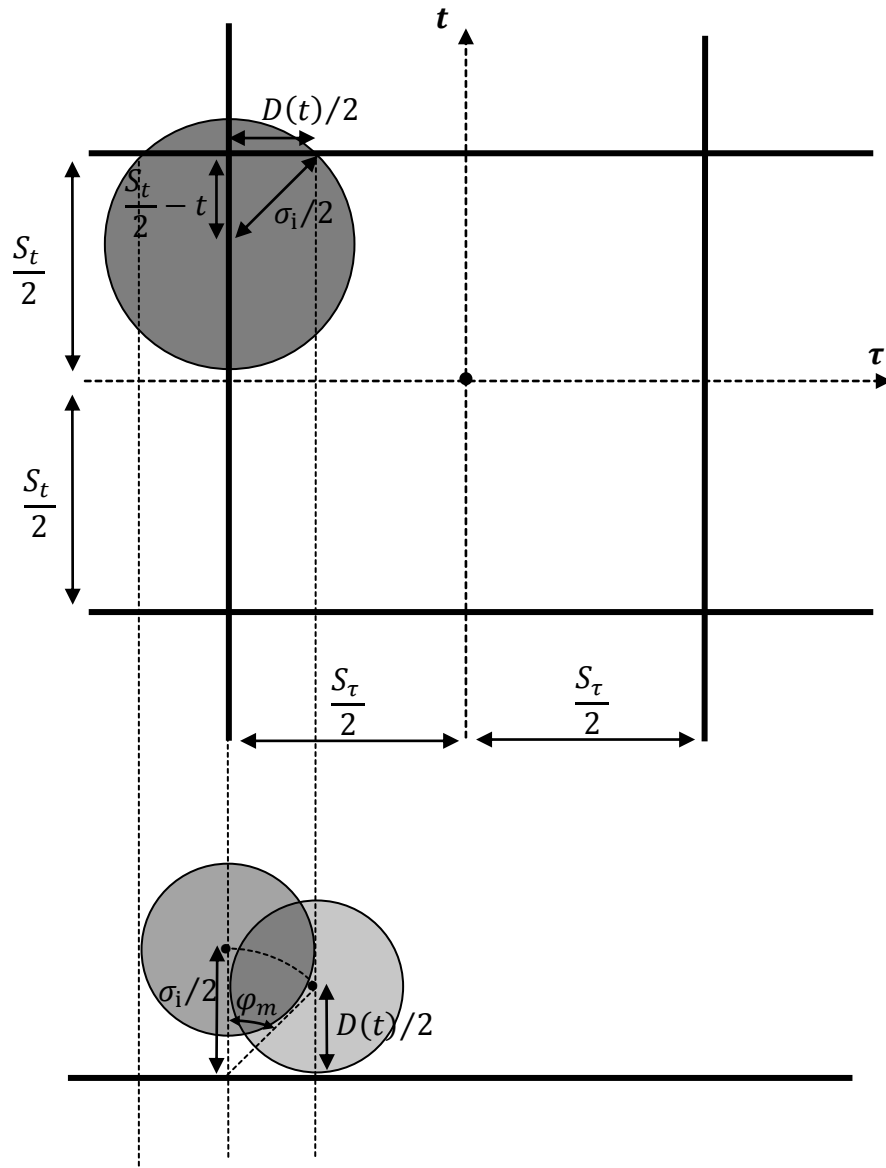
Figure 2: Top view (a) and side view (b) when a particle is in contact with a

fiber in the τ- direction

Figure 2b shows the maximum angle φ_m at which the circular slice of the particle will make

contact with the fiber in the τ-direction when it is rotated cylindrically about the t-fiber. In

Figure 2b,

$$\varphi_m(t) = \cos^{-1}\left[\frac{D(t)}{\sigma_i}\right] \quad . \tag{A1.6}$$

The limits of integration for τ are between 0 and $S_\tau/2$, and the corresponding angle φ_m is calculated according to equations (A1.1) through (A1.6) with t replaced by τ, and S_t replaced by S_τ.

Case #2: <u>When species i *cannot* pass through the sieve</u> (i.e. $\sigma_i < S_t$ and $\sigma_i > S_\tau$; or $\sigma_i > S_t$ and $\sigma_i > S_\tau$ where we can assume without loss in generality that $S_t \geq S_\tau$).

The t- integrations must be broken into two segments. In the first range of t,

$$0 < t < t^* \quad , \tag{A1.7}$$

(where the upper limit t^* of this range is to be determined) a particle that collides with a fiber in the t-direction will make contact with the adjacent fiber in t-direction as it is rotated cylindrically by an angle φ_m about the t-fiber with which it collides. From Figure 3b,

$$\varphi_m = \sin^{-1}\left[\frac{S_\tau}{\sigma_i}\right] \quad . \tag{A1.8}$$

However, for the values of t in the range

$$t^* < t < \frac{S_t}{2} \quad , \tag{A1.9}$$

the particle will make contact with a fiber in the τ-direction at a cylindrical angle of rotation φ_m that depends on the location t, and is given by equation (A1.6)

$$\varphi_m(t) = \cos^{-1}\left[\frac{D(t)}{\sigma_i}\right] \quad . \tag{A1.10}$$

The location t^* is where φ_m given by (A1.8) is equal to $\varphi_m(t^*)$ given by (A1.10). Equating the two angles gives

$$t^* = \frac{(S_t - S_\tau)}{2} \quad . \tag{A1.11}$$

The limits of integration for τ are between 0 and $S_\tau/2$, and the corresponding angle φ_m is given according to equation (A1.1) and (A1.10) with t replaced by τ, and S_t replaced by S_τ.
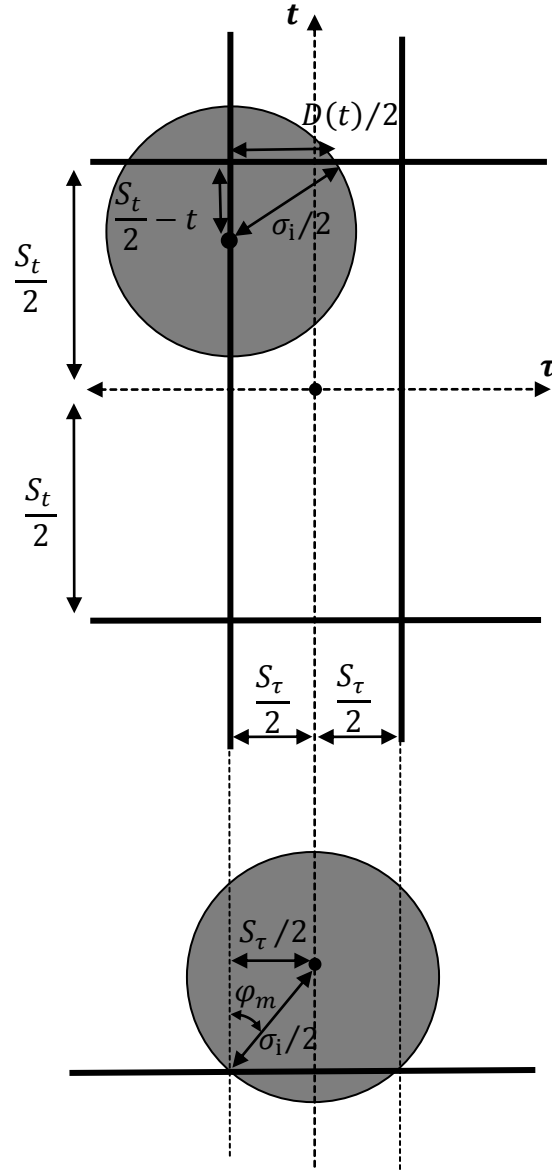
Figure 3: Top view (a) and side view (b) when a particle is in contact with a

fiber in the τ- direction

The integrations (5.29), (5.47), and (5.48) are of the form

$$
Z = \int_{-S_t/2}^{+S_t/2} \int_{-\varphi_m(t)}^{+\varphi_m(t)} F(\varphi)\, d\varphi dt \quad , \tag{A1.12}
$$

where $F(\varphi)$ is an even function of φ and $\varphi_m(t)$ is given by (A1.3) and (A1.6) when the particle

can pass through the sieve, and by (A1.8) and (A1.10) when the particle cannot pass through the

sieve. Using symmetry with respect to t and φ and reversing the order of integration, we can write J

$$Z = 4 \int_0^{\varphi_{max}} \int_0^{t_{max}(\varphi)} F(\varphi) \, dt \, d\varphi \quad , \tag{A1.13}$$

where $t_{max}(\varphi)$ is obtained by inverting equation (A1.6) or (A1.10):

$$t_{max} = \frac{(S_t - \sigma_i \sin \varphi)}{2} \quad ; \tag{A1.14}$$

and $\varphi_{max} = \pi/2$ when the particle can pass, and $\varphi_{max} = \sin^{-1}[S_\tau/\sigma_i]$ when the particle cannot pass. In this way, the t integrations can be carried out easily and J simplifies to the single integral

$$Z = \int_0^{\varphi_{max}} F(\varphi) \frac{(S_t - \sigma_i \sin \varphi)}{2} \, d\varphi \tag{A1.15}$$

Appendix 2

First Order Corrections to Transfer Rates at the Sieve

In Section 6.4, we have described the procedure to generate improvements to the quasi-steady solutions for flows of mono-sized assemblies through vibrating sieves. These improvements are based on the following decompositions of the rates of momentum and energy transferred at the boundary:

$$M^C(t) = M_0^C\big(m_t(t)\big) + M_1^C(v_0, \mathcal{T}_0, u_1) \quad ; \tag{A2.1}$$

$$\widetilde{M}^T(t) = \widetilde{M}_0^T\big(m_t(t)\big) + \widetilde{M}_1^T(v_0, \mathcal{T}_0, u_1) \quad ; \tag{A2.2}$$

$$\mathcal{F}(t) = \mathcal{F}_0\big(m_t(t)\big) + \mathcal{F}_1(v_0, \mathcal{T}_0, u_1) \quad ; \tag{A2.3}$$

$$\mathcal{D}(t) = \mathcal{D}_0\big(m_t(t)\big) + \mathcal{D}_1(v_0, \mathcal{T}_0, u_1) \quad ; \tag{A2.4}$$

and

$$\widetilde{\mathcal{E}}^T = \widetilde{\mathcal{E}}_0^T\big(m_t(t)\big) + \widetilde{\mathcal{E}}_1^T(v_0, \mathcal{T}_0, u_1) \quad ; \tag{A2.5}$$

as well as for the shielding factor at the boundary is:

$$\lambda(t) = \lambda_0\big(m_t(t)\big) + \lambda_1(v_0, \mathcal{T}_0, u_1) \quad . \tag{A2.6}$$

The mass flow rate $\dot{m}$, which like the mean velocity has no zeroth order contribution, has the lowest order contribution $\dot{m}_1\big(m_t(t)\big)$ given by equation (6.34).

The first order collisional momentum transfer rate M_1^C is, from (6.15), equal to the sum

$$M_1^C = M_{1t}^C + M_{1\tau}^C \quad . \tag{A2.7}$$

By employing (6.38), (6.39), (A2.1), and (A2.6) in integral (6.16), and by collecting first order terms, we find that

$$M_{1t}^C = \frac{2(1+e_w)r_\tau}{\sqrt{2}\pi^{3/2}} \left\{ v_0\lambda_0 \left[\frac{\pi^{1/2}}{2\sqrt{2}}\left(1 - \frac{r_t}{2}\right)\mathcal{T}_1 + u_1\alpha(\Omega_0^2 + V_\tau^2)^{1/2} \right. \right.$$

$$\times \int_0^{2\pi} (1 + R_\tau\cos^2\varphi)^{1/2}(1 - r_t\sin\varphi)\cos^2\varphi \, d\varphi$$

$$+ \frac{1}{2}\frac{\partial u_1}{\partial Y}\left[\alpha(\Omega_0^2 + V_\tau^2)^{1/2}\int_0^{\pi/2}(1 + R_\tau\cos^2\varphi)^{1/2}(1 - r_t\sin\varphi)(\cos^2\varphi - \cos^3\varphi)d\varphi\right]$$

$$+ (v_1\lambda_0 + v_0\lambda_1)\frac{\pi^{1/2}}{2\sqrt{2}}\left[\left(1 - \frac{r_t}{2}\right)\mathcal{T}_0 + \alpha^2\left(\frac{2}{3}V_n^2 + \frac{V_\tau^2}{3}\right) - \frac{\alpha^2 r_t}{4}(V_n^2 + V_\tau^2)\right]\right\},$$

$$\text{(A2.8)}$$

where R_t and R_τ are given by (6.17) and are evaluated at Ω_0. The term $M_{1\tau}^C$ in (A2.7) is given by (A2.8) in which r_t, r_τ, R_τ, and V_τ are replaced by r_τ, r_t, R_t, and V_t.

The transport contribution $\widetilde{M}_1^T$ is obtained by employing (6.38), (6.39), and (A2.2) in integral (6.14), and by collecting first order terms. In this manner we find that

$$\widetilde{M}_1^T = -\frac{(1 - r_t)(1 - r_\tau)}{2}\left[v_0\mathcal{T}_1 + v_1\mathcal{T}_0 + \frac{2v_0\mathcal{T}_0\Phi}{\pi^{1/2}}\right] \quad , \tag{A2.9}$$

where the ratios R_t and R_τ given by (6.17), and Φ given by (6.12) are evaluated at Ω_0.

The first order energy transfer rates $\mathcal{F}_1$ and $\mathcal{D}_1$ are, from (6.19), equal to the sums

$$\mathcal{F}_1 = \mathcal{F}_{1t} + \mathcal{F}_{1\tau} \quad \text{and} \quad \mathcal{D}_1 = \mathcal{D}_{1t} + \mathcal{D}_{1\tau} \quad . \tag{A2.10}$$

By employing (6.38), (6.39), (A2.3), and (A2.6) in integral (6.20), and by collecting first order terms, we find that

$$\mathcal{F}_{1t} = \frac{2(1+e_w)r_\tau\alpha(\Omega_0^2 + V_\tau^2)}{\sqrt{2}\pi^{3/2}}\left\{v_0\lambda_0\left[\int_0^{\pi/2}(1+R_\tau cos^2\varphi)^{1/2}\right.\right.$$

$$\times\left[\alpha^2(\Omega_0^2 + V_\tau^2)\frac{dR_\tau}{dT_0}\mathcal{T}_1cos^2\varphi + \mathcal{T}_1R_\tau cos^2\varphi\right](1-r_t sin\varphi)d\varphi$$

$$+\int_0^{\pi/2}\frac{1}{2}\frac{dR_\tau}{dT_0}\frac{\mathcal{T}_1cos^2\varphi}{(1+R_\tau cos^2\varphi)^{1/2}}[\alpha^2(\Omega_0^2 + V_\tau^2)(1+R_\tau cos^2\varphi) - \mathcal{T}_0](1-r_t sin\varphi)d\varphi$$

$$+\frac{1}{2}\frac{\mathcal{T}_1}{\alpha^2(\Omega_0^2 + V_\tau^2)}\int_0^{\pi/2}(1+R_\tau cos^2\varphi)^{1/2}[\alpha^2(\Omega_0^2 + V_\tau^2)(1+R_\tau cos^2\varphi) - \mathcal{T}_0](1-r_t sin\varphi)d\varphi\bigg]$$

$$+(v_1\lambda_0 + v_0\lambda_1)\int_0^{\pi/2}(1+R_\tau cos^2\varphi)^{1/2}[\alpha^2(\Omega_0^2 + V_\tau^2)(1+R_\tau cos^2\varphi) - \mathcal{T}_0](1-r_t sin\varphi)d\varphi\bigg\}$$

$$(A2.11)$$

where R_t and R_τ are given by (6.17) and are evaluated at Ω_0 . The term $\mathcal{F}_{1\tau}$ in (A2.10) is given by (A2.11) in which r_t, r_τ, R_τ, and V_τ are replaced by r_τ, r_t, R_t, and V_t.

By employing (6.38), (6.39), (A2.4), and (A2.6) in integral (6.21), and by collecting first order terms, we find that

$$\mathcal{D}_{1t} = \frac{(1-e_w^2)r_\tau}{\sqrt{2}\pi^{3/2}}\alpha^3(\Omega_0^2 + V_\tau^2)^{3/2}\left\{v_0\lambda_0\left[\frac{3}{2\alpha^2(\Omega_0^2 + V_\tau^2)}\mathcal{T}_1\right.\right.$$

$$\times\int_0^{\pi/2}(1+R_\tau cos^2\varphi)^{3/2}(1-r_t sin\varphi)d\varphi$$

$$+\int_0^{\pi/2}\frac{3}{2}\frac{dR_\tau}{dT_0}\mathcal{T}_1cos^2\varphi(1+R_\tau cos^2\varphi)^{1/2}(1-r_t sin\varphi)d\varphi\bigg]$$

$$+(\nu_1\lambda_0 + \nu_0\lambda_1) \int_0^{\pi/2} (1 + R_\tau cos^2\varphi)^{3/2}(1 - r_t sin\varphi)d\varphi \Bigg\}$$

<div align="right">(A2.12)</div>

where R_t and R_τ are given by (6.17) and are evaluated at Ω_0 . The term $\mathcal{D}_{1\tau}$ in (A2.10) is given by (A2.12) in which r_t, r_τ, R_τ, and V_τ are replaced by r_τ, r_t, R_t, and V_t.

The transport contribution $\tilde{\mathcal{E}}_1^T$ is obtained by employing (6.38), (6.39), and (A2.5) in integral (6.14), and by collecting first order terms. In this manner we find that

$$\tilde{\mathcal{E}}_1^T = \frac{(1 - r_t)(1 - r_\tau)\alpha^3}{2^{3/2}\pi^{1/2}\,(\Omega_0^2 + V_n^2)^{1/2}}\Big\{\nu_0\Omega_0^2\sqrt{\pi}\Phi\,(3 + \Omega_0^2) + \nu_1\Omega_0^2(3 + 2\Omega_0^2) + 2(\Omega_0^2 + V_n^2)\nu_0\Omega_1^2$$

$$+ \frac{\nu_0\Omega_1^2}{(\Omega_0^2 + V_n^2)}\left[\left(\frac{\Omega_0^2}{2} + V_n^2\right) + 2\Omega_0^2\left(\frac{3\Omega_0^2}{2} + 2V_n^2\right)\right]\Big\} - \frac{(1 - r_t)(1 - r_\tau)\alpha^2\nu_0\mathcal{T}_0}{2}u_1$$

<div align="right">(A2.13)</div>

where the ratios R_t and R_τ given by (6.17), and Φ given by (6.12) are evaluated at Ω_0.